BOLTZMANN APPROACH TO COUPLED SPIN AND HEAT CURRENTS

DISSERTATION

zur Erlangung des Grades eines
Doktors der Naturwissenschaften

am Fachbereich Physik der
Freien Universität Berlin

vorgelegt von

Rico Schmidt

Berlin, 2020

Erstgutachter   Prof. Dr. Piet W. Brouwer
Zweitgutachter   Prof. Felix von Oppen, PhD

Tag der Disputation: 24.02.2022

Abstract

These days, information technology does not only demand fast and secure transport of the information but also energy efficiency in the process of doing so. The unintentional generation of waste heat in electrically driven computers is an ongoing challenge. With the discovery of the spin Seebeck effect, a very potent candidate was found for reusing waste heat to drive spin currents that can be used for reliable long-range information transport.

The foundation for this effect was set at the beginning of the 19th century with the discovery of the Seebeck and Peltier effects. The Seebeck effect is referred to as a charge current flowing through the metal in response to a local temperature gradient whereas the Peltier effect describes the inverse phenomenon. Together these thermoelectric effects describe the mutual conversion of heat and charge currents and are widely used in technical applications for electrical cooling and reusing waste heat that is produced in large power supply machines.

Electrons do not only carry a charge but also a magnetic moment called spin. It opens up an additional degree of freedom for the interaction with heat currents. The corresponding very active research area is called spin caloritronics. The spin Seebeck effect is the magnetic analogon to the Seebeck effect in a ferromagnetic sample. It was shown that this effect even exists in insulating ferromagnets where no itinerant electrons are present, thus leading to very low damping of the excited magnetic spin waves and interesting applications.

The goal of this thesis is to set up a theoretical foundation for a description of the mutual interaction of lattice and spin waves based on the Boltzmann transport equation. It is crucial to understand spin-caloric effects as the spin Seebeck effect in ferromagnetic insulators on a microscopic level. In the first part, we explain how a phenomenological model of weakly interacting spin and lattice waves can be used to explain the magnetic-field dependence of the spin Seebeck effect at high temperatures when inelastic scattering dominates the relaxation of the lattice and spin waves. In the second part, we examine the influence of strong spin-orbit coupling that leads to hybridized spin-lattice transport, predominantly at low temperatures. Finally, we bridge the gap between coherent and incoherent regimes.

Kurzfassung

Heutzutage fordert die Informationstechnologie nicht nur einen schnellen und sicheren Transport von Informationen, sondern auch Energieeffizienz. Die ungewollte Erzeugung von Abwärme in elektrisch betriebenen Computern ist eine anhaltende Herausforderung. Mit der Entdeckung des Spin-Seebeck-Effekts wurde ein potentieller Kandidat für die Wiederverwendung von Abwärme gefunden um Spinströme anzutreiben, die für einen zuverlässigen Informationstransport über makroskopische Entfernungen verwendet werden können.

Der Grundstein für diesen Effekt wurde vor 200 Jahren mit der Entdeckung des Seebeck- und Peltier-Effekts gelegt. Als Seebeck-Effekt bezeichnet man den Ladungsstrom, der als Reaktion auf einen Temperaturgradienten durch ein Metall fließt. Der Peltier-Effekt ist das inverse Phänomen. Gemeinsam beschreiben diese thermoelektrischen Effekte die bilaterale Umwandlung von Wärme- und Ladungsströmen. Sie werden zur elektrischen Kühlung von Metallen und Wiederverwendung von Abwärme verwendet, die in großen Stromversorgungsmaschinen entsteht.

Elektronen tragen neben einer Ladung auch ein magnetisches Moment welches Spin genannt wird. Es eröffnet einen zusätzlichen Freiheitsgrad für die Wechselwirkung mit Wärmeströmen. Das Forschungsgebiet, welches sich damit befasst heißt Spin-Kaloritronik. Der Spin-Seebeck-Effekt ist das magnetische Analogon zum Seebeck-Effekt in einem Ferromagneten. Dieser Effekt tritt sogar in isolierenden Ferromagneten, bei denen keine freien Elektronen vorhanden sind, auf. Dadurch haben die angeregten magnetischen Wellen eine sehr geringe Dämpfung.

Ziel dieser Arbeit ist es eine theoretische Grundlage für eine Beschreibung der gegenseitigen Wechselwirkung von Gitter- und Spinwellen auf Basis der Boltzmann-Transportgleichung zu schaffen, da sie wichtig ist um Spin-Kalorische-Effekte wie den Spin-Seebeck-Effekt auf mikroskopischer Ebene zu verstehen. Im ersten Teil der Arbeit erklären wir, wie ein phänomenologisches Modell schwach wechselwirkender Gitter- und Spinwellen verwendet werden kann, um die Magnetfeldabhängigkeit des Spin-Seebeck-Effekts in ferromagnetischen Isolatoren bei hohen Temperaturen zu erklären, wenn inelastische Streuung die Relaxation der Gitter- und Spinwellen dominiert. Im zweiten Teil untersuchen wir bei niedrigen Temperaturen den Einfluss einer starken Spin-Bahn-Kopplung, die zu hybridisiertem Spin-Gitter-Transport führt.

Contents

1

Introduction

Almost two hundred years after the discovery of the thermoelectric Seebeck and Peltier effects [1], the observation of the spin Seebeck effect [2] in 2008 has created excitement and stimulating research in the emerging field of spin caloritronics which describes the interaction of spin and heat currents. The spin Seebeck effect was observed in a variety of materials such as metals [2], semiconductors [3], and even ferromagnetic insulators [4]. It is distinguished between "local" or also called "longitudinal" spin Seebeck effect [5, 6, 7], and "non-local" or "transverse" spin Seebeck configurations [4, 8, 9, 10, 11, 12, 13], and it shows interesting features in broad temperature and magnetic-field ranges [14, 15]. Besides the classical steady-state configurations, time-resolved measurements [16, 17, 18] gain increasing attention. Already in the early days of the experimental observations, it was pointed out that magnon-phonon interaction [19, 20] and strong phonon drag [21] are important for the understanding of the spin Seebeck effect. The importance of magnon-phonon coupling to spin-caloric effects was also indicated in other phenomena as the spin Peltier effect [22, 23, 24] which is the inverse of the spin Seebeck effect, acoustic spin pumping experiments [25, 26, 27] where spin currents in ferromagnets are generated by injecting acoustic sound waves, the Einstein–de Haas effect [28, 29] where spin angular momentum transfer to the lattice leads to mechanical rotation of the system, and long-range spin transport [30, 31] in ferromagnet–insulator heterostructures where the inter-conversion of spin currents to phonon angular momentum currents is a potent candidate for spin transport over long distances.

Surprisingly, despite its importance, most existing theories of the spin Seebeck

effect and of the general role of spin-lattice interaction in spin-caloric phenomena treat the magnon-phonon coupling only on a phenomenological level either in terms of stochastic random fields [19, 32, 33, 34] or in simplified relaxation time approximations [35, 36, 37] which are mostly represented by single numbers and give no insight into the microscopic origin of the interaction. Mostly, these models do not differentiate between magnon-phonon processes that conserve the spin angular momentum but only exchange energy between the two sub-systems and those based on relativistic effects that do not conserve the magnetization and lead to direct creation of spin currents due to phonon-to-magnon conversion. An already better investigation of magnon-phonon interaction is possible with phenomenological models based on the magneto-elastic energy [38, 20] that is derived from macroscopic symmetry considerations of the sample geometry, similarly to the phenomenological theory of "elastic strains" [39] that is used to describe phonon dynamics.

In this thesis, we go beyond these phenomenological approaches and extend the present theory by a systematic investigation of a microscopic spin-lattice model that reproduces the phenomenological state-of-the-art theory and can be used to describe coherent [20, 40] and incoherent [41] magnon-phonon transport in ferromagnetic insulators. We apply our theory to quantitatively explain the longitudinal spin Seebeck effect in YIG–Pt bilayers at low and intermediate temperatures.

The outline of the thesis is as follows:

Chapter 1 summarizes the phenomenology of the field of spin caloric transport and reviews the effects that are important to run spin Seebeck devices. Existing theories of spin-lattice transport and the spin Seebeck effect in ferromagnetic insulators are briefly summarized. We show how quasiparticle excitations of spin and lattice waves, known as magnons and phonons, are derived from Heisenberg exchange interaction and harmonic lattice Hamiltonians. The basic theory of the Boltzmann transport equation, its applications and limitations, and common techniques to reduce the complexity of the system are presented.

In Chapter 2, we evaluate the coupled spin and heat transport for a weakly coupled system of magnons and phonons in ferromagnetic insulators. We imply a hierarchy of scattering mechanisms to derive a set of "hydrodynamic" equations within a continuum model that goes beyond the relaxation time approximation. Magnon-number conserving and nonconserving magnon-phonon couplings are explicitly included in the collision integrals. We use our theory to calculate the spin Seebeck effect with a focus on the magnetic-field dependence and find that the direct conversion of phonons to magnons causes significant peaks in the spin Seebeck voltage at two critical magnetic fields [20] .

In Chapter 3, we derive a set of microscopic Boltzmann equations for strongly correlated magnon and phonon systems from a minimalistic – yet effective – spin-lattice model including spin-conserving exchange interaction as well as spin-nonconserving

spin-orbit coupling as resources for magnon-phonon coupling. We extend the most recent theory [37, 20, 41] that relies on strong inelastic magnon-magnon and phonon-phonon background scattering which instantaneously relaxes the polaron distribution functions to Planck-like distributions. We explicitly account for those processes in the collision integral. Thus, we can separate between the contributions from elastic and inelastic scattering and quantify the role of strong magnon-phonon coupling that leads to the formation of coherent magnon polaron mixed-modes. We apply our theory to longitudinal spin Seebeck setups in ferromagnetic insulators where we separate between acoustic and magnetic clean systems.

Chapter 4 concludes our findings. We present an outlook on how the steady-state theory can be extended to evaluate time-dependent spin-lattice transport. We illustrate how even in a single sublattice ferromagnetic insulator with only spin-conserving scattering a transient spin Seebeck effect can occur.

1.1 Thermoelectricity

In 1821 Thomas Johann Seebeck discovered that a steady temperature bias between the ends of a metal leads to an electrostatic potential which results in an electrical current $\mathbf{j}$ flowing through the system in the direction of the thermal gradient,

$$\mathbf{j} = -S\nabla T, \tag{1.1}$$

where S is the material-specific Seebeck coefficient and ∇T is the applied temperature gradient. The (group) velocity of the electrons is linked to their energy $\hbar\omega$ via $v = \partial\omega/\partial q$, q being the wavevector, and thus the velocity increases with energy. As a result, hot electrons move faster to the cold end than vice versa. In the progress of this energy-equilibrating process, a heat current flows through the metal which is accompanied by a charge current as each electron also carries a charge. The hotter the one end of the sample gets, the larger the temperature gradient and therefore also the charge current.

The effect can be measured in a thermocouple, which consists of two different metals that are connected to a common heat reservoir at one end and to a voltmeter at the other (cold) end of the sample, see Figure 1.1. The cold end is kept at a constant temperature. The Peltier effect describes the inverse phenomenon of controlling the heat current in metals by applying an electrical current to it. By inverting the sign of the voltage the metal can be heated up or cooled down, which makes the Peltier effect a powerful tool to electrically cool down metals [42]. The two processes are invertible and can be linked by an Onsager relation [43],

$$\Pi = TS, \tag{1.2}$$

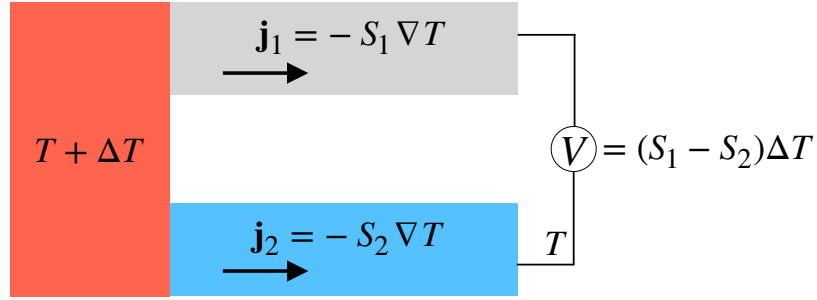where T is the system temperature and Π is the Peltier coefficient.

Figure 1.1: Seebeck effect in a thermocouple. Two metals with different Seebeck coefficients $S_{1,2}$ are connected to a common heat reservoir, held at temperature $T + \Delta T$, to the one end and to a voltmeter at a temperature T to the other end. The resulting charge currents $\mathbf{j}_{1,2}$ in the metals is proportional to the temperature gradient $\nabla T = \Delta T / L$ and leads to a Seebeck voltage $V = (S_1 - S_2)\Delta T$.

In ferromagnets the electron scattering rates for spin-up and spin-down electrons differ, which leads to spin-dependent conductivities $\sigma_{\uparrow,\downarrow}$ and Seebeck coefficients $S_{\uparrow,\downarrow}$ [44]. The spin-dependent electron current densities can be written in linear response [45],

$$\mathbf{j}_{\uparrow,\downarrow} = -\sigma_{\uparrow,\downarrow}\left(\frac{1}{e}\nabla\mu_{\uparrow,\downarrow} + S_{\uparrow,\downarrow}\nabla T\right), \tag{1.3}$$

where e is the electron charge, and $\mu_{\uparrow,\downarrow}$ are spin-chemical potentials. When a temperature gradient is applied across a magnet, different currents are generated for majority and minority spins which leads, in addition to a conventional charge current density $\mathbf{j} = \mathbf{j}_\uparrow + \mathbf{j}_\downarrow$, to a spin accumulation across the sample that drives a non-vanishing spin current density $\mathbf{j}^s = \mathbf{j}_\uparrow - \mathbf{j}_\downarrow$. This spin current generation in response to a temperature gradient was observed in ferromagnetic metals in local [2] and nonlocal geometries [46].

1.2 Spin transfer torque and spin pumping

Spin transfer torque and spin pumping describe reciprocal phenomena of the interaction of (electron) spin accumulation with the magnetization dynamics $\mathbf{M}(\mathbf{r}, t)$ of a ferromagnet. To show the interplay of spin-dependent electron dynamics in a magnetic metal and the collective magnetization dynamics in an insulating ferromagnet, we review the occurrence of a spin transfer torque $\boldsymbol{\tau}$ that electron spins exert on the magnetization of an adjacent ferromagnet. Therefore, we use a simplified model of a metal, which is situated at the half-space $x < 0$, containing unpolarized (free) electrons in a mixed state which are characterized by two-component spinors. The ferromagnetic insulator at $x > 0$ is modeled within a macrospin approximation

magnetized along the direction of $\mathbf{m} = \mathbf{M}/M_{\mathrm{s}}$, where M_{s} is the saturation magnetization of the ferromagnet. The band offset of the ferromagnet is much larger than the Fermi energy and it is assumed to be infinitely long such that the electrons are totally reflected at the interface $x = 0$. During this reflection process, the spinors can pick up a (spin-selective) phase and thereby change their spin angular momentum. Two-component spinor column-vectors $a_{\mathrm{i}}(\varepsilon)$ and $a_{\mathrm{r}}(\varepsilon)$ are used to denote the annihilation operators for electrons with energy ε moving in the positive and negative x-directions, respectively. Thus, $a_{\mathrm{i}}(\varepsilon)$ describes electrons incident on the interface whereas $a_{\mathrm{r}}(\varepsilon)$ refers to electrons which are reflected from the interface. The relation between the operators $a_{\mathrm{i}}(\varepsilon)$ and $a_{\mathrm{r}}(\varepsilon)$ is given by the reflection matrix,

$$a_{\mathrm{r}}(\varepsilon) = \hat{r} a_{\mathrm{i}}(\varepsilon), \tag{1.4}$$

where

$$\hat{r} = r_{\mathrm{c}} \mathbb{1} + r_{\mathrm{s}} \mathbf{m} \cdot \boldsymbol{\sigma}. \tag{1.5}$$

Here, $r_{\mathrm{c,s}} = (r_{\uparrow} \pm r_{\downarrow})/2$ with $|r_{\uparrow,\downarrow}|^2 = 1$ are reflection coefficients for spin-up/spin-down electrons that account for the phase picked by the spinor with the reflection at the FN interface, and $\boldsymbol{\sigma} = (\sigma_x, \sigma_y, \sigma_z)$ is a vector of Pauli spin-matrices. These reflection coefficients can be linked to the spin-mixing conductance

$$g_{\uparrow\downarrow} = 1 - r_{\uparrow} r_{\downarrow}^*. \tag{1.6}$$

which plays a central role in the exchange of magnetic moment between electron spins and the magnetization dynamics of a ferromagnet. The expectation value of the incoming electron operators is $\langle a_{\mathrm{i}}^{\dagger}(\varepsilon) a_{\mathrm{i}}(\varepsilon) \rangle = f(\varepsilon)$ where $a_{\mathrm{i}}^{\dagger}(\varepsilon)$ denotes the two-component row-vector spinor which describes the creation of an electron and $f(\varepsilon)$ is the electron distribution function. Electrons in the metal incident on the FN interface have a Fermi-Dirac like distribution with a chemical potential μ and a non-zero spin accumulation $\boldsymbol{\mu}_{\mathrm{s}}$. In linear response, the electron distribution is given by

$$f(\varepsilon) = f^0(\varepsilon) + \left(-\frac{\partial f^0}{\partial \varepsilon} \right) \frac{1}{2} \boldsymbol{\mu}_{\mathrm{s}} \cdot \boldsymbol{\sigma} \tag{1.7}$$

where

$$f^0(\varepsilon) = \frac{1}{e^{(\varepsilon - \mu)/k_{\mathrm{B}}T} + 1} \tag{1.8}$$

is the Fermi-Dirac distribution. From DC circuit theory [47], the spin current through the FN interface then is

$$\mathbf{j}_x^{\mathrm{s}} = \frac{1}{4\pi} \int d\varepsilon \left\langle a_{\mathrm{r}}^{\dagger}(\varepsilon) \boldsymbol{\sigma} a_{\mathrm{r}}(\varepsilon) - a_{\mathrm{i}}^{\dagger}(\varepsilon) \boldsymbol{\sigma} a_{\mathrm{i}}(\varepsilon) \right\rangle. \tag{1.9}$$

Inserting the definitions for the spinor operators (1.4) and the reflection coefficients (1.5) into the spin current definition (1.9), with a bit of algebra the final result,

$$\mathbf{j}_x^{\mathrm{s}} = \frac{1}{4\pi}[g'_{\uparrow\downarrow}\mathbf{m} \times (\mathbf{m} \times \boldsymbol{\mu}_{\mathrm{s}}) + g''_{\uparrow\downarrow}\mathbf{m} \times \boldsymbol{\mu}_{\mathrm{s}}], \tag{1.10}$$

is obtained, where $g'_{\uparrow\downarrow}$ and $g''_{\uparrow\downarrow}$ are the real and imaginary parts of the spin-mixing conductance $g_{\uparrow\downarrow} = g'_{\uparrow\downarrow} + ig''_{\uparrow\downarrow}$, respectively. Due to angular momentum conservation, the spin transfer torque per unit area $\boldsymbol{\tau}$ on the magnetization is determined by the component normal to the interface of the electron spin current hitting on the interface area [48, 49], $\boldsymbol{\tau} = -\mathbf{j}_x^{\mathrm{s}}$. The spin transfer torque which results from Eq. (1.10) vanishes for spins that are aligned collinear with the magnetization $\boldsymbol{\mu}_{\mathrm{s}} \parallel \mathbf{m}$ of the ferromagnet. Without spin filtering by the ferromagnet $r_\uparrow = r_\downarrow$, the spin-mixing conductance (1.6) and consequentually also the spin-transfer torque vanish.

Spin pumping describes the generation of a spin current in N which is driven by the magnetization dynamics in F and is the inverse process to an electron spin transfer torque on the magnetization. A precessing magnetization $\mathbf{M}(\mathbf{r}, t)$ of the ferromagnet pumps a spin current into an adjacent metal layer [50]. In the literature [47, 51, 52], an expression for the spin current density is derived in the adiabatic pumping limit of a slowly varying magnetization which involves a time-dependent scattering matrix. Here, we present an alternative approach. We consider a reference system for the spin degree of freedom that rotates with angular frequency $\boldsymbol{\omega}$ and show how the spin accumulation $\boldsymbol{\mu}_{\mathrm{s}}$ and the magnetization vector $\mathbf{m}$ transform in the rotating frame. The transformation for the electron annihilation operator can be described by a rotation matrix [53] via,

$$a(t) = e^{-\frac{i\boldsymbol{\omega} \cdot \boldsymbol{\sigma}t}{2}} a(t)', \tag{1.11}$$

where $a(t)'$ refers to the operator in the rotating frame. Fourier transforming Eq. (1.11) leads to

$$a(\varepsilon) = a(\varepsilon - \frac{\hbar}{2}\boldsymbol{\sigma} \cdot \boldsymbol{\omega})'. \tag{1.12}$$

The electron distribution function $f(\varepsilon)$ which is the expectation value of $a^\dagger(\varepsilon)a(\varepsilon)$ therefore transforms identically, $f(\varepsilon) = f(\varepsilon - \hbar\boldsymbol{\sigma} \cdot \boldsymbol{\omega}/2)'$. In linear response, this leas to a shift of the spin chemical potential in Eq. (1.7),

$$\boldsymbol{\mu}_{\mathrm{s}} = \boldsymbol{\mu}'_{\mathrm{s}} + \hbar\boldsymbol{\omega}. \tag{1.13}$$

For a classical magnetization vector $\mathbf{m}$ the general transformation to a frame which rotates with $\boldsymbol{\omega}$ changes the frequency of the classical Larmor precession by a frequency ω,

$$\dot{\mathbf{m}} = \dot{\mathbf{m}}' + \boldsymbol{\omega} \times \mathbf{m}. \tag{1.14}$$
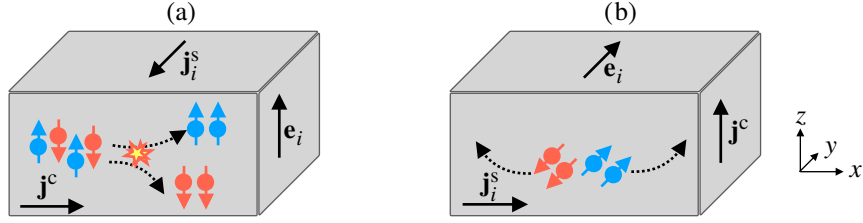
Figure 1.2: Schematic depiction of the spin Hall effect (a) and the inverse spin Hall effect (b).

The spin pumping current density does not depend on the choice of the coordinate system for the spin $\mathbf{j}_x^{\mathrm{s}} = \mathbf{j}_x'^{\mathrm{s}}$. In a frame where the rotating magnetization vector is at rest $\dot{\mathbf{m}}' = 0$, the spin current is given by the time-independent Eq. (1.10). Transforming the system back to the rotating system with the application of the shifts (1.13) and (1.14) and assuming a perfect spin-sink such that $\boldsymbol{\mu}_{\mathrm{s}} = 0$, we arrive at the final equation for the spin pumping [50, 19]

$$\mathbf{j}_x^{\mathrm{s}} = \frac{\hbar}{4\pi} \left(g_{\uparrow\downarrow}' \mathbf{m} \times \dot{\mathbf{m}} - g_{\uparrow\downarrow}'' \dot{\mathbf{m}} \right).\qquad(1.15)$$

As for the spin transfer torque, the spin-mixing conductance plays a central role in the spin pumping.

1.3 Spin Hall effect

The spin Hall effect (SHE) describes the generation of a spin current density $\mathbf{j}^{\mathrm{s}}$ transverse to a charge current density $\mathbf{j}^{\mathrm{c}}$ due to spin-orbit coupling [54, 55, 56]. It was observed in a variety of metals [57, 58, 59] and semiconductors [60, 61]. It is caused either by asymmetric scattering for majority and minority spins off impurities [55, 62], referred to as "extrinsic spin Hall effect" or by a spin-dependent band-structure [63, 64], named "intrinsic spin Hall effect". Both mechanisms cause a spin accumulation perpendicular to the direction of the charge current. In general, the spin current density j_{ij}^{s} is a tensor with a polarization direction i in spin space and a flow direction j in real space. The spin Hall effect then refers to the general relation between electron charge and spin current densities $j_{ij}^{\mathrm{s}} = -(\hbar\theta_{\mathrm{SH}}/2e) \sum_k \epsilon_{ijk} j_k^{\mathrm{c}}$. The (phenomenological) relation between the charge current density $\mathbf{j}^{\mathrm{c}}$ and the vector of the spin current density $\mathbf{j}_j^{\mathrm{s}}$ which flows in the spatial direction j, $i.e$ $j_{ij}^{\mathrm{s}} = \mathbf{j}_j^{\mathrm{s}} \cdot \mathbf{e}_i$ reads [65, 66], see Figure 1.2(a),

$$\mathbf{j}_j^{\mathrm{s}} = -\frac{\hbar}{2e}\theta_{\mathrm{SH}} \, \mathbf{e}_j \times \mathbf{j}^{\mathrm{c}}.\qquad(1.16)$$

Here θ_{SH} is the "spin Hall angle" which measures the efficiency of the current conversion [67].

The inverse effect, referred to as inverse spin Hall effect (ISHE), describes the conversion of a spin current into a charge current via $j_i^c = (2e\theta_{\mathrm{SH}}/\hbar) \sum_{jk} \epsilon_{ijk} j_{jk}^s$. As schematically shown in Figure 1.2(b), the contribution from spins which point along $\mathbf{e}_j$ and a spin current density $\mathbf{j}_j^s$ along the spatial j-direction induce a charge current density $\mathbf{j}^c$. The relation between electron spin current density and the charge current density is

$$\mathbf{j}^c = \frac{2e}{\hbar} \theta_{\mathrm{SH}} \, \mathbf{j}_j^s \times \mathbf{e}_j. \tag{1.17}$$

The ISHE provides a powerful tool to detect spin currents [59, 2, 4].

1.4   Spin Seebeck effect

In the narrow sense, the spin Seebeck effect (SSE) describes the generation of a spin current in a magnetic material, that is driven by collective spin waves in response to a temperature gradient applied across the material. The spin Seebeck effect was first observed in Permalloy [2], which is a metallic magnet consisting of nickel and iron. In quick succession, it then has also been reported in the magnetic semiconductor gallium manganese arsenide (GaMnAs) [3] and the ferrimagnetic insulator yttrium iron garnet (YIG) [4] which is remarkable as YIG is an electrical insulator.

A spin current in a metallic ferromagnet can be carried by conduction electrons, which refers to the spin-dependent Seebeck effect discussed above, and by collective spin waves also called "magnons". Thus, the measured spin current is always a sum of both processes. In contrast, in a ferromagnetic insulator (F) the spin current is carried exclusively by spin waves as the electron degrees of freedom are frozen out. This allows for the detection of the pure magnonic contribution to the spin Seebeck effect. The direct detection of the generated spin current inside the ferromagnetic insulator is not possible. The detection relies on transferring the spin current to a paramagnetic metal (N) layer attached to the magnet by the spin pumping mechanism discussed in Sec. 1.2 and the detection of the spin current in that metal via the inverse spin Hall effect. For that reason in the broader sense often the combination of these three effects: 1. The generation of a spin current in response to a temperature gradient, 2. Pumping the spin current into a metal, and 3. Converting the spin current in the metal to a charge current, is referred to as the spin Seebeck effect.

The spin Seebeck effect was originally proposed in two distinct configurations: the "longitudinal" or "local" spin Seebeck effect and the "transverse" spin Seebeck effect, see Figure 1.3(a) and (b). The effect in the transverse configuration in which the directions of the generated spin current and temperature gradient are perpendicular, remains controversial. The originally reported results [2, 3, 4, 69] could
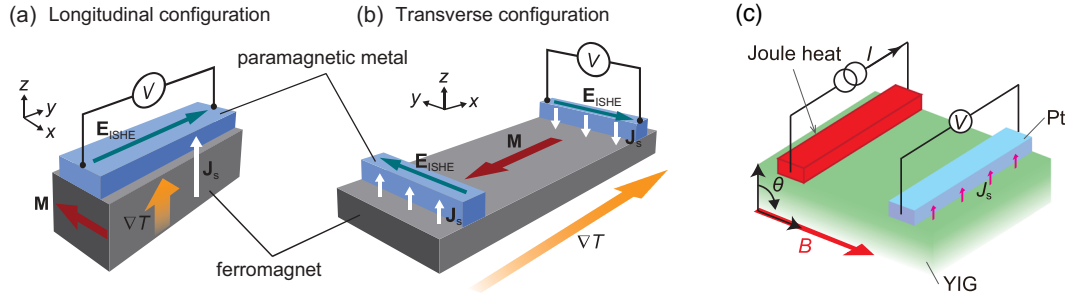
Figure 1.3: Schematic depiction of the spin Seebeck effect (a) in the longitudinal configuration, (b) in the transverse configuration, and in a nonlocal geometry (c). Figures (a) and (b) are adopted from Uchida *et al.* [68]. Figure (c) is adopted from Oyanagi *et al.* [13].

not be reproduced by other groups [70, 33]. The originally reported results were addressed to possible effects from out-of-plane temperature gradients [70]. The longitudinal spin Seebeck effect in which the temperature gradient and the spin current are collinear was reproduced by many groups [71, 25, 26, 68, 33, 72, 6, 7]. In more recent experiments alternative spin Seebeck configurations were realized. In the "nonlocal" spin Seebeck setup a heating wire induces a magnon spin current into a ferromagnet (insulator) that is re-converted into a charge current in a second (detection) wire, attached a distance d apart from the injector [8, 10, 13], see Figure 1.3(c). It was also shown that in the longitudinal configuration a spin Seebeck effect can be created by using the same normal metal layer, which is used to detect the spin current as a joule heater to create a temperature bias between electrons in N and spin waves in F [73, 74]. The spin Seebeck effect was also observed in antiferromagnets [75, 76, 77]. Theories of the spin Seebeck effect are reviewed separately in Section 1.7.

1.5 Phonons, magnons, and magnon polarons

Phonons

In a simple picture, a solid is referred to as an arrangement of atoms in a regular periodic lattice which is characterized by a periodic lattice potential $U(\mathbf{r}_j)$, connecting the atoms at positions $\mathbf{r}_j$. When the lattice atoms are not on their rest positions $\mathbf{r}_j^0$ but displaced by an amount $\mathbf{u}_j = \mathbf{r}_j - \mathbf{r}_j^0$ where $\mathbf{r}_j$ is the actual position of the j-th atom in the lattice, the atoms start oscillating around their equilibrium positions. Because the atoms are coupled via the periodic lattice potential, the displacement of

atoms causes propagating "lattice waves" in the solid. The elementary excitations of these lattice waves are called "phonons".

In Chapter 3 we give a detailed derivation of phonon modes in a microscopic lattice model. A simple description of phonons can also be derived in an elastic continuum model. The Hamiltonian of this system is [78],

$$
H_{\mathrm{p}} = \int dV \sum_{\alpha,\beta} \left[\frac{p_\alpha^2(\mathbf{r})}{2\rho} \delta_{\alpha,\beta} + (c_{\mathrm{l}}^2 - c_{\mathrm{t}}^2) \frac{\rho}{2} \frac{\partial u_\alpha(\mathbf{r})}{\partial x_\alpha} \frac{\partial u_\beta(\mathbf{r})}{\partial x_\beta} + c_{\mathrm{t}}^2 \frac{\rho}{2} \frac{\partial u_\alpha(\mathbf{r})}{\partial x_\beta} \frac{\partial u_\alpha(\mathbf{r})}{\partial x_\beta} \right],
$$

$$(1.18)$$

with $\mathbf{p}(\mathbf{r})$ and $\mathbf{u}(\mathbf{r})$ being the momentum and displacement vectors. ρ is the mass density of the body, $c_{\mathrm{l,t}}$ denotes the longitudinal and transverse sound velocities, and $\alpha, \beta = x, y, z$ are spatial coordinates.

To find the elementary excitations, the Hamiltonian (1.18) is quantized and diagonalized. Therefore, the momentum and displacement vectors are quantized in terms of bosonic creation $b_{\mathbf{q},\lambda}^\dagger$ and annihilation $b_{\mathbf{q},\lambda}$ operators with commutation relation $[b_{\mathbf{q},\lambda}, b_{\mathbf{q}',\lambda'}^\dagger] = \delta_{\mathbf{q},\mathbf{q}'} \delta_{\lambda,\lambda'}$ via [43, 78, 79],

$$
\mathbf{u}(\mathbf{r}_j) = \frac{1}{\sqrt{N}} \sum_{\mathbf{q},\lambda} \mathbf{e}_{\mathbf{q},\lambda} \sqrt{\frac{\hbar}{2m\omega_{\mathbf{q},\lambda}}} (b_{\mathbf{q},\lambda} + b_{-\mathbf{q},\lambda}^\dagger) e^{i\mathbf{q}\cdot\mathbf{r}_j},
$$

$$
\mathbf{p}(\mathbf{r}_j) = -\frac{i}{\sqrt{N}} \sum_{\mathbf{q},\lambda} \mathbf{e}_{\mathbf{q},\lambda} \sqrt{\frac{\hbar m\omega_{\mathbf{q},\lambda}}{2}} (b_{\mathbf{q},\lambda} - b_{-\mathbf{q},\lambda}^\dagger) e^{i\mathbf{q}\cdot\mathbf{r}_j}, \qquad (1.19)
$$

where $\mathbf{q}$, $\omega_{\mathbf{q},\lambda}$, and $\mathbf{e}_{\mathbf{q},\lambda}$ are the wavevector, frequency, and polarization vector with $\lambda = 1, 2, 3$ being the polarization. With a bit of algebra the well known diagonalized Hamiltonian

$$
H_{\mathrm{p}} = \sum_{\mathbf{q},\lambda} \hbar\omega_{\mathbf{q},\lambda} b_{\mathbf{q},\lambda}^\dagger b_{\mathbf{q},\lambda} \qquad (1.20)
$$

is derived. The shape of the Hamiltonian equals the one of an uncoupled harmonic oscillator [53]. Its eigenfunctions are harmonic waves with dispersion relation $\omega_{\mathbf{q},\lambda}$,

$$
\omega_{\mathbf{q},\lambda} = c_\lambda |\mathbf{q}|, \qquad (1.21)
$$

with polarization-dependent group velocity $c_\lambda = c_{\mathrm{l}}$ for the longitudinal mode ($\lambda = 1$) and $c_\lambda = c_{\mathrm{t}}$ for the two degenerate transverse modes ($\lambda = 2, 3$) which are also commonly referred to as sound velocities [1]. These type of phonons are called "acoustic" phonons. Anharmonicities of the inter-ionic lattice potential $U(\mathbf{r}_j)$ give rise to phonon-phonon interaction. The leading contribution to these anharmonicities are three-phonon interactions. In the continuum theory they can be described by a

Hamiltonian of the shape [43],

$$H = \iiint d^3r \sum_{\alpha,\delta} \sum_{\beta,\epsilon} \sum_{\gamma,\sigma} \frac{\partial u_\alpha}{\partial r_\delta} \frac{\partial u_\beta}{\partial r_\epsilon} \frac{\partial u_\gamma}{\partial r_\sigma} A^{\delta\epsilon\sigma}_{\alpha\beta\gamma}, \tag{1.22}$$

where $A^{\delta\epsilon\sigma}_{\alpha\beta\gamma}$ is a strain tensor. As three-phonon interactions do not conserve the number of phonons, the thermal equilibrium phonon distribution $n_{\mathbf{q},\lambda} = \langle b^\dagger_{\mathbf{q},\lambda} b_{\mathbf{q},\lambda} \rangle$ is a Planck-distribution

$$n_{\mathbf{q},\lambda} = \frac{1}{e^{\hbar\omega_{\mathbf{q},\lambda}/k_{\mathrm{B}}T} - 1}. \tag{1.23}$$

Magnons

Ferromagnets are materials that have a magnetic order even when they are not exposed to an external magnetic field. This spontaneous magnetization breaks down above a critical temperature T_{C} called Curie temperature. In a microscopic model, a ferromagnet can be described by localized magnetic moments or "spins" $\mathbf{S}_j$ sitting on the lattice ions at positions $\mathbf{r}_j$ of a periodic lattice. The interaction between the respective spins can be described to a good approximation, due to Heisenberg [39], by the interaction Hamiltonian

$$H_{\mathrm{m}} = -J \sum_{\langle i,j \rangle} \mathbf{S}_i \cdot \mathbf{S}_j - \sum_j \mu\mathbf{B} \cdot \mathbf{S}_j, \tag{1.24}$$

where J is the exchange coupling, $\mu = g\mu_{\mathrm{B}}$ is the magnetic moment of a spin, with g and μ_{B} being the Landé factor and Bohr magneton, $\mu\mathbf{B}$ is the magnetic Zeeman field, and $i, j \in \{0, \dots, N\}$ are indices that in general run over the lattice positions of the whole solid where $i \neq j$. Typically [80] the exchange constant drops off quickly as a function of the inter-atomic distance. As a consequence the sum is restricted to pairs of neighboring spins $\langle i, j \rangle$ with nearest-neighbor coupling J where each pair in the sum is counted only once. The ground state of the system is the state with minimal energy with respect to the Hamiltonian (1.24). Taking a deeper look at the two terms, for ferromagnets which are characterized by a positive coupling constant $J > 0$, the energy is minimized by the choice $\mathbf{S}_i \parallel \mathbf{S}_j$ leading to parallel alignment of the spins whereas $J < 0$ leads to anti-parallel alignment of respective neighboring spins. Thus the second class of materials is called "antiferromagnets" and for $|\mathbf{S}_i| \neq |\mathbf{S}_j|$ one refers to "ferrimagnets". For the remainder of this work, we focus on the ferromagnetic case $i.e.$ $J > 0$. Considering only Heisenberg exchange coupling between the spins, the direction of the respective parallel aligned spins is arbitrary. This is where the Zeeman term in the Hamiltonian (1.24) comes into play. It pins the spins to a parallel alignment with the applied magnetic field $\mathbf{B}$ leading to the ground state where all spins $\mathbf{S}_j \parallel \mathbf{B}$ are aligned collinear with the external magnetic
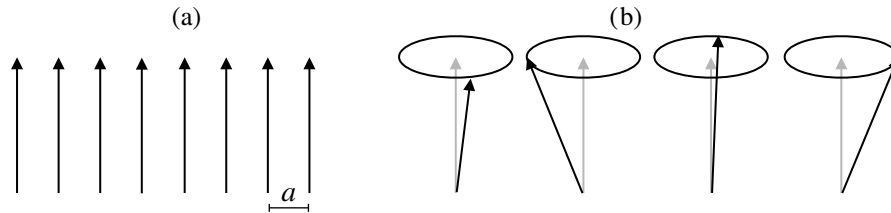
Figure 1.4: Simple depiction of a chain of spins $\mathbf{S}_j$ sitting on a lattice with spacing a between neighboring sites for ferromagnetic order (a). The low lying excitations can be described by a small tilting of the spins (b).

field, see Figure 1.4(a). Another (intrinsic) mechanism that aligns the spins in a certain direction is magnetocrystalline anisotropy [80]. It can be caused by spin-orbit coupling, dipole-dipole interactions, and anisotropy of the exchange interaction. In a phenomenological model, the leading order to the magnetic anisotropy in a cubic lattice can be written,

$$H = -\sum_{j,\alpha} K_\alpha (S_j^\alpha)^2, \qquad (1.25)$$

where K_α is an anisotropy constant, and $\alpha = x, y, z$ are cartesian coordinates. For example $K_{x,y} = 0$, $K_z > 0$ would lead to an easy-axis anisotropy in the z-direction which pins the spins to the z-axis. [80].

The energy cost of the intuitive first excited state that could be reached by entirely flipping a single spin is $4JS^2$. For a typical exchange constant, this refers to a magnetic field of several Tesla [39]. Lower energy gains can be achieved by instead tilting all spins slightly away from their equilibrium axis as shown in Figure 1.4(c). The elementary excitations of the resulting spin waves, called "magnons" are the magnetic analogon to the lattice vibrations which were discussed above. A direct derivation of magnons for a discrete lattice model like Eq.(1.24) is explained in detail in Chapter 3. Here, we introduce magnons in the framework of a phenomenological Landau-Lifshitz-Gilbert equation [51, 19] for the unit vector $\mathbf{m}(\mathbf{r}, t) = \mathbf{M}(\mathbf{r}, t)/M_\mathrm{s}$ of the continuous magnetization density $\mathbf{M}(\mathbf{r}, t)$ where M_s is the saturation magnetization.

The Landau-Lifshitz-Gilbert equation can be derived from the spin Hamiltonian (1.24), treating the spins as classical angular momentum vectors, which Larmor precess around the magnetic field vector. Their (classical) equation of motion is derived from

$$\dot{\mathbf{S}}_j = -\mathbf{S}_j \times \frac{\partial H}{\partial \mathbf{S}_j}. \qquad (1.26)$$

The continuum limit is reached by assuming that the spins slowly vary in space $\mathbf{S}_j = S\mathbf{e}(\mathbf{r}_j)$, where S is the magnitude of the spin angular momentum and $\mathbf{e}(\mathbf{r}_j)$ is

a unit vector that points in the direction of $\mathbf{S}_j$. Recalling that the directions of the magnetic moment $\mathbf{m}$ and the spin $\mathbf{e}$ are opposite *i.e.* $\mathbf{m} = -\mathbf{e}$, the LLG equation reads

$$\dot{\mathbf{m}}(\mathbf{r}, t) = \mathbf{m} \times (\gamma \mathbf{B} + \iota \nabla^2 \mathbf{m}), \tag{1.27}$$

where γ is the gyromagnetic ratio. In the continuum theory the exchange stiffness constant $\iota = JSa^2/\hbar$ is commonly used, a being the lattice constant.

To obtain the elementary excitations of a disturbance in the magnetic system, the magnetic moment $\mathbf{m}$ in the LLG equation (1.27) is quantized by a set of creation and annihilation operators $a_{\mathbf{q}}^\dagger$, $a_{\mathbf{q}}$ with commutation relation $[a_{\mathbf{q}}, a_{\mathbf{q}'}^\dagger] = \delta_{\mathbf{q},\mathbf{q}'}$,

$$m_x(\mathbf{r}, t) = \sqrt{\frac{\mu}{2M_{\mathrm{s}}V}} \sum_{\mathbf{q}} (a_{\mathbf{q}} + a_{-\mathbf{q}}^\dagger) e^{i(\mathbf{q}\cdot\mathbf{r} - \omega t)},$$

$$m_y(\mathbf{r}, t) = -i\sqrt{\frac{\mu}{2M_{\mathrm{s}}V}} \sum_{\mathbf{q}} (a_{\mathbf{q}} - a_{-\mathbf{q}}^\dagger) e^{i(\mathbf{q}\cdot\mathbf{r} - \omega t)},$$

$$m_z(\mathbf{r}, t) = 1 - \frac{\mu}{M_{\mathrm{s}}V} \sum_{\mathbf{q}} a_{\mathbf{q}}^\dagger a_{\mathbf{q}}. \tag{1.28}$$

These transformations – expanding the spin angular momentum in terms of Bosonic creating and annihilation operators and Fourier transforming them to momentum space – are commonly referred to as Holstein-Primakoff transformations in the literature [81, 82, 80]. They yield a solution to the equation of motion (1.27) with the dispersion relation

$$\hbar\omega_{\mathbf{q}} = JSa^2|\mathbf{q}|^2 + \mu B. \tag{1.29}$$

The same Holstein-Primakoff transformations (1.28) also diagonalize the magnon Hamiltonian [83, 80],

$$H_{\mathrm{m}} = \sum_{\mathbf{q}} \hbar\omega_{\mathbf{q}} a_{\mathbf{q}}^\dagger a_{\mathbf{q}}. \tag{1.30}$$

The structure of Eq. (1.30) is yet another harmonic oscillator. Thus, the magnons can be treated as quasiparticles. In a pure Heisenberg ferromagnet (1.24) without relativistic effects *e.g.* due to spin-orbit coupling or long-range dipole-dipole interaction the spin and therefore also the magnon number is conserved. These magnon-number conserving processes can lead to energy redistribution and consequentually equilibrate the magnon temperature without changing the total number of magnons. This calls for a non-vanishing chemical potential in the Planck-distribution (1.23) For this reason the thermal equilibrium magnon distribution $n_{\mathbf{q}} = \langle a_{\mathbf{q}}^* a_{\mathbf{q}} \rangle$ obeys Bose-Einstein statistics with a finite chemical potential [37],

$$n_{\mathbf{q}} = \frac{1}{e^{(\hbar\omega_{\mathbf{q}} - \mu)/k_{\mathrm{B}}T} - 1}. \tag{1.31}$$

A finite magnon chemical potential also leads to the possibility of forming a magnon Bose-Einstein condensate which was also realized experimentally [84, 85].

Magnon polarons

The interaction between the spin and the lattice systems can be modeled within a phenomenological continuum theory like the well studied magneto-elastic coupling [86, 87, 80, 38, 88] where all processes allowed by symmetry in a cubic crystal are taken into account,

$$H_{\mathrm{me}} = \int \frac{d^3 r}{a^3} \sum_{\alpha,\beta} [B_{\alpha\beta} e_{\alpha\beta} m_\alpha(\mathbf{r}) m_\beta(\mathbf{r}) + (A_{\alpha\beta} e_{\alpha\beta} \partial_\alpha \mathbf{m} \cdot \partial_\beta \mathbf{m} + A'_{\alpha\beta} e_{\alpha\alpha} |\partial_\beta \mathbf{m}|^2].$$

(1.32)

Here, $e_{\alpha\beta} = (1/2)\,(\partial_\beta u_\alpha + \partial_\alpha u_\beta)$ the symmetrized strain tensor, the coupling tensors are $B_{\alpha\beta} = B_1 \delta_{\alpha\beta} + B_2(1 - \delta_{\alpha\beta})$, $A_{\alpha\beta} = A_1 \delta_{\alpha\beta} + A_2(1 - \delta_{\alpha\beta})$, and $A'_{\alpha\beta} = A'(1 - \delta_{\alpha\beta})$, where $B_{1,2}$, $A_{1,2}$, and A' are magneto-elastic constants [80]. The magneto-elastic Hamiltonian can also be recovered from a microscopic spin-lattice interaction Hamiltonian on a discrete lattice in the long-wavelength limit which is explained in great detail in Chapter 3. The leading order contribution to the magneto-elastic coupling is a one-magnon-one-phonon Hamiltonian,

$$H_{\mathrm{mp}} = 2 \sum_{\mathbf{q},\lambda} (a_{\mathbf{q}}^\dagger \Delta_{\mathbf{q},\lambda} + a_{-\mathbf{q}} \Delta_{-\mathbf{q},\lambda}^*)(b_{\mathbf{q},\lambda} + b_{-\mathbf{q},\lambda}^\dagger),$$

(1.33)

which couples the phonon and magnon Hamiltonians (1.18) and (1.24) by off-diagonal terms $\Delta_{\mathbf{q},\lambda}$. In another iteration, the coupled magnon-phonon Hamiltonian can be diagonalized with respect to new bosonic eigenmodes,

$$a_{\mathbf{q}} = \sum_{\nu=1}^{4} \left(V_{\mathbf{q},4,\nu} \alpha_{\mathbf{q},\nu} - V_{\mathbf{q},4,\nu+4} a_{-\mathbf{q},\nu}^\dagger \right),$$

(1.34)

$$b_{\mathbf{q},\lambda} = \sum_{\nu=1}^{4} \left(V_{\mathbf{q},\lambda,\nu} \alpha_{\mathbf{q},\nu} - V_{\mathbf{q},\lambda,\nu+4} a_{-\mathbf{q},\nu}^\dagger \right),$$

(1.35)

that obey the commutation relation $[\alpha_{\mathbf{q},\nu}, \alpha_{\mathbf{q}',\nu'}^\dagger] = \delta_{\mathbf{q},\mathbf{q}'} \delta_{\nu,\nu'}$. The details of this symplectic diagonalization as well as expressions for the magnon-phonon coupling $\Delta_{\mathbf{q},\lambda}$ and the transformation matrix $V_{\mathbf{q}}$ are presented in Chapter 3. The hybridization with respect to these "magnon polaron" modes leads to a shift of the magnon and phonon dispersions. This shift is strongest at the "resonance points" where the crossings of the dispersions move to avoided crossings, see Figure 1.5. The formation of magnon polarons was not only observed in spin Seebeck measurements but manifest in a variety of phenomena in the vicinity of strong magneto-elastic coupling
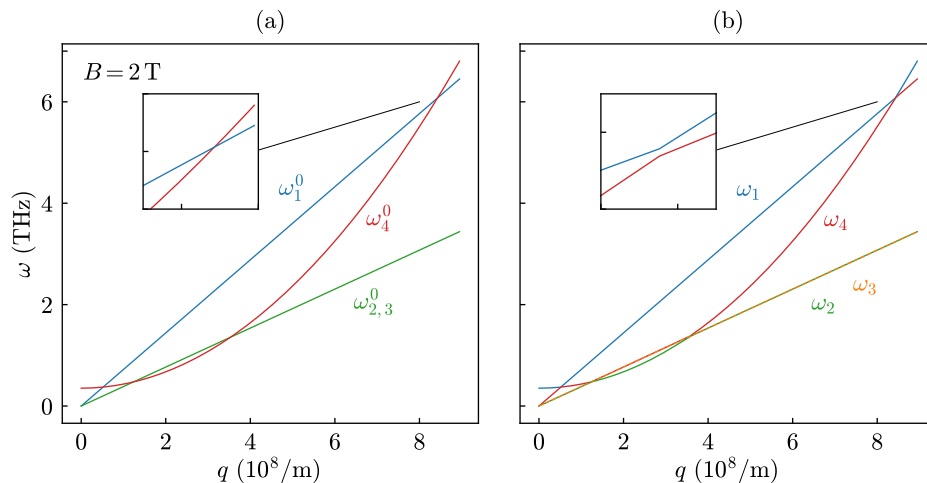
Figure 1.5: Dispersions for magnons and phonons (a) without magnon-phonon coupling from Eqs. (1.29) and (1.21) and dispersions for magnon polarons with magnon-phonon coupling (b) that transform the crossings of the dispersions to avoided crossings.

[89, 90]. The direct probing of magnons *e.g.* is restricted to the low-frequency part of the spectrum in the GHz regime [91]. The spin Seebeck effect thus is a good candidate for experimentally proving features that are in the THz regime.

1.6 Boltzmann transport theory

To study the transport associated with the spins and lattice ions equations of motion can be set up from the Hamiltonians (1.18) and (1.24) together with possible additional Hamiltonians, which describe interactions among them (see the following chapters for details). From classical Hamilton mechanics the equations of motion for the variables $\mathbf{S}_j$, $\mathbf{u}_j$, and $\mathbf{p}_j$ are

$$\dot{\mathbf{u}}_j = \frac{\partial H}{\partial \mathbf{p}_j}, \quad \dot{\mathbf{p}}_j = -\frac{\partial H}{\partial \mathbf{u}_j}, \quad \dot{\mathbf{S}}_j = -\mathbf{e} \times \frac{\partial H}{\partial \mathbf{S}_j}. \tag{1.36}$$

Describing the coupled motion of each of the magnonic and phononic oscillators in the lattice is practically impossible for macroscopic systems. Originally formulated to describe the transport of particles in low concentration gases and fluids in response to thermal gradients, the Boltzmann transport theory is a powerful tool to reduce the complexity of large systems by aggregating the quasiparticles within a volume element $d\mathbf{r}$ and representing them by a (continuous) average distribution function $n_{\mathbf{q}} = \langle a_{\mathbf{q}}^* a_{\mathbf{q}} \rangle$.

This transition is applicable if position $\mathbf{r}$ and momentum $\hbar\mathbf{q}$ are well-defined

quantities at the same time *i.e.* their uncertainties Δr and Δq are small [92]. For the momentum this is fulfilled if $\Delta q \ll q$. The wavevectors of thermally excited magnons and phonons are of the order $q_{\mathrm{m}} \sim \sqrt{k_{\mathrm{B}}T/JSa^2}$ and $q_{\mathrm{p}} \sim k_{\mathrm{B}}T/\hbar c_{\mathrm{p}}$ where c_{p} is the average phonon sound velocity. For the position, the resolution Δr must be much better than the mean free path l of the particles before undergoing interactions *i.e.* $\Delta r \ll l$. From Heisenberg uncertainty

$$\Delta q \cdot \Delta r \gtrsim 1 \quad \Leftrightarrow \quad \Delta q \gtrsim \frac{1}{\Delta r} \tag{1.37}$$

we conclude that the condition

$$q \gg \Delta q \gtrsim \frac{1}{\Delta r} \gg \frac{1}{l} \quad \Leftrightarrow \quad l \gg \frac{1}{q} \tag{1.38}$$

must hold. So the aggregation of the particles into a classical distribution function is valid if the average length between scattering events l is much larger than the inverse thermal wavevector $1/q$. For the ferromagnetic insulator YIG which we describe in Chapters 2 and 3, the wavevectors for temperatures down to $T = 1\,\mathrm{K}$ are of the order $1/q_{\mathrm{m}} \approx 8\,\mathrm{nm}$ and $1/q_{\mathrm{p}} \approx 60\,\mathrm{nm}$. The mean free paths are $l \gtrsim \mu\mathrm{m}$ (see Figure 3.3) and thus fulfill the condition well for the temperature range $T \simeq 1 - 50\,\mathrm{K}$ that we investigate in our work.

The Boltzmann transport equation for an out-of-equilibrium distribution function $n_{\mathbf{q}}(\mathbf{r}(t))$ is [1, 39],

$$\mathbf{v}_{\mathbf{q}} \cdot \frac{\partial n_{\mathbf{q}}}{\partial \mathbf{r}} + \frac{\partial n_{\mathbf{q}}}{\partial t} = I_{\mathbf{q}} \tag{1.39}$$

where $I_{\mathbf{q}}$ is the collision integral which relaxes the non-equilibrium distribution function back towards a local equilibrium and $\mathbf{v}_{\mathbf{q}} = \partial \omega_{\mathbf{q}}/\partial \mathbf{q}$ is the group velocity of the particles. The collision integral on the right hand side of Eq. (1.39) describes the relaxation of the distribution back to a local equilibrium $n_{\mathbf{q}}^0$ and is the difference between particles entering the state $\mathbf{q}$ and particles leaving it,

$$I_{\mathbf{q}} = I_{\mathbf{q}}^{\mathrm{in}} - I_{\mathbf{q}}^{\mathrm{out}} \tag{1.40}$$

In a simple "relaxation-time approximation" the collision integral is approximated by an average relaxation time $\tau_{\mathbf{q}}$ that determines the timescale on which the equilibration of the out-of-equilibrium distribution $n_{\mathbf{q}}$ towards a "local equilibrium" $n_{\mathbf{q}}^0$ in which the temperature, momentum density, and if applicable, chemical potential, deviate from the global equilibrium takes place,

$$I_{\mathbf{q}} = -\frac{n_{\mathbf{q}} - n_{\mathbf{q}}^0}{\tau_{\mathbf{q}}}. \tag{1.41}$$

This approximation, despite its simplicity, lacks microscopic insight into the underlying scattering mechanisms. In a more detailed treatment the collision integrals
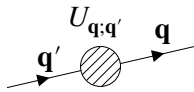
Figure 1.6: Schematic magnon-impurity collision diagram.

are evaluated from the (small) sub-leading contributions to the phonon and magnon Hamiltonians (1.18) and (1.24) with the use of Fermi's golden rule [93, 94]. The procedure is explained in great detail in Chapters 2 and 3. We demonstrate the construction of collision integrals and possible conservation laws for elastic magnon-impurity interaction, depicted in Figure 1.6. From the $\mathbf{q}$-magnon's point of view the contributions to the collision integral read

$$I_{\mathbf{q}}^{\text{in}} = \frac{2\pi}{\hbar} \sum_{\mathbf{q}'} |U_{\mathbf{q};\mathbf{q}'}|^2 \delta(\omega_{\mathbf{q}} - \omega_{\mathbf{q}'})(1 + n_{\mathbf{q}})n_{\mathbf{q}'}, \tag{1.42}$$

$$I_{\mathbf{q}}^{\text{out}} = \frac{2\pi}{\hbar} \sum_{\mathbf{q}'} |U_{\mathbf{q};\mathbf{q}'}|^2 \delta(\omega_{\mathbf{q}} - \omega_{\mathbf{q}'})n_{\mathbf{q}}(1 + n_{\mathbf{q}'}), \tag{1.43}$$

where $U_{\mathbf{q};\mathbf{q}'}$ is the matrix element of the interaction. The $n_{\mathbf{q}'}$ and $(1 + n_{\mathbf{q}})$ factors can be understood analogously to the processes of absorption, stimulated emission, and spontaneous emission of photons in a two-level system. In $I_{\mathbf{q}}^{\text{in}}$ the probability to scatter from $\mathbf{q}' \to \mathbf{q}$ is proportional to the number of particles in $\mathbf{q}'$ as they are obligatory for the scattering process. By the process of stimulated emission bosons that are already in the state $\mathbf{q}$ can stimulate the creation of even more bosons with frequency $\omega_{\mathbf{q}}$, thus the process is proportional to $n_{\mathbf{q}}$. In addition, regardless of the boson density $n_{\mathbf{q}}$ bosons in the state $\mathbf{q}$ can be created by spontaneous emission. This yields the total factor $(1 + n_{\mathbf{q}})$.

In the present thesis, within the description of the spin Seebeck effect, we mainly investigate the response of the distribution function to an applied temperature bias between two reservoirs that are attached to the ends of the system. In linear response, for weak distortions the distribution function can be expanded around its local equilibrium via

$$n_{\mathbf{q}}(\mathbf{r}) = n_{\mathbf{q}}^0 + \left(-\frac{\partial n^0}{\partial \omega}\right) \psi_{\mathbf{q}}(\mathbf{r}) \tag{1.44}$$

where $\psi_{\mathbf{q}}(\mathbf{r})$ is a small correction to the local equilibrium $n_{\mathbf{q}}^0$. This expansion is also used in Chapter 2 and 3. In Chapter 3 a slightly different notation is used, however, in which $\psi_{\mathbf{q}}$ in Eq. (1.44) is replaced by $\omega \psi_{\mathbf{q}}(\mathbf{r})$. The linearized collision integral $I_{\mathbf{q}}^{\text{lin.}}$ for this expansion is

$$I_{\mathbf{q}}^{\text{lin.}} = \frac{2\pi}{\hbar} \left(-\frac{\partial n^0}{\partial \omega}\right) \sum_{\mathbf{q}'} |U_{\mathbf{q};\mathbf{q}'}|^2 \delta(\omega_{\mathbf{q}} - \omega_{\mathbf{q}'})(\psi_{\mathbf{q}'} - \psi_{\mathbf{q}}). \tag{1.45}$$
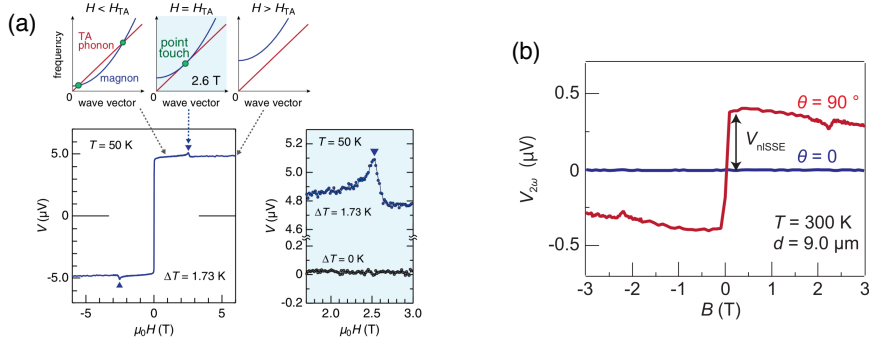
Figure 1.7: Spin Seebeck voltage V as a function of the applied magnetic field B. The lower panels of (a) show the spin Seebeck voltage from a longitudinal spin Seebeck setup, adopted from Kikkawa et $al.$ [15]. In (b) the spin Seebeck voltage in a nonlocal configuration is shown, adopted from Oyanagi et $al.$ [13]. The signal shows distinct features at $B = 2.6\,\mathrm{T}$ where the magnon and the transverse phonon dispersions have a touching point as shown in the top panel of (a).

The collisions in Fig. 1.6 conserve energy $\hbar\omega_{\mathbf{q}} = \hbar\omega_{\mathbf{q}'}$ which is encoded in the delta function of Eq. (1.45) and particle number. Consequentially, a test function that is equilibrated with respect to these processes i.e. enforces $I_{\mathbf{q}}^{\mathrm{lin.}} = 0$ reads

$$\psi_{\mathbf{q}}(\mathbf{r}) = \mu_{\mathrm{m}}(\mathbf{r}) + \frac{\omega}{T}\Delta T_{\mathrm{m}}(\mathbf{r}). \tag{1.46}$$

The corresponding physical quantities that enter the distribution function are the constants of the expansion. They are identified as a chemical potential of the magnons $\mu_{\mathrm{m}}(\mathbf{r})$ [37] and a temperature deviation $\Delta T_{\mathrm{m}}(\mathbf{r}) = T_{\mathrm{m}}(\mathbf{r}) - T$ from the equilibrium temperature T. A similar procedure will be employed in Chapter 2 to further reduce the complexity of the Boltzmann equation to a very small set of "hydrodynamic equations".

1.7 Theories of the spin Seebeck effect

Already in the pioneering theoretical works by Xiao et $al.$ [19] and Adachi et $al.$ [34] the role of magnon-phonon interaction for the microscopic origin of the effect was pointed out. One piece of evidence was that the temperature dependence of the spin Seebeck effect closely follows the temperature dependence of the phonon thermal conductivity [34]. Another milestone was the observation of significant peaks/dips at two "critical" magnetic fields in magnetic-field dependence measurements of the spin Seebeck effect by Kikkawa et $al.$ [15], see Figure 1.7. These features are present in a broad temperature range and coincide with the magnetic fields where

the magnon and phonon dispersions have touching points [20], see Figure 1.7 (a) top panel. They were also observed by other groups and other setups as the nonlocal spin Seebeck effect [10, 13], and the spin Peltier effect [95] which is the inverse to the spin Seebeck effect.

Existing theories of the spin Seebeck effect can be separated into three groups. First, theories which are based on the Landau-Lifshitz-Gilbert equation where the spin-lattice interaction enters via a dissipative contribution to the spin current from a random magnetic field [19, 34, 32, 33]. The second class [35, 96, 36] uses a Boltzmann transport equation to evaluate the coupled magnon and phonon temperatures that drive the magnon spin and heat currents. For the case of strong spin-conserving scattering a magnon chemical potential, as explained in Section 1.5, is added to the Planck distribution of the magnons [37]. The phonon drag onto the magnons enters via a thermal magnon-phonon lifetime, derived in the relaxation time approximation. The third class of theories [20] includes the strong one-magnon-one-phonon coupling from relativistic effects into the dispersion relation which leads to the formation of strongly hybridized "magnon-polaron" mixed-modes. These hybridized modes then relax via magnon-impurity and phonon-impurity interactions. The Boltzmann theories have in common that a hidden background interaction ensures that at any time the magnon, phonon, and magnon-polaron distributions have Bose-Einstein-like and Planck- like distributions.

The first theoretical descriptions of the spin Seebeck were given by Xiao *et al.* [19] and Hoffman *et al.* [32] based on the Landau-Lifshitz-Gilbert phenomenology. The spin pumping at the FN interface is described in terms of a classical, continuous, time-dependent magnetization unit vector $\mathbf{m}(\mathbf{r}, t) = \mathbf{M}(\mathbf{r}, t)/M_{\mathrm{s}}$ as introduced in Section 1.5. This is valid if the ferromagnet is large and the spatial deviation of the magnetization density is slowly varying. The motion of the magnetization vector $\mathbf{m}(\mathbf{r}, t)$ in the ferromagnet is described by the Landau-Lifshitz-Gilbert equation,

$$\dot{\mathbf{m}} = -\mathbf{m} \times (\gamma \mathbf{B} + \iota \nabla^2 \mathbf{m} + \gamma \mathbf{h}) + \alpha \mathbf{m} \times \dot{\mathbf{m}}, \qquad (1.47)$$

where α is the Gilbert damping [50] that relaxes deviations of $\mathbf{m}$ from equilibrium, and $\mathbf{h}$ is a random stochastic field with the correlator,

$$\langle h_i(\mathbf{r}, t), h_j(\mathbf{r}', t') \rangle = \frac{2\alpha}{\gamma M_{\mathrm{s}}} k_{\mathrm{B}} T_{\mathrm{p}}(\mathbf{r}) \delta_{i,j} \delta(\mathbf{r} - \mathbf{r}') \delta(t - t'), \qquad (1.48)$$

where T_{p} is the local phonon temperature. The random magnetic field encapsulates the dissipation of spin current into the phonon system. In addition to the Landau-Lifshitz-Gilbert equation (1.27), terms proportional to the random magnetic field $\mathbf{h}$ and Gilbert damping α were taken into account. They govern the dissipation of magnetic moment from the spin system into the phonon system. The coupling to

the interfaces is modeled by boundary conditions [32],

$$\frac{\partial \mathbf{m}}{\partial x} = 0 \quad , \quad x = 0, \tag{1.49}$$

$$A\frac{\partial \mathbf{m}}{\partial x} + \frac{\hbar g'_{\uparrow\downarrow}}{4\pi}\frac{\partial \mathbf{m}}{\partial t} - \mathbf{h}' = 0 \quad , \quad x = L, \tag{1.50}$$

where $A = \hbar \iota M_{\mathrm{s}}/\mu$. The boundary conditions describe the coupling to an insulator at $x = 0$ and to a metal contact at $x = L$ with a finite spin pumping that causes dissipation of magnetic moment into the metal where $\mathbf{h}'$ is another stochastic field, defined as in Eq. (1.48) with $T_{\mathrm{p}} \to T_{\mathrm{e}}$, where T_{e} is the electron temperature in the metal. It describes the dissipation of magnetic moment into electron spins due to spin pumping.

Their final result for the spin current at the ferromagnet–normal metal interface that drives the spin Seebeck effect in response a the temperature gradient in the phonon system in linear response is [1] [19, 32],

$$j_x^{\mathrm{s}} = \frac{\hbar g'_{\uparrow\downarrow}}{\pi S A}\frac{1}{N}\sum_{\mathbf{q}} \omega_{\mathbf{q}}^2 \left(-\frac{\partial n^0}{\partial \omega}\right)\frac{\Delta T_{\mathrm{me}}}{T} \tag{1.51}$$

where $n_{\mathbf{q}}^0 = 1/(e^{\hbar\omega_{\mathbf{q}}/k_{\mathrm{B}}T} - 1)$ is the equilibrium magnon Planck distribution with energy $\hbar\omega_{\mathbf{q}}$. Equation (1.51) states that the spin Seebeck current at the FN interface is proportional to the temperature difference ΔT_{me} of the magnons T_{m} at the ferromagnetic side of the interface and the electrons T_{e} at the normal metal side of the interface with the assumption that the electrons and phonons are at the same temperature. The spin-mixing conductance, reviewed in Section 1.2 plays a crucial role in the spin Seebeck current. The general structure of the pumped spin current at the FN interface, see also Eq. (3.85) in Chapter 3 for a detailed derivation, is approximately given by $j^{\mathrm{s}} \sim P v \delta n$ where P is the spin pumping probability of a magnon at the FN interface, v is the magnon velocity, and δn the non-equilibrium part of the magnon distribution. In linear response, for a small spin-mixing conductance the spin pumping probability is (see Eq. (B.59) in Appendix B) $P \sim \sqrt{\omega}g'_{\uparrow\downarrow}$ and the magnon velocity is $v \sim \sqrt{\omega}$. For a non-equilibrium magnon temperature, according to Eq. (1.46), the non-equilibrium part of the magnon distribution is $\delta n \sim \omega(-\partial n^0/\partial\omega)\Delta T_{\mathrm{m}}/T$. This is also the structure of the spin Seebeck current in Eq. (1.51).

To determine the magnon electron temperature difference ΔT_{me} at the FN interface, the magnon temperature in the ferromagnet was derived in linear response in a two-temperature model [33], which was first introduced by Sanders and Walton

---

[1]In the final expression (42) of Hoffman *et al.* [32], the sum $1/N \sum_{\mathbf{q}} \to \int d\omega \nu(\omega)$, where $\nu(\omega)$ is the magnon density of states, was converted to a continuous integral over the magnon frequencies.
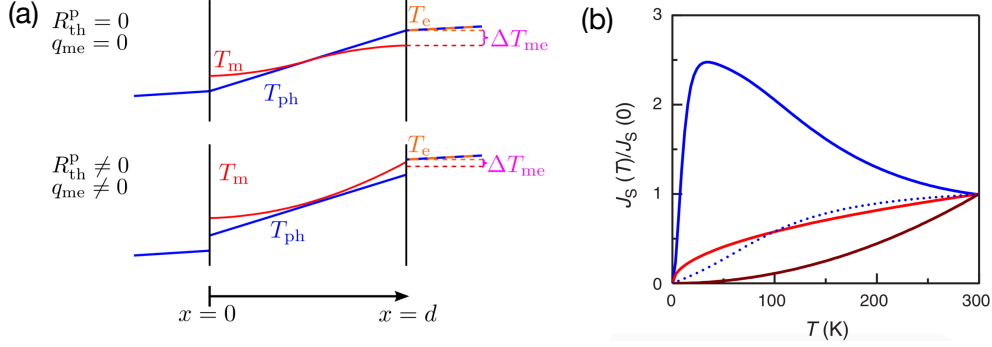
Figure 1.8: Schematic magnon and phonon temperature profiles (a) for perfectly coupled phonons $R_{\text{th}}^{\text{p}} = 0$ and isolated magnons $(R_{\text{th}}^{\text{m}})^{-1} = q_{\text{me}} = 0$ (top panel) and with finite Kapitza resistances (bottom panel). Figure (a) is adopted from Schreier *et al.* [33]. Spin Seebeck currents as a function of temperature T from Eq. (1.54) (red) and from Eq. (1.56) and $\tau_{\mathbf{q}} = \text{const.}$ (brown), and from Eq. (1.56) with different T-dependence models for $\tau_{\mathbf{q}}$ including magnon-magnon interaction as explained in Ref. [35] (blue). Figure (b) is adopted from Rezende *et al.* [35].

[97],

$$\frac{\partial^2 T_{\text{m}}}{\partial x^2} = \frac{C_{\text{m}} C_{\text{p}}}{C_{\text{m}} + C_{\text{p}}} \frac{1}{\kappa_{\text{m}} \tau_{\text{mp}}} (T_{\text{m}} - T_{\text{p}}),$$
$$\frac{\partial^2 T_{\text{p}}}{\partial x^2} = \frac{C_{\text{m}} C_{\text{p}}}{C_{\text{m}} + C_{\text{p}}} \frac{1}{\kappa_{\text{p}} \tau_{\text{mp}}} (T_{\text{p}} - T_{\text{m}}), \tag{1.52}$$

where $C_{\text{m,p}}$ and $\kappa_{\text{m,p}}$ are the magnon/phonon heat capacities and thermal conductivities, respectively, and τ_{mp} is the thermal magnon-phonon lifetime. The connection of the magnon and phonon systems to the heat baths, held at temperatures $T_{\text{I,N}}$, are modeled using thermal Kapitza resistances [98, 99]. The boundary conditions for the temperatures are

$$\left. \kappa_{\text{m,p}} \frac{\partial T_{\text{m,p}}}{\partial x} \right|_{x=0} = \frac{1}{R_{\text{th}}^{\text{m,p}}} [T_{\text{I}} - T_{\text{m,p}}(0)],$$
$$\left. \kappa_{\text{m,p}} \frac{\partial T_{\text{m,p}}}{\partial x} \right|_{x=L} = \frac{1}{R_{\text{th}}^{\text{m,p}}} [T_{\text{m,p}}(L) - T_{\text{N}}], \tag{1.53}$$

where $R_{\text{th}}^{\text{m,p}}$ are the interfacial thermal Kapitza resistances of the magnons and phonons. Schematic plots of coupled magnon and phonon temperature profiles are shown in Figure 1.8(a). Combining Eqs. (1.52) and (1.53), they find for the temperature difference between magnons and electrons at the ferromagnet–normal metal interface, in case of perfect phonon coupling to the heat reservoirs $R_{\text{th}}^{\text{p}} = 0$, and a

phonon dominated thermal bulk transport $\kappa_\mathrm{p} \gg \kappa_\mathrm{m}$,

$$\Delta T_\mathrm{me} = \frac{\Delta T}{L} \left(\frac{1}{\lambda} \coth\left(\frac{L}{2\lambda} \right) + \frac{1}{R_\mathrm{th}^\mathrm{m} \kappa_\mathrm{m}} \right)^{-1}, \tag{1.54}$$

where $\lambda \sim \sqrt{T}\sqrt{\tau_\mathrm{m}\tau_\mathrm{mp}}$ is the thermal magnon-phonon mean free path, and τ_m is an average magnon relaxation-time.

The weakness of this phenomenological treatment of the magnon-phonon coupling in a single relaxation time τ_mp is that no predictions of how τ_mp depends on temperature and magnetic field are possible. There is no differentiation between spin-conserving and spin-nonconserving processes and the energy averaged lifetimes lack insight into the relative importance of the respective magnon modes with frequency ω to the total spin current.

In a more microscopic approach, Rezende *et al.* [35, 96, 36] set up a theory to the spin Seebeck effect based on a Boltzmann theory of the magnon distribution $n_\mathbf{q}$ to describe the bulk transport in the ferromagnet, using the relaxation time approximation (which was introduced in Section 1.6),

$$\mathbf{v_q} \cdot \frac{\partial n_\mathbf{q}}{\partial \mathbf{r}} = -\frac{n_\mathbf{q} - n_\mathbf{q}^0}{\tau_\mathbf{q}}, \tag{1.55}$$

where $\mathbf{v_q}$ is the magnon group velocity and $\tau_\mathbf{q}$ is a relaxation time. They separated the magnon distribution into two isotropic moments, a magnon accumulation δn_m (that can be linked to a magnon chemical potential), and a magnon temperature T_m, as well as two corresponding anisotropic moments $j_x^{\mathrm{s},\delta n}$, and $j_x^{\mathrm{s},T}$ that contribute to the total spin current density j_x^s. The anisotropic moments can be identified in terms of spin and energy current densities, as explained in Chapter 2. For the boundaries they implied the connection to an insulator at $x = 0$ where $j_x^\mathrm{s} = 0$ and to a metallic magnet at $x = L$ with a finite spin pumping (1.15). They also find Eq. (1.51) for the spin current at the ferromagnet–normal metal interface with the wavevector-dependent magnon electron temperature difference

$$\Delta T_\mathrm{me} = \frac{\Delta T}{L} \frac{\tau_\mathbf{q} v_\mathbf{q}^2}{2\omega_\mathbf{q}} \frac{\tanh(L/2\lambda)}{c_1 + c_2 g'_{\uparrow\downarrow} \coth(L/\lambda)} \frac{\sum_{\mathbf{q}'} \omega_{\mathbf{q}'} \left(-\frac{\partial n^0}{\partial \omega'} \right)}{\sum_{\mathbf{q}'} \left(-\frac{\partial n^0}{\partial \omega'} \right)}, \tag{1.56}$$

where $c_{1,2}$ are constants, that depend on the bulk magnon properties in the ferromagnet. The general structure of the spin current arising from the temperature difference in Eq. (1.56) is similar to the one derived by Xiao *et al.* in Eq. (1.51). The two results (1.51) and (1.56) for the spin Seebeck current are shown in Figure 1.8(b).

We set up a similar Boltzmann theory for the magnon and phonon temperatures in Chapter 2. In addition to the theories of Xiao *et al.* and Rezende *et al.*, we go beyond the Gilbert damping phenomenology and relaxation-time-approximation and

we explicitly account for magnon-phonon interaction in the collision integrals (1.39). We individually treat spin-conserving magnon-phonon collisions, that predominantly originate from exchange coupling and number-nonconserving collisions from relativistic effects in the magneto-elastic coupling (1.32). Being able to study the scattering rates in a microscopic model, we find that the magnon number-nonconserving magnon-phonon interaction is drastically enhanced near two resonance points in the frequency domain where the magnon and phonon dispersions have crossing points (see Figure 1.5). This enhancement of the magnon-phonon interaction leads to sharp features in the spin current and explains the experimentally observed peaks in the longitudinal spin Seebeck effect measurements by Kikkawa *et al.* [15].

In the two classes of spin Seebeck theories reviewed so far, the coupling between magnons and phonons was only treated on a phenomenological level encoded in a Gibert damping and random stochastic field by Xiao *et al.* and Hoffman *et al.*, and by a single magnon-phonon relaxation time as in Rezende *et al.*. A big step towards a microscopic theory was done in the coherent theory by Flebus *et al.* [20]. They use a continuum model magneto-elastic theory [38] to describe strong magnon-phonon coupling on a microscopic level, which manifests in off-diagonal elements in the second quantization magnon and phonon Hamiltonians, and leads to the formation of strongly correlated magnon polaron modes, as introduced in Section 1.5. To evaluate the bulk magnon heat and spin currents, they use a relaxation-time approximation Boltzmann transport equation for the polarons with Bose-Einstein-like distributions $n_{\mathbf{q},\nu}$ where $\nu = 1, 2, 3, 4$ counts the one magnon and three phonon-like polaron branches,

$$\mathbf{v}_{\mathbf{q},\nu} \cdot \frac{\partial n_{\mathbf{q},\nu}}{\partial \mathbf{r}} = -\frac{n_{\mathbf{q},\nu} - n_{\mathbf{q},\nu}^0}{\tau_{\mathbf{q},\nu}}, \tag{1.57}$$

where $\mathbf{v}_{\mathbf{q},\nu}$ is the group velocity of the ν-th polaron branch and $\tau_{\mathbf{q},\nu}$ is the relaxation time. For small temperature gradients, in linear response they find for the bulk magnon spin current

$$j_x^{\mathrm{s}} = -S_{xx} \frac{\partial T}{\partial x}, \tag{1.58}$$

with the bulk spin Seebeck coefficient,

$$S_{xx} = \frac{1}{V} \sum_{\mathbf{q},\nu} (|V_{\mathbf{q},4,\nu}|^2 + |V_{\mathbf{q},8,\nu}|^2) \hbar \omega_{\mathbf{q},\nu} \left(-\frac{\partial n^0}{\partial \omega} \right) v_{\mathbf{q},\nu x}^2 \tau_{\mathbf{q},\nu}, \tag{1.59}$$

where $|V_{\mathbf{q},4,\nu}|^2$, and $|V_{\mathbf{q},8,\nu}|^2$ are the amplitude of the magnonic contribution to the polaron branch ν as in Eq. (1.35). These matrix elements describe the relation between the magnon and phonon modes and the magnon-polaron modes. Based on experiments by Kikkawa *et al.* [15], they predict that depending on the magnetic and acoustic qualities of the sample, that manifest in the ratio between magnon and

impurity scattering, peaks or dips in the spin Seebeck coefficient appear at "critical" magnetic fields where the magnon and phonon dispersions have touching points and the magnon-phonon interaction is drastically enhanced. In general, YIG is known for both its low acoustic and magnetic damping, which results in long magnon and phonon mean free paths [100]. For differences in the magnon and phonon mean free paths (or equally lifetimes), for magnetic cleaner samples, $\tau_{\mathbf{q}}^{\text{mag}} > \tau_{\mathbf{q}}^{\text{pho}}$, the magnon lifetime is reduced due to strong magnon-phonon coupling which leads, according to Flebus et $al.$, to a reduction of the spin Seebeck coefficient (1.59) and the occurrence of dips near the critical magnetic fields. Vice versa for acoustic cleaner samples, $\tau_{\mathbf{q}}^{\text{mag}} < \tau_{\mathbf{q}}^{\text{pho}}$, the magnon lifetime is enhanced by the phonons. Consequentially, Flebus et $al.$ predict peaks in the spin Seebeck coefficient.

The theory of Flebus et $al.$ relies on strong inelastic background interaction that relaxes the polaron distributions $n_{\mathbf{q},\nu}$ to Bose-Einstein-like distributions. This condition is likely to perform well at elevated temperatures, as for low temperatures transport is dominated by scattering off impurities [101, 100] which cannot redistribute energy. In addition, they do only account for the bulk contribution to the spin Seebeck effect. In our theory, presented in Chapter 3, we also include the coupling of magnon polarons to the insulator and normal metal reservoirs. We predict that for the experimentally relevant system sizes there always occur peaks, independent of the type of sample quality.

2

Weakly Coupled Magnons and Phonons

In this Chapter we develop a Boltzmann transport theory of the coupled magnon-phonon transport in ferromagnetic insulators. The explicit treatment of the magnon-phonon coupling within the Boltzmann approach allows us to calculate the low-temperature magnetic-field dependence of the spin Seebeck voltage. Within the Boltzmann theory we find that this magnetic field dependence shows similar features as found by Flebus *et al.* [Phys. Rev. B **95**, 144420 (2017)] for a strongly coupled magnon phonon system that forms magnon polarons, and consistent with experimental findings in yttrium iron garnet by Kikkawa *et al.* [Phys. Rev. Lett. **117**, 207203 (2016)]. In addition to the anomalous magnetic-field dependence of the spin Seebeck effect, we also predict a dependence on the system size.

This chapter is based on the publication:

2.1   Introduction

The spin Seebeck effect (SSE) describes the generation of a spin current in a magnetic material in response to a temperature gradient applied across the sample [2, 3, 4, 45]. The spin current can be transferred to a paramagnetic metal (NM) layer attached to the magnet and is then typically detected via the inverse spin Hall effect (ISHE) [102, 57, 58, 59]. Although the spin Seebeck effect was first observed in metals [2], it has also been reported for magnetic semiconductors [3] and magnetic insulators [4]. While the SSE remains controversial in the transverse configuration, in which spin current and temperature gradient are perpendicular, due to possible effects from out-of-plane temperature gradients, the longitudinal SSE, in which the temperature gradient and the spin current are collinear, has been reproduced by many groups [71, 69, 25, 26, 68, 33, 72, 6, 7]. Recently, the spin Seebeck effect has also been observed in antiferromagnets [75, 76].

Whereas a spin current in a metallic ferromagnet can be carried by both conduction electrons and spin waves, in a ferromagnetic insulator (FMI) the spin current of the SSE is carried exclusively by spin waves or, using a quantum-mechanical language, "magnons". At the same time, in an FMI the applied temperature gradient primarily affects the lattice vibrations, *i.e.*, the phonons. The initial theoretical works by Xiao *et al.* [19] and Hoffman *et al.* [32], which treat the spin dynamics in the FMI in a Landau-Lifshitz-Gilbert approach, describe the effect of phonons on the magnetization dynamics by means of an effective temperature-dependent noise term.

A second class of theoretical calculations by Rezende and co-workers [35, 96, 36] is based on a Boltzmann approach. Whereas this approach tackles the role of magnon-magnon interaction to the SSE inside the FMI in great detail, it attributes the (phonon-related) thermal relaxation processes of the magnons in terms of a phenomenological thermal lifetime τ_{mp}. In both theories, the magnon-phonon interaction plays a key role in the determination of the magnon mean free path and, thus, of the system-size and the magnetic field dependence of the magnon-driven SSE. A purely phenomenological treatment of the phonon-magnon interaction, however, is not sufficient for a microscopic understanding of these parameter dependences of the SSE.

The importance of a microscopic understanding of the magnonic properties inside ferromagnetic insulators was also illustrated in a first series of magnetic-field dependence and length-scale probing measurements at ambient temperature [100, 103, 14, 104, 105, 37, 106]. Again, as the attached heat baths couple to the phonons inside the FMI only, the magnonic transport properties are exclusively driven by magnon-phonon coupling, so that it is crucial to study the magnon-phonon interaction processes inside the ferromagnet to understand the microscopic

origin of the SSE transport properties. Evidence of a "phonon drag" in the SSE was pointed out earlier in temperature-dependent measurements of the SSE, when the shape of the magnon conductivity showed the same temperature dependence as the corresponding phonon conductivity [21, 69]. Recently, very direct evidence of the importance of the phonon-magnon interaction for the SSE was found in low-temperature measurements [15] of the SSE in YIG, which showed sharp peaks in the spin Seebeck signal at the two specific magnetic fields where the magnon and phonon dispersions have touching points. This phenomenon was explained by the existence of "magnon-polarons" that describe mixed states which are neither purely magnonic nor phononic [20].

In this chapter we present a Boltzmann transport theory to describe the coupled magnon-phonon scattering mechanism in a simple model ferromagnetic insulator. In contrast to Ref. [20] we employ separate, incoherent magnon and phonon distributions, which, in the diffusive regime, may be described using an isotropic moment — corresponding to a local phonon or magnon temperature — and an anisotropic moment — corresponding to a phonon or magnon (momentum) current density. We assume that the relaxation due to magnon-number non-conserving scattering processes, such as magnon dipole-dipole interaction, is faster than magnon-phonon scattering processes, so that no magnon chemical potential needs to be introduced [37]. Despite the absence of coherence between magnon and phonon excitations, our findings qualitatively explain the experimental observation of peaks in the longitudinal spin Seebeck effect at low temperatures [15].

The remainder of this chapter is organized as follows: In Sec. 2.2 we present the Boltzmann equations for the magnons and phonons. We find microscopic expressions for the corresponding lifetimes from quantum-mechanically derived collision integrals. Upon imposing a hierarchy of "fast" and "slow" relaxation processes, the theory is reformulated in terms of a set of coupled hydrodynamic equations for the magnon and phonon distribution functions. The conversion of magnonic to electronic spin current at the ferromagnet–normal-metal interface is described using the spin-mixing conductance of the interface [50]. In Sec. 2.7 we apply our theory to the ferrimagnetic insulator $Y_3Fe_5O_{12}$ (YIG), choosing model parameters such that the properties of a YIG|Pt heterostructure at low temperatures are well approximated [83, 80]. We also present quantitative results for the relaxation rates, and transport coefficients of the magnon and phonon currents based on analytical evaluations, and compare our findings to the coherent magnon-polaron theory [20]. In Sec. 2.8 we summarize our findings.
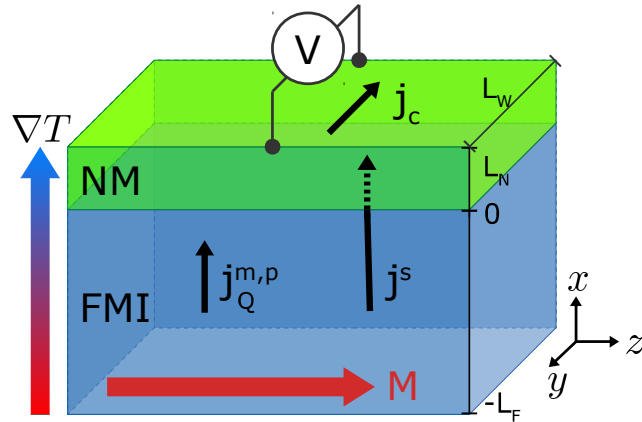
Figure 2.1: Illustration of the model setup for the longitudinal spin Seebeck effect. A ferromagnetic insulator of thickness L_F (bottom, blue) is coupled to a normal metal of thickness L_N (top, green). The coordinate axes are chosen such that the x axis is perpendicular to the ferromagnet–normal metal interface plane. A temperature difference ΔT applied across the entire system results in the flow of a spin current $\mathbf{j}^\mathrm{s}$ across the ferromagnet–normal metal interface, which can be measured by means of the inverse spin Hall effect.

2.2 Model Setup

We consider a system consisting of a ferromagnetic insulator of thickness L_F attached to a normal metal of thickness L_N as illustrated in Fig. 2.1. We choose coordinates such that the x axis is perpendicular to the ferromagnet–normal metal interface, the ferromagnet and the normal metal occupying the space $-L_\mathrm{F} < x < 0$ and $0 < x < L_\mathrm{N}$, respectively. The system is coupled to heat baths on the bottom and top, which are held at temperatures $T \pm \Delta T/2$, see Fig. 2.1. The magnetization direction and the applied magnetic field $\mathbf{B}$ are in the z-direction. We restrict ourselves to a low temperature regime, where umklapp scattering of magnons and phonons can be neglected, and optical magnons and phonons are frozen out. In YIG this corresponds to temperatures of a few K [82, 80].

The magnon and phonon distributions in the ferromagnetic insulator are described using their distribution functions $b_\mathbf{q}(\mathbf{r}, t)$ and $n_{\mathbf{q},\lambda}(\mathbf{r}, t)$, where $\mathbf{q}$ are the magnon and phonon wavevectors, and λ denotes the phonon polarization. The distribution functions $b_\mathbf{q}(\mathbf{r}, t)$ and $n_{\mathbf{q}\lambda}(\mathbf{r}, t)$ satisfy coupled Boltzmann equations, which are the starting point of our analysis.

2.3 Magnon Boltzmann equation

The Boltzmann equation for the magnon distribution $b_{\mathbf{q}}(\mathbf{r}, t)$ has the general form

$$\frac{\partial b_{\mathbf{q}}(\mathbf{r}, t)}{\partial t} + \mathbf{v}_{\mathbf{q}} \cdot \frac{\partial b_{\mathbf{q}}(\mathbf{r}, t)}{\partial \mathbf{r}} = \left. \frac{db_{\mathbf{q}}(\mathbf{r}, t)}{dt} \right|_{\text{coll.}}, \tag{2.1}$$

where $\mathbf{v}_{\mathbf{q}} = \partial \omega_{\mathbf{q}} / \partial \mathbf{q}$ is the group velocity of magnons with wavevector $\mathbf{q}$. The collision term is separated into contributions from impurity/boundary scattering (i), magnon-magnon scattering (m), and magnon-phonon scattering (p),

$$\left. \frac{db_{\mathbf{q}}}{dt} \right|_{\text{coll.}} = \left. \frac{db_{\mathbf{q}}}{dt} \right|_{\text{i}} + \left. \frac{db_{\mathbf{q}}}{dt} \right|_{\text{m}} + \left. \frac{db_{\mathbf{q}}}{dt} \right|_{\text{p}}. \tag{2.2}$$

For the impurity or boundary scattering contribution we use the relaxation-time form,

$$\left. \frac{db_{\mathbf{q}}(\mathbf{r}, t)}{dt} \right|_{\text{i}} = -\frac{b_{\mathbf{q}}(\mathbf{r}, t) - b_{\mathbf{q}}^0(\mathbf{r}, t)}{\tau_{\mathbf{q}}^{\text{im}}}. \tag{2.3}$$

Here $b_{\mathbf{q}}^0(\mathbf{r}, t)$ is the equilibrium magnon distribution at temperature $T(\mathbf{r}, t)$ and $\tau_{\mathbf{q}}^{\text{im}}$ is the relaxation time.

The magnon-magnon collision integral contains three-magnon processes which originate from dipole-dipole interaction as well as four-magnon processes which represent exchange scattering (see Tab. 2.1),

$$\begin{aligned}
\left. \frac{db_{\mathbf{q}}}{dt} \right|_{\text{m}} = &\frac{2\pi}{V^2} \sum_{\mathbf{q}_2, \mathbf{q}_1', \mathbf{q}_2'} |V_{\mathbf{q}_1', \mathbf{q}_2'; \mathbf{q}, \mathbf{q}_2}^{\text{ex}}|^2 \delta(\omega_{\mathbf{q}} + \omega_{\mathbf{k}_2} - \omega_{\mathbf{q}_1'} - \omega_{\mathbf{q}_2'}) \delta_{\mathbf{q}+\mathbf{q}_2, \mathbf{q}_1'+\mathbf{q}_2'} \\
&\qquad \times \left[(1 + b_{\mathbf{q}})(1 + b_{\mathbf{q}_2}) b_{\mathbf{q}_1'} b_{\mathbf{q}_2'} - b_{\mathbf{q}} b_{\mathbf{q}_2} (1 + b_{\mathbf{q}_1'})(1 + b_{\mathbf{q}_2'}) \right] \\
&+ \frac{2\pi}{V} \sum_{\mathbf{q}_2, \mathbf{q}'} |V_{\mathbf{q}, \mathbf{q}_2; \mathbf{q}'}^{\text{dip}}|^2 \delta(\omega_{\mathbf{q}} + \omega_{\mathbf{q}_2} - \omega_{\mathbf{q}'}) \delta_{\mathbf{q}', \mathbf{q}+\mathbf{q}_2} \\
&\qquad \times \left[(1 + b_{\mathbf{q}})(1 + b_{\mathbf{q}_2}) b_{\mathbf{q}'} - b_{\mathbf{q}} b_{\mathbf{q}_2} (1 + b_{\mathbf{q}'}) \right] \\
&+ \frac{\pi}{V} \sum_{\mathbf{q}_2', \mathbf{q}_1'} |V_{\mathbf{q}_2', \mathbf{q}_1'; \mathbf{q}}^{\text{dip}}|^2 \delta(\omega_{\mathbf{q}} - \omega_{\mathbf{q}_2'} - \omega_{\mathbf{q}_1'}) \delta_{\mathbf{q}, \mathbf{q}_2'+\mathbf{q}_1'} \\
&\qquad \times \left[(1 + b_{\mathbf{q}}) b_{\mathbf{q}_2'} b_{\mathbf{q}_1'} - b_{\mathbf{q}} (1 + b_{\mathbf{q}_2'})(1 + b_{\mathbf{q}_1'}) \right].
\end{aligned} \tag{2.4}$$

The first term on the right hand side of this expression represents the four-magnon processes, which are predominantly mediated by exchange processes. The corresponding symmetrized squared matrix element is [107, 80]

$$|V_{\mathbf{q}_1', \mathbf{q}_2'; \mathbf{q}, \mathbf{q}_2}^{\text{ex}}|^2 = 2 \left(\frac{\mu \iota}{M} \right)^2 (\mathbf{q} \cdot \mathbf{q}_2)^2, \tag{2.5}$$

where ι is the magnon exchange stiffness, $\mu = g\mu_B$ is the magnetic moment of a magnon with μ_B the Bohr magneton, $g = 2$ the Landé g-factor, M is the saturation magnetization, and V is the volume of the FMI. The second and third terms on the right hand side of Eq. (2.4) account for magnon confluence processes and magnon splitting processes [108, 80]. The factor $1/2$ in the collision integral of the splitting processes was inserted to avoid double counting. These processes arise from dipole-dipole interactions or from relativistic effects and after symmetrization one has [80]

$$|V_{\mathbf{q},\mathbf{q}';\mathbf{q}+\mathbf{q}'}^{\text{dip}}|^2 = \left(\frac{\mu_0}{4\pi}\right)^2 \frac{\pi^2 \mu^3 M}{8\hbar^2} \left| \frac{q_z q_+}{q^2} + \frac{q_z' q_+'}{q'^2} \right|^2, \tag{2.6}$$

where μ_0 is the vacuum permeability and $q_+ = q_x + i q_y$.

The third contribution to the magnon collision integral is from magnon-phonon collisions. The collision integral can be derived from the magneto-elastic Hamiltonian of Kaganov *et al.* [108, 87] and reads

$$\begin{aligned}
\frac{db_{\mathbf{q}}}{dt}\bigg|_{\mathrm{p}} &= \frac{2\pi}{V} \sum_{\mathbf{q}_2,\lambda} \sum_{\mathbf{q}'} |U_{\mathbf{q},\mathbf{q}_2,\lambda;\mathbf{q}'}|^2 \delta(\omega_{\mathbf{q}} + \omega_{\mathbf{q}_2,\lambda} - \omega_{\mathbf{q}'}) \delta_{\mathbf{q}+\mathbf{q}_2-\mathbf{q}'} \\
&\quad \times [(1+b_{\mathbf{q}})(1+n_{\mathbf{q}_2,\lambda})b_{\mathbf{q}'} - b_{\mathbf{q}} n_{\mathbf{q}_2,\lambda}(1+b_{\mathbf{q}'})] \\
&\quad + \frac{2\pi}{V} \sum_{\mathbf{q}_2',\lambda'} \sum_{\mathbf{q}'} |U_{\mathbf{q}',\mathbf{q}_2',\lambda';\mathbf{q}}|^2 \delta(\omega_{\mathbf{q}} - \omega_{\mathbf{q}_2',\lambda'} - \omega_{\mathbf{q}'}) \delta_{\mathbf{q}-\mathbf{q}_2'-\mathbf{q}'} \\
&\quad \times \left[(1+b_{\mathbf{q}})n_{\mathbf{q}_2',\lambda'}b_{\mathbf{q}'} - b_{\mathbf{q}}(1+n_{\mathbf{q}_2',\lambda'})(1+b_{\mathbf{q}'})\right] \\
&\quad + \frac{2\pi}{V} \sum_{\mathbf{q}',\lambda'} \sum_{\mathbf{q}_2} |W_{\mathbf{q}',\lambda'}^{(2)}|^2 \delta(\omega_{\mathbf{q}} - \omega_{\mathbf{q}',\lambda'} + \omega_{\mathbf{q}_2}) \delta_{\mathbf{q}+\mathbf{q}_2-\mathbf{q}'} \\
&\quad \times [(1+b_{\mathbf{q}})(1+b_{\mathbf{q}_2})n_{\mathbf{q}',\lambda'} - b_{\mathbf{q}} b_{\mathbf{q}_2}(1+n_{\mathbf{q}',\lambda'})] \\
&\quad + \frac{2\pi}{V} \sum_{\mathbf{q}',\lambda'} |W_{\mathbf{q}',\lambda'}^{(1)}|^2 \delta(\omega_{\mathbf{q}} - \omega_{\mathbf{q}',\lambda'}) \delta_{\mathbf{q}-\mathbf{q}'} \left[(1+b_{\mathbf{q}})n_{\mathbf{q}'\lambda'} - b_{\mathbf{q}}(1+n_{\mathbf{q}'\lambda'})\right], \tag{2.7}
\end{aligned}$$

The squares $|U|^2$ and $|W|^2$ are expressed in terms of the magnon exchange stiffness ι and two magneto-elastic constants B_l and B_t that represent dipole-dipole as well as spin-orbit interaction [108, 86]. The first two terms on the right hand side of this expression represent "normal" collision processes, in which the magnon number is conserved. The corresponding squared matrix element reads [38]

$$|U_{\mathbf{q},\mathbf{q}_2,\lambda;\mathbf{q}'}|^2 = \frac{\hbar}{2\varrho\omega_{\mathbf{q},\lambda}} \left[\frac{\iota}{2} \left((\mathbf{q} \cdot \mathbf{q}_2)\mathbf{q}' + (\mathbf{q}' \cdot \mathbf{q}_2)\mathbf{q} \right) \cdot \hat{e}_\lambda + \frac{B_l}{S}(\mathbf{q} - 3q_z\hat{e}_z) \cdot \hat{e}_\lambda \right]^2, \tag{2.8}$$

where $\hat{e}_\lambda$ is the unit vector indicating the polarization direction of the phonon mode $(\mathbf{q}, \lambda)$ and $S = MV_a/\mu$ is the macrospin of a unit cell of volume V_a. The first term in this expression can also be derived from a Heisenberg model, by expanding the exchange couplings to lowest order in small displacements of the atomic positions,

Magnon processes					
process	in (+)	out (-)	process	in (+)	out (-)
magnon impurity	*(diagram)*	*(diagram)*	phonon to magnon	*(diagram)*	*(diagram)*
4-magnon exchange	*(diagram)*	*(diagram)*	phonon to 2 magnon	*(diagram)*	*(diagram)*
3-magnon confluence	*(diagram)*	*(diagram)*	phonon emission	*(diagram)*	*(diagram)*
3-magnon splitting	*(diagram)*	*(diagram)*	phonon absorption	*(diagram)*	*(diagram)*

Table 2.1: Schematic overview of the relevant magnon-magnon and magnon-phonon scattering processes.

see Refs. [109, 86]. The third term describes the pairwise creation or annihilation of magnons,

$$|W_{\mathbf{q},\lambda}^{(2)}|^2 = \frac{\hbar}{2\varrho\omega_{\mathbf{q},\lambda}} \left[\left(\frac{B_\text{l}}{2S}(q_x\hat{e}_x - q_y\hat{e}_y) \cdot \hat{e}_\lambda \right)^2 + \left(\frac{B_\text{t}}{2S}(q_y\hat{e}_x + q_x\hat{e}_y) \cdot \hat{e}_\lambda \right)^2 \right]. \quad (2.9)$$

Finally, the fourth term on the right hand side of Eq. (2.7) describes the conversion of a magnon into a single phonon and vice versa, with [87, 38]

$$|W_{\mathbf{q},\lambda}^{(1)}|^2 = \frac{\hbar}{2\varrho\omega_{\mathbf{q},\lambda}} \frac{B_\text{t}^2}{2S} \left[((q_z\hat{e}_x + q_x\hat{e}_z) \cdot \hat{e}_\lambda)^2 + ((q_z\hat{e}_y + q_y\hat{e}_z) \cdot \hat{e}_\lambda)^2 \right]. \quad (2.10)$$

In principle, the latter process gives rise to the existence of "magnon polarons" [110, 111], a coherent superposition of a magnon and phonon excitation. Sufficiently strong phonon-phonon and magnon-magnon scattering processes destroy the magnon-phonon coherence, however, validating our incoherent description in terms of the distribution function only. (Note that Ref. [15, 20] uses a fully coherent description, finding results that do not differ qualitatively from ours.) The three types of magnon-phonon scattering processes are illustrated schematically in Table 2.1.

2.4 Phonon Boltzmann equation

The Boltzmann equation for the phonon distribution function $n_{\mathbf{q},\lambda}(\mathbf{r}, t)$ reads

$$\frac{\partial n_{\mathbf{q},\lambda}(\mathbf{r}, t)}{\partial t} + \mathbf{c}_{\mathbf{q},\lambda} \cdot \frac{\partial n_{\mathbf{q},\lambda}(\mathbf{r}, t)}{\partial \mathbf{r}} = \left. \frac{dn_{\mathbf{q},\lambda}(\mathbf{r}, t)}{dt} \right|_\text{coll.}, \quad (2.11)$$

where $\mathbf{c}_{\mathbf{q},\lambda} = \partial\omega_{\mathbf{q},\lambda}/\partial\mathbf{q}$ is the group velocity of phonons with wavevector $\mathbf{q}$ and polarization λ. The collision term is separated into contributions from impurity/boundary scattering (i), phonon-phonon scattering (p), and phonon-magnon scattering (m). As in the case of the magnons, we will describe phonon-impurity scattering using the relaxation-time approximation,

$$\left.\frac{dn_{\mathbf{q},\lambda}(\mathbf{r},t)}{dt}\right|_{\mathrm{i}} = -\frac{n_{\mathbf{q},\lambda}(\mathbf{r},t) - n_{\mathbf{q},\lambda}^0(\mathbf{r},t)}{\tau_{\mathbf{q},\lambda}^{\mathrm{ip}}} \tag{2.12}$$

where $\tau_{\mathbf{q},\lambda}^{\mathrm{ip}}$ is the corresponding phonon-impurity scattering time. The expression for the phonon-magnon collision term reads

$$\begin{aligned}
\left.\frac{dn_{\mathbf{q},\lambda}}{dt}\right|_{\mathrm{m}} &= \frac{2\pi}{V} \sum_{\mathbf{q}_2,\mathbf{q}'} |U_{\mathbf{q}_2,\mathbf{q},\lambda;\mathbf{q}'}|^2 \delta(\omega_{\mathbf{q},\lambda} + \omega_{\mathbf{q}_2} - \omega_{\mathbf{q}'})\delta_{\mathbf{q}+\mathbf{q}_2,\mathbf{q}'} \\
&\quad \times [(1 + b_{\mathbf{q}_2})(1 + n_{\mathbf{q},\lambda})b_{\mathbf{q}'} - b_{\mathbf{q}_2}n_{\mathbf{q},\lambda}(1 + b_{\mathbf{q}'})] \\
&\quad + \frac{2\pi}{V} \sum_{\mathbf{q}'} |W_{\mathbf{q},\lambda}^{(1)}|^2 \delta(\omega_{\mathbf{q},\lambda} - \omega_{\mathbf{q}'})\delta_{\mathbf{q}-\mathbf{q}'}[b_{\mathbf{q}'}(1 + n_{\mathbf{q},\lambda}) - (1 + b_{\mathbf{q}'})n_{\mathbf{q},\lambda}] \\
&\quad + \frac{\pi}{V} \sum_{\mathbf{q}_1',\mathbf{q}_2'} |W_{\mathbf{q},\lambda}^{(2)}|^2 \delta(\omega_{\mathbf{q},\lambda} - \omega_{\mathbf{q}_1'} - \omega_{\mathbf{q}_2'})\delta_{\mathbf{q},\mathbf{q}_1'-\mathbf{q}_2'} \\
&\quad \times \left[b_{\mathbf{q}_1'}b_{\mathbf{q}_2'}(1 + n_{\mathbf{q},\lambda}) - (1 + b_{\mathbf{q}_1'})(1 + b_{\mathbf{q}_2'})n_{\mathbf{q},\lambda}\right]. \tag{2.13}
\end{aligned}$$

We will not give an explicit expression for the phonon-phonon collision integral, since the corresponding collision rates do not enter in our final expressions (see the discussion below).

2.5 Ansatz for the distribution function

To simplify the analysis of the coupled Boltzmann equations for the magnon and phonon distribution functions, we consider small deviations from equilibrium only and linearize the distribution functions $b_{\mathbf{q}}(\mathbf{r},t)$ and $n_{\mathbf{q},\lambda}(\mathbf{r},t)$ around the equilibrium distributions $b_{\mathbf{q}}^0 = 1/(e^{\hbar\omega_{\mathbf{q}}/k_BT} - 1)$ and $n_{\mathbf{q},\lambda}^0 = 1/(e^{\hbar\omega_{\mathbf{q},\lambda}/k_BT} - 1)$,

$$b_{\mathbf{q}}(\mathbf{r},t) = b_{\mathbf{q}}^0 + \left(-\frac{\partial b^0}{\partial\omega}\right)\phi_{\mathbf{q}}(\mathbf{r},t), \tag{2.14}$$

$$n_{\mathbf{q},\lambda}(\mathbf{r},t) = n_{\mathbf{q},\lambda}^0 + \left(-\frac{\partial n^0}{\partial\omega}\right)\psi_{\mathbf{q},\lambda}(\mathbf{r},t). \tag{2.15}$$

We further assume that the magnon-magnon and phonon-phonon interactions are strong enough, when compared to the magnon-phonon interactions, that the magnon

and phonon distributions everywhere are in a *local equilibrium*, characterized by energy and momentum densities $\rho_E^{\mathrm{m,p}}$ and $\rho_{\mathbf{q}}^{\mathrm{m,p}}$. This corresponds to the parameterization [43]

$$\phi_{\mathbf{q}}(\mathbf{r}, t) = \frac{\omega_{\mathbf{q}}}{T} \Delta T^{\mathrm{m}} + \mathbf{q} \cdot \mathbf{v}^{\mathrm{m}},$$

$$\psi_{\mathbf{q},\lambda}(\mathbf{r}, t) = \frac{\omega_{\mathbf{q},\lambda}}{T} \Delta T^{\mathrm{p}} + \mathbf{q} \cdot \mathbf{v}^{\mathrm{p}}, \tag{2.16}$$

where $\Delta T^{\mathrm{m,p}}$ is the difference local magnon/phonon temperature and the (global) equilibrium temperature T and $\mathbf{v}^{\mathrm{m,p}}$ parameterizes the magnon/phonon momentum density. The temperature differences $\Delta T^{\mathrm{m,p}}$ and the velocities $\mathbf{v}^{\mathrm{m,p}}$ are related to the corresponding energy and momentum densities as

$$\Delta \rho_E^{\mathrm{m,p}} = C^{\mathrm{m,p}} \Delta T^{\mathrm{m,p}},$$

$$\rho_{q_\alpha}^{\mathrm{m,p}} = \sum_\beta \mathcal{C}_{\alpha\beta}^{\mathrm{m,p}} v_\beta^{\mathrm{m,p}}, \tag{2.17}$$

which defines the specific heat capacities

$$C^{\mathrm{m}} = \frac{1}{V} \sum_{\mathbf{q}} \frac{\partial b^0}{\partial T} \hbar \omega_{\mathbf{q}},$$

$$C^{\mathrm{p}} = \frac{1}{V} \sum_{\mathbf{q},\lambda} \frac{\partial n^0}{\partial T} \hbar \omega_{\mathbf{q},\lambda}, \tag{2.18}$$

and the tensor coefficients

$$\mathcal{C}_{\alpha\beta}^{\mathrm{m}} = \frac{1}{V} \sum_{\mathbf{q}} \left(-\frac{\partial b^0}{\partial \omega} \right) q_\alpha q_\beta,$$

$$\mathcal{C}_{\alpha\beta}^{\mathrm{p}} = \frac{1}{V} \sum_{\mathbf{q},\lambda} \left(-\frac{\partial n^0}{\partial \omega} \right) q_\alpha q_\beta. \tag{2.19}$$

One verifies that the magnon-magnon and phonon-phonon collision integrals are zero for a distribution function of this form, since magnon-magnon and phonon-phonon collisions conserve energy and momentum. (Recall that we neglect umklapp processes.)

The velocities $\mathbf{v}^{\mathrm{m,p}}$ are related to the magnon spin current density $\mathbf{j}^{\mathrm{s}}$ and heat current densities $\mathbf{j}_Q^{\mathrm{m,p}}$,

$$\mathbf{j}^{\mathrm{s}} = \frac{\hbar}{V} \sum_{\mathbf{q}} \mathbf{v}_{\mathbf{q}} b_{\mathbf{q}}, \tag{2.20}$$

$$\mathbf{j}_Q^{\mathrm{m}} = \frac{1}{V} \sum_{\mathbf{q}} \hbar \omega_{\mathbf{q}} \mathbf{v}_{\mathbf{q}} b_{\mathbf{q}}, \tag{2.21}$$

$$\mathbf{j}_Q^{\mathrm{p}} = \frac{1}{V} \sum_{\mathbf{q},\lambda} \hbar \omega_{\mathbf{q},\lambda} \mathbf{c}_{\mathbf{q},\lambda} n_{\mathbf{q},\lambda}. \tag{2.22}$$

Upon substitution of the Ansatz (2.14) one finds

$$j_\alpha^s = \sum_\beta \mathcal{J}_{\alpha\beta} v_\beta^m, \tag{2.23}$$

$$j_{Q\alpha}^{m,p} = \sum_\beta \mathcal{I}_{\alpha\beta}^{m,p} v_\beta^{m,p} \tag{2.24}$$

with

$$\mathcal{J}_{\alpha\beta} = \frac{\hbar}{V} \sum_{\mathbf{q}} \left(-\frac{\partial b^0}{\partial \omega} \right) v_{\mathbf{q}\beta} q_\alpha,$$

$$\mathcal{I}_{\alpha\beta}^m = \frac{1}{V} \sum_{\mathbf{q}} \left(-\frac{\partial b^0}{\partial \omega} \right) \hbar\omega_{\mathbf{q}} v_{\mathbf{q}\beta} q_\alpha,$$

$$\mathcal{I}_{\alpha\beta}^p = \frac{1}{V} \sum_{\mathbf{q},\lambda} \left(-\frac{\partial n^0}{\partial \omega} \right) \hbar\omega_{\mathbf{q},\lambda} c_{\mathbf{q},\lambda\beta} q_\alpha. \tag{2.25}$$

Impurity scattering and magnon-phonon scattering cause a further relaxation of the distribution functions. Impurity scattering tends to suppress any finite values of $\mathbf{v}^m$ and $\mathbf{v}^p$ but leaves ΔT^m and ΔT^p unaffected; magnon-phonon scattering suppresses differences $\Delta T^m - \Delta T^p$ and $\mathbf{v}^m - \mathbf{v}^p$. To derive the continuity equations for $\Delta T^{m,p}$ and $\mathbf{v}^{m,p}$ we substitute the Ansatz (2.16) into the Boltzmann equations for the magnon and phonon distribution functions and calculate the rate of change of the energy and momentum densities. This gives

$$C^m \frac{\partial \Delta T^m}{\partial t} + \sum_{\alpha,\beta} \mathcal{I}_{\alpha\beta}^m \frac{\partial v_\alpha^m}{\partial x_\beta} = -G(\Delta T^m - \Delta T^p), \tag{2.26}$$

$$C^p \frac{\partial \Delta T^p}{\partial t} + \sum_{\alpha,\beta} \mathcal{I}_{\alpha\beta}^p \frac{\partial v_\alpha^p}{\partial x_\beta} = -G(\Delta T^p - \Delta T^m), \tag{2.27}$$

$$\sum_\alpha \left(\frac{\mathcal{I}_{\beta\alpha}^m}{T} \frac{\partial \Delta T^m}{\partial x_\alpha} + \mathcal{C}_{\alpha\beta}^m \frac{\partial v_\alpha^m}{\partial t} \right) = -\sum_\alpha \left[\mathcal{G}_{\alpha\beta}^{im} v_\alpha^m + \mathcal{G}_{\alpha\beta}(v_\alpha^m - v_\alpha^p) \right], \tag{2.28}$$

$$\sum_\alpha \left(\frac{\mathcal{I}_{\beta\alpha}^p}{T} \frac{\partial \Delta T^p}{\partial x_\alpha} + \mathcal{C}_{\alpha\beta}^p \frac{\partial v_\alpha^p}{\partial t} \right) = -\sum_\alpha \left[\mathcal{G}_{\alpha\beta}^{ip} v_\alpha^p + \mathcal{G}_{\alpha\beta}(v_\alpha^p - v_\alpha^m) \right], \tag{2.29}$$

where the tensor coefficients $\mathcal{I}_{\alpha\beta}^{m,p} = \partial j_{Q\alpha}^{m,p}/\partial v_\alpha^{m,p} = \partial j_{k\alpha\beta}^{m,p}/\partial \Delta T^{m,p}$, with $\mathbf{j}_Q^{m,p}$ and $\mathbf{j}_{\mathbf{q}}$ the energy and momentum current densities, respectively. The right hand side of Eqs. (2.26)–(2.29) describes energy and momentum exchange between magnons and phonons and momentum exchange between magnons or phonons and impurities.

The rates for these processes are

$$\mathcal{G}_{\alpha\beta}^{\text{im}} = \frac{1}{V}\sum_{\mathbf{q}}\left(-\frac{\partial b^0}{\partial\omega}\right)\frac{q_\alpha q_\beta}{\tau_{\mathbf{q}}^{\text{im}}}, \quad \mathcal{G}_{\alpha\beta}^{\text{ip}} = \frac{1}{V}\sum_{\mathbf{q},\lambda}\left(-\frac{\partial n^0}{\partial\omega}\right)\frac{q_\alpha q_\beta}{\tau_{\mathbf{q}\lambda}^{\text{ip}}},$$

$$G = \frac{1}{V}\sum_{\mathbf{q},\lambda}\frac{\hbar\omega_{\mathbf{q},\lambda}^2}{k_B T^2}\gamma_{\mathbf{q},\lambda}, \quad \mathcal{G}_{\alpha\beta} = \frac{1}{V}\sum_{\mathbf{q},\lambda}\frac{q_\alpha q_\beta}{k_B T}\gamma_{\mathbf{q},\lambda}, \tag{2.30}$$

where we abbreviated

$$\gamma_{\mathbf{q},\lambda} = \frac{2\pi}{V}\sum_{\mathbf{q}'} n_{\mathbf{q},\lambda}^0 \left[|U_{\mathbf{q}',\mathbf{q},\lambda;\mathbf{q}+\mathbf{q}'}|^2 b_{\mathbf{q}'}^0 (1+b_{\mathbf{q}+\mathbf{q}'}^0)\delta(\omega_{\mathbf{q},\lambda}+\omega_{\mathbf{q}'}-\omega_{\mathbf{q}+\mathbf{q}'})\right.$$

$$+\frac{1}{2}|W_{\mathbf{q},\lambda}^{(2)}|^2(1+b_{\mathbf{q}-\mathbf{q}'}^0)(1+b_{\mathbf{q}'}^0)\delta(\omega_{\mathbf{q},\lambda}-\omega_{\mathbf{q}'}-\omega_{\mathbf{q}-\mathbf{q}'})$$

$$\left.+|W_{\mathbf{q},\lambda}^{(1)}|^2(1+b_{\mathbf{q}'}^0)\delta_{\mathbf{q}-\mathbf{q}'}\delta(\omega_{\mathbf{q},\lambda}-\omega_{\mathbf{q}'})\right]. \tag{2.31}$$

Equations (2.26)–(2.29) fully describe the coupled energy and momentum transport of the magnon and phonon systems. In the steady state, Eqs. (2.28) and (2.29) describe "phonon drag" and "magnon drag", the appearance of an anisotropic component of the magnon and phonon distributions in response to a gradient of the temperatures. The isotropic moment in Eqs. (2.26) and (2.27) describes the relaxation of the magnon temperature towards the phonon temperature.

2.6 Boundary conditions and spin Seebeck voltage

At the ferromagnetic insulator—insulator boundary at $x = -L_F$ the magnon spin current (2.20) is zero, which implies $v^{\text{m}}(-L_F) = 0$, whereas the phonon temperature $\Delta T^{\text{p}}(-L_F) = \Delta T/2$ is determined by the temperature of the bottom heat bath, see Fig. 2.1. Similarly, at the normal-metal interface $x = 0$ the phonon temperature T^{p} satisfies the boundary condition $\Delta T^{\text{p}}(0) = -\Delta T/2$. The boundary condition for the magnon current at the normal-metal interface $x = 0$ takes the form

$$j_x^{\text{s}}(0) = S_{\text{m}}'(\Delta T^{\text{m}}(0) - \Delta T^{\text{e}}(0)), \tag{2.32}$$

where $\Delta T^{\text{e}}(0) = -\Delta T/2$ is the (deviation of the) electron temperature at the interface at $x = 0$ and S_{m}' is the interface spin Seebeck coefficient [112], which can be expressed in terms of the real part g_{r} of the spin mixing conductance [19],

$$S_{\text{m}}' = \frac{g_{\text{r}}}{\pi A S}\frac{1}{N}\sum_{\mathbf{q}}\hbar\omega_{\mathbf{q}}\frac{\partial b^0}{\partial T}, \tag{2.33}$$

where S is the spin of the unit cell. A derivation of the boundary condition (2.32) and a microscopic model leading to the expression for (2.33) for the interface spin Seebeck coefficient S'_{m} are given in appendix A.2.

The relation between the spin current $j^{\mathrm{s}}_x(0)$ at the ferromagnet–normal metal interface and the transverse spin Seebeck voltage follows the theory of the inverse spin Hall effect. A nonzero spin current density implies a finite gradient of the spin accumulation $\mu_{\mathrm{s}} = \mu_{\uparrow} - \mu_{\downarrow}$ [113]

$$\mathbf{j}^{\mathrm{s}} = -\sigma_{\mathrm{s}} \partial_{\mathbf{r}} \mu_{\mathrm{s}}, \tag{2.34}$$

where σ_{s} is the spin conductivity. The spin accumulation satisfies the equation [113]

$$\lambda^2_{\mathrm{sf}} \partial^2_{\mathbf{r}} \mu_{\mathrm{s}} = \mu_{\mathrm{s}}, \tag{2.35}$$

where λ_{sf} is the spin-flip length. Together with the boundary condition $j^{\mathrm{s}}_x(L_{\mathrm{N}}) = 0$ at the interface between the normal metal and the top heat bath, this gives the solution

$$j^{\mathrm{s}}_x(x) = j^{\mathrm{s}}_x(0) \frac{\sinh((L_{\mathrm{N}} - x)/\lambda_{\mathrm{sf}})}{\sinh(L_{\mathrm{N}}/\lambda_{\mathrm{sf}})}. \tag{2.36}$$

The spin Seebeck voltage equals [19]

$$V_{\mathrm{SSE}}(x) = \frac{2e}{\hbar} \theta_{\mathrm{SH}} L_{\mathrm{W}} \rho j^{\mathrm{s}}_x(x), \tag{2.37}$$

where L_{W} is the sample width, ρ the electric resistivity, and θ_{SH} is the spin Hall angle of the normal metal. Averaging over x gives

$$\begin{aligned} V_{\mathrm{SSE}} &= \frac{1}{L_{\mathrm{N}}} \int_0^{L_{\mathrm{N}}} dx V_{\mathrm{SSE}}(x) \\ &= \theta_{\mathrm{SH}} \rho \frac{2e}{\hbar} \frac{L_{\mathrm{W}}}{L_{\mathrm{N}}} \lambda_{\mathrm{sf}} j^{\mathrm{s}}_x(0) \tanh\left(\frac{L_{\mathrm{N}}}{2\lambda_{\mathrm{sf}}}\right). \end{aligned} \tag{2.38}$$

2.7 Longitudinal spin Seebeck effect

We use our theory to describe the longitudinal spin Seebeck effect in YIG|Pt heterostructures, where we put our focus on the magnetic field dependence measurements at low temperatures as performed by Kikkawa $et\ al.$ [14, 15]. Since the longitudinal spin Seebeck effect is a steady-state phenomenon, driven by a time-independent temperature difference ΔT applied across the ferromagnet–normal-metal bilayer, we may neglect the time derivatives in the continuity equations (2.26)–(2.29) and restrict our attention to time-independent solutions. Also, for the one-dimensional geometry of Fig. 2.1, all spatial dependences will be as a function of the coordinate x only.

At low temperatures we may take a parabolic band for the magnon dispersion,

$$\omega_{\mathbf{q}} = \iota|\mathbf{q}|^2 + \frac{\mu}{\hbar}(B + \mu_0 M), \tag{2.39}$$

with an offset due to the intrinsic exchange splitting and the Zeeman shift. Here B denotes the applied magnetic field and $\mu_0 M$ is the exchange gap. For the phonons we restrict ourselves to the acoustic branches,

$$\omega_{\mathbf{q},\lambda} = c_\lambda|\mathbf{q}|, \tag{2.40}$$

where c_λ is the sound velocity and $\mathbf{q}$ the phonon wave vector. For a YIG crystal oriented along the $\langle 100 \rangle$ axis there are one longitudinal as well as two transverse polarized acoustic phonon branches. The values of the corresponding material properties which are used for our numerical calculation are summarized in Table 2.2. For this simple model description the system is isotropic, so that the tensors $\mathcal{I}^{\mathrm{m,p}}$, $\mathcal{G}^{\mathrm{im,ip}}$, and $\mathcal{G}$ are proportional to the diagonal tensor.

Substituting the explicit expressions we find, for temperatures low enough that the dispersions (2.39) and (2.40) are valid for all thermally excited magnons and phonons, that

$$\mathcal{I}^{\mathrm{m}} = \frac{5}{16}\frac{(k_{\mathrm{B}}T/\hbar)^{5/2}}{(\pi\iota)^{3/2}}e^{-\hbar\omega_0/(k_{\mathrm{B}}T)}, \tag{2.41}$$

with $\omega_0 = \mu(B + \mu_0 M)/\hbar$, and

$$\mathcal{I}^{\mathrm{p}} = \sum_\lambda \frac{2\pi^2(k_{\mathrm{B}}T)^4}{45c_\lambda^3\hbar^4}. \tag{2.42}$$

In the steady-state limit the velocities $\mathbf{v}^{\mathrm{m}}$ and $\mathbf{v}^{\mathrm{p}}$ can be obtained from Eqs. (2.28) and (2.29),

$$\mathbf{v}^{\mathrm{m}} = -\frac{1}{T}\frac{(\mathcal{G}^{\mathrm{ip}} + \mathcal{G})\mathcal{I}^{\mathrm{m}}\partial_{\mathbf{r}}\Delta T^{\mathrm{m}} + \mathcal{G}\mathcal{I}^{\mathrm{p}}\partial_{\mathbf{r}}\Delta T^{\mathrm{p}}}{\mathcal{G}^{\mathrm{im}}\mathcal{G}^{\mathrm{ip}} + \mathcal{G}\mathcal{G}^{\mathrm{im}} + \mathcal{G}\mathcal{G}^{\mathrm{ip}}}, \tag{2.43}$$

$$\mathbf{v}^{\mathrm{p}} = -\frac{1}{T}\frac{(\mathcal{G}^{\mathrm{im}} + \mathcal{G})\mathcal{I}^{\mathrm{p}}\partial_{\mathbf{r}}\Delta T^{\mathrm{p}} + \mathcal{G}\mathcal{I}^{\mathrm{m}}\partial_{\mathbf{r}}\Delta T^{\mathrm{m}}}{\mathcal{G}^{\mathrm{im}}\mathcal{G}^{\mathrm{ip}} + \mathcal{G}\mathcal{G}^{\mathrm{im}} + \mathcal{G}\mathcal{G}^{\mathrm{ip}}}, \tag{2.44}$$

They imply a relation between the magnon spin current $\mathbf{j}^{\mathrm{s}}$, and between the magnon and phonon heat currents $\mathbf{j}_Q^{\mathrm{m,p}}$ and the gradients of the magnon and phonon temperatures,

$$\mathbf{j}^{\mathrm{s}} = -S_{\mathrm{m}}\partial_{\mathbf{r}}\Delta T^{\mathrm{m}} - S_{\mathrm{d}}\partial_{\mathbf{r}}\Delta T^{\mathrm{p}}, \tag{2.45}$$

$$\mathbf{j}_Q^{\mathrm{m,p}} = -\kappa_{\mathrm{m,p}}\partial_{\mathbf{r}}\Delta T^{\mathrm{m,p}} - \kappa_{\mathrm{d}}\partial_{\mathbf{r}}\Delta T^{\mathrm{p,m}}, \tag{2.46}$$

YIG continuum theory parameters

	Quantity	Value	Reference
lattice constant	a (YIG)	1.24 nm	[80]
exchange stiffness	ι	8.06×10^{-6} m^2/s	[114]
saturation magnetization	$\mu_0 M$	0.18 T	[115]
long. sound velocity	c_l	7209 m/s	[38]
trans. sound velocity	c_t	3843 m/s	[38]
mass density	ϱ	21450 kg/m^3	[83]
long. magneto-elastic constant	B_l	1 THz	[38]
trans. magneto-elastic constant	B_t	2 THz	[38]

Pt and YIG/Pt interface parameters

	Quantity	Value	Reference
lattice constant	a (Pt)	0.39 nm	[1]
spin mixing conductance	g_r/A	10^{16} 1/m^2	[115]
spin Hall angle	θ_{SH}	0.0037	[59]
spin diffusion length	λ_{sf}	7.3 nm	[116]
electrical resistivity	ρ	0.91×10^{-6} Ω/m	[5]
sample dimensions	$L_N \times L_W$	5 nm $\times$ 2 mm	

Table 2.2: Parameter values used for the numerical calculations. The last column lists the relevant references where these values were obtained.

with the (bulk) spin Seebeck coefficients

$$S_m = \frac{1}{T} \frac{\mathcal{J}(\mathcal{G}^{ip} + \mathcal{G})\mathcal{I}^m}{\mathcal{G}^{im}\mathcal{G}^{ip} + \mathcal{G}\mathcal{G}^{im} + \mathcal{G}\mathcal{G}^{ip}},$$

$$S_d = \frac{1}{T} \frac{\mathcal{J}\mathcal{G}\mathcal{I}^p}{\mathcal{G}^{im}\mathcal{G}^{ip} + \mathcal{G}\mathcal{G}^{im} + \mathcal{G}\mathcal{G}^{ip}}, \tag{2.47}$$

and thermal conductivities

$$\kappa_m = \frac{1}{T} \frac{(\mathcal{G}^{ip} + \mathcal{G})(\mathcal{I}^m)^2}{\mathcal{G}^{im}\mathcal{G}^{ip} + \mathcal{G}\mathcal{G}^{im} + \mathcal{G}\mathcal{G}^{ip}},$$

$$\kappa_p = \frac{1}{T} \frac{(\mathcal{G}^{im} + \mathcal{G})(\mathcal{I}^p)^2}{\mathcal{G}^{im}\mathcal{G}^{ip} + \mathcal{G}\mathcal{G}^{im} + \mathcal{G}\mathcal{G}^{ip}},$$

$$\kappa_d = \frac{1}{T} \frac{\mathcal{G}\mathcal{I}^p\mathcal{I}^m}{\mathcal{G}^{im}\mathcal{G}^{ip} + \mathcal{G}\mathcal{G}^{im} + \mathcal{G}\mathcal{G}^{ip}}. \tag{2.48}$$

The coefficients S_d and κ_d describe the "phonon drag", the anisotropic component of the magnon distribution in response to a gradient of the phonon temperature.

To obtain a numerical estimate of the relevant relaxation rates, we use the values given in Table 2.2. For impurity scattering we assume that the phonon-impurity and magnon-impurity scattering times $\tau_{\mathbf{q}\lambda}^{\mathrm{ip}} = \tau_{\mathrm{ip}}$ and $\tau_{\mathbf{q}}^{\mathrm{im}} = \tau_{\mathrm{im}}$ are independent of $\mathbf{q}$ and λ, respectively, and extract these times from the low-temperature thermal conductivity and its magnetic field dependence as in Boona *et al.* [100]. This gives the values $\tau_{\mathrm{im}} = 3.4 \times 10^{-8}$ s and $\tau_{\mathrm{ip}} = 5.6 \times 10^{-8}$ s. Figure 2.2 shows the temperature and magnetic-field dependences of the three contributions to the magnon-phonon relaxation rates $\mathcal{G}$ and of the impurity rates $\mathcal{G}^{\mathrm{im}}$ and $\mathcal{G}^{\mathrm{ip}}$.

The phonon-to-magnon conversion and phonon-to-two-magnons conversion cease to contribute to the relaxation rate $\mathcal{G}$ above a "critical" magnetic field, because of energy and momentum conservation considerations. Since the phonon and magnon dispersions are tangential at the critical magnetic field, see Fig. 2.2c and d, the magnon-to-phonon conversion rates diverges upon approaching the critical field from below [1]. There are two such divergences, because longitudinal and transversal phonons have different velocities and, hence, different critical fields. In our approach the divergences should be broadened by the (maximum of the) phonon-phonon and magnon-magnon scattering rates. These rates do not appear explicitly in the continuity equations (2.26)–(2.29). Instead, they are only considered implicitly in our theory, because they enforce the local equilibrium form (2.16) of the magnon and phonon distribution functions. For that reason, the broadening of the divergences in Figs. 2.2 and 2.3 has to take place *a posteriori*. We have broadened the divergence of the results shown in Figs. 2.2 and 2.3 by an average magnon-magnon lifetime $\tau_{\mathrm{m}} = 10^{-10}$ s [35] due to magnon number conserving scattering which corresponds to an energy broadening $\epsilon = \hbar/2\tau_{\mathrm{m}} = 10^{-6}$ eV. For comparison, in the coherent theory of Refs. [15, 20] the magnon-magnon and phonon-phonon relaxation rates are assumed to be much smaller than the coherent magnon-phonon coupling and the broadening of the sharp magnetic-field dependent features is determined by the magnon-phonon coupling energy. The (relativistic) phonon-to-two-magnons conversion shows a monotonous decay upon increasing the magnetic field.

The isotropic moment in Eqs. (2.26) and (2.27) describes the relaxation of the magnon temperature towards the phonon temperature. Of special interest for the calculation of the spin Seebeck current is the so-called thermal decay length λ, which describes the length scale over which a difference between magnon and phonon temperatures at the interface relaxes towards the center of the ferromagnet. Upon substituting the velocities (2.43) and (2.44) into the continuity equations (2.26) and (2.27) we obtain two second order differential equation for the magnon and phonon

---

[1]The divergence is partially suppressed once deviations from the fully isotropic dispersions (2.39) and (2.40) are taken into account.

temperatures,

$$\kappa_m \partial_x^2 \Delta T^m + \kappa_d \partial_x^2 \Delta T^p = G(\Delta T^m - \Delta T^p)$$
$$\kappa_p \partial_x^2 \Delta T^p + \kappa_d \partial_x^2 \Delta T^m = G(\Delta T^p - \Delta T^m). \tag{2.49}$$

The general solution of these equations is of the form

$$\Delta T^m(x) = \Delta T_0 + \alpha x + (\kappa_p + \kappa_d) \sum_{\pm} \delta_{\pm} e^{\pm x/\lambda}$$

$$\Delta T^p(x) = \Delta T_0 + \alpha x - (\kappa_m + \kappa_d) \sum_{\pm} \delta_{\pm} e^{\pm x/\lambda}, \tag{2.50}$$

with the decay length

$$\lambda^2 = \frac{\kappa_m \kappa_p - \kappa_d^2}{G(\kappa_p + \kappa_m + 2\kappa_d)} \tag{2.51}$$

and with coefficients ΔT_0, α, and $\delta_{\pm}$ that are determined by the boundary conditions.

Taking the parameter values for YIG, see Table 2.2, we find that find that $\kappa_p \gg \kappa_{m,d}$. In the limit $\kappa_p \gg \kappa_{m,d}$, Eq. (2.50) gives a strictly linear spatial profile for the phonon temperature, so that $\Delta T_0 = 0$ and $\alpha = -\Delta T/L_F$. The remaining parameters $\delta_{\pm}$ can then be obtained from the boundary conditions for the magnon spin current at $x = -L_F$ and $x = 0$. The result for the (magnon) spin current $j_x^s(0)$ at the ferromagnet–normal metal interface is

$$j_x^s(0) = \frac{\Delta T}{L} \frac{(S_m + S_d)\tanh(L/2\lambda)}{S_m/(\lambda S_m') + \coth(L/\lambda)}. \tag{2.52}$$

Substitution of Eq. (2.52) into the expression (2.38) gives the corresponding spin Seebeck voltage. An analytic solution of the equations is possible without the simplifications associated with the limit $\kappa_p \gg \kappa_{m,d}$, too, although the resulting expression for $j_x^s(0)$ is not as concise as Eq. (2.52).

Figure 2.3 shows the resulting spin Seebeck voltage V_{SSE} for two different temperatures, as a function of the applied magnetic field. Although V_{SSE} generally decreases upon increasing the magnetic field, sharp features exist near the "critical" magnetic fields at which the magnon-to-phonon conversion rate diverges. The magnitude of those features depends on the impurity lifetimes $\tau_{im,p}$, and the length of the FMI. These results are similar to those obtained by Kikkawa *et al.* and Flebus *et al.* [15, 20], where the magnon-to-phonon conversion processes were treated coherently. The incoherent approach taken here should be valid if the incoherent processes dominate over the coherent ones, *i.e.*, if the magnon-to-phonon conversion matrix elements are small in comparison to the phonon-phonon and/or magnon-magnon scattering lifetimes. At a fixed applied magnetic field the dependence of the longitudinal spin Seebeck effect on the thickness L_F of the ferromagnetic layer is governed by the combination $\lambda S_m'/S_m$, which controls the experimentally observed saturation of the LSSE signal towards bulk ferromagnetic samples [103].
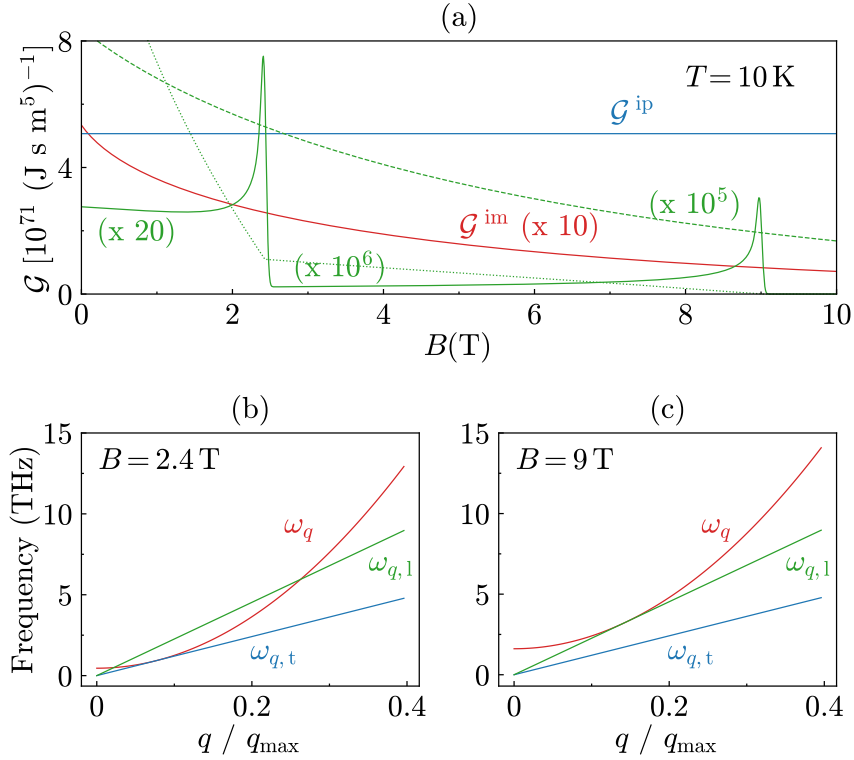
Figure 2.2: (a) Three contributions to the magnon-phonon relaxation rate $\mathcal{G}$, the magnon-impurity rate $\mathcal{G}^{\text{im}}$, and the phonon-impurity rate $\mathcal{G}^{\text{im}}$, as a function of the applied magnetic field B. The three contributions to the magnon-phonon rate are from magnon-phonon-scattering (solid), phonon-to-magnon conversion (dashed), and phonon-to-two-magnon conversion (dotted). The magnon and phonon energy dispersions for the "critical" applied magnetic fields $B_{\text{t}} = 2.4$ T and $B_{\text{l}} = 9$ T are shown in panels (b) and (c), respectively.
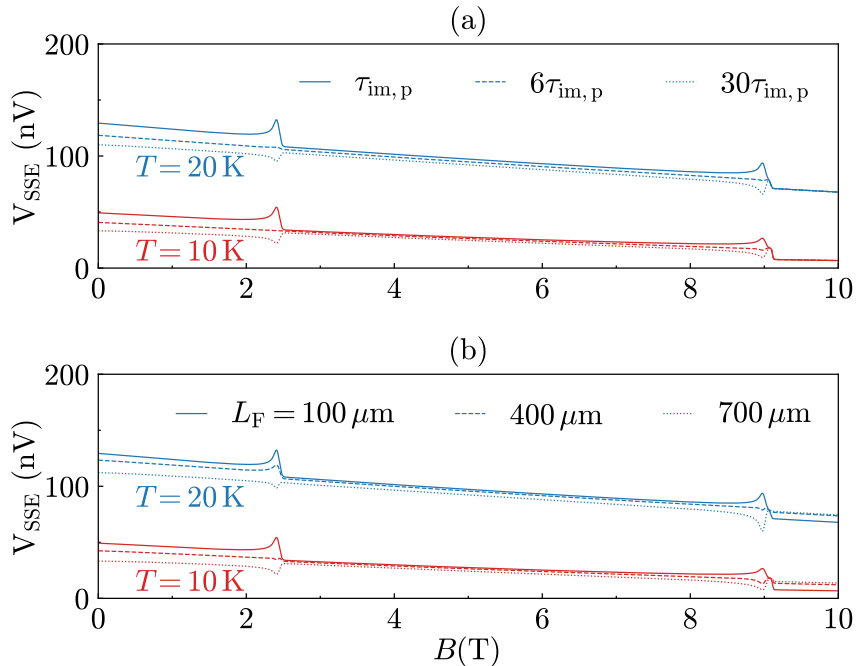
Figure 2.3: Spin Seebeck voltage as a function of the applied magnetic field for different temperatures. (a) Three magnon/phonon impurity rates $\tau_{\mathrm{im,p}}$ at fixed length $L_{\mathrm{F}} = 100\mu$m. (b) Three different lengths for fixed $\tau_{\mathrm{im,p}}$ as in Tab. 2.2.

2.8   Summary

In this chapter we constructed a Boltzmann description for the coupled magnon-phonon transport in a simple model ferromagnetic insulator. In our description the magnon-phonon coupling is accounted for explicitly through its appearance in the collision integrals. Phonon-phonon and magnon-magnon relaxation processes, on the other hand, are taken into account implicitly, as they impose a local-equilibrium form of the magnon and phonon distribution functions. The magnon-phonon coupling leads to a "phonon drag" contribution to the magnon spin current in the ferromagnetic insulator.

At low temperatures, of the three types of magnon-phonon coupling terms that we consider — phonon-to-magnon conversion, phonon-to-two-magnon conversion, and magnon-phonon interaction — the first process causes sharp peaks or dips in the magnon-phonon scattering rate at a critical magnetic field strength, where the magnon and phonon dispersions have touching points. In general there are two such critical magnetic field strengths, corresponding to longitudinal and transverse phonon branches. Whether a peak or dip is observed depends on the relative magni-

tudes of the other scattering rates involved, such as magnon-impurity and phonon-impurity rates, and the size of the ferromagnetic sample. These findings agree qualitatively with the experimental observations of Kikkawa *et al.* [15]. In particular, our incoherent Boltzmann approach yields similar features for the resulting spin Seebeck voltage as the theory of Refs. [15, 20], which used a fully coherent coupling of magnon and phonon systems, leading to the formation of "magnon-polarons".

In particular in the limit of thick ferromagnetic layers, the strength of the spin Seebeck effect may depend strongly on the properties of the ferromagnet–normal-metal interface. We expanded the spin-pumping interface model of Xiao *et al.*, which uses the spin-mixing conductance to characterize the interface properties, beyond the classical high temperature limit, to describe the low temperature regime. In addition we showed the consistency of the spin mixing conductance model to the alternatively used description of the interface coupling in terms of an *sd*-like exchange coupling between magnons in the ferromagnet and spin-polarized electrons in the normal metal as in Ref. [112].

Our quantitative calculations rely on a few simplifying approximations, such as the absence of Umklapp processes, the local-equilibrium assumption, and the use of low-energy approximations for the magnon and phonon dispersions, see Eqs. (2.39) and (2.40). Going beyond the simplifying assumptions made in our calculation is necessary for a quantitative description of the magnetic-field dependence of the spin Seebeck effect near room temperature, where Umklapp processes become important and the low-energy approximations of the magnon and phonon dispersions are no longer sufficient. Such an improved theoretical description could be formulated along the lines of Ref. [117], which used a description featuring different temperatures for different magnon modes. Whereas some of our approximations are expected to break down at higher temperatures, we expect that the existence of the sharp magnetic-field dependent features in the spin-Seebeck voltage does not depend on these approximations and that these features will (in principle) continue to exist — albeit that their broading will quickly increase with increasing temperature, consistent with the observation of Ref. [15].

Possible further extensions of our theory include a more microscopic treatment of the magnon-magnon interactions or the inclusion of time-dependent effects. In particular, we can use our approach to investigate the temporal evolution of spatially inhomogeneous magnon and phonon temperatures and investigate the relevant time scales, that govern the evolution of the spin Seebeck effect on short time scales [17].

3

Hybridized Magnon Polarons

Using a simplified microscopic model of coupled spin and lattice excitations in a ferromagnetic insulator we evaluate the magnetic-field dependence of the spin Seebeck effect at low temperatures. The model includes Heisenberg exchange coupling, a harmonic lattice potential, and a pseudo-dipolar exchange interaction. Our approach goes beyond previous work [Phys. Rev. B **98**, 134421 (2018)] in that it does not rely on the *a priori* assumption of a fast equilibration of the magnon and phonon distributions. Our theory shows that singular features in the magnetic-field dependence of the spin Seebeck effect at low temperatures observed by Kikkawa *et al.* [Phys. Rev. Lett. **117**, 207203 (2016)] are independent of the relative strength of magnon-impurity and phonon-impurity scattering.

3.1 Introduction

The spin Seebeck effect refers to the phenomenon that an applied temperature gradient causes the flow of a spin current [2, 3, 4, 45]. This effect takes a central position in the field of "spin caloritronics", the study of the interplay of spin degrees of freedom and heat. A particularly pure form of the spin Seebeck effect exists in magnetic insulators, because in this case spin transport takes place exclusively via spin waves or "magnons", whereas the electronic degrees of freedom are frozen out. Since phonons are the dominant carriers of heat in an insulator, spin caloritronic effects in magnetic insulators depend strongly on the magnon-phonon interaction. Because of its low magnetic damping and high acoustic quality, most experimental studies of the magnon-driven spin Seebeck effect focus on the synthetic ferromagnetic insulator Yttrium Iron Garnet $Y_3Fe_5O_{12}$ (YIG) [118, 119].

The important role of magnon-phonon coupling for the spin Seebeck effect was already pointed out in the initial theoretical works [19, 21, 33], where it was suggested that a so-called "phonon-drag" is the cause of the significant enhancement of the spin Seebeck voltage at low temperatures, which follows the temperature dependence of the phonon thermal conductivity [21]. The experimental demonstration of "acoustic spin pumping", the generation of a spin current by injection of acoustic waves, instead of the application of a temperature gradient, is another indicator of the importance of magnon-phonon coupling in the spin Seebeck effect [25, 26, 27]. Specific evidence of the strong coupling between the two subsystems was the discovery of distinct peaks in the magnetic field dependence of the spin Seebeck voltage at two "critical" magnetic fields, at which the acoustic magnon and phonon dispersions have touching points [15]. These features were associated with the formation of "magnon polarons" [15, 20, 10], coherent superpositions of magnon and phonon excitations formed near the "resonant" frequencies at which their dispersions cross [120, 121, 122]. (Strictly speaking, magnon polarons are formed at all frequencies, but at generic frequencies the magnon polaron modes are either "magnon-like" or "phonon-like", *i.e.*, their weight exists mainly in either the spin or the lattice sector, with a small admixture of the other subsystem.) Magnon polarons were also observed outside the context of the spin Seebeck effect. References [123] and [124] report an accumulation of magnon polarons and anomalies in the spin pumping efficiency in the spectral region near the magnon-phonon resonance following parametric magnon excitation, respectively. Reference [125] reported the direct observation of wave-like excitations in the lattice subsystem after excitation of the spin subsystem.

In a recent work together with Wilken and Nunner [41], we have shown that the observed peak structure of the spin Seebeck voltage as a function of the magnetic field can also be explained using an incoherent picture, arising from a critical enhancement of the magnon-phonon scattering rate when their dispersions have a

touching point. Both the incoherent theory of Ref. [41] and the magnon-polaron theory of Refs. [15, 20, 10] make the assumption that magnon-magnon and phonon-phonon relaxation processes are strong enough that the distribution functions of magnons and phonons or magnon polarons are given by Planck- or Bose-Einstein-type local equilibrium distributions at all times. A Planck-type local equilibrium distribution for magnons is justified if the relaxation processes are dominated by number-non-conserving three-magnon confluence or splitting processes [35, 41]; A Bose-Einstein-type distribution function is applicable if number-conserving four-magnon processes dominate [37]. At low temperatures and for magnetic fields in the vicinity of the critical values, inelastic magnon-magnon and phonon-phonon scattering are suppressed and relaxation is dominated by the interaction with impurities [126, 101, 100, 38]. Impurity scattering is elastic and cannot relax distribution functions to the Planck- or Bose-Einstein form. Instead, at low temperatures, one expects that the distribution function of magnon polarons has a singular frequency dependence near the magnon-phonon resonance frequencies and that it cannot be approximated by a Planck-type or Bose-Einstein-type distribution function.

In this chapter, we present a theory of the longitudinal spin Seebeck effect in a ferromagnetic insulator and for close-to-critical magnetic fields that is tailored to temperatures low enough and/or system lengths small enough that no *a priori* assumption of strong relaxation to a Planck-type or Bose-Einstein-type magnon-polaron distribution function can be made. This includes the range of temperatures and system sizes that were considered in the experiment of Ref. [15]. We consider elastic scattering from impurities as well as inelastic processes and describe the full crossover between the extreme low-temperature regime, in which elastic scattering dominates the spin Seebeck effect, and the intermediate-temperature regime, in which relaxation by inelastic processes imposes a local-equilibrium form of the distribution functions, so that the distribution can be characterized by a "magnon temperature" or a "magnon chemical potential" [15, 20, 10, 127, 41, 128, 129]. Our theory is based on the solution of the Boltzmann equation for the distribution function of magnon-polaron modes. Whereas the dominance of impurity scattering at low and intermediate temperatures allows us to use a simplified *ansatz* for the angle dependence of the distribution functions, the full frequency dependence of the distribution functions is kept at all stages of the calculation.

A central role in the Boltzmann theory is played by transition rates for elastic scattering from impurities as well as for inelastic interactions of magnons and phonons. Although they are often treated as phenomenological parameters, to capture parameter dependences, such as the dependence on an external magnetic field or on temperature, it is necessary to obtain transition rates from a microscopic picture. For YIG, which is a synthetic ferrimagnetic insulator of complex structure, elaborate effective spin Hamiltonians have been developed [80, 82, 83, 130, 131, 132], which have been found to predict the experimentally observed magnon spectrum

well. At low temperatures, however, only a single magnon band is relevant, and an effective model of spins on a cubic lattice already provides an accurate description of the magnon spectrum, consistent with experiments [133, 83]. Building on the success of this simplified description of YIG, we here link the magnonic transition rates in the Boltzmann theory as well as the magnon-polaron dispersion to a simple model of spins on a cubic lattice and with nearest-neighbor interactions only. The phonon system is included by a simple harmonic potential between nearest and next-nearest-neighboring atoms. The magnon-phonon coupling is included by accounting for the dependence of these interactions on the displacement of lattice sites [86, 87]. Although the spin-spin interactions are predominantly of the isotropic Heisenberg exchange type, an additional weak anisotropic interaction, such as a pseudodipolar anisotropic exchange interaction or the relativistic Dzyaloshinskii-Moryia interaction [134, 135], must be included to generate the magnon number-non-conserving processes required to obtain magnon-polaron modes and to reproduce the observed low-temperature phenomenology of the magnetic field-dependent spin Seebeck effect. The same phenomenology can also be derived upon replacing the microscopic model by a phenomenological "magneto-elastic" Hamiltonian [136, 86, 87, 38, 88] and we compare the two approaches in the appendix.

Adjusting the parameters in the microscopic model to reproduce low-temperature magnetic and acoustic (transport) properties of YIG, we find that for system sizes up to $L = 10\,\mu\text{m}$ the magnon-polaron distribution is well approximated by completely neglecting inelastic processes for all temperatures at which our model description is valid, $T \lesssim 30\,\text{K}$. Even for larger system sizes $L \lesssim 100\,\mu\text{m}$ — which is far beyond the range of system sizes investigated experimentally —, we find that a theory based on elastic impurity scattering only remains an excellent approximation for $T \lesssim 10\,\text{K}$. For these system sizes and temperatures, a theory with elastic scattering only gives a strongly frequency dependent distribution function, in which the population of magnon-like magnon-polaron modes has a sharp singularity in the immediate vicinity of the magnon-phonon resonance. Such distribution functions are not at all well approximated by a Planck-like or Bose-Einstein-like form. Indeed, our theory leads to a number of predictions that differ qualitatively from previous theories of the magnon-polaron-mediated spin Seebeck effect. Most notably, we find that the spin current always shows a peak at the critical magnetic fields at which magnon and phonon dispersions touch. In contrast, Refs. [15, 20] predict a peak only if the sample is of a better acoustic quality than magnetic quality (mean free path l_{pi} for phonon-impurity scattering larger than mean free path l_{mi} for magnon-impurity scattering). This implies that the experimental observation of peaks in the magnetic-field dependence of the spin Seebeck coefficient in Ref. [15] can not be used to determine the relative magnitude of l_{mi} and l_{pi}.

The ferromagnetic insulator–normal metal (FN) interface is a crucial ingredient to the magnonic spin Seebeck effect. In a theory based on magnon polarons, the

key processes at the FN interface are the conversion of magnon polarons in the ferromagnetic insulator (F) into phonons in the normal metal (N) [110, 137] and "spin pumping" [50], the excitation of spin current in the normal metal by a precessing magnetization. It is the spin pumping process that facilitates the conversion of a non-equilibrium accumulation of magnon polarons at the FN interface into a spin current in N. However, spin pumping also has an important inverse effect on the magnon-polaron distribution: It equilibrates the population of magnon-like magnon polarons in F to the equilibrium distribution of the conduction electrons in N. This inverse effect is absent in a perturbative treatment of the FN interface, in which the distribution of magnon-like magnon polarons is calculated with reflecting boundary conditions at the FN interface [19, 37, 41].

The remainder of this chapter is organized as follows. In Sec. 3.2 we present a microscopic model of a ferromagnetic insulator based on a simple cubic lattice and show that the model has magnon-polaron modes as its elementary excitations. In Sec. 3.3 we then review the Boltzmann transport theory of magnon-polaron modes, discuss the relevant relaxation processes, and address the boundary conditions at the interface between the ferromagnetic insulator and a non-magnetic insulator (which serves as the heat source that causes the thermal gradient) and a non-magnetic metal. In Sec. 3.4 we apply our theory to a spin Seebeck heterostructure, using typical material parameters for the ferrimagnetic insulator YIG attached to a thin Platinum (Pt) film. We conclude in Sec. 3.5.

3.2   Model

We consider the conventional setup for the longitudinal spin Seebeck effect, which consists of a ferromagnetic insulator–normal metal heterostructure as illustrated in Fig. 3.1. The system is coupled to heat baths to the top and bottom, which are held at a temperature difference ΔT. We assume that the system is isotropic and choose coordinate axes such that the temperature gradient and the resulting spin currents are in the x-direction, see Fig. 3.1. We focus on the low-temperature regime in which Umklapp scattering and excitation of optical magnons and phonons is strongly suppressed. Spin and heat transport in the ferromagnetic insulator is governed by the interaction of acoustic magnons and phonons as well as by scattering from impurities.

3.2.1   Lattice model and continuum limit

We first present a minimal lattice model of classical spins, which serves as a microscopic starting point for the derivation of the continuum theory of coupled magnon and phonon modes. The subsequent continuum theory may also be derived from
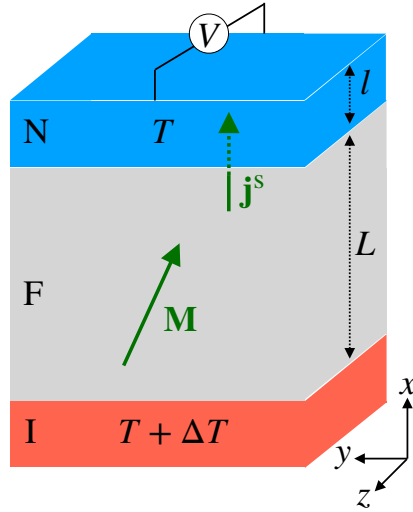
Figure 3.1: Geometry for the longitudinal spin Seebeck effect: A ferromagnetic insulator F of length L (center, gray) is placed between an insulator I (bottom, red) and a normal metal N of thickness l (top, blue), which also act as heat reservoirs held at a temperature difference ΔT. Via magnon-phonon coupling, the applied temperature gradient leads to a nonequilibrium magnon distribution, which causes the flow of a spin current $\mathbf{j}^{\mathrm{s}}$ into the normal metal. The spin current can be measured in the normal metal by means of the inverse spin Hall effect.

phenomenological considerations, such as the magneto-elastic theory of Refs. [136, 86, 87, 38].

Lattice model.— The guiding principle for the construction of the minimal model is the accepted wisdom that at low temperatures YIG may be well described as a ferromagnetic insulator with effective spins $\mathbf{S}_j$ of magnitude S, located at the sites $\mathbf{r}_j$ of a simple cubic lattice with lattice constant a [83]. The lattice ions have mass m, displacement $\mathbf{u}_j$, and momentum $\mathbf{p}_j$. We consider the classical Hamiltonian

$$H = H^{\mathrm{pho}} + H^{\mathrm{mag}} + H^{\mathrm{mag-pho}}, \tag{3.1}$$

in which the three terms H^{mag}, H^{pho}, and $H^{\mathrm{mag-pho}}$ describe classical "magnons" and "phonons", collective small excursions from the equilibrium state of the spins and the lattice, respectively, and the interaction between these.

For term H^{pho}, which describes lattice vibrations, we impose a harmonic lattice potential [79] with coupling constants K_1 and K_2, involving couplings between

nearest-neighbor lattice atoms $\langle i, j \rangle$ and between next-nearest neighbors $\langle\langle i, j \rangle\rangle$,

$$H^{\text{pho}} = \sum_j \frac{|\mathbf{p}_j|^2}{2m} + \frac{K_1}{2} \sum_{\langle i,j \rangle} |\mathbf{u}_{ij} \cdot \mathbf{e}_{ij}|^2 + \frac{K_2}{2} \sum_{\langle i,j \rangle} |\mathbf{u}_{ij}|^2 + \frac{K_1}{2} \sum_{\langle\langle i,j \rangle\rangle} |\mathbf{u}_{ij} \cdot \mathbf{e}_{ij}|^2, \quad (3.2)$$

where $\mathbf{e}_{ij} = (\mathbf{r}_i - \mathbf{r}_j)/|\mathbf{r}_i - \mathbf{r}_j|$ is the unit vector pointing from $\mathbf{r}_i$ to $\mathbf{r}_j$, and we abbreviated $\mathbf{u}_{ij} = \mathbf{u}_i - \mathbf{u}_j$. In the summations over nearest neighbors and next-nearest neighbors every pair is summed over only once. The use of two coupling constants K_1 and K_2 is necessary to obtain different velocities for longitudinal and transverse phonon modes; the next-nearest-neighbor coupling term is required to reproduce an isotropic phonon dispersion in the long-wavelength limit [78].

The term H^{mag}, which describes the collective excitations of the spin system, derives from the Zeeman coupling to an external magnetic field $\mathbf{B}$ and the Heisenberg exchange interaction,

$$H^{\text{mag}} = -J \sum_{\langle i,j \rangle} \mathbf{S}_i \cdot \mathbf{S}_j - \mu \mathbf{B} \cdot \sum_j \mathbf{S}_j, \quad (3.3)$$

where $\mu = g\mu_{\text{B}}$ is the magnetic moment of the spins, with μ_{B} and g the Bohr magneton and Landé factor, respectively. To derive the magnon Hamiltonian we take $\mathbf{e}$ to be the unit vector pointing in the direction of the external magnetic field $\mathbf{B} = B\mathbf{e}$, and parameterize (similar to the Holstein-Primakoff transformation for quantum spins [81])

$$\mathbf{S}_j = \mathbf{e} \sqrt{S^2 - Sn_j^2} + \mathbf{n}_j \sqrt{S}, \quad (3.4)$$

where $\mathbf{n}_j \perp \mathbf{e}$ is the (suitably renormalized) transverse magnetization amplitude and $n_j = |\mathbf{n}_j|$. Expanding H^{mag} to quadratic order in the amplitudes $\mathbf{n}_j$ gives the magnon Hamiltonian

$$H^{\text{mag}} = \frac{JS}{2} \sum_{\langle i,j \rangle} |\mathbf{n}_i - \mathbf{n}_j|^2 + \frac{\mu B}{2} \sum_j \mathbf{n}_j^2. \quad (3.5)$$

Taking the exchange constant J in the Heisenberg Hamiltonian (3.5) to depend on the displacements $\mathbf{u}_j$ of the lattice ions one obtains a magnon-phonon interaction. This interaction, however, conserves the magnon number, so that it alone does not allow for a steady-state spin Seebeck effect. Moreover, since its leading contribution is of (combined) cubic order in the small amplitudes $\mathbf{n}_j$ and $\mathbf{u}_j$, the effect of the exchange-based magnon-phonon coupling is strongly suppressed at low temperatures. Instead, at low temperatures the magnon-phonon coupling is dominated by relativistic corrections to the Hamiltonian, which give corrections to the Hamiltonian of (combined) quadratic order in $\mathbf{n}_i$ and $\mathbf{u}_i$. As an example of such a relativistic correction we here consider the Van Vleck pseudo-dipolar exchange interaction [138]. It results from the combination of Heisenberg exchange and spin-orbit

coupling [135, 139] and can be written as

$$H^{\mathrm{pd}} = \sum_{\langle i,j \rangle} D_{ij}(\mathbf{S}_i \cdot \mathbf{e}_{ij})(\mathbf{S}_j \cdot \mathbf{e}_{ij}). \tag{3.6}$$

Again, we consider nearest-neighbor interactions only. To leading order in S the contribution of H^{pd} to the magnon Hamiltonian in Eq. (3.5) causes a weakly anisotropic shift of the magnon frequency, which we neglect because typically $D_{ij} \ll J$ for neighboring spins. To obtain the magnon-phonon coupling Hamiltonian $H^{\mathrm{mag-pho}}$, we take the dipolar exchange constant D_{ij} to depend on the relative displacement $\mathbf{u}_{ij} = \mathbf{u}_i - \mathbf{u}_j$ of nearest-neighbor atoms and expand to linear order $\mathbf{u}_{ij}$,

$$D_{ij} \to D + D' \mathbf{u}_{ij} \cdot \mathbf{e}_{ij}. \tag{3.7}$$

We also expand the unit vectors $\mathbf{e}_{ij}$ to linear order in $\mathbf{u}_{ij}$,

$$\mathbf{e}_{ij} \to \mathbf{e}_{ij} + \frac{\mathbf{u}_{ij} - (\mathbf{u}_{ij} \cdot \mathbf{e}_{ij})\,\mathbf{e}_{ij}}{a}. \tag{3.8}$$

Expanding H^{pd} to linear order in both $\mathbf{u}_i$ and $\mathbf{n}_i$ then gives the magnon-phonon Hamiltonian

$$H^{\mathrm{mag-pho}} = \sum_{\langle i,j \rangle} (\mathbf{n}_i + \mathbf{n}_j) \cdot \mathcal{D}_{ij}(\mathbf{u}_i - \mathbf{u}_j), \tag{3.9}$$

where the 3×3 matrix $\mathcal{D}_{ij}$ reads (with dyadic products $\mathbf{e}_{ij}\mathbf{e}^{\mathrm{T}}$ and $\mathbf{e}_{ij}\mathbf{e}_{ij}^{\mathrm{T}}$)

$$\mathcal{D}_{ij} = S^{3/2}(\mathbf{e} \cdot \mathbf{e}_{ij}) \left[D'\mathbf{e}_{ij}\mathbf{e}_{ij}^{\mathrm{T}} + \frac{D}{a}(\mathbb{1} - 2\mathbf{e}_{ij}\mathbf{e}_{ij}^{\mathrm{T}}) \right] + S^{3/2}\frac{D}{a}\mathbf{e}_{ij}\mathbf{e}^{\mathrm{T}}. \tag{3.10}$$

The equations of motion for the displacements $\mathbf{u}_j$ and the magnetization amplitudes $\mathbf{n}_j$ take the familiar Hamilton form

$$\dot{\mathbf{u}}_j = \frac{\partial H}{\partial \mathbf{p}_j}, \quad \dot{\mathbf{p}}_j = -\frac{\partial H}{\partial \mathbf{u}_j}, \quad \dot{\mathbf{n}}_j = -\mathbf{e} \times \frac{\partial H}{\partial \mathbf{n}_j}. \tag{3.11}$$

The property that $\mathbf{n}_j \perp \mathbf{e}$ is conserved under these equations of motion.

Fourier transform and continuum limit.— To obtain a formulation in terms of classical phonons and magnons we introduce the Fourier transforms

$$\mathbf{u}_j = \frac{1}{\sqrt{N}} \sum_{\mathbf{q}} \mathbf{u}_{\mathbf{q}} e^{i\mathbf{q} \cdot \mathbf{r}_j},$$

$$\mathbf{p}_j = \frac{1}{\sqrt{N}} \sum_{\mathbf{q}} \mathbf{p}_{\mathbf{q}} e^{i\mathbf{q} \cdot \mathbf{r}_j},$$

$$\mathbf{n}_j = \frac{1}{\sqrt{N}} \sum_{\mathbf{q}} \mathbf{n}_{\mathbf{q}} e^{i\mathbf{q} \cdot \mathbf{r}_j}, \tag{3.12}$$

where we assume a lattice with $N = V/a^3$ lattice sites and periodic boundary conditions. In terms of the Fourier-transformed amplitudes, the Hamiltonian reads

$$H = \frac{1}{2} \sum_{\mathbf{q}} \left\{ \frac{|\mathbf{p_q}|^2}{m} + \mathcal{B}(\mathbf{q})|\mathbf{n_q}|^2 + \mathbf{u_q^*} \cdot \mathcal{K}(\mathbf{q})\mathbf{u_q} + 2\operatorname{Re} \mathbf{n_q^*} \cdot \mathcal{D}(\mathbf{q})\mathbf{u_q} \right\}. \tag{3.13}$$

In the long-wavelength limit $q \to 0$, which is the relevant limit at low temperatures, one has

$$\mathcal{K}(\mathbf{q}) = \frac{m}{a^3} \left[c_{\mathrm{t}}^2 q^2 \mathbb{1} + (c_{\mathrm{l}}^2 - c_{\mathrm{t}}^2)\mathbf{q}\mathbf{q}^{\mathrm{T}} \right], \tag{3.14}$$

where c_{l} and c_{t} are the velocities of the longitudinal and transverse phonon modes in the lattice model (3.1),

$$c_{\mathrm{l}}^2 = \frac{a^2}{m}(K_1 + K_2), \quad c_{\mathrm{t}}^2 = \frac{a^2}{m}(3K_1 + K_2). \tag{3.15}$$

In the limit $q \to 0$, the energy of the magnon modes is

$$\mathcal{B}(\mathbf{q}) = \mu B + JSa^2 q^2 \tag{3.16}$$

and the magnon-phonon coupling is described by the 3×3 matrix

$$\mathcal{D}(\mathbf{q}) = 2i \left(\frac{S}{a} \right)^{3/2} \sum_\alpha q_\alpha \left[D\mathbf{e}_\alpha \mathbf{e}^{\mathrm{T}} \right.$$
$$\left. + (\mathbf{e} \cdot \mathbf{e}_\alpha)(aD'\mathbf{e}_\alpha \mathbf{e}_\alpha^{\mathrm{T}} + D(\mathbb{1} - 2\mathbf{e}_\alpha \mathbf{e}_\alpha^{\mathrm{T}})) \right], \tag{3.17}$$

where $\mathbf{e}_\alpha$ denotes the unit vector in the spatial directions $\alpha = x, y, z$, and $\mathbf{e}_\alpha \mathbf{e}_\alpha^{\mathrm{T}}$ is the dyadic product. A real-space formulation in the long-wavelength limit $q \to 0$ can be obtained by inverse Fourier transform of Eq. (3.13). This amounts to the replacement of the lattice amplitudes $\mathbf{u}_j$, $\mathbf{p}_j$, and $\mathbf{n}_j$ by smooth functions $\mathbf{p}(\mathbf{r})$, $\mathbf{u}(\mathbf{r})$, and $\mathbf{n}(\mathbf{r})$ of the position $\mathbf{r}$ and the substitution $\mathbf{q} \to -i\nabla$ in the Hamiltonian (3.13). Expressions for $\mathcal{K}(\mathbf{q})$, $\mathcal{B}(\mathbf{q})$, and $\mathcal{D}(\mathbf{q})$ for the full lattice model (3.1), without the approximation $q \to 0$, can be found in Appendix B.1.

Boundary conditions. — In the lattice model, the magnetic medium F exists for $0 < x < L$ with $L = N_x a$, N_x being the number of lattice sites in the x-direction, see Fig. 3.1. At $x = L$ there is a boundary to a non-magnetic metal N; at $x = 0$ there is a boundary to a non-magnetic insulator I. In both the non-magnetic insulator I and the normal metal N we consider phonon degrees of freedom only, described by the Hamiltonian H^{pho} of Eq. (3.2). At the boundaries at $x = 0$ and $x = L$ the magnon Hamiltonian H^{mag} and the magnon-phonon coupling $H^{\mathrm{mag-pho}}$ are truncated by omitting any on-site terms or nearest-neighbor contributions involving lattice sites in the non-magnetic metal N or the non-magnetic insulator I. In the long-wavelength limit $q \to 0$, one can show that this amounts to the boundary conditions [140, 110]

$$\mathbf{u}(0^-) = \mathbf{u}(0^+), \quad 0 = \frac{\partial \mathbf{n}(0^+)}{\partial x}, \tag{3.18}$$

and

$$\frac{\partial \mathcal{K}(\mathbf{q})}{\partial q_x}\mathbf{u}(0^-) = \frac{\partial \mathcal{K}(\mathbf{q})}{\partial q_x}\mathbf{u}(0^+) + 2\frac{\partial \mathcal{D}(\mathbf{q})^\dagger}{\partial q_x}\mathbf{n}(0^+),\tag{3.19}$$

for the IF interface at $x = 0$, with q_x replaced by $-i\partial/\partial x$. For the FN boundary at $x = L$, the boundary conditions for the displacement field $\mathbf{u}(\mathbf{r})$,

$$\mathbf{u}(L^-) = \mathbf{u}(L^+),\tag{3.20}$$

$$\frac{\partial \mathcal{K}(\mathbf{q})}{\partial q_x}\mathbf{u}(L^-) = \frac{\partial \mathcal{K}(\mathbf{q})}{\partial q_x}\mathbf{u}(L^+) + 2\frac{\partial \mathcal{D}(\mathbf{q})^\dagger}{\partial q_x}\mathbf{n}(L^+),\tag{3.21}$$

are the same as at the interface between the ferromagnetic insulator and the normal metal. The boundary condition for the spin wave amplitude at $x = L$ is different for the FN interface, because magnons can excite conduction electrons in the normal metal [50, 32],

$$-a^2 JS\,\mathbf{e} \times \frac{\mathbf{n}(L^-)}{\partial x} = \frac{\mu}{4\pi M_s}\left[\sigma'_{\uparrow\downarrow}\mathbf{e} \times \dot{\mathbf{n}}(L^-) - \sigma''_{\uparrow\downarrow}\dot{\mathbf{n}}(L^-)\right].\tag{3.22}$$

Here $M_s = \mu S/a^3$ is the magnetic moment per unit volume and $\sigma_{\uparrow\downarrow} = \sigma'_{\uparrow\downarrow} + i\sigma''_{\uparrow\downarrow}$ is the spin-mixing conductance per unit area.

3.2.2 Phonons, magnons, and magnon polarons

Classical phonons and magnons.— A formulation in terms of classical phonons and magnons is obtained upon switching to complex phasor variables $b_{\mathbf{q},\lambda}$ with $\lambda = 1, 2, 3, 4$,

$$\mathbf{u_q} = \sum_{\lambda=1}^{3}\sqrt{\frac{\hbar}{2m\omega^0_{\mathbf{q},\lambda}}}(b_{\mathbf{q},\lambda} + b^*_{-\mathbf{q},\lambda})\mathbf{e}_{\mathbf{q},\lambda},$$

$$\mathbf{p_q} = -i\sum_{\lambda=1}^{3}\sqrt{\frac{\hbar m\omega^0_{\mathbf{q},\lambda}}{2}}(b_{\mathbf{q},\lambda} - b^*_{-\mathbf{q},\lambda})\mathbf{e}_{\mathbf{q},\lambda},$$

$$\mathbf{n_q} = \sqrt{\hbar}\left(b_{\mathbf{q},4}\mathbf{e}_- + b^*_{-\mathbf{q},4}\mathbf{e}_+\right),\tag{3.23}$$

where we introduced Planck's constant $\hbar$ to obtain a formal analogy with a quantum-mechanical treatment of the same problem. The phasor variables $b_{\mathbf{q},\lambda}$ with $\lambda = 1$ and $\lambda = 2, 3$ describe the longitudinal and transverse phonon modes, respectively. In the long-wavelength limit, the phonon frequencies are

$$\omega^0_{\mathbf{q},1} = c_l q, \quad \omega^0_{\mathbf{q},2} = \omega^0_{\mathbf{q},3} = c_t q.\tag{3.24}$$

The polarization vectors $\mathbf{e}_{\mathbf{q},\lambda} = \mathbf{e}^*_{-\mathbf{q},\lambda}$ are the corresponding eigenvectors of $\mathcal{K}(\mathbf{q})$. In the limit $q \to 0$, the unit vector $\mathbf{e}_{\mathbf{q},1}$ is collinear with $\mathbf{q}$; $\mathbf{e}_{\mathbf{q},2}$ and $\mathbf{e}_{\mathbf{q},3}$ are orthogonal

to $\mathbf{q}$. Since the transverse phonon modes $\omega^0_{\mathbf{q},2}$ and $\omega^0_{\mathbf{q},3}$ are degenerate, the polarization vectors $\mathbf{e}_{\mathbf{q},2}$ and $\mathbf{e}_{\mathbf{q},3}$ are not uniquely determined at this stage. The magnon frequency is

$$\omega^0_{\mathbf{q},4} = \mathcal{B}(\mathbf{q}). \tag{3.25}$$

The magnon polarization vectors $\mathbf{e}_+ = \mathbf{e}^*_-$ are complex unit vectors satisfying the property $\mathbf{e}_\pm \times \mathbf{e} = \pm i \mathbf{e}_\pm$.

After this variable transformation, the Hamiltonian (3.1) and the equations of motion (3.11) can be written in the compact form [15, 20]

$$H = \frac{1}{2} \sum_{\mathbf{q}} \mathbf{b}^\dagger_{\mathbf{q}} \cdot H_{\mathbf{q}} \mathbf{b}_{\mathbf{q}}, \quad \dot{b}_{\mathbf{q},\lambda} = -\frac{i}{\hbar} \frac{\partial H}{\partial b^*_{\mathbf{q},\lambda}}, \tag{3.26}$$

where $\mathbf{b}_{\mathbf{q}}$ is the eight-component column vector

$$\mathbf{b}_{\mathbf{q}} = \begin{pmatrix} b_{\mathbf{q},\lambda} \\ b^*_{-\mathbf{q},\lambda} \end{pmatrix}_{\lambda=1,2,3,4} \tag{3.27}$$

and $H_{\mathbf{q}}$ the 8×8 hermitian matrix

$$H_{\mathbf{q}} = \begin{pmatrix} \hbar\omega^0_{\mathbf{q},\lambda}\delta_{\lambda\lambda'} & \Delta^*_{\mathbf{q},\lambda} & 0 & \Delta_{-\mathbf{q},\lambda} \\ \Delta_{\mathbf{q},\lambda'} & \hbar\omega^0_{\mathbf{q},4} & \Delta_{\mathbf{q},\lambda'} & 0 \\ 0 & \Delta^*_{\mathbf{q},\lambda} & \hbar\omega^0_{\mathbf{q},\lambda}\delta_{\lambda\lambda'} & \Delta_{-\mathbf{q},\lambda} \\ \Delta^*_{-\mathbf{q},\lambda'} & 0 & \Delta^*_{-\mathbf{q},\lambda'} & \hbar\omega^0_{\mathbf{q},4} \end{pmatrix}_{\lambda,\lambda'=1,2,3}. \tag{3.28}$$

The diagonal elements of $H_{\mathbf{q}}$ contain the frequencies of the phonon and magnon modes; the off-diagonal elements $\Delta_{\mathbf{q},\lambda}$, $\lambda = 1, 2, 3$, describe the magnon-phonon coupling,

$$\Delta_{\mathbf{q},\lambda} = \sqrt{\frac{\hbar a^3}{2m\omega^0_{\mathbf{q},\lambda}}} \mathbf{e}_+ \cdot \mathcal{D}(\mathbf{q})\mathbf{e}_{\mathbf{q},\lambda}, \tag{3.29}$$

where the 3×3 matrix $\mathcal{D}(\mathbf{q})$ was defined in Eq. (3.17).

Magnon-polaron modes. — The magnon-polaron modes are the eigenmodes of the full magnon-phonon Hamiltonian (3.26). To find their dispersion we perform a canonical transformation that diagonalizes the matrix $H_{\mathbf{q}}$ of Eq. (3.26),

$$H_{\mathbf{q}} = V_{\mathbf{q}} \hbar\Omega_{\mathbf{q}} V^\dagger_{\mathbf{q}}, \tag{3.30}$$

where the entries of the diagonal matrix

$$\Omega_{\mathbf{q}} = \begin{pmatrix} \omega_{\mathbf{q},\nu} & 0 \\ 0 & \omega_{-\mathbf{q},\nu} \end{pmatrix}_{\nu=1,2,3,4} \tag{3.31}$$

are the frequencies of the magnon-polaron modes and the symplectic transformation matrix $V_{\mathbf{q}}$ satisfies the condition $\Sigma_3 V^\dagger_{\mathbf{q}} \Sigma_3 = V^{-1}_{\mathbf{q}}$ with $\Sigma_3 = \mathrm{diag}(\mathbb{1}_4, -\mathbb{1}_4)$. The

phasor variables $b_{\mathbf{q},\lambda}$ of the phonon and magnon modes are related to the phasor variables $a_{\mathbf{q},\nu}$ of the magnon-polaron modes via

$$\mathbf{a_q} = V_{\mathbf{q}}^{\dagger} \mathbf{b_q}, \quad \mathbf{a_q} = \begin{pmatrix} a_{\mathbf{q},\nu} \\ a_{-\mathbf{q},\nu}^{*} \end{pmatrix}_{\nu=1,2,3,4}. \tag{3.32}$$

This transformation brings H to diagonal form

$$H = \sum_{\mathbf{q},\nu} \hbar \omega_{\mathbf{q},\nu} a_{\mathbf{q},\nu}^{*} a_{\mathbf{q},\nu}. \tag{3.33}$$

The equations of motion for the phasor variables $a_{\mathbf{q},\nu}$ read

$$\dot{a}_{\mathbf{q},\nu} = -\frac{i}{\hbar} \frac{\partial H}{\partial a_{\mathbf{q},\nu}^{*}}, \quad \nu = 1, 2, 3, 4. \tag{3.34}$$

To construct a quantum theory, one simply replaces the complex amplitudes $a_{\mathbf{q},\nu}$ and $a_{\mathbf{q},\nu}^{*}$ by operators $\hat{a}_{\mathbf{q},\nu}$ and $\hat{a}_{\mathbf{q},\nu}^{\dagger}$ with commutation relations $[\hat{a}_{\mathbf{q},\nu}, \hat{a}_{\mathbf{q},\nu}^{\dagger}] = 1$.

The magnon-polaron modes are linear superpositions of wave-like excitations of the spins and of the lattice, *i.e.* of magnons and phonons. The precise form of the superposition is described by the matrix $V_{\mathbf{q}}$ that transforms between the formulation (3.26) in terms of phonon and magnon modes and the formulation (3.33) in terms of magnon-polaron modes, see Eq. (3.32). At generic frequencies, the mixing of spin and lattice degrees of freedom is small. One of the magnon-polaron modes is magnon-like, with a small admixture of longitudinal and transverse phonon modes, whereas three of the magnon-polaron modes are phonon-like. Two of the phonon-like modes have a small magnon admixture; the third mode is a pure transverse phonon mode. (This follows because the perturbation proportional to Δ in Eq. (3.28) does not have maximal rank.) At the resonant frequencies at which magnon and phonon dispersions cross, two of the magnon-polaron modes have significant spin and lattice components, one mode is phonon-like with a small magnon component, and one mode is a pure transverse phonon mode.

The magnon-polaron frequencies $\omega_{\mathbf{q},\nu}$ and the matrices $V_{\mathbf{q}}$ that diagonalize the magnon-polaron Hamiltonian satisfy the symmetry constraints

$$\omega_{\mathbf{q},\nu} = \omega_{-\mathbf{q},\nu} \tag{3.35}$$

and

$$V_{-\mathbf{q}} = I V_{\mathbf{q}}, \quad I = \mathrm{diag}\,(\mathbb{1}_3, -1, \mathbb{1}_3, -1). \tag{3.36}$$

For a more elaborate discussion of the symmetry properties of the 8×8 matrices appearing in this discussion we refer to App. B.2.

Numerical values.— To obtain numerical values for YIG, we take the material parameters from Table 3.1. Since the pseudo-dipolar exchange interaction (3.6)

YIG continuum theory parameters

	Quantity	Value	Ref.
lattice constant	a	1.24 nm	[80]
exchange stiffness	JSa^2	8.5×10^{-40} J m^2	[83]
exchange coupling	J'	J/a	
mass density	m/a^3	5170 kg/m^3	[83]
pseudo-dipolar exchange	D/J	8.3×10^{-3}	[141]
pseudo-dipolar exchange	D'	D/a	
saturation magnetization	M_s	1.4×10^5 A/m	[80]
long. sound velocity	c_l	7209 m/s	[38]
trans. sound velocity	c_t	3843 m/s	[38]
anharmonicity	K'	2×10^{10} J/m^3	[43]

Pt and YIG/Pt interface parameters

	Quantity	Value	Ref.
spin mixing conductivity	$\sigma_{\uparrow\downarrow}$	1.3×10^{18} 1/m^2	[142]
spin Hall angle	θ_sh	0.0037	[59]
spin diffusion length	λ_sf	7.3 nm	[116]
electrical resistivity	ϱ	0.91×10^{-6} Ω/m	[5]
sample dimensions	$l \times w$	5 nm $\times$ 2 mm	

Table 3.1: Parameter values used for the numerical evaluation for the spin Seebeck effect in a YIG—Pt bilayer, together with the relevant references where these values were obtained.

describes an anisotropic spin-spin interaction, we must specify the polarization direction **e** of the ferromagnetic ground state. Following Ref. [131] we choose the polarization direction to be the (111) direction. To determine the strength of the pseudo-dipolar anisotropic exchange coupling D and its derivative $D' \sim D/a$ we compare the amplitudes of the magnon-phonon processes with the results of the phenomenological magneto-elastic energy, see appendix B.3, which gives $D/J \approx 8.3 \times 10^{-2}$. This confirms that the pseudo-dipolar contribution to the magnon dispersion is indeed small compared to the Heisenberg exchange coupling for these parameters.

Figure 3.2 shows the magnon-polaron dispersions $\omega_{\mathbf{q},\nu}$ as a function of the wavevector q. The magnon and longitudinal phonon dispersions cross at wavevectors

$$q_{\mathrm{l,t}}^{\pm} = \frac{1}{2} \left(q_{\mathrm{l,t}}^0 \pm \sqrt{(q_{\mathrm{l,t}}^0)^2 - 4\mu B/JSa^2} \right) \tag{3.37}$$

where $q_{\mathrm{l,t}}^0 = \hbar c_{\mathrm{l,t}}/JSa^2$ is the crossing of the magnon and longitudinal/transverse phonon dispersion without an applied magnetic field. The hybridization of magnons and phonons is strongest at these intersection points. Without magnon-phonon in-
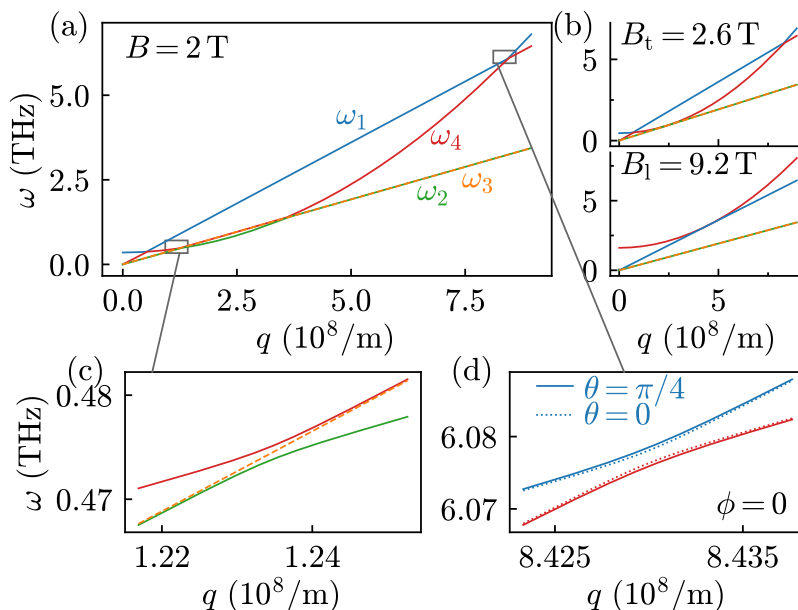
Figure 3.2: (a) Magnon-polaron frequency dispersions: ω_1 (blue), ω_2 (green), transverse phonon dispersion ω_3 (orange, dashed), and ω_4 (red). In panel (b) the polaron dispersions for the "critical" applied magnetic fields $B_t = 2.6\,\text{T}$ and $B_l = 9.2\,\text{T}$ are shown. Magnifications of the dispersions: (c) around the crossing of the magnon-polaron mode with the transverse phonon mode and (d) longitudinal phonon mode for different angles θ defined by $q_x = q\cos\theta$.

teraction the transverse phonon branches $\omega_{\mathbf{q},2}^0$ and $\omega_{\mathbf{q},3}^0$ are degenerate. This degeneracy is lifted by the magnon-phonon interaction. Note, that only one of the two transverse phonon modes interacts with the magnons to form a magnon-polaron mode. The range of wavevectors $\mathbf{q}$ with strong magnon-phonon interaction is significantly enhanced when reaching "critical" magnetic fields $B_{l,t} = JSa^2(q_{l,t}^0)^2/4\mu$ [15, 20].

3.3 Boltzmann theory

We describe the four propagating magnon-polaron modes in the magnetic insulator in terms of a distribution function $n_{\mathbf{q},\nu}(x)$, which counts the occupation of the (quantized) magnon-polaron mode $(\mathbf{q},\nu)$, $\nu = 1, 2, 3, 4$. The distribution function is related to the energy current carried by the magnon-polaron modes as

$$j_x = \sum_{\mathbf{q},\nu} \hbar\omega_{\mathbf{q},\nu} v_{\mathbf{q},\nu x} n_{\mathbf{q},\nu}(x), \tag{3.38}$$

where $v_{\mathbf{q},\nu x} = \partial\omega_{\mathbf{q},\nu}/\partial q_x$ is the group velocity of the magnon-polaron mode. (The x direction is the direction along the applied temperature gradient.) In equilibrium, *i.e.*, without applying a temperature gradient across the magnetic insulator, the distribution function $n_{\mathbf{q},\nu} = n^0(\omega_{\mathbf{q},\nu})$ is given by the Planck distribution

$$n^0(\omega) = \frac{1}{e^{\hbar\omega/k_B T} - 1}. \tag{3.39}$$

Because of the symmetry condition (3.35), the frequency $\omega_{\mathbf{q},\nu}$ and the velocity $v_{\mathbf{q},\nu x}$ are even and odd functions of $\mathbf{q}$, respectively, ensuring that $j_x = 0$ in equilibrium.

The out-of-equilibrium distribution function $n_{\mathbf{q},\nu}(x)$ can be solved from the steady-state Boltzmann equation, which has the general form

$$v_{\mathbf{q},\nu x}\frac{\partial n_{\mathbf{q},\nu}(x)}{\partial x} = I_{\mathbf{q},\nu}, \tag{3.40}$$

where $I_{\mathbf{q},\nu}$ is the collision integral. The role of the collision integral $I_{\mathbf{q},\nu}$ is to regulate the relaxation of the distribution function towards a local equilibrium. We discuss a simplified ansatz of the distribution function $n_{\mathbf{q},\nu}$ in the linear-response regime in Sec. 3.3.2 and the specific form of the collision integral in Sec. 3.3.3. The boundary conditions at interfaces of the ferromagnetic insulator F with the non-magnetic insulator I and the normal metal N are considered in Sec. 3.3.4, together with the spin current that is emitted into N.

3.3.1 Qualitative considerations

Before we enter into a quantitative description of the formalism, we discuss the relevant relaxation processes and length scales qualitatively. In Fig. 3.3 we show relaxation lengths for magnons and phonons — *i.e.*, without taking into account magnon-polaron formation — at two different temperatures and magnetic fields. The relaxation lengths shown in the figure are based on the material parameters of Table 3.1 and the collision integrals that will be discussed in Sec. 3.3.3. The relevant elastic and inelastic scattering processes are shown schematically in Table 3.2.

The key observation underlying our theoretical analysis is that at low temperatures, elastic impurity scattering dominates over the inelastic processes. Elastic scattering not only causes a quick relaxation of the propagation direction, but it also causes scattering between different magnon-polaron modes. The length scale λ_{imp} for such impurity-mediated inter-mode scattering of magnon polarons is shown by the dashed curve in Fig. 3.3. The impurity-mediated inter-mode scattering is strongest close to the "resonance frequencies", because there magnon-polaron modes have significant magnon and phonon content. The relaxation length λ_{imp} remains shorter than the inelastic scattering lengths for a small but finite window around the resonance frequencies. Moreover, it remains shorter than the length scale for relativistic
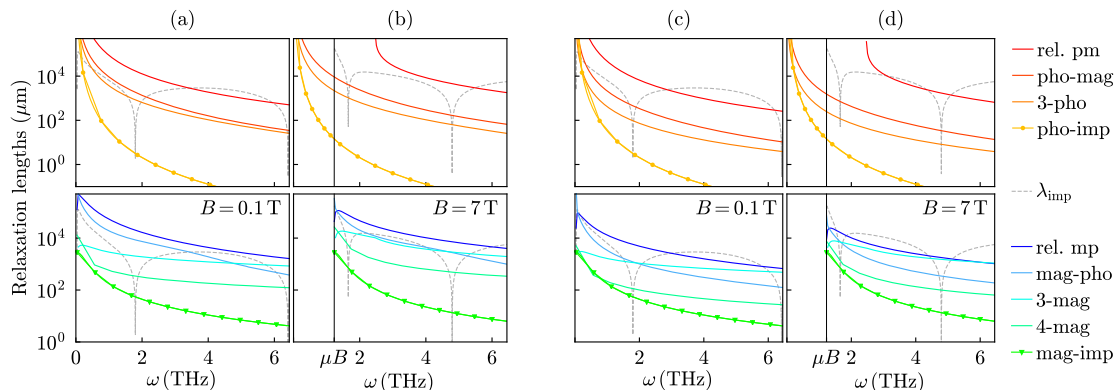
Figure 3.3: Relaxation lengths for various scattering mechanisms in a magnetic insulator for temperatures $T = 10$ K (a and b) and $T = 30$ K (c and d). Panels (a) and (c) are for a magnetic field $B = 0.1$ T; panels (b) and (d) are for $B = 7$ T. Top and bottom panels show relaxation lengths for phonons and magnons, respectively. Material parameters for YIG are taken from Table 3.1. The microscopic model for impurity scattering and for the inelastic scattering processes is discussed in Sec. 3.3.3; values for the impurity potential are taken from Table 3.3, center column. The relaxation lengths for phonon modes are averaged over polarization. The scattering processes shown in the figure are: magnon-impurity and phonon-impurity scattering, three-magnon, four-magnon, three-phonon, exchange-based magnon-phonon scattering, and relativistic or dipole-dipole-based inelastic magnon-phonon scattering. These processes are shown schematically in Table 3.2. The dashed curve shows the length scale λ_{imp} for impurity-mediated inter-mode scattering of magnon polarons.

or dipole-dipole-based inelastic phonon-to-two-magnon conversion at all frequencies for temperatures $T \lesssim 30$ K. Although it is significantly weaker than intra-mode impurity scattering at generic frequencies, impurity-mediated inter-mode scattering will be found to be the dominant source of the spin Seebeck effect at low temperatures.

The strong frequency dependence of the degree of mixing of magnon and phonon modes implies a strong frequency dependence of the distribution function $n_{\mathbf{q},\nu}$, especially at temperatures low enough that the system size L is not much larger than the inelastic relaxation lengths. As a consequence, a frequency-averaged description in terms of a (mode-dependent) "temperature" or "chemical potential" [15, 20, 10, 127, 41, 128, 129] is unlikely to be an accurate characterization of the magnon-polaron distribution at low temperatures. Instead, the full frequency dependence of the distribution must be retained in a theoretical description. At the same time, the dominance of intra-mode impurity scattering justifies a simplified description of the distribution function in which the full angle dependence is replaced by one isotropic and one anisotropic moment only. These considerations are
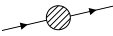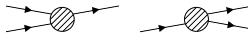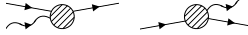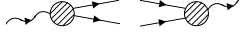
<u>magnon-impurity</u>	
<u>phonon-impurity</u>	
<u>phonon-phonon</u>	
three-phonon	
<u>magnon-magnon</u>	
four-magnon	
three-magnon	
<u>magnon-phonon</u>	
phonon emission/absorption (mainly exchange-based)	
2-magnon conversion (relativistic or dipole-dipole)	

Table 3.2:   Schematic representation of the relevant microscopic scattering processes for magnon polarons: magnon-impurity, phonon-impurity, three-magnon, three-phonon, four-magnon, and magnon-phonon scattering. Solid arrows represent magnons; wavy arrows represent phonons.

the basis for the approach we outline in Secs. 3.3.2 and 3.3.3.

The insignificance of inelastic relaxation processes at low temperatures means that coherent superpositions of magnon-polaron modes could in principle be long lived. Such coherent positions occur naturally, *e.g.* when a magnon polaron scatters from a magnetic impurity, which couples to its spin content only. In that case, the excitation that exists immediately after the scattering event is a *coherent* superposition of magnon polarons at the same frequency, with amplitudes that are such that excitation is (initially, in this case) of pure magnon type. For such a coherent superposition of magnon polarons, the phonon and magnon content of the excitation undergo Rabi-like oscillations upon propagation. The length scale for these oscillations is $l_{\mathrm{coh}}(\omega) \sim 1/\min_\lambda(\Delta q_\lambda(\omega))$, where $\Delta q_\lambda(\omega)$ is the difference of the wavenumbers of magnon-like and phonon-like magnon-polaron modes at the same frequency ω. Only after a propagation length much larger than l_{coh} the excitation can be described as a "classical" mixture of different magnon-polaron modes. Like any theory that describes excitations in terms of their distribution function, the Boltzmann theory of this Section does not include coherence effects. This means that the Boltzmann approach is valid only on length scales larger than $l_{\mathrm{coh}}(\omega)$. For generic frequencies ω, $l_{\mathrm{coh}}(\omega)$ is of the order of the wavelength, so that this condition is not a serious limitation on the applicability of the Boltzmann approach. However, close to the resonance frequencies, $l_{\mathrm{coh}}(\omega)$ may become appreciable and the Boltzmann theory could possibly overestimate the rate of impurity-mediated scattering between different magnon-polaron modes. Indeed, taking numerical values from Table 3.1, we estimate that close to the resonance frequencies, $l_{\mathrm{coh}}(\omega)$ may be several μm, which is only slightly below typical system sizes or impurity scattering lengths.

3.3.2 Linear response

Distribution function.— To simplify the analysis of the coupled Boltzmann equations for the magnon-polaron distribution functions we consider small deviations from equilibrium only and linearize the distribution functions $n_{\mathbf{q},\nu}(x)$ around their equilibrium distributions,

$$n_{\mathbf{q},\nu} = n^0(\omega_{\mathbf{q},\nu}) + \omega_{\mathbf{q},\nu}\left(-\frac{\partial n^0}{\partial \omega}\right)\psi_{\mathbf{q},\nu}, \qquad (3.41)$$

where $n^0(\omega_{\mathbf{q},\nu}) = 1/(e^{\hbar\omega_{\mathbf{q},\nu}/k_{\mathrm{B}}T} - 1)$ is the Planck distribution. In local thermal equilibrium at temperature $T + \Delta T(x)$, one has $\psi_{\mathbf{q},\nu}(x) = \Delta T(x)/T$. Similarly, the distribution functions $n_{\mathrm{I}}(\omega)$ and $n_{\mathrm{N}}(\omega)$ in the non-magnetic regions to the left and right of the magnetic insulator are written

$$n_{\mathrm{I,N}}(\omega) = n^0(\omega_{\mathbf{q},\nu}) + \omega_{\mathbf{q},\nu}\left(-\frac{\partial n^0}{\partial \omega}\right)\psi_{\mathrm{I,N}}, \qquad (3.42)$$

63

where $\psi_{\mathrm{I,N}} = \Delta T_{\mathrm{I,N}}/T$. The Boltzmann equation (3.40) for the linearized distribution function reads

$$v_{\mathbf{q},\nu x}\frac{\partial \psi_{\mathbf{q},\nu}}{\partial x} = J_{\mathbf{q},\nu}, \tag{3.43}$$

where $J_{\mathbf{q},\nu}$ is a linearized version of the collision integral, see Sec. 3.3.3.

Simplified angular dependence. — Anticipating that impurity scattering suppresses most variations of $\psi_{\mathbf{q},\nu}$ with the propagation direction $\mathbf{v}_{\mathbf{q},\nu}$ of the magnon-polaron mode, for $\psi_{\mathbf{q},\nu}$ we assume a simplified dependence on the wavevector $\mathbf{q}$ such that at each frequency ω there is one isotropic moment (even in $\mathbf{q}$) and one anisotropic moment (odd in $\mathbf{q}$),

$$\psi_{\mathbf{q},\nu} = \psi_{0,\nu}(\omega_{\mathbf{q},\nu}) + v_{\mathbf{q},\nu x}\psi_{1,\nu}(\omega_{\mathbf{q},\nu}). \tag{3.44}$$

The isotropic moment and the anisotropic moment are obtained from the full distribution function $\psi_{\mathbf{q},\nu}$ as

$$\psi_{0,\nu}(\omega) = \frac{1}{V\mathcal{E}_{2,\nu}(\omega)}\sum_{\mathbf{q}}\psi_{\mathbf{q},\nu}v_{\mathbf{q},\nu x}^2\delta(\omega_{\mathbf{q},\nu} - \omega),$$

$$\psi_{1,\nu}(\omega) = \frac{1}{V\mathcal{E}_{2,\nu}(\omega)}\sum_{\mathbf{q}}\psi_{\mathbf{q},\nu}v_{\mathbf{q},\nu x}\delta(\omega_{\mathbf{q},\nu} - \omega), \tag{3.45}$$

where the normalization factor $\mathcal{E}_{n,\nu}(\omega)$ is defined as

$$\mathcal{E}_{n,\nu}(\omega) = \frac{1}{V}\sum_{\mathbf{q}}|v_{\mathbf{q},\nu x}|^n\delta(\omega_{\mathbf{q},\nu} - \omega), \quad n = 0, 1, 2, \ldots. \tag{3.46}$$

For an isotropic dispersion one has

$$\mathcal{E}_{n,\nu}(\omega) = \mathcal{E}_{0,\nu}(\omega)\frac{v_\nu(\omega)^n}{n + 1}, \tag{3.47}$$

where $v_\nu(\omega) = |\partial\omega_{\mathbf{q},\nu}/\partial\mathbf{q}|$ is the group velocity of the magnon-polaron mode ν at frequency ω.

3.3.3 Collision integral

The collision integral $J_{\mathbf{q},\nu}$ in the linearized Boltzmann equation (3.43) has the general form

$$J_{\mathbf{q},\nu} = \frac{1}{V}\sum_{\mathbf{q}',\nu'}\Gamma_{\mathbf{q},\nu;\mathbf{q}',\nu'}(\psi_{\mathbf{q}',\nu'} - \psi_{\mathbf{q},\nu}), \tag{3.48}$$

with an effective linearized collision rate $\Gamma_{\mathbf{q},\nu;\mathbf{q}',\nu'}$ that describes both elastic and inelastic scattering processes,

$$\Gamma_{\mathbf{q},\nu;\mathbf{q}',\nu'} = \Gamma_{\mathbf{q},\nu;\mathbf{q}',\nu'}^{\mathrm{el}}\delta(\omega_{\mathbf{q},\nu} - \omega_{\mathbf{q}',\nu'}) + \Gamma_{\mathbf{q},\nu;\mathbf{q}',\nu'}^{\mathrm{inel}}. \tag{3.49}$$

Magnon-impurity and phonon-impurity scattering contribute to the elastic term in the collision integral. The dominant microscopic inelastic scattering processes are "three-magnon" and "three-phonon" scattering — splitting or confluence processes in which one phonon or magnon scatters into two or vice versa —, "four-magnon" processes, exchange-based magnon-phonon interaction, and relativistic or dipole-dipole-based inelastic magnon-phonon scattering, which includes processes in which one phonon creates a pair of magnons and vice versa. These processes are illustrated schematically in Table 3.2. In this Section we describe representative model Hamiltonians for the dominant scattering mechanisms and give an overview of the structure of the corresponding linearized collision rates for the magnon-polaron system.

Magnon-impurity scattering— As a simple model for impurity scattering of magnetic modes, we consider the Heisenberg interaction Hamiltonian (3.3) with a random fluctuating magnetic field $B_j = B + \delta B_j$ and a random value $S_j = S + \delta S_j$ of the magnitude of the spin at each lattice site, δB_j and δS_j being randomly distributed with zero mean and with variance $\langle \delta B^2 \rangle \equiv \langle \delta B_j^2 \rangle \ll B^2$ and $\langle \delta S^2 \rangle \equiv \langle \delta S_j^2 \rangle \ll S^2$. In terms of the magnon polarons, the magnon-impurity Hamiltonian reads

$$H^{\mathrm{mi}} = \frac{\hbar}{\sqrt{V}} \sum_{\mathbf{q},\mathbf{q}'} \sum_{\nu,\nu'} U^{\mathrm{mi}}_{\mathbf{q}\nu;\mathbf{q}'\nu'} a^*_{\mathbf{q},\nu} a_{\mathbf{q}',\nu'}, \qquad (3.50)$$

plus terms that create or annihilate two magnon polarons. Since such processes do not conserve energy they do not contribute to the collision integral. The matrix element for magnon-impurity scattering is

$$U^{\mathrm{mi}}_{\mathbf{q}\nu;\mathbf{q}'\nu'} = U^{\mathrm{mi},0}_{\mathbf{q};\mathbf{q}'} \left(V^*_{\mathbf{q},4,\nu} V_{\mathbf{q}',4,\nu'} + V^*_{\mathbf{q},8,\nu} V_{\mathbf{q}',8,\nu'} \right). \qquad (3.51)$$

with $U^{\mathrm{mi},0}_{\mathbf{q};\mathbf{q}'}$ the corresponding matrix element in the absence of magnon-phonon coupling. The matrix $V_{\mathbf{q}}$ is the symplectic 8×8 matrix that diagonalizes the magnon-phonon Hamiltonian $H_{\mathbf{q}}$ of Eq. (3.28), see Eq. (3.30). Statistically, the mean $\langle U^{\mathrm{mi},0}_{\mathbf{q};\mathbf{q}'} \rangle$ vanishes, whereas the fluctuations of $U^{\mathrm{mi},0}_{\mathbf{q};\mathbf{q}'}$ are given by

$$\langle |U^{\mathrm{mi},0}_{\mathbf{q};\mathbf{q}'}|^2 \rangle = \frac{a^7 J^2}{4} \langle \delta S^2 \rangle (q^2 + q'^2)^2 + \mu^2 a^3 \langle \delta B^2 \rangle. \qquad (3.52)$$

Phonon-impurity scattering— As a simple model for impurity scattering of lattice vibrations, we consider the phonon Hamiltonian (3.2) with a random value $m_j = m + \delta m_j$ of the masses of the lattice ions. Again, we take δm_j randomly distributed with zero mean and with variance $\langle \delta m^2 \rangle \equiv \langle \delta m_j^2 \rangle \ll m^2$. In terms of the magnon-polaron modes we find the phonon-impurity Hamiltonian

$$H^{\mathrm{pi}} = \frac{\hbar}{\sqrt{V}} \sum_{\mathbf{q},\mathbf{q}'} \sum_{\nu,\nu'} U^{\mathrm{pi}}_{\mathbf{q}\nu;\mathbf{q}'\nu'} a^*_{\mathbf{q},\nu} a_{\mathbf{q}',\nu'} \qquad (3.53)$$

where

$$U^{\text{pi}}_{\mathbf{q}\nu;\mathbf{q}'\nu'} = \sum_{\lambda,\lambda'} (V^*_{\mathbf{q},\lambda,\nu} + V^*_{\mathbf{q},\lambda+4,\nu})(V_{\mathbf{q}',\lambda',\nu'} + V_{\mathbf{q}',\lambda'+4,\nu'})U^{\text{pi},0}_{\mathbf{q}\lambda;\mathbf{q}'\lambda'}. \tag{3.54}$$

We have again left out contributions that create or annihilate two magnon polarons, because these do not contribute to the collision integrals. The statistical average of the phonon-impurity matrix element vanishes, $\langle U_{\mathbf{q}\lambda;\mathbf{q}'\lambda'}\rangle = 0$. The variance is [1]

$$\langle |U^{\text{pi},0}_{\mathbf{q},\lambda;\mathbf{q}',\lambda'}|^2\rangle = \frac{a^3\langle\delta m^2\rangle}{4m^2}|\mathbf{e}^*_{\mathbf{q},\lambda}\cdot\mathbf{e}_{\mathbf{q}',\lambda'}|^2\omega^0_{\mathbf{q}\lambda}\omega^0_{\mathbf{q}'\lambda'}. \tag{3.55}$$

The linearized collision rate that is derived from the magnon-impurity interaction (3.50) and phonon interaction (3.53) reads

$$\Gamma^{\text{el}}_{\mathbf{q},\nu;\mathbf{q}',\nu'} = 2\pi\left(\langle|U^{\text{mi}}_{\mathbf{q}\nu;\mathbf{q}'\nu'}|^2\rangle + \langle|U^{\text{pi}}_{\mathbf{q}\nu;\mathbf{q}'\nu'}|^2\rangle\right). \tag{3.56}$$

Numerical values.— To obtain numerical values for the variances $\langle\delta B^2\rangle$ and $\langle\delta S^2\rangle$, we relate these to the corresponding magnon mean free path l_{mi}, which determines low-temperature measurements of the respective magnon thermal conductivities,

$$l^{-1}_{\text{mi}}(\omega) = \frac{1}{4\pi J^2 S^2 a}\left[\mu^2\langle\delta B^2\rangle + \frac{\langle\delta S^2\rangle}{S^2}(\omega - \mu B)^2\right]. \tag{3.57}$$

Similarly, we relate the variance $\langle\delta m^2\rangle$ to the phonon mean free paths $l_{\text{pi},\lambda}$, which is related to the phonon thermal conductivity,

$$l^{-1}_{\text{pi},\lambda}(\omega) = \tau_{\text{pi}}(\omega)^{-1}c^{-1}_\lambda, \tag{3.58}$$

with

$$\tau_{\text{pi}}(\omega)^{-1} = \frac{a^3}{12\pi\hbar^4}\frac{\langle\delta m^2\rangle}{m^2}\sum_{\lambda'}\frac{1}{c^3_{\lambda'}}\omega^4, \tag{3.59}$$

where $c_1 = c_{\text{l}}$ is the longitudinal phonon velocity and $c_2 = c_3 = c_{\text{t}}$ the transverse phonon velocity. Our microscopic model coincides with the shape of the best fit to the impurity rates in Ref. [101]. Comparison of Eqs. (3.57) and (3.58) with the mean free paths reported in Ref. [101] yields the variances $\langle\delta S^2\rangle$, $\langle\delta B^2\rangle$, and

---

[1]The phonon-impurity Hamiltonian of Ref. [20] has a statistically independent mode-diagonal matrix elements $U^{\text{pi},0}_{\mathbf{q}\lambda;\mathbf{q}'\lambda'} \propto \delta_{\lambda\lambda'}$ for the three phonon modes that do not scatter between the two degenerate transverse phonon modes. This is unphysical, since the assignment of the polarization vectors for the degenerate transverse phonon modes is arbitrary. Moreover, in spite of its simplicity, the microscopic model (3.55) clearly shows that impurity scattering approximately equally connects phonon modes of all polarizations, longitudinal as well as transverse.

Quantity	Value	Alternative value with $l_{\mathrm{mi}} < l_{\mathrm{pi}}$
$\sqrt{\langle \delta m^2 \rangle}/m$	0.09	0.009
$\sqrt{\langle \delta S^2 \rangle}/S$	0.05	0.16
$\sqrt{\langle \delta B^2 \rangle}$	$0.07\,\mathrm{T}$	$0.22\,\mathrm{T}$
$u_{\mathrm{mi}}/\sqrt{a^3}$	$65\,\mathrm{GHz}$	$650\,\mathrm{GHz}$
$u_{\mathrm{pi}}/\sqrt{a^3}$	$332\,\mathrm{GHz}$	$33.2\,\mathrm{GHz}$

Table 3.3: Numerical values for the model parameters for impurity scattering.

$\langle \delta m^2 \rangle$ given in the center column Table 3.3. The corresponding mean free paths l_{mi} and l_{pi} are shown in Fig. 3.3. The phonon mean free path l_{pi} obtained from this procedure is about two orders of magnitude smaller than the mean free path l_{mi} for magnon-impurity scattering. To allow for a comparison with the theory of Refs. [15, 20], which infers a smaller magnon-impurity mean free path from the low-temperature spin Seebeck effect measurements, we also consider parameter values in which the orders of magnitude for phonon-impurity and magnon-impurity scattering are interchanged, which corresponds to a sample that is of higher acoustic than magnetic quality. These values are shown in the rightmost column of Table 3.3.

To make is easier to separate different contributions to the spin Seebeck effect, in some of our calculations we also use a phenomenological white-noise model for the impurity scattering rates, for which the mean free paths l_{pi} and l_{mi} have a weaker frequency dependence than for the microscopic model of Eqs. (3.52) and (3.55). The phenomenological white-noise model is defined by setting

$$\langle |U_{\mathbf{q};\mathbf{q}'}^{\mathrm{mi},0}|^2 \rangle = u_{\mathrm{mi}}^2/V, \quad \langle |U_{\mathbf{q},\lambda;\mathbf{q}',\lambda'}^{\mathrm{pi},0}|^2 \rangle = u_{\mathrm{pi}}^2/3V. \tag{3.60}$$

The variances u_{mi}^2 and u_{pi}^2, which determine the mean free paths

$$l_{\mathrm{mi}}^{-1}(\omega) = \frac{u_{\mathrm{mi}}^2}{4\pi a^4 J^2 S^2} \ , \quad l_{\mathrm{pi},\lambda}^{-1}(\omega) = \frac{u_{\mathrm{pi}}^2}{3\pi c_\lambda} \sum_{\lambda'} \frac{1}{c_{\lambda'}^3} \omega^2, \tag{3.61}$$

are adjusted to low temperature measurements of the magnon and phonon thermal mean free paths in Ref. [100]. Numerical values for the case of a sample with higher magnetic than acoustic quality and alternative values for the case of a higher acoustic than magnetic quality are shown in Table 3.3.

Inelastic scattering— At low temperatures the elastic scattering with impurities dominates the relaxation of the magnon polarons. With increasing temperature or decreasing impurity concentration the relative importance of inelastic scattering increases. Here we supply the leading-order contributions to the corresponding magnon-polaron Hamiltonians and collision integrals. Except for the three-phonon interaction, the underlying magnon-magnon and magnon-phonon Hamiltonians can

67

be derived from the microscopic model presented in Section 3.2.1, by expanding the Heisenberg and pseudo-dipolar interactions to higher orders in the magnon amplitudes $\mathbf{n}_j$ and the displacement vectors $\mathbf{u}_j$. The leading inelastic interaction involving phonons only is the three-phonon interaction. It arises from anharmonicities of the lattice potential and can effectively be derived within a continuum elastic strain model [43], see appendix B.5.

In terms of magnon polarons the three-polaron interaction Hamiltonian may be written as

$$
H^{\mathrm{in},3} = \frac{1}{\sqrt{V}} \sum_{\mathbf{q},\nu} \sum_{\mathbf{q}',\nu'} \sum_{\mathbf{q}'',\nu''} (U^{\mathrm{in},3}_{\mathbf{q}\nu;\mathbf{q}'\nu',\mathbf{q}''\nu''} a^*_{\mathbf{q},\nu} a_{\mathbf{q}',\nu'} a_{\mathbf{q}'',\nu''}
$$
$$
+ U^{\mathrm{in},3}_{\mathbf{q}\nu,\mathbf{q}'\nu';\mathbf{q}''\nu''} a^*_{\mathbf{q},\nu} a^*_{\mathbf{q}',\nu'} a_{\mathbf{q}'',\nu''}) \tag{3.62}
$$

where we left out contributions that create or annihilate three magnon polarons, because these do not contribute to the collision integral. The matrix element $U^{\mathrm{in},3}_{\mathbf{q}\nu;\mathbf{q}'\nu',\mathbf{q}''\nu''} = U^{\mathrm{in},3}_{\mathbf{q}\nu;\mathbf{q}''\nu'',\mathbf{q}'\nu'}$ of this general three-polaron interaction is assumed to be symmetric. It has contributions from three-phonon scattering (with matrix element $U^{\mathrm{3p},0}_{\mathbf{q}\lambda;\mathbf{q}'\lambda',\mathbf{q}''\lambda''}$ in the absence of magnon-phonon coupling), three-magnon scattering (with matrix element $U^{\mathrm{3m},0}_{\mathbf{q};\mathbf{q}',\mathbf{q}''}$ in the absence of magnon-phonon coupling), one-phonon-two-magnon scattering (with matrix element $U^{\mathrm{mp},0}_{\mathbf{q};\mathbf{q}'\lambda,\mathbf{q}''}$ in the basis of phonon and magnon states), and relativistic one-phonon-two-magnon scattering (with matrix element $U^{\mathrm{rel},0}_{\mathbf{q}\lambda;\mathbf{q}',\mathbf{q}''}$ in the basis of phonon and magnon states),

$$
U^{\mathrm{in},3}_{\mathbf{q}\nu;\mathbf{q}'\nu',\mathbf{q}''\nu''} = \Bigg\{ \sum_\lambda \sum_{\lambda'} \sum_{\lambda''} U^{\mathrm{3p},0}_{\mathbf{q}\lambda;\mathbf{q}'\lambda',\mathbf{q}''\lambda''}
$$
$$
\times (V^*_{\mathbf{q},\lambda,\nu} - V^*_{\mathbf{q},\lambda+4,\nu})(V_{\mathbf{q}',\lambda',\nu'} - V_{\mathbf{q}',\lambda'+4,\nu'})(V_{\mathbf{q}'',\lambda'',\nu''} - V_{\mathbf{q}'',\lambda''+4,\nu''})
$$
$$
+ \sum_\lambda U^{\mathrm{mp},0}_{\mathbf{q};\mathbf{q}'\lambda,\mathbf{q}''} \bigg[\frac{1}{2} (V^*_{\mathbf{q},4,\nu} V_{\mathbf{q}'',4,\nu''} + V^*_{\mathbf{q},8,\nu} V_{\mathbf{q}'',8,\nu''})(V_{\mathbf{q}',\lambda,\nu'} - V_{\mathbf{q}',\lambda+4,\nu'})
$$
$$
+ \frac{1}{2} (V^*_{\mathbf{q},4,\nu} V_{\mathbf{q}',4,\nu'} + V^*_{\mathbf{q},8,\nu} V_{\mathbf{q}',8,\nu'})(V_{\mathbf{q}'',\lambda,\nu''} - V_{\mathbf{q}'',\lambda+4,\nu''}) \bigg]
$$
$$
+ \sum_\lambda U^{\mathrm{rel},0}_{\mathbf{q}\lambda;\mathbf{q}',\mathbf{q}''} (V^*_{\mathbf{q},\lambda,\nu} - V^*_{\mathbf{q},\lambda+4,\nu})(V_{\mathbf{q}',4,\nu'} V_{\mathbf{q}'',4,\nu''} + V_{\mathbf{q}',8,\nu'} V_{\mathbf{q}'',8,\nu''})
$$
$$
+ U^{\mathrm{3m},0}_{\mathbf{q};\mathbf{q}',\mathbf{q}''} (V^*_{\mathbf{q},4,\nu} V_{\mathbf{q}',4,\nu'} V_{\mathbf{q}'',4,\nu''} - V^*_{\mathbf{q},8,\nu} V_{\mathbf{q}',8,\nu'} V_{\mathbf{q}'',8,\nu''}) \Bigg\} \delta_{\mathbf{q},\mathbf{q}'+\mathbf{q}''}.
$$
$$
\tag{3.63}
$$

Here the indices λ, λ', and λ'' label the polarization state of phonons and, hence, take the values 1, 2, 3. The corresponding linearized three-polaron transition rate

is

$$\Gamma^{\text{in},3}_{\mathbf{q},\nu;\mathbf{q}',\nu'} = \frac{2\pi}{\hbar^2} \frac{\omega_{\mathbf{q}',\nu'}}{\omega_{\mathbf{q},\nu}(1+n^0_{\mathbf{q},\nu})} \sum_{\mathbf{q}'',\nu''} \left\{ |U^{\text{in},3}_{\mathbf{q}'\nu';\mathbf{q}\nu,\mathbf{q}''\nu''}|^2 \delta(\omega_{\mathbf{q},\nu} - \omega_{\mathbf{q}',\nu'} + \omega_{\mathbf{q}'',\nu''})(1+n^0_{\mathbf{q}',\nu'})n^0_{\mathbf{q}'',\nu''} \right.$$
$$- |U^{\text{in},3}_{\mathbf{q}''\nu'';\mathbf{q}\nu,\mathbf{q}'\nu'}|^2 \delta(\omega_{\mathbf{q},\nu} + \omega_{\mathbf{q}',\nu'} - \omega_{\mathbf{q}'',\nu''})n^0_{\mathbf{q}',\nu'}(1+n^0_{\mathbf{q}'',\nu''})$$
$$\left. + |U^{\text{in},3}_{\mathbf{q}\nu;\mathbf{q}'\nu',\mathbf{q}''\nu''}|^2 \delta(\omega_{\mathbf{q},\nu} - \omega_{\mathbf{q}',\nu'} - \omega_{\mathbf{q}'',\nu''})(1+n^0_{\mathbf{q}',\nu'})(1+n^0_{\mathbf{q}'',\nu''}) \right\}.$$
(3.64)

The main contribution to the four-polaron Hamiltonian results from the Heisenberg exchange interaction (3.3). As the underlying four-magnon Hamiltonian conserves the magnon number, see Eq. (B.38), the four-polaron scattering is also dominated by processes that conserve the polaron number. These processes are described by the Hamiltonian

$$H^{\text{in},4} = \frac{1}{V} \sum_{\mathbf{q},\nu} \sum_{\mathbf{q}_2,\nu_2} \sum_{\mathbf{q}',\nu'} \sum_{\mathbf{q}'_2,\nu'_2} U^{\text{in},4}_{\mathbf{q}\nu,\mathbf{q}_2\nu_2,\mathbf{q}'\nu',\mathbf{q}'_2\nu'_2} a^*_{\mathbf{q},\nu} a^*_{\mathbf{q}_2,\nu_2} a_{\mathbf{q}',\nu'} a_{\mathbf{q}'_2,\nu'_2} + \text{H.c.}, \qquad (3.65)$$

where the matrix element $U^{\text{in},4}_{\mathbf{q}\nu,\mathbf{q}_2\nu_2,\mathbf{q}'\nu',\mathbf{q}'_2\nu'_2}$ is expressed in terms of the matrix element $U^{\text{4m},0}_{\mathbf{q}\nu,\mathbf{q}_2\nu_2,\mathbf{q}'\nu',\mathbf{q}'_2\nu'_2}$ of the four-magnon Hamiltonian in the absence of magnon-phonon coupling as

$$U^{\text{in},4}_{\mathbf{q}\nu,\mathbf{q}_2\nu_2,\mathbf{q}'\nu',\mathbf{q}'_2\nu'_2} = U^{\text{4m},0}_{\mathbf{q}\nu,\mathbf{q}_2\nu_2,\mathbf{q}'\nu',\mathbf{q}'_2\nu'_2} (V^*_{\mathbf{q},4,\nu} V^*_{\mathbf{q}_2,4,\nu_2} V_{\mathbf{q}',4,\nu'} V_{\mathbf{q}'_2,4,\nu'_2}$$
$$+ V^*_{\mathbf{q},8,\nu} V^*_{\mathbf{q}_2,8,\nu_2} V_{\mathbf{q}',8,\nu'} V_{\mathbf{q}'_2,8,\nu'_2})\delta_{\mathbf{q}+\mathbf{q}_2,\mathbf{q}'+\mathbf{q}'_2}. \quad (3.66)$$

The contribution of four-polaron processes to the inelastic collision rate reads

$$\Gamma^{\text{in},4}_{\mathbf{q},\nu;\mathbf{q}',\nu'} = \frac{2\pi}{\hbar^2} \frac{\omega_{\mathbf{q}',\nu'}}{\omega_{\mathbf{q},\nu}(1+n^0_{\mathbf{q},\nu})} \sum_{\mathbf{q}_2,\nu_2} \sum_{\mathbf{q}'_2,\nu'_2} n^0_{\mathbf{q}'_2,\nu'_2}$$
$$\times \left\{ (1+n^0_{\mathbf{q}',\nu'})n^0_{\mathbf{q}_2,\nu_2} |U^{\text{in},4}_{\mathbf{q}\nu,\mathbf{q}_2\nu_2;\mathbf{q}'\nu',\mathbf{q}'_2\nu'_2}|^2 \delta(\omega_{\mathbf{q},\nu} + \omega_{\mathbf{q}_2,\nu_2} - \omega_{\mathbf{q}',\nu'} - \omega_{\mathbf{q}'_2,\nu'_2}) \right.$$
$$\left. - \frac{1}{2} n^0_{\mathbf{q}',\nu'}(1+n^0_{\mathbf{q}_2,\nu_2}) |U^{\text{in},4}_{\mathbf{q}\nu,\mathbf{q}'\nu';\mathbf{q}_2\nu_2,\mathbf{q}'_2\nu'_2}|^2 \delta(\omega_{\mathbf{q},\nu} + \omega_{\mathbf{q}',\nu'} - \omega_{\mathbf{q}_2,\nu_2} - \omega_{\mathbf{q}'_2,\nu'_2}) \right\}.$$
(3.67)

Explicit expressions for the matrix elements $U^{\text{3p},0}$, $U^{\text{mp},0}$, $U^{\text{3m},0}$, and $U^{\text{4m},0}$ in the framework of the microscopic model of Sec. 3.2 are given in App. B.5. The inelastic rates $\Gamma_{\mathbf{q},\nu;\mathbf{q}',\nu'}$ can then be calculated using the numerical values given in Table 3.1. To obtain the inelastic magnon and phonon relaxation lengths $\lambda_{\text{m,p}}$ of Fig. 3.3, we first calculate the frequency-resolved scattering rate $\tau^{-1}_{\text{m,p}}(\omega)$ of magnons and

phonons using Fermi's Golden rule and then determine the corresponding relaxation lengths $\lambda_{\mathrm{m,p}}(\omega)$ as

$$\lambda_{\mathrm{m,p}}(\omega) = l_{\mathrm{mi,pi}}(\omega)\sqrt{\frac{\tau_{\mathrm{m,p}}(\omega)}{\tau_{\mathrm{mi,pi}}(\omega)}}, \tag{3.68}$$

where l_{mi} and l_{pi} are the mean free paths for magnon-impurity and phonon-impurity scattering, see Eqs. (3.57) and (3.58), and τ_{mi} and τ_{pi} are the corresponding lifetimes.

Simplified angular dependence.— In Eq. (3.45) a simplified ansatz for the linearized distribution function, with one isotropic moment $\psi_{0,\nu}(\omega)$ and one anisotropic moment $\psi_{1,\nu}(\omega)$ per mode ν and frequency ω was introduced. Because of the symmetry property (3.36) of the matrix elements $V_{\mathbf{q},\lambda,\nu}$, the linearized transition rates $\Gamma_{\mathbf{q},\nu;\mathbf{q}',\nu'}$ for the magnon polarons satisfy the symmetry property

$$\Gamma_{\mathbf{q},\nu;\mathbf{q}',\nu'} = \Gamma_{-\mathbf{q},\nu;-\mathbf{q}',\nu'} \tag{3.69}$$

if the microscopic rates in the absence of magnon-phonon coupling also satisfy this symmetry. Combining this symmetry property with the antisymmetry of the magnon-polaron velocity $v_{\mathbf{q},\nu x}$, one finds that the general form (3.48) of the linearized collision integral results in two coupled equations for the isotropic and anisotropic moments $\psi_{0,\nu}(\omega)$ and $\psi_{1,\nu}(\omega)$,

$$\frac{\partial \psi_{1,\nu}(\omega)}{\partial x} = -\int d\omega' \sum_{\nu'} \mathcal{G}^0_{\nu,\nu'}(\omega,\omega')\psi_{0,\nu'}(\omega'),$$

$$\frac{\partial \psi_{0,\nu}(\omega)}{\partial x} = -\int d\omega' \sum_{\nu'} \mathcal{G}^1_{\nu,\nu'}(\omega,\omega')\psi_{1,\nu'}(\omega'). \tag{3.70}$$

Here the 4×4 matrices $\mathcal{G}^0$ and $\mathcal{G}^1$ are defined as

$$\mathcal{G}^0_{\nu,\nu'}(\omega,\omega') = \frac{1}{V^2 \mathcal{E}_{2,\nu}(\omega)} \sum_{\mathbf{q},\mathbf{q}''} \sum_{\nu''} \Gamma_{\mathbf{q},\nu;\mathbf{q}',\nu''}\delta(\omega - \omega_{\mathbf{q},\nu})$$

$$\times [\delta_{\nu,\nu'}\delta(\omega' - \omega) - \delta_{\nu',\nu''}\delta(\omega' - \omega_{\mathbf{q}'',\nu''})],$$

$$\mathcal{G}^1_{\nu,\nu'}(\omega,\omega') = \frac{1}{V^2 \mathcal{E}_{2,\nu}(\omega)} \sum_{\mathbf{q},\mathbf{q}''} \sum_{\nu''} \Gamma_{\mathbf{q},\nu;\mathbf{q}',\nu''}\delta(\omega - \omega_{\mathbf{q},\nu})$$

$$\times [\delta_{\nu,\nu'}\delta(\omega' - \omega)v^2_{\mathbf{q},\nu x} - \delta_{\nu',\nu''}\delta(\omega' - \omega_{\mathbf{q}'',\nu''})v_{\mathbf{q},\nu x}v_{\mathbf{q}'',\nu''x}]. \tag{3.71}$$

The normalization coefficients $\mathcal{E}_{2,\nu}(\omega)$ are defined in Eq. (3.46). For elastic scattering from impurities the transition rate $\Gamma_{\mathbf{q},\nu;\mathbf{q}',\nu'}$ contains an additional delta function $\delta(\omega_{\mathbf{q},\nu} - \omega_{\mathbf{q}',\nu'})$, which nullifies the frequency integration in Eq. (3.70), so that one arrives at a set of eight coupled differential equations, which can be solved for each frequency separately.

The matrix $\mathcal{G}^0_{\nu,\nu'}$ in the isotropic Boltzmann moment obeys the condition

$$\int d\omega' \sum_{\nu'} \mathcal{G}^0_{\nu,\nu'}(\omega,\omega') = 0. \tag{3.72}$$

This ensures that the uniform isotropic solution $\psi_{0,\nu} = \psi$ and $\psi_{1,\nu} = 0$, with ψ a constant, is a solution of the equations. In the case of elastic scattering only, $\psi_{0,\nu}(\omega) = \psi(\omega)$ is a solution of the equations, with $\psi(\omega)$ an arbitrary function of ω.

3.3.4 Reflection coefficients at interfaces

To describe the boundary conditions at the IF and FN interfaces at $x = 0$ and $x = L$, we note that the frequency ω and the transverse wavevector $\mathbf{q}_\perp = q_y \mathbf{e}_y + q_z \mathbf{e}_z$ are conserved at the interface. Hence, instead of using the wavevector $\mathbf{q}$ to label the magnon-polaron modes, we use the triple $(\omega, \mathbf{q}_\perp, \sigma_\mathbf{q})$, where the sign $\sigma_\mathbf{q} = \mathrm{sign}\,(v_{\mathbf{q},\nu x})$ is the sign of the propagation direction. The range of the transverse wavevector $\mathbf{q}_\perp$ is restricted to those values of $\mathbf{q}_\perp$ for which the magnon-polaron mode ν is propagating at frequency ω, *i.e.*, for which q_x is real.

The boundary condition at the IF interface at $x = 0$ relates the distribution function of magnon-polaron modes moving away from the interface to the distribution of magnon-polaron modes and phonon modes moving towards the interface,

$$n_\nu(\omega, \mathbf{q}_\perp, +) = \sum_{\nu'} R_{\nu\nu'}(\omega, \mathbf{q}_\perp) n_{\nu'}(\omega, \mathbf{q}_\perp, -) + \sum_{\lambda''} T_{\nu\lambda''}(\omega, \mathbf{q}_\perp) n_\mathrm{I}(\omega). \qquad (3.73)$$

Here $R_{\nu\nu'}(\omega, \mathbf{q}_\perp)$ is the probability that a magnon polaron ν' incident on the IF interface reflects as a magnon-polaron mode ν, see Fig. 3.4(a). Similarly, $T_{\nu\lambda''}(\omega, \mathbf{q}_\perp)$ is the probability that a phonon mode λ'' incident on the IF interface from I is transmitted as a magnon-polaron mode ν. Only modes that are propagating at frequency ω and transverse wavevector $\mathbf{q}_\perp$ enter the summations over ν' and λ''. The distribution function of phonons approaching the interface from I is $n_\mathrm{I}(\omega)$, see Eq. (3.42). Energy conservation at the IF interface at $x = 0$ implies the unitarity condition [140, 110]

$$\begin{aligned} 1 &= \sum_{\nu'} R_{\nu\nu'}(\omega, \mathbf{q}_\perp) + \sum_{\lambda''} T_{\nu\lambda''}(\omega, \mathbf{q}_\perp) \\ &= \sum_{\nu'} R_{\nu'\nu}(\omega, \mathbf{q}_\perp) + \sum_{\lambda''} T_{\lambda''\nu}(\omega, \mathbf{q}_\perp) \end{aligned} \qquad (3.74)$$

With the help of the unitarity condition (3.74), the boundary condition (3.73) is written in terms of the reflection coefficients $R_{\nu\nu'}(\omega, \mathbf{q}_\perp)$ for magnon-polaron modes only,

$$n_\nu(\omega, \mathbf{q}_\perp, +) = \sum_{\nu'} R_{\nu\nu'}(\omega, \mathbf{q}_\perp) n_{\nu'}(\omega, \mathbf{q}_\perp, -) + \sum_{\nu'} [\delta_{\nu\nu'} - R_{\nu\nu'}(\omega, \mathbf{q}_\perp)] n_\mathrm{I}(\omega). \quad (3.75)$$

Similarly, for the FN interface at $x = L$ the boundary condition relates the distribution function of magnon-polaron modes moving away from the interface to the

distribution of magnon-polaron modes and phonon modes moving towards the interface. In addition to considering reflection coefficients $R_{\nu\nu'}(\omega, \mathbf{q}_\perp)$ and transmission coefficients $T_{\nu\lambda''}(\omega, \mathbf{q}_\perp)$ at the FN interface, one also has to account for the possibility that a magnon polaron incident on the FN interface excites a spinful excitation of the conduction electrons in the normal metal, and for the inverse process. Since the total energy current at the FN interface is conserved, we find the probability $P_{\nu\mathrm{N}}(\omega, \mathbf{q}_\perp)$ that a magnon polaron in mode ν emerging from the FN interface was excited there by an incident a spinful excitation of the conduction electrons as

$$\sum_{\nu'} R_{\nu\nu'}(\omega, \mathbf{q}_\perp) + \sum_{\lambda''} T_{\nu\lambda''}(\omega, \mathbf{q}_\perp) = 1 - P_{\nu\mathrm{N}}(\omega, \mathbf{q}_\perp). \tag{3.76}$$

Similarly, the probability $P_{\mathrm{N}\nu}(\omega, \mathbf{q}_\perp)$ that a magnon polaron in mode ν incidents on the FN interface excites a spinful excitation of the conduction electrons is

$$\sum_{\nu'} R_{\nu'\nu}(\omega, \mathbf{q}_\perp) + \sum_{\lambda''} T_{\lambda''\nu}(\omega, \mathbf{q}_\perp) = 1 - P_{\mathrm{N}\nu}(\omega, \mathbf{q}_\perp). \tag{3.77}$$

Using Eq. (3.76), the boundary condition at the FN interface then reads

$$n_\nu(\omega, \mathbf{q}_\perp, -) = \sum_{\nu'} R_{\nu\nu'}(\omega, \mathbf{q}_\perp) n_{\nu'}(\omega, \mathbf{q}_\perp, +) + \sum_{\nu'} [\delta_{\nu\nu'} - R_{\nu\nu'}(\omega, \mathbf{q}_\perp)] n_\mathrm{N}(\omega),$$
$$\tag{3.78}$$

where $n_\mathrm{N}(\omega)$ is the equilibrium distribution function for the non-magnetic normal metal, see Eq. (3.42).

The reflection and transmission coefficients $R_{\nu\nu'}$ and $T_{\nu\lambda''}$ can be computed from the equations of motion for the magnon-polaron modes and the boundary conditions at the interfaces at $x = 0$ and $x = L$, see Eqs. (3.18)–(3.22). Details of this calculation, which follows the ideas of the Landauer-Büttiker formalism [143], can be found in App. B.4.

Simplified angular dependence.— Boundary conditions for the isotropic moment $\psi_{0,\nu}(\omega)$ and the anisotropic moment $\psi_{1,\nu}(\omega)$ of the linearized distribution function are obtained from Eqs. (3.75) and (3.78) by enforcing consistency for the frequency-resolved energy current density $j_{\nu x}(\omega)$ at the interface carried by the magnon-polaron mode ν, which is uniquely linked to the anisotropic moment via

$$j_{\nu x}(\omega) = \mathcal{E}_{2,\nu}(\omega)\hbar\omega^2 \left(-\frac{\partial n^0}{\partial\omega}\right)\psi_{1,\nu}(\omega). \tag{3.79}$$

The consistency condition for the anisotropic moment at the IF interface reads

$$\frac{\mathcal{E}_{2,\nu}(\omega)}{\mathcal{E}_{1,\nu}(\omega)} \sum_{\nu'} [\delta_{\nu\nu'} + \mathcal{R}_{1,\nu\nu'}(\omega)]\psi_{1,\nu'}(\omega) =$$
$$\sum_{\nu'} [\delta_{\nu\nu'} - \mathcal{R}_{0,\nu\nu'}(\omega)][\psi_\mathrm{I}(\omega) - \psi_{0,\nu'}(\omega)], \tag{3.80}$$
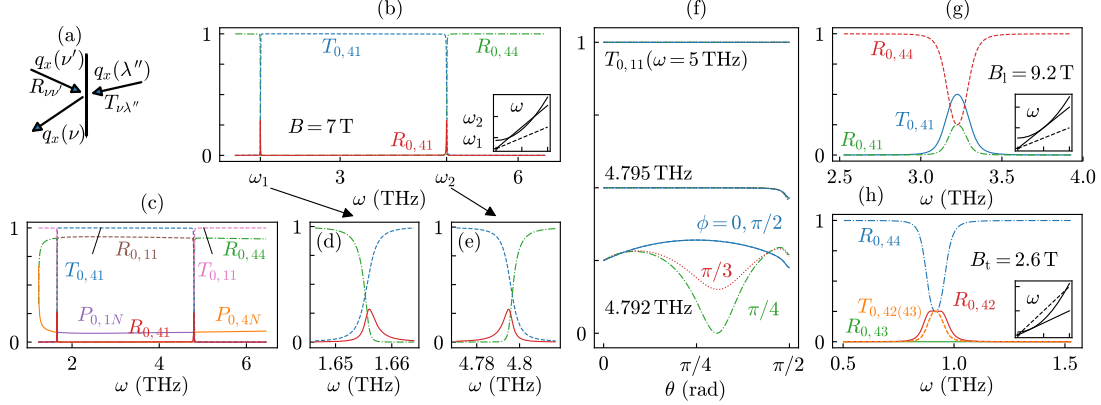
Figure 3.4: (a) Schematic picture of the interface reflection of a magnon polaron from branch ν', and transmission of a phonon from branch λ'', into a magnon polaron of branch ν with the respective reflection and transmission coefficients $R_{\nu\nu'}$ and $T_{\nu\lambda''}$. (b) Angle-averaged reflection and transmission coefficients $R_{0,\nu\nu'}$ and $T_{0,\nu\lambda''}$ at the IF interface for scattering into magnon-polaron mode $\nu = 4$ as a function of the frequency. (c) Coefficients $R_{0,\nu\nu'}$ and $T_{0,\nu\lambda''}$ at the FN interface for magnon-polaron modes $\nu = 1, 4$, as well as the probability $P_{0,\nu N}$ that the magnon-polaron mode ν at the FN interface is excited by a spinful excitation of the conduction electrons in the normal metal. Panels (d) and (e) show magnifications of the resonant regions in (b). The coefficients shown in panels (b)–(e) are for incident longitudinal-phonon-like or magnon-like modes $\nu' = 1, 4$ (in F) and $\lambda'' = 1$ (in I or N). Coefficients for the transverse-phonon-like incident modes $\nu' = 2, 3$ or $\lambda' = 2, 3$ are approximately zero (not shown). Within the accuracy of the figure, the probability $P_{0,N\nu}$ that the magnon-polaron mode ν' incident on the FN interface excites a spinful excitation of the conduction electrons in N is equal to $P_{0,\nu N}$. In (f) the transmission amplitude T_{11} is shown as a function of the polar angle θ and azimuthal angles ϕ for different frequencies ω in the vicinity of the resonance frequency. Panels (b)-(f) are evaluated for an applied magnetic field $B = 7\,\text{T}$. The non-zero reflection and transmission coefficients at the critical magnetic fields $B_l \approx 9.2\,\text{T}$ and $B_t \approx 2.6\text{T}$ are shown as a function of the frequency in panels (g) and (h), respectively. In panels (b)–(h) material parameters for YIG are taken from Table 3.1.

where

$$\mathcal{R}_{0,\nu\nu'}(\omega) = \frac{2}{(2\pi)^3} \int \frac{d\mathbf{q}_\perp}{\mathcal{E}_{1,\nu}(\omega)} R_{\nu\nu'}(\omega, \mathbf{q}_\perp), \tag{3.81}$$

$$\mathcal{R}_{1,\nu\nu'}(\omega) = \frac{2}{(2\pi)^3} \int \frac{d\mathbf{q}_\perp}{\mathcal{E}_{2,\nu}(\omega)} R_{\nu\nu'}(\omega, \mathbf{q}_\perp) |v_{\nu'x}(\omega, \mathbf{q}_\perp, -)|.$$

The boundary condition at the interface at $x = L$ is derived in the same way and reads

$$\frac{\mathcal{E}_{2,\nu}(\omega)}{\mathcal{E}_{1,\nu}(\omega)} \sum_{\nu'} [\delta_{\nu\nu'} + \mathcal{R}_{1,\nu\nu'}(\omega)] \psi_{1,\nu'}(\omega) =$$

$$\sum_{\nu'} [\delta_{\nu\nu'} - \mathcal{R}_{0,\nu\nu'}(\omega)][\psi_{0,\nu'}(\omega) - \psi_{\mathrm{N}}(\omega)]. \tag{3.82}$$

Although the boundary conditions (3.80) and (3.82) are not quantitatively exact implementations of the microscopic boundary conditions (3.75) and (3.78) — an exact implementation of these boundary conditions is not compatible with the ansatz (3.44) — they are good quantitative approximations. For example, for an interface with perfect transparency and a single mode, they correctly take into account interface effects in the ballistic and diffusive limits, and deviate less than 2.5% from the exact result in the ballistic-to-diffusive crossover [144]. In App. B.7 we compare distribution functions for a ballistic system of length $L \ll l_{\mathrm{mi}},\ l_{\mathrm{pi}}$ and find that the difference between an exact calculation and a calculation based on the angle-averaged boundary conditions (3.80) and (3.82) differs less than 5%.

Numerical values. — The angle-averaged reflection and transmission coefficients (3.81) at the IF and FN interfaces are shown in Figure 3.4(b)–(e) for $B = 7\,\mathrm{T}$. Material parameters are as listed in Table 3.1. At this value of the magnetic field, the magnon dispersion crosses that of longitudinal phonons, but not the disperson of transverse phonons, as shown in the inset of Fig. 3.4(b). The resonant frequencies at which the dispersions cross are at $\omega \approx 1.65\,\mathrm{THz}$ and $\omega \approx 4.8\,\mathrm{THz}$. The magnon-polaron modes are labeled such that $\nu = 1$ refers to a magnon-like mode for $1.65\,\mathrm{THz} < \omega < 4.8\,\mathrm{THz}$ and to a longitudinal-phonon-like mode otherwise. The mode $\nu = 4$ is longitudinal-phonon-like for $1.65\,\mathrm{THz} < \omega < 4.8\,\mathrm{THz}$ and magnon-like otherwise. The modes $\nu = 2$ and $\nu = 3$ are transverse-phonon-like for all frequencies. The label $\lambda'' = 1$ refers to the longitudinal phonon mode in the non-magnetic insulator I or the normal metal N. Figure 3.4(b) shows the angle-averaged reflection and transmission probabilities $R_{0,\nu\nu'}$ and $T_{0,\nu\lambda''}$ into the magnon-polaron mode $\nu = 4$ at the IF interface, with close-ups near the resonance frequencies in panels (d) and (e). Figure 3.4(c) shows $R_{0,\nu\nu'}$, $T_{0,\nu\lambda''}$ at the FN interface for outgoing modes $\nu = 1$ and $\nu = 4$, as well as the probability $P_{0,\nu\mathrm{N}}$ that the magnon polaron mode ν was excited by a spinful excitation of the conduction electrons in N. The incident modes in panels (b)–(e) are $\nu' = 1$ and 4 (corresponding to longitudinal-phonon-like and

magnon-like magnon polaron modes in F) and $\lambda'' = 1$ (longitudinal phonon mode in I or N); Reflection and transmission coefficients $R_{0,\nu\nu'}$ and $T_{0,\nu\lambda''}$ with $\nu = 1$ or 4 and ν' and λ'' equal to 2 or 3 (which corresponds to transverse-phonon-like incident modes in F and I or N, respectively) are approximately zero (not shown). In contrast to the IF interface, where the reflection and transmission probabilities obey a unitary condition, see Fig. 3.4(b), the spin pumping into the normal metal at the FN interface at $x = L$ significantly influences the reflection of magnon-like magnon polarons, see Fig. 3.4(c). Figure 3.4(f) shows the angle-dependence of the transmission coefficient T_{11}, as a function of the polar angle θ and the azimuthal angle ϕ of the wavevector $\mathbf{q}$ of the outgoing mode. A significant angle dependence exists only in the immediate vicinity of the crossing points of the magnon and phonon dispersions.

Significant mixing between different magnon-polaron modes takes place only for frequencies near the crossings of the magnon and phonon dispersions at the resonant frequencies $\omega \approx 1.65\,\mathrm{THz}$ and $\omega \approx 4.8\,\mathrm{THz}$ [140, 110]. The frequency range for which the interfaces mix different modes is strongly enhanced near the critical magnetic fields at which the magnon and phonon dispersions touch. This is illustrated in Figs. 3.4(g) and (h), which show reflection and transmission coefficients into mode $\nu = 4$ at the two critical magnetic fields $B \approx 9.2\,\mathrm{T}$ and $B \approx 2.6\,\mathrm{T}$. The magnon and phonon dispersions are shown schematically in the insets. For the critical field $B \approx 2.6\,\mathrm{T}$, at which the magnon dispersion touches that of the transverse phonons mode, the interface mixes magnon-like, longitudinal-phonon-like and transverse-phonon-like modes at the resonance frequency.

Spin current and spin Seebeck voltage.— The spin current j_x^{s} into the normal metal is calculated as the difference between the current of magnon polarons that excite a spin-1 excitation of the conduction electrons in the normal metal and the backflow of magnon polarons into the insulator that were excited by an incident spinful excitation of the conduction electrons (which are assumed to be at the same temperature as the phonons in N),

$$j_x^{\mathrm{s}} = \frac{\hbar}{V} \sum_{\mathbf{q}_+,\nu} v_{\mathbf{q},\nu x}(n_{\mathbf{q},\nu} - n_{\mathrm{N}}(\omega)) P_{\nu\mathrm{N}}(\omega,\mathbf{q}_\perp). \tag{3.83}$$

Substituting the linear-response form (3.41) of the distribution function and the simplified angular dependence, the spin current can be expressed in terms of the isotropic and anisotropic moments $\psi_{0,\nu}(\omega)$ and $\psi_{1,\nu}(\omega)$ of the distribution function,

$$j_x^{\mathrm{s}} = \int d\omega\, j_x^{\mathrm{s}}(\omega) \tag{3.84}$$

with

$$j_x^{\mathrm{s}}(\omega) = \hbar\omega \left(-\frac{\partial n^0}{\partial \omega}\right) \sum_{\nu} \sum_{n=0}^{1} \mathcal{P}_{n,\nu}(\omega)\psi_{n,\nu}(\omega) \tag{3.85}$$

where

$$\mathcal{P}_{n,\nu}(\omega) = \int \frac{d\mathbf{q}_\perp}{(2\pi)^3} P_{\mathrm{N}\nu}(\omega, \mathbf{q}_\perp) |v_{\nu,x}(\omega, \mathbf{q}_\perp, +)|^n. \tag{3.86}$$

The spin current at the interface is related to the spin Seebeck voltage in the normal metal via the inverse spin Hall effect [19] and equals, averaged over the width of the normal metal [41],

$$V_{\mathrm{sse}} = \theta_{\mathrm{sh}}\varrho\frac{2e}{\hbar}\lambda_{\mathrm{sf}}\frac{w}{l}\tanh\left(\frac{l}{2\lambda_{\mathrm{sf}}}\right) j_x^{\mathrm{s}}(L). \tag{3.87}$$

Here w, l, ϱ, θ_{sh}, and λ_{sf} are the width, length, electrical resistivity, the spin Hall angle, and the spin-flip diffusion length of the metal contact. Numerical values for these parameters of Pt can be found in Table 3.1.

3.4   Results

We use the theoretical formalism outlined in the previous two Sections to describe the steady-state longitudinal spin Seebeck effect of ferromagnetic insulator–normal metal structures. We consider the geometry of Fig. 3.1 and solve the linearized Boltzmann equation with the boundary conditions

$$\psi_{\mathrm{I}} = \Delta T/T, \quad \psi_{\mathrm{N}} = 0, \tag{3.88}$$

corresponding to a temperature difference ΔT applied across the magnetic insulator F. Numerical values for the material parameters are taken from Table 3.1.

The long-wavelength approximation is used throughout. We found that for the range of temperatures $T \lesssim 30$ K considered by us all frequency integrals converge for $\omega \sim 6\,c_{\mathrm{l}}q_{\mathrm{l}}^0$, where cq_{l}^0 is the frequency at which the magnon and longitudinal phonon dispersions cross at zero magnetic field, see Eq. (3.37). Comparing with realistic parameters for YIG, this corresponds to a convergence for wavenumbers $q \lesssim 1/a$, which a posteriori justifies the use of the long-wavelength approximation.

To evaluate the reflection and transmission probabilities at the IF and FN interfaces and the angular averages entering in the transition rates for the isotropic and anisotropic moments of the distribution function $\psi_{0,\nu}(\omega)$ and $\psi_{1,\nu}(\omega)$ we use a grid of 30×30 reference points for the polar angles (ϕ, θ) parameterizing the direction of $\mathbf{q}$. If necessary, reflection and transmission coefficients are interpolated linearly between grid points.

We first describe our results for the case of elastic impurity scattering only. We then discuss how these results are changed upon inclusion of inelastic scattering.

3.4.1 Elastic scattering only

Distribution functions.— After restriction of the distribution function to the simplified angular dependence with one isotropic moment $\psi_{0,\nu}(\omega)$ and one anisotropic moment $\psi_{1,\nu}(\omega)$, the steady-state Boltzmann equation reduces to a set of 2×4 coupled linear equations for these moments, see Eq. (3.70). For impurity scattering, different frequencies decouple, which makes an efficient solution of the equations possible. For convenience of notation, we here introduce a matrix notation in which $\psi_{0,\nu} \to \boldsymbol{\psi}_0$ and $\psi_{1,\nu} \to \boldsymbol{\psi}_1$ are four-component column vectors. Then the linearized Boltzmann equation (3.70) takes the simple form

$$\frac{\partial \boldsymbol{\psi}_1}{\partial x} = -\mathcal{G}_0 \boldsymbol{\psi}_0, \quad \frac{\partial \boldsymbol{\psi}_0}{\partial x} = -\mathcal{G}_1 \boldsymbol{\psi}_1, \tag{3.89}$$

where the 4×4 matrices $\mathcal{G}_0$ and $\mathcal{G}_1$ were defined in Eq. (3.71) (a delta function for frequencies is factored out and we switch notation from superscripts 0 and 1 to subscripts). The condition (3.72) ensures that the uniform isotropic solution $\psi_{0,\nu} = \psi$ and $\psi_{1,\nu} = 0$, with ψ an arbitrary function of ω, is a solution of the equations.

The matrix product $\mathcal{G}_1 \mathcal{G}_0$, which describes the relaxation towards local equilibrium, is non-negative. We diagonalize the matrix $\mathcal{G} = \sqrt{\mathcal{G}_1 \mathcal{G}_0}$ as

$$\mathcal{G} = \mathcal{U} \operatorname{diag}(0, \lambda_1^{-1}, \lambda_2^{-1}, \lambda_3^{-1}) \mathcal{U}^{-1}, \tag{3.90}$$

with $\mathcal{U}$ a 4×4 matrix, $\lambda_0 = 0$ and $0 < \lambda_1 < \lambda_2 < \lambda_3$. The three non-zero relaxation lengths λ_i, $i = 1, 2, 3$, are shown in Fig. 3.5 for the parameter values of Table 3.1 and the impurity scattering parameters of Table 3.3, center column. We also show the relaxation lengths l_{mi} and $l_{\mathrm{pi},\lambda}$ for the white-noise impurity model of Eqs. (3.60), for which the relaxation lengths have a weaker systematic dependence on the frequency ω.

The longest relaxation length λ_3, which is the length scale for full equilibration of all four magnon-polaron modes, is the impurity-mediated inter-mode scattering length for magnon polarons,

$$\lambda_{\mathrm{imp}}(\omega) = \lambda_3(\omega). \tag{3.91}$$

For generic frequencies, magnon-phonon hybridization is weak, so that impurity scattering has a very small inter-mode component. This explains why λ_{imp} is much larger than the mean free paths l_{mi} and l_{pi} for magnon-impurity and phonon-impurity scattering, see the dotted lines in Fig. 3.5. For the parameter values of Table 3.3, for which phonon-impurity scattering is stronger than magnon-impurity scattering, the two shorter relaxation lengths $\lambda_{1,2} \approx l_{\mathrm{pi}}$ describe the equilibration of the three phonon modes among each other. The frequency dependence of the relaxation lengths $\lambda_{1,2}$ reflects the frequency dependence of the phonon-impurity scattering.
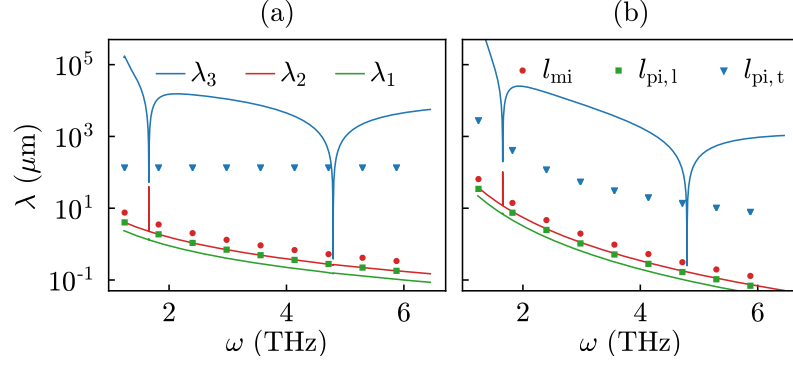
Figure 3.5: Relaxation lengths $\lambda_i(\omega)$, $i = 1, 2, 3$, of Eq. (3.90) for the material parameters given in Table 3.1 and impurity scattering parameters from Table 3.3 (center column) for the white-noise impurity model (3.60) with the mean free paths (3.61) (a) and for the microscopic model (3.52), (3.55) with mean free paths from Eqs. (3.57) and (3.58) (b). The dots indicate the magnon-impurity (blue) and phonon-impurity scattering lengths (green and red).

To obtain a formal solution of the coupled equations (3.89), we use $\mathbf{u}_i$ to denote the i-th column of $\mathcal{U}$. Condition (3.72) implies that we may set the first column $\mathbf{u}_0 = (1, 1, 1, 1)^{\mathrm{T}}$. The general solution of the isotropic distribution moment then reads

$$\boldsymbol{\psi}_0(x) = \sum_{i=0}^{3} \sum_{j=0}^{1} \beta_{ij}(x) c_{ij} \mathbf{u}_i, \tag{3.92}$$

where c_{ij} are constants that are determined by the boundary conditions, and

$$\beta_{i0}(x) = \begin{cases} x/L, & i = 0, \\ e^{(x-L)/\lambda_i}, & i = 1, 2, 3, \end{cases}$$

$$\beta_{i1}(x) = \begin{cases} 1 - x/L, & i = 0, \\ e^{-x/\lambda_i}, & i = 1, 2, 3. \end{cases} \tag{3.93}$$

The anisotropic moment is obtained via Eq. (3.89) by taking the matrix inverse,

$$\boldsymbol{\psi}_1 = -\mathcal{G}_1^{-1} \frac{\partial \boldsymbol{\psi}_0}{\partial x}. \tag{3.94}$$

In matrix notation, the boundary conditions (3.80) and (3.82) at the IF interface at $x = 0$ and the FN interface at $x = L$ read

$$\boldsymbol{\psi}_1(0) = \mathcal{S}_{\mathrm{I}}[\boldsymbol{\psi}_{\mathrm{I}} - \boldsymbol{\psi}_0(0)],$$
$$\boldsymbol{\psi}_1(L) = \mathcal{S}_{\mathrm{N}}[\boldsymbol{\psi}_0(L) - \boldsymbol{\psi}_{\mathrm{N}}], \tag{3.95}$$

where $\boldsymbol{\psi}_{\mathrm{I,N}} = \psi_{\mathrm{I,N}} \mathbf{u}_0$ are four-component vectors describing the equilibrium distributions in the reservoirs I and N, see Eq. (3.88). The matrices $\mathcal{S}_{\mathrm{I,N}}$ are defined

as

$$\mathcal{S}_{\mathrm{I,N}} = \frac{\mathcal{E}_1}{\mathcal{E}_2}(\mathbb{1}_4 + \mathcal{R}_{1\mathrm{I,N}})^{-1}(\mathbb{1}_4 - \mathcal{R}_{0\mathrm{I,N}}), \tag{3.96}$$

where the angle-averaged reflection coefficient matrices $\mathcal{R}_{0,\nu\nu'}$ and $\mathcal{R}_{1,\nu\nu'}$ are defined in Eq. (3.81).

These equations have a formal solution near the FN interface at $x = L$ if $L \gg \lambda_{\mathrm{imp}}$. The vicinity of the FN interface is what is relevant for the calculation of the spin Seebeck effect, see Eq. (3.85). Using the vector notation, one has

$$\boldsymbol{\psi}_0(x) = \frac{(L-x)\Delta T}{LT}\mathbf{u}_0 + e^{(x-L)\mathcal{G}}\boldsymbol{\psi}_0(L), \tag{3.97}$$
$$\boldsymbol{\psi}_1(x) = \frac{\Delta T}{LT}\mathcal{G}_1^{-1}\mathbf{u}_0 - \mathcal{G}_1^{-1}\mathcal{G}e^{(x-L)\mathcal{G}}\boldsymbol{\psi}_0(L),$$

where

$$\boldsymbol{\psi}_0(L) = \frac{\Delta T}{LT}(\mathcal{G} + \mathcal{G}_1 R_{\mathrm{N}})^{-1}\mathbf{u}_0. \tag{3.98}$$

A solution near the IF interface at $x = 0$ can be obtained in a similar way. If the condition $L \gg \lambda_{\mathrm{imp}}$ is not satisfied, the boundary conditions at the two interfaces at $x = 0$ and $x = L$ have to be implemented simultaneously, which is easily carried out numerically.

In Fig. 3.6 we show the frequency dependence of the isotropic moment $\psi_{0,\nu}(\omega)$ at the FN interface, *i.e.*, for $x = L$, as well as the spatial dependence of $\psi_{0,\nu}(\omega)$ for a generic frequency away from the crossing points of longitudinal phonon and magnon dispersions and at a crossing point. To keep the discussion simple, we have chosen the magnetic field $B = 7$ T. At this value of the magnetic field the dispersions of magnons and longitudinal phonons cross, but not of magnons and transverse phonons, see Fig. 3.2, so that there are only two "resonance frequencies" $\omega \approx 1.65\,\mathrm{THz}$ and $\omega \approx 4.8\,\mathrm{THz}$. To avoid artifacts from the strong frequency dependence of the impurity scattering lengths in the microscopic model, we use the white-noise model (3.60) for the impurity potential. We consider three system sizes L: a length L much larger than the impurity-mediated inter-mode scattering length λ_{imp} (top panels), an intermediate length L smaller than λ_{imp}, but still much larger than the individual elastic magnon and phonon mean free paths l_{mi} and l_{pi} (center panels), and a very short system size $L \ll \lambda_1 \approx l_{\mathrm{pi}}$, in which the only source of equilibration between magnon-like and phonon-like magnon-polaron modes is at the interfaces (bottom panels). In the intermediate regime the three phonon modes equilibrate among each other, but magnon-like and phonon-like modes remain out of equilibrium, except for the immediate vicinity of the resonance frequencies. The three system sizes considered are indicated by horizontal lines in Fig. 3.6(b) (reproduced from Fig. 3.5). Taking material parameters from Tables 3.1 and the
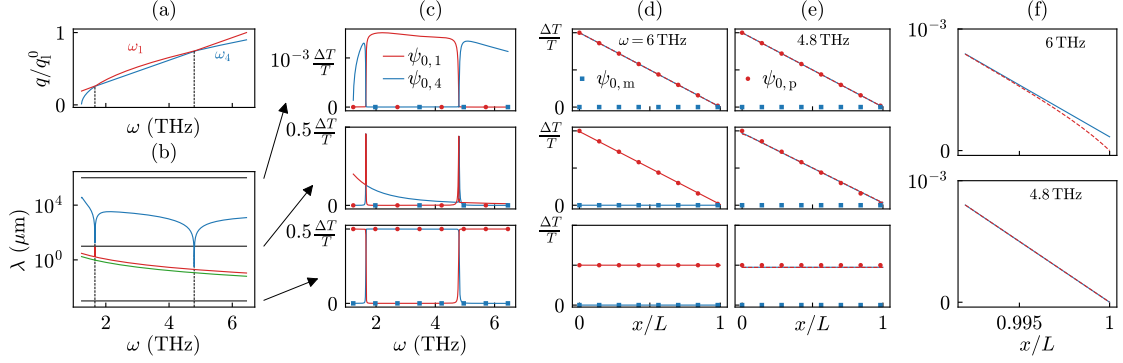
Figure 3.6:   Isotropic moment for impurity scattering only.   We take material parameters from Table 3.1 and set the magnetic field equal to $B = 7\,\mathrm{T}$, so that the magnon dispersion crosses that of the longitudinal phonons, but not the transverse phonons, see panel (a). To keep the presentation of the frequency dependence of the isotropic moment (3.44) as simple as possible we use white-noise impurity scattering rates (3.60) with potentials according to Table 3.3, center column. Panels (c)–(e) show the isotropic moment $\psi_0(\omega)$ of the distribution function for three choices of the system length L as compared to the relaxation lengths λ_i, as schematically indicated in (b). Panel (c) shows the frequency dependence of the isotropic moment $\psi_0(\omega)$ at the FN interface at $x = L$. Panels (d) and (e) show the dependence on position x for a generic frequency ($\omega = 6\,\mathrm{THz}$, panel (d)) and a frequency at the crossing point of the magnon and phonon dispersions ($\omega = 4.8\,\mathrm{THz}$, panel (e)). Panel (f) shows a close-up of the spatial dependences near the FN interface for the longest system length considered.

center column of 3.3, only the intermediate range of length scales l_{mi}, $l_{\mathrm{pi}} \lesssim L \lesssim \lambda_{\mathrm{imp}}$ is of experimental relevance.

We first discuss the isotropic moment $\psi_{0,\nu}(\omega)$ for the case without magnon-phonon coupling, shown by the dots in Fig. 3.6(c)–(e). Without magnon-phonon coupling, the isotropic moment $\psi_{0,\mathrm{m}}(\omega)$ of the magnon distribution is at the equilibrium value corresponding to the temperature of the conduction electrons in N. This is the case, because the magnons are coupled to the conduction electrons in N via the spin mixing conductance at the FN interface, see Sec. 3.3.4. In the top and center panels of Fig. 3.6 (c)–(e), which describe system lengths L large in comparison to the phonon-impurity mean free path l_{pi}, the distribution function $\psi_{0,\mathrm{p}}(\omega)$ of the phonon linearly interpolates between its values at the warm and cold reservoirs I and N and $x = 0$ and $x = L$. In the bottom panels, which are for a length $L \ll l_{\mathrm{pi}}$, the isotropic moment $\psi_{0,\mathrm{p}}(\omega)$ of phonon distribution is at a characteristic temperature $T + \Delta T/2$ precisely between the temperatures of the hot and cold reservoirs. A full discussion of the case of zero magnon-phonon coupling using our formalism can be found in App. B.6.

To interpret the curves in Fig. 3.6(c)–(e) that show the isotropic moment $\psi_{0,\nu}(\omega)$ in the presence of magnon-phonon coupling (solid curves), one should take into account that the label ν of the "magnon-like" magnon-polaron mode is "4" (blue curves) for frequencies ω between the crossing points at 1.65 THz and 4.8 THz, and "1" otherwise, see Fig. 3.6(a). The character of the magnon-polaron mode changes at the crossing points of the dispersion.

For the largest system size $L \gg \lambda_{\mathrm{imp}}$ (top panels in Fig. 3.6(c)–(e)), all magnon-polaron modes are in local equilibrium in the bulk of the sample, as shown in Fig. 3.6(d) and (e). At the FN interface, the magnon-like mode has a weakly elevated population, when compared to the temperature of the N reservoir, whereas the temperature of the phonon-like modes is very close to that of the N reservoir, as shown in detail in Fig. 3.6(f). This difference occurs, because magnon-like modes are mostly reflected at the FN interface, whereas the phonon-like modes are almost perfectly transmitted. At the resonance frequencies there is a sharp "dip" in the population of magnon-like magnon-polaron modes at the FN interface, reflecting the increased equilibration between different magnon-polaron modes at those frequencies. As a result, close to the resonance frequencies the thickness of the layer near the FN interface in which different magnon-polaron modes have different distribution functions is much thinner than for generic frequencies, see Fig. 3.6(f).

For the intermediate system size (center panels in Fig. 3.6(c)–(e)), the magnon-like magnon-polaron modes are no longer in equilibrium with the phonon modes for generic frequencies ω and, hence, have an occupation consistent with that of the cold reservoir N, to which they are coupled via the spin mixing conductance. For frequencies in the close vicinity of the crossing points, they still equilibrate with the phonons, and their occupation is essentially the same as in the case $L \gg \lambda_{\mathrm{imp}}$ discussed above.

At the shortest system length $L \ll \lambda_1 \approx l_{\mathrm{pi}}$, the isotropic moments are constants as a function of position. From the boundary conditions (3.95) at the IF and FN interfaces one finds

$$\boldsymbol{\psi}_0 = (\mathcal{S}_{\mathrm{I}} + \mathcal{S}_{\mathrm{N}})^{-1}(\mathcal{S}_{\mathrm{I}}\boldsymbol{\psi}_{\mathrm{I}} + \mathcal{S}_{\mathrm{N}}\boldsymbol{\psi}_{\mathrm{N}}). \tag{3.99}$$

At generic frequencies, magnon-like modes have an occupation corresponding to the temperature of the cold reservoir, whereas the isotropic moment of the distribution of phonon-like modes corresponds to a temperature $T + \Delta T/2$ precisely intermediate between the temperatures of cold and warm reservoirs. For frequencies close to the crossing points, reflection at the IF and FN interfaces still leads to an equilibration of magnons and phonons. Since the magnon-like modes are coupled to the cold reservoir, but not to the warm reservoir, the occupation corresponds to a temperature slightly below $\Delta T/2$, see Fig. 3.6(e).

Spin current. — Results for the spin current are shown in Fig. 3.7, using the white-noise model (3.60) with parameter values from the center column of Table 3.3 for the

impurity scattering rates. The relaxation lengths $\lambda_i(\omega)$ for this set of parameters are shown in Fig. 3.5(a). Figure 3.7 shows the frequency-resolved spin current $j_x^s(\omega)$ for system lengths $L = 0.1\,\mu\text{m}$, $L = 0.5\,\text{mm}$, $L = 10\,\text{mm}$, and $L = 1\,\text{m}$. At the shortest length $L = 0.1\,\mu\text{m}$, magnon and phonon dynamics are ballistic and no equilibration between magnon-like and phonon-like magnon-polaron modes takes place, except in the immediate vicinity of the resonance frequencies. Consequentially, the frequency-resolved spin current differs appreciably from zero only near these frequencies. At the intermediate sample length $L = 0.5\,\text{mm}$ magnon and phonon transport is diffusive, whereas for generic frequencies the sample size is still larger than λ_{imp}. Here, the spin current is still carried at frequencies close to the crossing points, although the frequency-resolved spin current shows a narrow dip precisely at the crossing point because the strong mixing of magnons and phonons, combined with the large transparency of the FN interface for phonons, suppresses an accumulation of magnon polarons at the FN interface at that frequency. To illustrate what happens upon further increasing the system length L, Fig. 3.7 also shows the case $L = 10\,\text{mm}$ and the unrealistically large length $L = 1\,\text{m}$, at which all frequencies contribute to the spin current, except for narrow dips at the frequencies at which magnon and phonon dispersions cross. Figure 3.7 also contains a comparison with the asymptotic large-L result (3.97), showing that the comparison becomes quantitatively accurate only for lengths L far outside the experimentally relevant range.

Magnon and phonon dynamics are ballistic for the shortest system length considered in Fig. 3.7, $L \ll \lambda_1 \approx l_{\text{pi}}$. With ballistic dynamics, the validity of the parameterization (3.45) breaks down. To estimate the error, in App. B.7 we compare the spin current obtained using the parameterization (3.45) with an exact calculation for the ballistic short-L limit.

Spin Seebeck coefficient. — The spin Seebeck voltage V_{SSE} and the spin Seebeck coefficient

$$S = \frac{V_{\text{sse}}}{\Delta T} \tag{3.100}$$

can be obtained from Eq. (3.87). Figure 3.8 shows the spin Seebeck coefficient S as a function of the applied magnetic field B. We use the microscopic model of Eqs. (3.52) and (3.55), with parameter values taken from Table 3.3 (center column), to describe magnon-impurity and phonon-impurity scattering. The spin Seebeck coefficient shows sharp features near the critical magnetic fields at which the magnon and phonon dispersions touch, reflecting the drastic enhancement of the frequency window of strong magnon-phonon coupling at those magnetic fields. For short and intermediate lengths $L \lesssim \lambda_{\text{imp}}$, the magnitude of the spin Seebeck effect, including the singular features at the critical magnetic field, increases with the temperature, see Fig. 3.8(a). The spin Seebeck coefficient and the singular features at the critical magnetic fields depend non-monotonically on the length L or the impurity concentration, as shown in Fig. 3.8(b). Whereas S shows peaks at the critical magnetic fields if the system size is $\lesssim \lambda_{\text{imp}}$, the spin Seebeck coefficient exhibits a dip at the
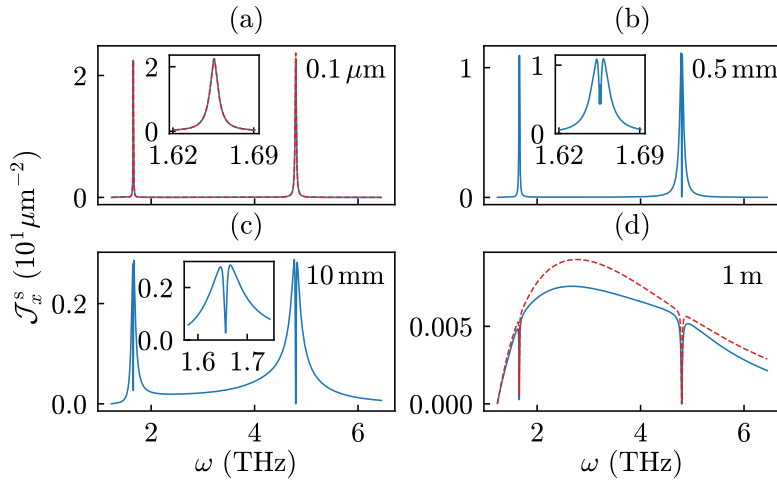
Figure 3.7: Frequency-resolved spin current $j_x^s(\omega) = \hbar \mathcal{J}_x^s(\omega) \Delta T / T$ at $T = 10\,\mathrm{K}$ at the FN interface (blue, solid) for $B = 7\,\mathrm{T}$ at sample length $L = 0.1\,\mu\mathrm{m}$ (a), $L = 0.5\,\mathrm{mm}$ (b), $L = 10\,\mathrm{mm}$ (c), and $L = 1\,\mathrm{m}$ (d). System parameters are taken from Table 3.1. Impurity scattering of magnon and phonons is described by the white-noise model (3.60), with parameter values taken from the center column of Table 3.3. For comparison, panels (a) and (d) also show the frequency-resolved spin current calculated from the short-length approximation of Eq. (3.99) and the long-length approximation (3.97), respectively (red, dashed).

critical magnetic fields if $L \gtrsim \lambda_{\mathrm{imp}}$. This dip originates from the narrow dip in the frequency-resolved spin current for frequencies close to the resonance frequencies, see Fig. 3.7, and reflects the increase of the resonant frequency range at the critical magnetic fields. The non-monotonous length dependence of the spin Seebeck coefficient is also shown in panel (c). For short lengths, the spin Seebeck coefficient is small, because magnons are excited only in a very narrow frequency window around the resonance frequencies. Upon increasing L, the width of this frequency window is increased, which is what leads to an increase of S with L. The spin Seebeck coefficient reaches a maximum as a function of L, when all frequencies contribute to the spin current. A further increasing of L leads to a suppression of S because of the increase of the thermal resistance with L. The maximum occurs at smaller lengths (but higher spin Seebeck coefficient) for magnetic fields close to the critical field, because there the widths of the peaks of the frequency-resolved spin current at the resonant frequency is largest.

Figure 3.8 also addresses the dependence of the spin Seebeck coefficient on the spin mixing conductivity $\sigma_{\uparrow\downarrow}$ and on the strength of the magnon-phonon coupling. A decrease of the spin mixing conductivity — a lower transparency of the FN interface — leads to a smaller spin Seebeck voltage and less pronounced features as a function of magnetic field, see Fig. 3.8(d) and (e) for a system short and long in comparison to
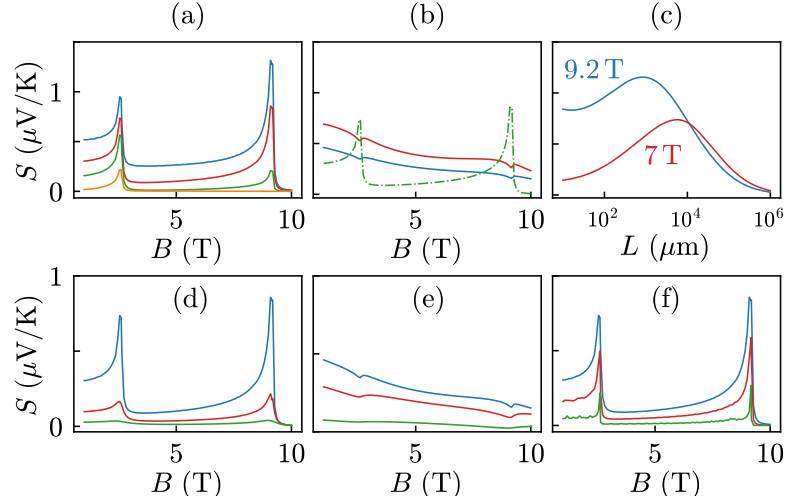
Figure 3.8: Spin Seebeck coefficient for elastic scattering only. Material parameters are taken from Table 3.1 and impurity scattering of magnon and phonons is described by the microscopic model of Eqs. (3.52) and (3.55) with parameter values taken from the center column of Table 3.3, unless noted otherwise. Panel (a) shows the spin Seebeck coefficient at $L = 10\,\mu$m for temperatures $T = 2\,$K, $5\,$K, $10\,$K, and $20\,$K (bottom to top). Panel (b) shows the spin Seebeck coefficient for $T = 10\,$K at different system lengths $L = 10\,\mu$m (green), $5\,$cm (red), and $10\,$cm (blue). Panel (c) shows S for $B = 7\,$T and $B = 9.2\,$T as a function of the system length L. Panels (d) and (e), which are evaluated at $T = 10\,$K and at $L = 10\,\mu$m and $L = 1\,$cm, respectively, show the spin Seebeck coefficient S vs. magnetic field B for spin mixing conductivity $\sigma_{\uparrow\downarrow}$ equal to 1, 10^{-1}, and 10^{-2} times the value listed in Table 3.1, from top to bottom, respectively. Panel (f) shows the spin Seebeck coefficient for $L = 10\,\mu$m, $T = 10\,$K, and magnon-phonon coupling parameters D and D' a factor 1, 0.5, and 0.1 times the values listed in Table 3.1, from top to bottom.

λ_{imp}, respectively. A decrease of the magnon-phonon coupling below the value listed in Table 3.1 leads to a smaller spin Seebeck coefficient only if the system is short enough, see Fig. 3.8(f). If $L \gg \lambda_{\mathrm{imp}}$, a decrease of the magnon-phonon coupling has no significant effect on the spin Seebeck coefficient (data not shown).

Relative strength of magnon-impurity and phonon-impurity scattering.— The numerical values used for Figs. 3.6–3.8 have a magnon-impurity scattering length that is a factor ~ 10–100 larger than the phonon-impurity length. For comparison, Fig. 3.9 shows the relaxation lengths λ_i, the distribution function at the FN interface, the frequency-resolved spin current, and the spin Seebeck coefficient for a system that is of higher acoustic quality than of magnetic quality. The parameters for the impurity model are such that the orders of magnitude of the corresponding scattering rates are interchanged (see Table 3.3, right column). This interchange leads to a significant increase in the two smallest relaxation lengths $\lambda_{1,2} \approx l_{\mathrm{pi}}$,
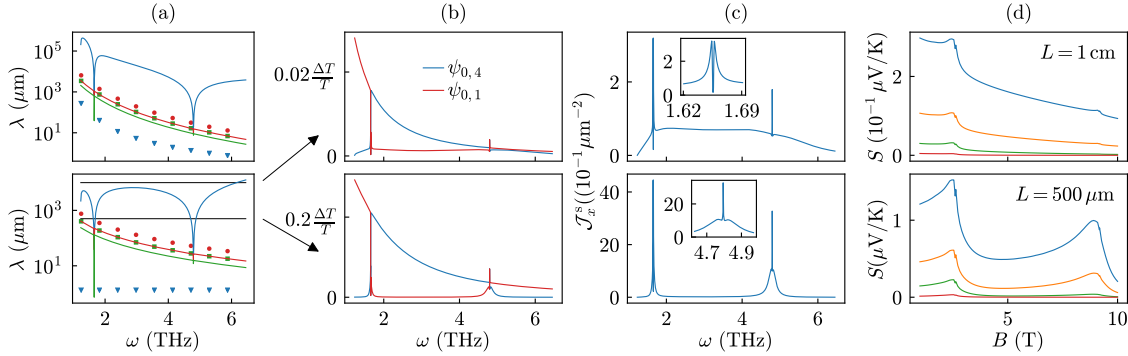
Figure 3.9: Relaxation lengths (a), isotropic distribution function $\psi_0(\omega)$ at the FN interface (b), frequency-resolved spin current $j_x^s(\omega) = \hbar \mathcal{J}_x^s(\omega)\Delta T/T$ at $T = 10$ (c), and spin Seebeck coefficient S vs. magnetic field B (d) for a system in which magnon-impurity scattering is stronger than phonon-impurity scattering. Material parameters are taken from Table 3.1. Impurity scattering is described by the microscopic model of Eqs. (3.52) and (3.55) (a, top panel, and d) and the white-noise model of Eq. (3.60) (a, bottom panel, and b, c) with parameters taken from the right column in Table 3.3. Dots in panel (a) indicate the magnon-impurity mean free path (blue) and the phonon-impurity mean free paths (green and red) in the absence of magnon-phonon coupling. The system length L for panels (b)–(d) is indicated by the horizontal lines in panel (a). The spin Seebeck coefficient in panel (d) is evaluated for temperatures $T = 2\,\mathrm{K}$, $5\,\mathrm{K}$, $10\,\mathrm{K}$, and $20\,\mathrm{K}$ (bottom to top).

which describe the relaxation between the three phonon-like polaron modes, but hardly affects the longest relaxation length $\lambda_3 = \lambda_{\mathrm{imp}}$, which describes the impurity-mediated inter-mode scattering of magnon polarons. For short system lengths $L \lesssim \lambda_{\mathrm{imp}}$ (but L larger than the phonon and magnon mean free paths l_{pi} and l_{mi}), the distribution function at the FN interface has the same singular frequency dependence near the resonant frequencies as in the phonon-impurity-dominated case discussed above. As a result, the frequency-resolved spin current $j_x^s(\omega)$ is strongly peaked near the resonance frequencies, and the spin Seebeck coefficient S has a peak at the "critical" values of the magnetic field for which the magnon and phonon dispersions are tangential to each other. For large lengths $L \gtrsim \lambda_{\mathrm{imp}}$, the frequency-resolved spin current shows sharp peaks at the resonant frequencies (as opposed to sharp dips in the case of stronger phonon-impurity scattering). Correspondingly, the spin Seebeck coefficient continues to exhibit peaks as a function of B for the critical magnetic fields in the limit of large sample length L.

3.4.2 With inelastic scattering

For temperatures $T \lesssim 30\,\mathrm{K}$, inelastic relaxation lengths remain well above the mean free paths l_{mi} and l_{pi} for magnon-impurity and phonon-impurity scattering for all frequencies of interest. In the vicinity of the resonance frequencies, the impurity-mediated inter-mode scattering length λ_{imp} is comparable to the mean free path for impurity scattering. Hence, near the resonance frequencies impurity-mediated inter-mode scattering remains the dominant scattering mechanism coupling phonon and magnon degrees of freedom. For generic frequencies, however, depending on the temperature and the magnetic field, λ_{imp} may well be larger than the inelastic relaxation length. If this is the case, the inclusion of inelastic scattering may lead to a modification of the elastic-scattering-only results that were derived in the previous Subsection, as we now discuss.

To describe inelastic processes in the Boltzmann equation (3.70), the collision integrals (3.64) and (3.67) are included in the transition matrices $\mathcal{G}_0(\omega, \omega')$ and $\mathcal{G}_1(\omega, \omega')$. Whereas these transition matrices were proportional to $\delta(\omega - \omega')$ for the elastic-scattering-only case, they acquire contributions off-diagonal in frequency if inelastic processes are included. Apart from this, the general structure of the Boltzmann equations for the isotropic and anisotropic moments (3.70) stays untouched.

The transition matrix $\mathcal{G}_0(\omega, \omega')$ governs the relaxation of the isotropic moment $\psi_0(\omega)$. Without inelastic scattering, $\mathcal{G}_0(\omega, \omega') = \mathcal{G}_0(\omega)\delta(\omega - \omega')$. As discussed in the previous Subsection, the 4×4 matrix $\mathcal{G}_0$ has three nonzero eigenvalues and one zero eigenvalue. The smallest nonzero eigenvalue is typically several orders of magnitude smaller than the two larger eigenvalues, because it contains the magnon-phonon coupling. (Without magnon-phonon coupling, $\mathcal{G}_0$ has two zero eigenvalues, see App. B.6.) Inclusion of inelastic processes is a significant perturbation to $\mathcal{G}_0$, because their strength has to be compared to the two smallest eigenvalues of $\mathcal{G}_0$. In contrast, for the elastic-scattering-only case the transition matrix $\mathcal{G}_1(\omega, \omega') = \mathcal{G}_1(\omega)\delta(\omega - \omega')$ has four nonzero eigenvalues at each frequency, of the order of the rates τ_{pi} and τ_{mi} for phonon-impurity and magnon-impurity scattering length, see App. B.6. For $T \lesssim 30\,\mathrm{K}$, these are much larger than the inverse inelastic scattering lengths, so that inelastic processes do not significantly affect $\mathcal{G}_1$. Motivated by these observations, we calculate $\mathcal{G}_1(\omega, \omega')$ without inclusion of inelastic processes, whereas to simplify the calculation of $\mathcal{G}_0(\omega, \omega')$ we replace the microscopic models for the various sources of inelastic scattering, see Sec. 3.3.3 and App. B.5, by an effective model in which the matrix elements depend on the frequencies of the magnon and phonon modes involved, but not on the polarization and (directions of the) wavevectors. The magnitude of the matrix elements in the effective models is chosen such that the angle average is the same as in the original microscopic model, so that the inelastic contribution to $\mathcal{G}_0(\omega, \omega')$ is still exact without the elastic magnon-phonon coupling. We keep the full wavevector dependence of the transformation matrix $V_{\mathbf{q}}$ between
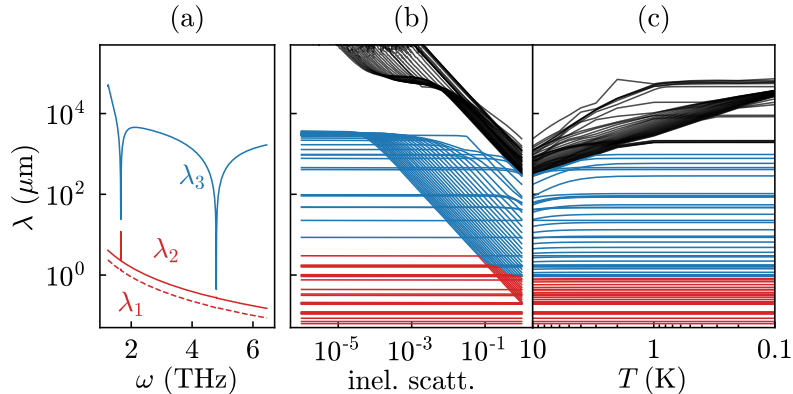
Figure 3.10: (a) Frequency-dependent relaxation lengths $\lambda_i(\omega)$, $i = 1, 2, 3$, for the case of elastic scattering only. (b) and (c) Relaxation lengths λ_j, $j = 1, \ldots, 4(N + 1) - 1$ in the presence of inelastic scattering, calculated for a frequency grid with $N = 200$ frequencies. For clarity, only every 20th relaxation length is shown. In (b) the relaxation lengths are shown vs. the strength of the inelastic scattering processes, normalized to the inelastic processes at $10\,\mathrm{K}$. In (c) the relaxation lengths are shown vs. temperature. The black curves represent those relaxation lengths that are divergent in absence of inelastic scattering.

magnon and phonon modes and magnon-polaron modes.

Once inelastic processes are included, the Boltzmann equation for the isotropic and anisotropic moments (3.70) couples distribution functions at different frequencies. To solve these resulting integro-differential equations, we choose a frequency grid with $(N + 1)$ frequencies ω_n with $0 \equiv \omega_0 < \omega_1 < \cdots < \omega_N$ and approximate the distribution functions $\psi_{0,\nu}(\omega_n)$ and $\psi_{1,\nu}(\omega_n)$ by linear interpolation between the grid frequencies. The density of reference frequencies is chosen to be high in regions in which $\psi_{0,\nu}(\omega_n)$ and $\psi_{1,\nu}(\omega_n)$ are strongly frequency dependent, such as in the vicinity of the crossing points of magnon and phonon branches. Frequency integrals over a function $f(\omega)$ can be discretized by a trapezoidal rule,

$$\int d\omega\, f(\omega) \to \sum_{n=1}^{N} [f(\omega_n) + f(\omega_{n-1})] \frac{\omega_n - \omega_{n-1}}{2}. \tag{3.101}$$

The resulting discretized equations then have the same structure as the equations for elastic scattering (3.89) — but with matrices $\mathcal{G}_0$ and $\mathcal{G}_1$ of dimension $4(N + 1)$ instead of 4 — and they can be efficiently solved with the same methods as discussed in the previous Subsection. The boundary conditions at the IF and FN interfaces do not mix frequencies and can be implemented in the same way as for the elastic-scattering-only case, see Eq. (3.95).

The eigenvalues of the matrix $\mathcal{G}^2 = \mathcal{G}_1 \mathcal{G}_0$, which are the inverse square relaxation

87

lengths λ_j^{-2}, compare with Eq. (3.90), again play an important role in the construction of the solution of the Boltzmann equation, which is given by Eqs. (3.92)–(3.94), with the summations over i and j running from 0 to $4(N+1)-1$ instead of 0 to 3. In contrast to elastic impurity scattering, which relaxes only differences between polaron branches ν at the same frequency, the matrix condition (3.72) for inelastic three and four-polaron interaction ensures that only the globally uniform solution $\psi_{0,\nu}(\omega) = \psi$, $\psi_{1,\nu}(\omega) = 0$ is an equilibrium solution. As a consequence the matrix $\mathcal{G}$ has only one zero eigenvalue. The nonzero eigenvalues give the inverse relaxation lengths. As an illustration, Fig. 3.10 shows the relaxation lengths λ_j, $j = 1, \ldots, 4(N+1)-1$ for the case of material parameters listed in Table 3.1 as a function of the inelastic scattering strength. Panel (b) shows how the relaxation lengths at temperature $10\,\mathrm{K}$ are connected with the frequency-dependent equilibration lengths for the case without inelastic processes if one smoothly "switches on" the inelastic processes; panel (c) shows the relaxation length as a function of temperature T. Without inelastic scattering, one of the four inverse square relaxation lengths λ_j^{-2} for each frequency ω_n is zero, $n = 0, \ldots, N$, so that there are $N+1$ divergent relaxation lengths in that limit. Upon switching on inelastic scattering, all but one of these relaxation lengths become finite (black curves in Fig. 3.10b).

The dominant inelastic processes are inelastic magnon-magnon and phonon-phonon scattering and exchange-based magnon-phonon scattering. Their main effect is to equilibrate the distributions of magnon-like and phonon-like magnon polarons between different frequencies. Except in the vicinity of the resonance frequencies, the exchange-based magnon-phonon interaction allows for the exchange of energy between the lattice and spin subsystems, but it cannot change the number of magnons. In the same way, at generic frequencies the phonon-phonon and magnon-magnon interactions cannot exchange energy between the subsystems, although the three-magnon interaction can change the number of magnons. The relativistic and dipole-dipole contributions to the inelastic magnon-phonon interaction, which can exchange energy between subsystems and change the magnon number, are weaker than the impurity-mediated inter-mode scattering processes for $T \lesssim 30\,\mathrm{K}$, see Fig. 3.3, so that these do not play a role in the spin Seebeck effect. We verified that all results shown in this Section are the same with or without inclusion of the relativistic and dipole-dipole contributions to the inelastic magnon-phonon interaction (data not shown).

Distribution functions and frequency-resolved spin current.— For system lengths L below the shortest inelastic length, an effect of inelastic processes on the distribution functions is trivially absent and the elastic-scattering-only theory of the previous Subsection applies. Taking the parameters listed in Tables 3.1 and 3.3, for $T \lesssim 30\,\mathrm{K}$ this includes the experimentally relevant range $L \sim 10\,\mu\mathrm{m}$. To illustrate the effect of inelastic processes on the distribution functions, in Fig. 3.11 we show the distribution function $\psi_0(\omega)$ at the FN interface and the frequency-resolved spin
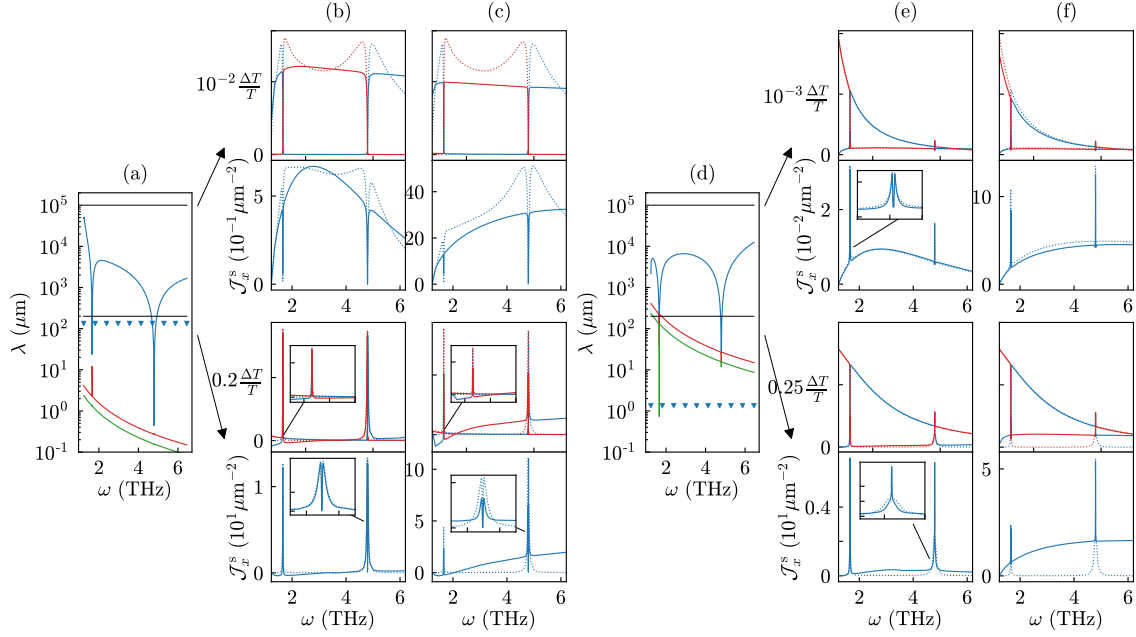
Figure 3.11: Relaxation lengths (a), (d) as in Fig. 3.5 with material parameters taken from Table 3.1. Frequency-resolved isotropic moment $\psi_0(\omega)$ and frequency-resolved spin currents $j_x^s(\omega) = \hbar \mathcal{J}_x^s(\omega) \Delta T / T$ at the FN interface for $T = 10\,\text{K}$ (b), (e) and $T = 30\,\text{K}$ (c), (f) together with the values obtained from a theory with elastic scattering only (dotted lines). Impurity scattering is modeled by the white-noise model (3.60) with parameters taken from the center column (panels (a)–(c)) and rightmost column (panels (d)–(e)) in Table 3.3, corresponding to the cases of higher magnetic and acoustic quality, respectively.

current for two larger system sizes $L = 200\,\mu\text{m}$ and $L = 100\,\text{mm}$.

The smaller system length $L = 200\,\mu\text{m}$ is below the impurity-mediated inter-mode scattering length λ_{imp}, so that $\psi_0(\omega)$ is sharply peaked at the resonance frequencies in the absence of inelastic processes. In this case, the main effect of inelastic processes is to change the occupation of magnon-like modes at generic frequencies, which, for $L = 200\,\mu\text{m}$, outweighs the effect of impurity-mediated processes for temperatures $T \gtrsim 10\,\text{K}$. At the same time the weight of the peaks at the resonance frequencies is decreased upon inclusion of inelastic processes. The exchange-based magnon-phonon interaction transfers energy from the phonon system into the magnon system without changing the magnon number. This leads to a population shift of the magnon-like modes from low to high frequencies, which can be seen in Fig. 3.11(b). Although via this mechanism inelastic processes can cause a small decrease of the frequency-resolved spin current $j_x^{\text{s}}(\omega)$ for low frequencies, for system lengths $L \lesssim \lambda_{\text{imp}}$ their over-all effect after integration over all frequencies is to *increase* the spin current above the value previously evaluated for elastic scattering. This increase may be quite substantial at the highest temperatures we consider (panel (c) in Fig. 3.11).

The larger system length $L = 100\,\text{mm}$ is well above λ_{imp}. In this case impurity-mediated inter-mode scattering processes already fully equilibrate phonon-like and magnon-like modes at all frequencies. Inclusion of inelastic processes leads to a quantitative, but not to a qualitative change of the distribution functions compared to the elastic-scattering-only case. For this large system length, inclusion of inelastic processes leads to a small *decrease* of the spin current. These conclusions apply to the impurity scattering parameters taken from Table 3.3 (Fig. 3.11(a)–(c)), for which the phonon-impurity length l_{pi} is much shorter than the magnon-impurity length l_{mi}, as well as to the case in which the strengths of phonon-impurity and magnon-impurity scattering are interchanged such that $l_{\text{pi}} \gg l_{\text{mi}}$ (Fig. 3.11d–f).

Spin Seebeck coefficient.— The spin Seebeck coefficient in the presence of inelastic scattering is shown in Fig. 3.12. As can be anticipated from the above results, inclusion of inelastic scattering leads to a small decrease of the spin Seebeck coefficient for ultralong system lengths $L \gg \lambda_{\text{imp}}$ (panel (a), $L = 100\,\text{mm}$) and to an increase of the spin Seebeck coefficient for $L = 200\,\mu\text{m}$, which is below λ_{imp}, provided the temperature is sufficiently high that inelastic processes become relevant at this system length. In both cases, inelastic processes reduce the visibility of the singular features at the critical values of the magnetic field. Because of the strong enhancement of the spin Seebeck coefficient for lengths $L \lesssim \lambda_{\text{imp}}$, the non-monotonicity of the length dependence of S is more pronounced with inelastic processes than without, see Fig. 3.12(c).

In our previous work [41], as well as in Ref. [20], inelastic magnon-magnon and phonon-phonon collisions were only accounted for indirectly as a "background interaction" that ensures the fast relaxation of the magnon and phonon distributions
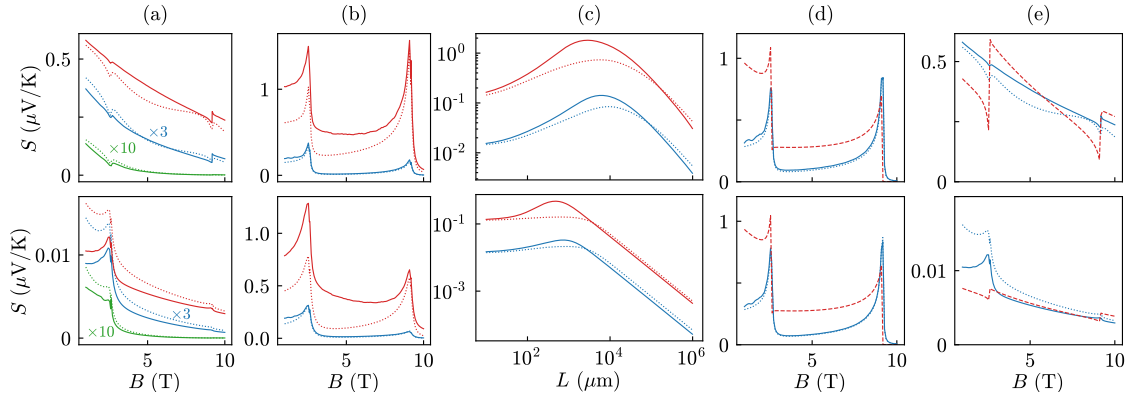
Figure 3.12: Spin Seebeck coefficient S for systems of higher magnetic quality (upper panels) and higher acoustic quality (lower panels), as a function of magnetic field for $L = 10\,\text{cm}$ and temperatures $T = 2\,\text{K}$, $5\,\text{K}$, and $10\,\text{K}$ from bottom to top (a) and for $L = 200\,\mu\text{m}$ and $T = 5\,\text{K}$ and $10\,\text{K}$ from bottom to top (b). Panel (c) shows S as a function of length $T = 10\,\text{K}$ (red) and $T = 5\,\text{K}$ (blue). Panels (d) and (e) show a comparison to the incoherent theory of Ref. [41] (red, dashed) for $L = 10\,\mu\text{m}$ (d) and $L = 10\,\text{cm}$ (e) and $T = 10\,\text{K}$. In all panels solid curves show results of the full theory, including inelastic scattering, whereas dotted curves include elastic scattering only. Material parameters are taken from Table 3.1. Impurity scattering of magnons and phonons is described by the microscopic model of Eqs. (3.52) and (3.55), with parameter values taken from Table 3.3.

(in Ref. [41]) or magnon-polaron distributions (in Ref. [20]) towards Planck and Bose-Einstein distributions, respectively, characterized by a temperature and chemical potential. In Fig. 3.12(d) and (e) we compare the predictions of the present theory with that of the Boltzmann theory of Ref. [41]. For an experimentally relevant system length $L = 10\,\mu\text{m}$, which is well below the inelastic scattering lengths at $T \lesssim 30\,\text{K}$, the two theories nevertheless give very similar predictions for the magnetic-field dependence of the spin Seebeck coefficient, see Fig. 3.12(d). This is remarkable, because the two theories have vastly different predictions for the frequency-resolved spin current. That the agreement is not always as good can be seen from Fig. 3.12(f), which compares the two theories for a much larger system length, showing that while both theories predict the same order of magnitude for the spin Seebeck coefficient, the singular features at the critical magnetic field are qualitatively different.

Anatomy of the spin Seebeck effect.— Given the multitude of physical processes contributing to the spin Seebeck effect, it is instructive to determine, which process or which combination of processes is responsible for the observed spin current. This is addressed in Fig. 3.13, in which we compare the spin currents at $L = 200\,\mu\text{m}$ (*i.e.*, for a length below λ_{imp}, but much larger than the length $L \approx 10\,\mu\text{m}$ relevant for ex-
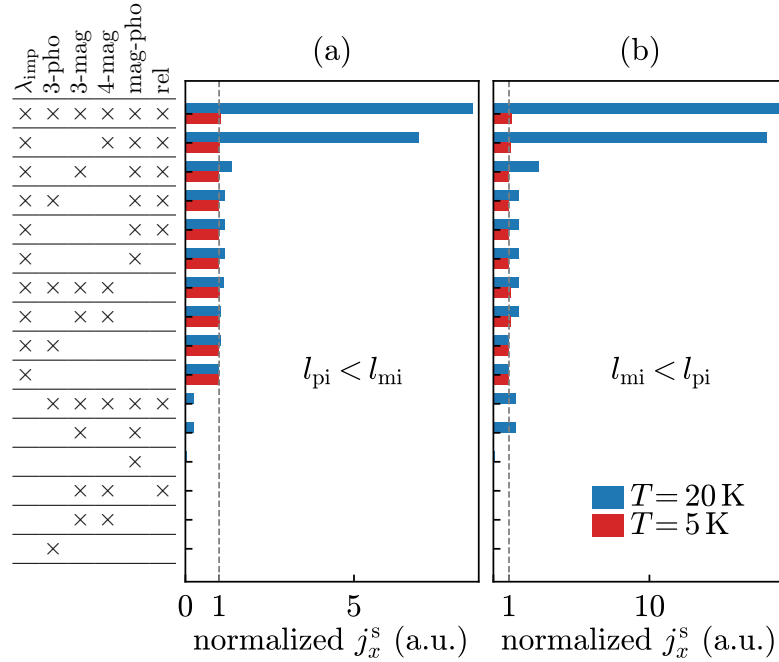
Figure 3.13:   Spin current j_x^s, normalized to the spin current for elastic scattering only at $T = 5\,\mathrm{K}$ and $T = 20\,\mathrm{K}$, $L = 200\,\mu\mathrm{m}$, and $B = 7\,\mathrm{T}$, with or without physical processes as indicated on the left. The physical processes are: Impurity-mediated inter-mode scattering (λ_{imp}), inelastic three-phonon scattering (3-pho), inelastic three-magnon scattering (3-mag), inelastic four-magnon scattering (4-mag), inelastic exchange-based magnon-phonon scattering (mag-pho), and relativistic/dipole-based inelastic magnon-phonon scattering (rel). Phonon-impurity and magnon-impurity scattering are included in all cases, using the microscopic model of Eqs. (3.52) and (3.55) with values taken from the center and right column of Table 3.3 (panels (a) and (b), respectively).

periments) at $T = 5\,\mathrm{K}$ and $T = 20\,\mathrm{K}$ with each of the contributing physical processes switched on or off. While we see that at the lowest temperatures impurity-mediated inter-mode scattering is the dominant cause of the spin Seebeck effect, at $T = 20\,\mathrm{K}$ it is the combination of impurity-mediated inter-mode scattering, exchange-based magnon-phonon scattering, and inelastic four-magnon scattering. Removing each one of these processes leads to a decrease of the spin Seebeck coefficient by an order of magnitude.

At the experimentally relevant length $L = 10\,\mu\mathrm{m}$, impurity-mediated inter-mode scattering is the sole cause of the spin Seebeck effect at all temperatures we considered (T up to $30\,\mathrm{K}$) (data not shown).

3.5 Summary

In this Chapter, we constructed a Boltzmann theory of the spin Seebeck effect at low temperatures. Our theory treats quadratic terms in the magnon-phonon Hamiltonian exactly, including terms that couple spin and lattice degrees of freedom. Such terms lead to the formation of magnon polarons, coherent superpositions of collective excitations of the spin and lattice subsystems [120, 121, 122]. Elastic scattering from impurities and inelastic relaxation processes are included via a collision integral. To accommodate the strong frequency dependence of the degree of magnon-phonon mixing, which predominantly takes place near the resonant frequencies at which the magnon and phonon dispersions cross, we keep the full frequency dependence of the distribution function at all stages of the calculation. In this respect, our calculation goes beyond previous theories of the spin Seebeck effect, which approximate the magnon and phonon distribution functions using a Planck-type or Bose-Einstein-type ansatz [15, 20, 10, 127, 41, 128, 145, 31]. Our theory treats the boundary between the magnetic insulator and the normal metal (into which the spin current is emitted) non-perturbatively, which allows us to treat bulk effects and the accumulation of magnon polarons at the interface to the normal metal on equal footing.

The magnon-polaron dispersion and the collision integrals are obtained from a simplified microscopic model of a ferromagnetic insulator. This model consists of spins placed on a simple cubic lattice, with isotropic Heisenberg exchange interaction and Zeeman coupling to an external magnetic field, a harmonic lattice potential, and a pseudo-dipolar anisotropic exchange interaction that couples the spin and lattice sub-systems. Although the model is highly simplified in comparison to the complexity of the synthetic ferrimagnetic insulator Yttrium Iron Garnet $Y_3Fe_5O_{12}$ (YIG) used in most experiments, having a true model at hand offers the possibility to have a faithful description of dependences on external parameters, such as the magnetic field or the temperature. This is an essential requirement for a description of the singular magnetic-field dependent features of the spin Seebeck coefficient observed at the critical magnetic fields at which magnon and phonon dispersions touch [15]. The characteristic momentum dependence of matrix elements of the magnon-phonon coupling from the anisotropic pseudodipolar interaction also sheds light on the relative importance of relativistic processes as a function of temperature.

The use of collision integrals obtained from a microscopic model (with parameters adjusted to reproduce known properties of YIG) has the advantage that no phenomenological relaxation terms are needed, such as a stochastic magnetic field [19, 32, 34, 146] or a relaxation-approximation-type exponential relaxation to the equilibrium form [35, 20]. This is important, because the use of such phenomenological relaxation terms may violate conservation laws that apply to the underlying microscopic processes. To see that such conservation laws can be a true barrier for

an efficient coupling between the lattice and spin systems, we note that only the weakest of all elastic and inelastic interactions of the spin and lattice system, the relativistic and dipole-dipole-based conversion of a phonon into a pair of magnons or vice versa, is by itself capable of sustaining a spin Seebeck effect with contributions from all frequencies. Taken separately, none of the other (stronger) interactions, such as the exchange-based magnon-phonon coupling (which conserves spin), elastic impurity scattering (which conserves energy), or inelastic three-magnon scattering (which does not couple to the lattice subsystem) can fully equilibrate lattice and spin subsystems. It is the interplay of these elastic and inelastic processes that eventually allows lattice excitations to create an excitation of the spin system that carries a steady-state spin current. A simple microscopic modeling that obeys the relevant conservation laws is better suited to describe the magnetic-field and temperature dependences characteristic of this combined effect than a phenomenological approach.

The predictions of our theory differ in an essential way from previous studies of the magnetic-field dependence of the spin Seebeck effect at low temperatures. We find that at experimentally relevant length scales, which are larger than the mean free paths for magnon-impurity and phonon-impurity scattering, but smaller than the inelastic relaxation lengths at low temperatures, the dominant mechanism coupling lattice and spin degrees of freedom is impurity-mediated scattering between different magnon-polaron modes. This impurity-mediated inter-mode scattering is strongest near the resonance frequencies at which magnon and phonon dispersions cross. Consequentially, the spin current is carried almost entirely by magnon polarons at those frequencies. Previous theories of the spin Seebeck effect explicitly or implicitly assumed a strong equilibration by inelastic magnon-magnon and phonon-phonon scattering processes [15, 20, 10, 127, 41, 128, 145, 31], which implies that the spin current carried by excitations at all frequencies, insofar as they are accessible for thermal excitation. Such assumption of strong relaxation is valid for high temperatures and large system sizes, but the equilibration length exceeds the system size at the low temperatures at which the singular features in the magnetic-field dependence of the spin Seebeck effect are observed [15]. In this parameter regime, our theory predicts a robust peak at the critical magnetic fields at which magnon and phonon dispersions cross, irrespective of the type of the underlying elastic relaxation mechanism. The peak arises, because at these magnetic fields the frequency window that contributes to the spin Seebeck effect is maximized. Our prediction differs from that of Refs. [15, 20], which predict a peak or a dip, depending on whether magnon-impurity scattering or phonon-impurity scattering dominates at low temperatures. Our predictions also differ from our own previous theory for the fully equilibrated regime [41], although the differences are more subtle.

Whereas the theory presented here treats the frequency dependence of the distribution function exactly, it does make approximations in other respects. The use of

the Boltzmann equation misses coherences between different magnon-polaron modes, which can lead to an overestimate of impurity-mediated inter-mode scattering near the resonance frequencies. This could be a relevant issue at very low temperatures, at which magnons and phonons are coherent over long distances. If elastic scattering dominates, such coherence effects can be treated theoretically within a calculation of the spin Seebeck effect using, *e.g.*, diagrammatic perturbation theory [147] or the Lindblad approach [148]. At system lengths shorter than the elastic mean free path or at temperatures high enough that the inelastic relaxation length become shorter than the elastic mean free paths, the approximation that we only take one isotropic moment and one anisotropic moment of the distribution function may no longer be strictly valid. In this case, a systematic quantitative improvement of the theory can be obtained by keeping higher moments in an expansion in spherical harmonics. However, as our comparison for the ballistic regime has shown, see App. B.7, the quantitative error associated with the use of a simplified angular dependence with one isotropic and one anisotropic moment is numerically small.

In the implementation of our formalism, we assumed that the magnon and phonon dispersions are isotropic. This is consistent with known properties of YIG in the long-wavelength limit [83, 149]. Inclusion of magnon-phonon coupling gives a small anisotropy, which our calculations do account for. When going to higher frequencies and temperatures, in principle, there can also be anisotropy of the magnon and phonon dispersions in the absence of magnon phonon coupling. If that is the case, the frequency region in which magnon and phonon dispersions cross will be enhanced. As a result, the impurity-mediated inter-mode scattering will be strong over a larger range of frequencies, leading to an enhancement of the spin Seebeck effect at short system sizes. At high temperatures, excitation of zone-boundary phonons or optical phonons (and, eventually, excitation of zone-boundary magnons and optical magnons and the appearance of Umklapp processes) will become important. Our lattice-based formulation of the Boltzmann theory should in principle be able to deal with this regime, although the simplified microscopic lattice model of Sec. 3.2 will need to be refined [131, 150, 151, 145].

Our formalism can also be used to study the spin Seebeck effect in the "nonlocal" geometry [30, 9, 10, 12], in which the driving source is the injection of magnons from a second normal metal, instead of the injection of phonons from an insulating non-magnetic heat bath. Low-temperature measurements of the nonlocal spin Seebeck effect, showing anomalous features at the critical magnetic fields, were recently reported [13]. The frequency-resolved theory can further be applied to model other manifestations of magnon-polaron formation, such as the accumulation of magnon polarons in the spectral region near the resonant frequencies after parametric excitation of magnons [123], anomalies in the spin pumping efficiency at resonance frequencies [124], or the direct observation of wave-like excitation in the lattice subsystem after excitation of the spin subsystem [125], where a frequency-resolved

description is natural and essential.

4

Conclusions and Outlook

This thesis dealt with the coupled transport of spin waves and lattice vibrations in ferromagnetic insulators. We found that the Boltzmann approach is suitable to analyze both the weak-coupling regime as well as the strong coupling between magnons and phonons which leads to the formation of hybridized magnon polaron modes.

In Chapter 2 we constructed a Boltzmann theory for weakly coupled magnons and phonons. We explicitly accounted for magnon-phonon interaction in the collision integrals and separated between spin-conserving and spin-nonconserving collisions. The interaction amplitudes of the collisions are based on a set of phenomenological models that derive from the magneto-elastic theory [86, 80, 38] and Heisenberg exchange interaction. The inelastic magnon-magnon and phonon-phonon interactions were treated implicitly. We assumed that these interactions are strong enough to enforce a local equilibrium with respect to the corresponding collision integrals at any time. This greatly reduced the complexity of the magnon and phonon distribution functions. The Boltzmann equation simplified to a set of four coupled "hydrodynamic" equations – two for the isotropic nonvanishing moments, identified as the magnon and phonon temperature deviations from the equilibrium temperature $\Delta T_{\mathrm{m,p}}$ and two for the nonvanishing anisotropic moments, identified as (averaged) momentum densities $\mathbf{v}_{\mathrm{m,p}}$. Impurity interaction and magnon-phonon collisions cause further relaxation of the distributions. Together with a set of boundary conditions for the insulator–ferromagnet and the ferromagnet–normal metal interfaces, we evaluated the spin pumping to the normal metal perturbatively, using insulating

97

boundaries for the spin system at both interfaces.

We found that the direct conversion process of phonons to magnons causes sharp features in the magnon-phonon collision rate around two magnetic fields where the magnon and (longitudinal/transverse) phonon dispersion have touching points, see Figure 2.2. These features also translated into the final expression for the spin Seebeck effect and agreed qualitatively with the experimental findings of Kikkawa *et al.* [15].

In contrast to the coherent theory by Flebus *et al.* [20], in our model the distinction if those features are dips or peaks did not only depend on the relative magnitude of the magnon and impurity lifetimes but also on the (thermal) magnon-phonon mean free path and the length of the ferromagnet. We found that for short systems of experimentally relevant length-scales $\sim \mu$m there are peaks in the spin Seebeck signal while for longer system sizes dips occur.

In our calculations, we implied strong inelastic magnon-magnon and phonon-phonon coupling, hence the model applicability generally increases with temperature. Although the results can technically also be extrapolated to low temperatures, there is no *a priori* justification for the model to be valid at low temperatures as impurity scattering is the dominating source of scattering at low temperatures [43, 101]. Elastic impurity scattering conserves the energy of the magnons/phonons and thus can't distribute energy among magnons and phonons. As the magnons are too good approximation confined to the ferromagnet and excited almost exclusively by phonons via magnon-phonon interaction this leads to singularities in the magnon distribution near the frequencies where the magnon and phonon dispersions cross and the magnon-phonon interaction is drastically enhanced. To cover these singularities in the magnon distribution additional terms in the power series expansion (2.16) of the distribution function should be included in the evaluation. There is no controlled way to predict *a priori* how many additional terms have to be added to the expansion until it converges.

Thus, in Chapter 3 we entirely released the assumption of strong magnon-magnon and phonon-phonon background interaction and instead kept the full frequency dependence of the isotropic and anisotropic moments (still accounting for one isotropic and one anisotropic moment in the expansion, which is valid for systems larger than the respective magnon-impurity and phonon-impurity rates) in the magnon and phonon distribution functions (3.44). To emphasize the importance of magnon-phonon coupling we set up a microscopic lattice model, based on a Heisenberg Hamiltonian, a harmonic lattice potential, and pseudo-dipolar exchange coupling, that reproduces the phenomenological theory in the continuum limit [86, 78, 80] (*i.e.* it reproduces the long-wavelength limits of the magnon and phonon dispersions as well as the magnon-phonon collision integrals) and gives additional insight in the underlying scattering mechanism on a microscopic level. In extension to the model in Chapter 2, we accounted for the one-magnon-one-phonon interaction in the cal-

culation of the eigenmodes of the magnon-phonon Hamiltonian instead of treating it as a weak coupling in the collision integrals. This is motivated by the divergence of the phonon-to-magnon collision rate at the critical magnetic fields where the dispersions have touching points, see Figure 2.2. The resulting hybridized eigenmodes describe mixed-states of magnons and phonons, referred to as "magnon polarons". Flebus *et al.* [20] restricted their analysis of the spin Seebeck effect to the evaluation of the bulk magnon spin current in the ferromagnet. We also evaluated the contributions from the reservoirs to the spin Seebeck effect. The interaction of the magnon polarons in the ferromagnet with the metal and the isolator reservoirs at the connecting interfaces was derived non-perturbatively from the magnon and phonon equations of motion in the discrete lattice model by matching the (conserved) energy currents at the interfaces. These microscopic boundary conditions extend the phenomenological Kapitza interface resistances [98, 99, 19, 33].

To apply our theory to experiments that suggest significant importance of magnon-phonon interaction, we quantitatively described magnetic-field dependence measurements of the longitudinal spin Seebeck effect at low temperatures. Previous theories imply strong magnon-magnon and phonon-phonon interaction that re-distributes energy among the magnon-polaron modes. Consequentially, the spin current is carried by polarons of all thermally accessible frequencies. This holds even for low temperatures and small system sizes where the mean free path of inelastic scattering processes far exceeds the experimentally used lengths of the ferromagnet, see Figure 3.3. These system lengths are typically still larger than the mean free paths of the magnon-impurity and phonon-impurity interactions such that the spin current is driven exclusively by magnon polarons near the magnon-phonon resonance frequencies where the impurity mediated heating of the magnons by phonons is strongest, see Figure 3.7. For such systems, we predicted persistent peaks in the spin Seebeck current independent of the magnetic and acoustic qualities of the ferromagnet. This is contrary to the theory by Flebus *et al.* who predict peaks for acoustic clean samples and dips for magnetic clean ones whereas the peaks vanish if the acoustic and magnetic qualities are the same. As a result, we concluded that the type (dips/peaks) of the features in the spin Seebeck coefficient does not allow any conclusions about the quality of the sample. When going to larger temperatures and system lengths where inelastic magnon-magnon, phonon-phonon, and two-magnon-one-phonon scattering becomes relevant, we predicted that the most efficient re-distribution of energy among magnon polarons is due to a combination of spin-conserving four-magnon and two-magnon-one-phonon interaction. This energy re-distribution activates the whole frequency spectrum of magnon polarons to contribute to the spin current and can significantly enhance the spin Seebeck effect.

Our theory is not limited to the study of the longitudinal spin Seebeck effect but can be extended and be applied to other interesting phenomena. In acoustic (long-range) spin pumping experiments [25, 26, 27] the phonons in the ferromagnet are

not excited thermally by contact to a heat reservoir but rather by (mode-selective) acoustic waves. By keeping the full frequency dependence in our Boltzmann theory, we can model strongly frequency-dependent transport in more detail compared to the low-order Legendre-polynomial expansions [35, 37, 20] that truncate the frequency dependence of the distribution functions to a small set of polynomials. Other interesting applications are non-local spin Seebeck setups [30, 9, 10, 12, 31] and systems where the magnons in the ferromagnet are directly excited via spin pumping and magnetization dynamics of adjacent materials through the boundaries. Both setups can be investigated within the developed Boltzmann approach with only a few adjustments to the boundary conditions in Section 3.3.4.

The ferromagnetic description of YIG (which is a ferrimagnetic insulator) is limited to low temperatures [83]. For room-temperature measurements, optical magnons are excited and contribute significantly to the magnon transport [152, 153]. Recently, the spin Seebeck effect was observed in antiferromagnetic insulators Cr_2O_3 [75, 154, 155], MnF_2 [76], FeF_2 [77], and Fe_2O_3 [154]. To describe the spin Seebeck effects in these materials our model can be extended by adding a second sub-lattice to describe spin-caloric transport in antiferromagnets and ferrimagnets. In contrast to a single-lattice ferromagnetic insulator where magnetization-conserving Heisenberg exchange interaction can not lead to a spin current by itself, in a two sub-lattice antiferromagnet it still conserves the total magnetization but allows for spin transfer between the sub-lattices which leads to spin currents within the sub-lattices [156, 157, 158, 159].

So far we focused our study on steady-state situations which led to a time-independent spin current in the ferromagnet. Seifert *et al.* [17] measured the spin Seebeck effect in a YIG–Pt bilayer that is generated in response to heating up the Pt with ultrashort laser pulses. They observed an instantaneous spin Seebeck effect in response to the normal metal heating as the temperature difference between magnons in YIG and electrons in Pt, which governs the spin Seebeck effect, see Eq. (A.6), which leads to an immediate response. To investigate the role of the magnons in the ferromagnet to the time-scales of the SSE, we suggest that heating up the magnons on the other end of the ferromagnetic sample directly or indirectly via the phonon system is leads to more insight into the role of the magnons (and of the magnon-phonon coupling). Similar measurements by Kimling *et al.* [16] and Jamison *et al.* [18] who also heated up the Pt in a Yig–Pt spin Seebeck setup also observed an instantaneous spin Seebeck effect which they addressed to the rapidly generated temperature bias $\Delta T_{\mathrm{m}} - \Delta T_{\mathrm{e}}$ between magnons and electrons at the FN interface. In addition Jamison *et al.* observed that there is a second timescale $\sim 100 \,\mu\mathrm{s}$ involved where the spin Seebeck voltage further increases until saturation. They addressed this to a contribution from the magnon chemical potential. With the extension of our model in Chapter 2 by a magnon chemical potential as in Ref. [37], the Boltzmann theory in Chapter 2 can be used to describe the time-scales of

the spin Seebeck effect beyond a simple two-temperature model used in Ref. [18].

Reviewing Chapter 2, in the Boltzmann equation (2.26)-(2.29) we already introduced the full time-dependent components to the Boltzmann equation. This allows us to theoretically study the effect of spin conserving and spin nonconserving scattering on the temporal evolution of the spin Seebeck effect. Without spin-nonconserving scattering the Planck-like distribution function of the magnons, characterized by a temperature T_m is extended by a magnon chemical potential μ_m [37] towards a Bose-like distribution whereas the phonons are still governed by a Planck-like distribution as a consequence of dominating three-phonon interaction. Magnon-number conserving two-magnon-phonon interaction leads to an energy transfer from the phonon into the magnon system without affecting the net magnetization. In a steady-state situation this led to a re-distribution of magnons from low to high frequencies, see Figure 3.11 in Chapter 3, which also affected the frequency-resolved spin current $j_x^\mathrm{s}(\omega)$. In combination with spin-nonconserving scattering, these magnon-phonon collisions can have a significant effect on the spin Seebeck effect for system sizes longer than the corresponding magnon-phonon mean free path. In contrast, this process alone is not able to create a net spin current, as can be seen after integration of the spin current $j_x^\mathrm{s}(\omega)$ over all frequencies, see Figure 3.13. In a time-dependent setup, the re-distribution of magnons simultaneously affects the magnon temperature and chemical potential in such a way that the magnon number does not vary. As the magnon temperature and the magnon chemical potential both contribute to the spin Seebeck effect [37] with different spin pumping contributions, in contrast to a steady-state, we predict a finite time-dependent transient spin Seebeck effect even in a pure Heisenberg ferromagnet where only spin-conserving scattering is present. Relativistic effects like anisotropic exchange and dipole-dipole interactions do not conserve the number of magnons and relax the magnetization via spin non-conserving scattering which leads to an additional spin current. Studying the time scales on which both processes contribute to the spin Seebeck effect is important to understand the time-dependent spin Seebeck effect phenomena.

The study of these effects poses interesting ideas for the expansion of the work presented in this thesis and future research.

A

Appendices Chapter 2

A.1 Magnon-electron coupling at FN interface

As in the main text of chapter 2, we consider a ferromagnetic insulator occupying the region $-L_\mathrm{F} < x < 0$, coupled to a normal metal at $0 < x < L_\mathrm{N}$. If the normal metal is at zero temperature, the spin current density at the ferromagnetic insulator–metal interface is [50]

$$j_x^\mathrm{s} = \frac{\hbar}{4\pi} \frac{g_\mathrm{r}}{A} \left\langle \mathbf{m} \times \dot{\mathbf{m}} \right\rangle_x , \tag{A.1}$$

where g_r is the real part of the spin-mixing conductance and $\mathbf{m}$ is a unit vector pointing in the direction of the magnetization at the interface. (We omit a second contribution to j_x^s, which is proportional to the imaginary part of the spin-mixing conductance and vanishes upon time averaging.) Expressing $\mathbf{m}(\mathbf{r})$ in terms of magnon creation and annihilation operators $a^\dagger(\mathbf{r})$ and $a(\mathbf{r})$ for a macrospin of magnitude S located at position $\mathbf{r}$ and normal ordering, one finds

$$\left\langle \mathbf{m}(\mathbf{r}) \times \dot{\mathbf{m}}(\mathbf{r}) \right\rangle_x = \frac{i}{S} \langle \dot{a}(\mathbf{r})^\dagger a(\mathbf{r}) - a(\mathbf{r})^\dagger \dot{a}(\mathbf{r}) \rangle. \tag{A.2}$$

Substituting the mode expansion

$$a(\mathbf{r}) = \sum_{\mathbf{k}} \sqrt{\frac{2 - \delta_{\mathbf{k},0}}{N}} \cos(k_x x) e^{ik_y y + ik_z z} a_{\mathbf{k}}, \tag{A.3}$$

where N is the number of macrospins in the ferromagnetic insulator and the position $\mathbf{r}$ is taken at the center of the unit cell, we find, for $\mathbf{r}$ at the ferromagnetic insulator–normal metal interface at $x = 0$,

$$\langle \mathbf{m}(\mathbf{r}) \times \dot{\mathbf{m}}(\mathbf{r}) \rangle_x = \frac{2}{NS} \sum_{\mathbf{k}} \frac{(2 - \delta_{\mathbf{k},0}) \varepsilon_{\mathbf{k}}}{\hbar} b_{\mathbf{k}}^0, \tag{A.4}$$

so that

$$j_x^{\mathrm{s}} = \frac{g_{\mathrm{r}}}{\pi A S} \frac{1}{2N} \sum_{\mathbf{k}} (2 - \delta_{\mathbf{k},0}) \varepsilon_{\mathbf{k}} b_{\mathbf{k}}^0. \tag{A.5}$$

If the normal metal is at a finite temperature, the net spin current across the ferromagnet–normal metal interface is the sum of the spin current (A.5) and a counterflow temp given by the same expression, but with the magnon temperature T_{m} replaced by the electron temperature T_{e}. Hence, with a small temperature difference $\Delta T = T_{\mathrm{m}} - T_{\mathrm{e}}$ between normal metal and ferromagnetic insulator, one finds

$$j_x^{\mathrm{s}} = -S_{\mathrm{m}}' \Delta T, \tag{A.6}$$

with

$$S_{\mathrm{m}}' = \frac{g_{\mathrm{r}}}{\pi A S} \frac{1}{2N} \sum_{\mathbf{k}} (2 - \delta_{\mathbf{k},0}) \varepsilon_{\mathbf{k}} \frac{db_{\mathbf{k}}^0}{dT}. \tag{A.7}$$

This is the same expression as Eq. (2.33) of the main text, where the limit of a macroscopic sample with no exception for $\mathbf{k} = 0$ was taken.

A.2   Simple model for magnon-electron coupling at FN interface

To make the general expression (A.7) concrete, we describe the interface between a ferromagnetic insulator (for $x < 0$) and a normal metal (for $x > 0$) using the Hamiltonian

$$\mathcal{H} = \frac{\hbar^2 (\mathbf{p}^2 - p_{\mathrm{F}}^2)}{2m} + V(x) + J_{\mathrm{sd}} \mathbf{S}(\mathbf{r}) \cdot \boldsymbol{\sigma}, \tag{A.8}$$

where $\mathbf{p}$ is the electron wavevector, p_{F} the Fermi wavenumber, m the electron mass, J_{sd} the sd exchange interaction between conduction electrons and localized spins, $V(x)$ a potential chosen such that $V(x) = V_0 > \hbar^2 p_{\mathrm{F}}^2 / 2m$ in the ferromagnetic insulator (for $x < 0$) and $V(x) = 0$ in the normal metal (for $x > 0$), see Fig. A.1. The spin operator

$$\mathbf{S}(\mathbf{r}) = \frac{1}{V_a} \sum_j \mathbf{S}_j \delta(\mathbf{r} - \mathbf{r}_j), \tag{A.9}$$
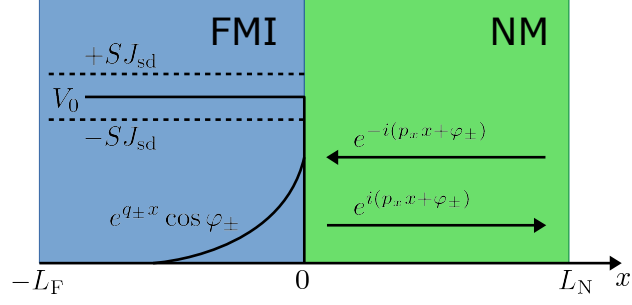
Figure A.1: Simple interface model: Electrons incident from the normal metal ($x > 0$) reflect from the ferromagnetic insulator with a scattering phase shift $\varphi_\pm$ for majority ($+$) and minority ($-$) electrons. The ferromagnetic insulator is modeled by a band offset V_0 larger than the Fermi energy, ensuring that the electron wavefunction decays exponentially inside the insulator.

where $\mathbf{S}_j$ is the macrospin operator and V_a is the size of the unit cell. For small deviations from a uniform magnetization in the z direction we may write

$$S_{jz} = S, \quad S_{j+} = \sqrt{2S}a(\mathbf{r}_j), \quad S_{j-} = \sqrt{2S}a(\mathbf{r}_j)^\dagger, \tag{A.10}$$

where $\mathbf{r}_j$ is the center of the jth unit cell, S is the size of the macrospin, and $a(\mathbf{r})$ the magnon operator, which has the mode expansion given in Eq. (A.3). For this model, we now calculate the mixing conductance g_r and the spin current $j_x^\mathrm{s}(0)$.

Calculation of the mixing conductance.— The wavefunction of an electron with wavevector $\mathbf{p}_\parallel$ to the interface, $|\mathbf{p}| = p_\mathrm{F}$, and spin $\pm$ is

$$\psi_\pm(x) = \sqrt{\frac{2}{V_\mathrm{N}}}e^{i\mathbf{p}_\parallel \cdot \mathbf{r}} \times \begin{cases} \cos(p_x x + \varphi_\pm) & \text{if } x > 0, \\ e^{q_\pm x}\cos\varphi_\pm & \text{if } x < 0, \end{cases} \tag{A.11}$$

where V_N is the volume of the normal metal, $q_\pm^2 = 2m(V_0 \pm SJ_\mathrm{sd}) - p_x^2$, $\tan\varphi_\pm = -q_\pm/p_x$, and $p_x^2 = p_\mathrm{F}^2 - p_\parallel^2$. Replacing $\mathbf{S}(\mathbf{r})$ by $S\mathbf{e}_z$, we find for the real part of the mixing conductance

$$g_\mathrm{r} = 2\sum_{\mathbf{p}_\parallel} \sin^2(\varphi_+ - \varphi_-)$$

$$\approx 2\sum_{\mathbf{p}_\parallel} \frac{(SJ_\mathrm{sd})^2 p_x^2}{V_0^2(2mV_0 - p_x^2)}, \tag{A.12}$$

where in the second equality we expanded to second order in J_sd.

Calculation of the spin current $j_x^{\rm s}(0)$.— We calculate the spin current to order J_{sd}^2 using the Fermi Golden rule. From the matrix element

$$\langle \psi_-', n_{\mathbf{k}} - 1 | \mathcal{H} | \psi_+, n_{\mathbf{k}} \rangle = \frac{p_x^2 J_{\rm sd} \sqrt{S}}{m V_0 L_{\rm N} \sqrt{N(2mV_0 - p_x^2)}}$$
$$\times \sqrt{n_{\mathbf{k}}} \, \delta_{\mathbf{p}_\parallel' = \mathbf{p}_\parallel + \mathbf{k}_\parallel}, \tag{A.13}$$

where $|\psi_+, n_{\mathbf{k}}\rangle$ $(|\psi_-', n_{\mathbf{k}} - 1\rangle)$ is a state with an electron of spin $+$ $(-)$ and transverse wavevector $\mathbf{p}_\parallel$ $(\mathbf{p}_\parallel')$ and $n_{\mathbf{k}}$ $(n_{\mathbf{k}} - 1)$ magnons in the model labeled by the wavevector $\mathbf{k}$. In the calculation of the matrix element (A.13) we assumed that all magnon momenta are small in comparison to the Fermi momentum, so that we may neglect the change of the magnitude of the longitudinal wavevector component p_x of the electrons upon absorption of a magnon, and we neglected the exception arising from the different normalization of the $\mathbf{k} = 0$ magnon mode (see App. A.1). From the Fermi Golden rule we then obtain the spin current

$$j_x^{\rm s}(0) = \frac{1}{\pi A S} \left(\sum_{\mathbf{p}_\parallel} \frac{2(S J_{\rm sd})^2 p_x^2}{V_0^2 (2mV_0 - p_x^2)} \right) \left(\frac{1}{N} \sum_{\mathbf{k}} \varepsilon_{\mathbf{k}} \frac{db_{\mathbf{k}}^0}{dT} \right) \Delta T, \tag{A.14}$$

consistent with Eq. (A.7).

B

Appendices Chapter 3

B.1 Lattice model for magnon polarons

In this appendix we give the expressions for the Fourier representation of the lattice model in Section 3.2.1. The equations of motion for the Fourier-transformed lattice displacement $\mathbf{u_q}$, momentum $\mathbf{p_q}$, and magnetization amplitude $\mathbf{n_q}$ are

$$\dot{\mathbf{u}}_{\mathbf{q}} = \frac{\partial H}{\partial \mathbf{p}_{-\mathbf{q}}}, \quad \dot{\mathbf{p}}_{\mathbf{q}} = -\frac{\partial H}{\partial \mathbf{u}_{-\mathbf{q}}}, \quad \dot{\mathbf{n}}_{\mathbf{q}} = -\mathbf{e} \times \frac{\partial H}{\partial \mathbf{n}_{-\mathbf{q}}}. \tag{B.1}$$

Without the restriction of long-wavelengths $q \to 0$ the general expressions for the interaction matrices $\mathcal{B}(\mathbf{q})$, $\mathcal{K}(\mathbf{q})$, and $\mathcal{D}(\mathbf{q})$ in the Fourier-transformed magnon-phonon Hamiltonian (3.13) for the full lattice model read, for the magnon energy,

$$\mathcal{B}(\mathbf{q}) = 2JS \sum_{\alpha} (1 - \cos q_\alpha a) + \mu B, \tag{B.2}$$

for the phonon energy,

$$\mathcal{K}(\mathbf{q}) = 2 \sum_{\alpha,\beta} \left[\mathcal{K}_{\alpha\beta}(1 - \cos q_\alpha a) + \mathcal{K}'_{\alpha\beta} \sin(q_\alpha a) \sin(q_\beta a) \right.$$
$$\left. + \mathcal{K}''_{\alpha\beta}(1 - \cos(q_\alpha a) \cos(q_\beta a)) \right], \tag{B.3}$$

with the indices α and β summed over the three coordinate directions x, y, and z, and

$$\mathcal{K}_\alpha = (K_1 \mathbf{e}_\alpha \mathbf{e}_\alpha^{\mathrm{T}} + K_2 \mathbb{1})\delta_{\alpha,\beta},$$

$$\mathcal{K}'_{\alpha\beta} = \frac{1}{2}K_1(\mathbf{e}_\alpha \mathbf{e}_\beta^{\mathrm{T}} + \mathbf{e}_\beta \mathbf{e}_\alpha^{\mathrm{T}}),$$

$$\mathcal{K}''_{\alpha\beta} = \frac{1}{2}K_1(\mathbf{e}_\alpha \mathbf{e}_\alpha^{\mathrm{T}} + \mathbf{e}_\beta \mathbf{e}_\beta^{\mathrm{T}}), \tag{B.4}$$

and for the magnon-phonon coupling

$$\mathcal{D}(\mathbf{q}) = \frac{2iS^{3/2}}{a^{5/2}} \sum_\alpha \left\{ D[(\mathbf{e} \cdot \mathbf{e}_\alpha)\mathbb{1} + \mathbf{e}_\alpha \mathbf{e}^{\mathrm{T}}] \right.$$

$$\left. + \left(\frac{D'}{a} - 2D\right)(\mathbf{e} \cdot \mathbf{e}_\alpha)\mathbf{e}_\alpha \mathbf{e}_\alpha^{\mathrm{T}} \right\} \sin q_\alpha a. \tag{B.5}$$

Applying the long-wavelength approximation $q \to 0$ recovers the continuum theory expressions (3.14), (3.16), and (3.17) in the main text.

B.2 Magnon-polaron Hamiltonian

Symmetries of the magnon-polaron Hamiltonian. — The 8-component column vector $\mathbf{b_q}$ of Eq. (3.27) and the 8×8 hermitian matrix $H_\mathbf{q}$ of Eq. (3.28) satisfy the symmetry conditions

$$\mathbf{b_{-q}} = \Sigma_1 \mathbf{b_q^*}, \quad H_{-\mathbf{q}} = \Sigma_1 H_\mathbf{q}^* \Sigma_1, \tag{B.6}$$

where

$$\Sigma_1 = \begin{pmatrix} 0 & 1 \\ 1 & 0 \end{pmatrix}. \tag{B.7}$$

The symplectic matrix $V_\mathbf{q}$ and the diagonal matrix $\Omega_\mathbf{q}$ that diagonalize $H_\mathbf{q}$, see Eq. (3.30), satisfy the conditions

$$\Sigma_1 \Omega_{-\mathbf{q}} \Sigma_1 = \Omega_\mathbf{q},$$

$$\Sigma_3 V_\mathbf{q}^\dagger \Sigma_3 = V_\mathbf{q}^{-1},$$

$$\Sigma_1 V_{-\mathbf{q}} \Sigma_1 = V_\mathbf{q}^*, \tag{B.8}$$

with

$$\Sigma_3 = \begin{pmatrix} 1 & 0 \\ 0 & -1 \end{pmatrix}. \tag{B.9}$$

In addition to the symplectic structure outlined above, the Hamiltonian $H_\mathbf{q}$ satisfy the symmetry condition

$$H_{-\mathbf{q}} = I H_\mathbf{q} I^\dagger, \tag{B.10}$$

107

where

$$I = \begin{pmatrix} \mathbb{1}_3 & & & \\ & -1 & & \\ & & \mathbb{1}_3 & \\ & & & -1 \end{pmatrix}.$$ (B.11)

Since I commutes with Σ_1 and Σ_3, it follows that

$$V_{-\mathbf{q}} = IV_{\mathbf{q}}, \quad \Omega_{-\mathbf{q}} = \Omega_{\mathbf{q}}.$$ (B.12)

Together with the conditions (B.8), this implies that

$$V_{\mathbf{q}}^* = I\Sigma_1 V_{\mathbf{q}}\Sigma_1, \quad \omega_{\mathbf{q},\lambda} = \omega_{-\mathbf{q},\lambda}.$$ (B.13)

Symplectic diagonalization.— To (numerically) diagonalize the positive definite hermitian matrix $H_{\mathbf{q}}$ using the symplectic matrix $V_{\mathbf{q}}$ that satisfies the condition (B.8), we first consider the non-hermitian matrix $\Sigma_3 H_{\mathbf{q}}$ and diagonalize it with the 8×8 matrix V' as (we omit the subscript $\mathbf{q}$ in the following equations)

$$\Sigma_3 H = \frac{1}{2}V'\Sigma_3\Omega V'^{-1}.$$ (B.14)

Since H is hermitian, $\Sigma_3 H = \Sigma_3 H^\dagger$ and we have

$$\Sigma_3 H = \frac{1}{2}\Sigma_3(V'^\dagger)^{-1}\Sigma_3\Omega V'^\dagger\Sigma_3.$$ (B.15)

Uniqueness of the diagonalization of a matrix then implies that

$$D\Sigma_3 V'^{-1} = V'^\dagger\Sigma_3,$$ (B.16)

where D is a diagonal matrix. Moreover, D is positive definite, so that we may write $D = P^{-2}$, with P a diagonal matrix. It follows that

$$\Sigma_3 = (\Sigma_3 V'P)^\dagger\Sigma_3(\Sigma_3 V'P).$$ (B.17)

One then easily verifies that the matrix $V = \Sigma_3 V'P$ diagonalizes H via

$$H = \frac{1}{2}V\Omega V^\dagger$$ (B.18)

and satisfies the condition (B.8).

B.3 Magnon-phonon coupling from magneto-elastic theory

Here, we review the magneto-elastic theory of magnon-phonon interaction and show how microscopic magnon-phonon Hamiltonians from magnetic dipole-dipole interaction and magnetic anisotropy compare to it.

Magneto-elastic coupling— Based only on symmetry considerations in a continuous medium Kittel [136] and Kaganov *et al.* [86, 87] proposed a phenomenological magneto-elastic coupling energy. The leading-order contribution to magnon-phonon coupling in the presence of a cubic symmetry takes the form

$$H^{\mathrm{me}} = \int \frac{dV}{a^3} \sum_{\alpha,\beta} B_{\alpha\beta} e_{\alpha\beta} s_\alpha(\mathbf{r}) s_\beta(\mathbf{r}), \qquad (B.19)$$

where $\mathbf{s}(\mathbf{r}_j)$ is the continuous spin density in the long-wavelength limit, $e_{\alpha\beta} = (1/2)\left(\partial_\beta u_\alpha + \partial_\alpha u_\beta\right)$ the symmetrized strain tensor, the integral is over the volume V of the magnetic insulator, and $B_{\alpha\beta} = B_1\delta_{\alpha\beta} + B_2(1 - \delta_{\alpha\beta})$ is the magneto elastic coupling tensor. The constants B_1 and B_2 are material-specific constants describing the strength of the magneto-elastic coupling. For YIG these constants were fitted to magnetostriction experiments at 300 K [141] as $B_1 = 0.08J$ and $B_2 = 0.16J$.

The magneto-elastic Hamiltonian (B.19) can be written in terms of magnon and phonon creation and annihilation operators by applying Eqs. (3.4) and (3.23). Taking the magnetization direction $\mathbf{e}$ in the (111) direction, we can compare the magneto-elastic Hamiltonian with the magnon-phonon Hamiltonian obtained for a simple cubic lattice model with nearest-neighbor pseudo-dipolar exchange interactions, see Sec. 3.2.1. Comparing Eq. (B.19) with Eq. (3.9) shows that the two Hamiltonians agree if we set $B_1 = aD'$ and $B_2 = 2D$.

We now discuss two additional contributions to the microscopic simple cubic spin model of Sec. 3.2.1 that also lead to magnon-phonon coupling and that can easily be included into the phenomenological magneto-elastic Hamiltonian: an on-site magnetic anisotropy and the long-range dipole-dipole interaction. The numerical evaluations reported in this article are obtained without these two additional contributions.

On-site magnetic anisotropy.— A model with cubic symmetry allows an on-site magnetic anisotropy term of the form [136]

$$H^{\mathrm{a}} = \sum_{\langle i,j \rangle} K_{ij}(\mathbf{S}_i \cdot \mathbf{e}_{ij})^2, \qquad (B.20)$$

where $\mathbf{e}_{ij}$ is the unit vector connecting nearest-neighbor lattice sites i and j and the coupling constant K_{ij} depends on the direction of $\mathbf{e}_{ij}$ and the distance $|\mathbf{r}_i - \mathbf{r}_j|$ between the sites i and j. Although such a magnetic anisotropy term does not affect the magnon dispersion in a system with cubic symmetry, there is a magnon-phonon interaction resulting from it. Passing to the continuum limit, we find that the on-site anisotropy Hamiltonian (B.20) yields the same magnon-phonon coupling as the pseudo-dipolar exchange coupling (3.9) with the on-site anisotropy constants chosen as $K = D$ and $K' = D'$, where $K' = dK_{ij}/d|\mathbf{r}_i - \mathbf{r}_j|$.

Dipole-dipole interaction— The weak but long-range dipole-dipole coupling between magnetic dipoles corresponds to the Hamiltonian

$$H^{\mathrm{di}} = \frac{1}{2} \sum_{i,j} \frac{\mu^2}{r_{ij}^3} \left[\mathbf{S}_i \cdot \mathbf{S}_j - \frac{3}{r_{ij}^2} (\mathbf{S}_i \cdot \mathbf{r}_{ij})(\mathbf{S}_j \cdot \mathbf{r}_{ij}) \right], \qquad (\mathrm{B.21})$$

where $r_{ij} = |\mathbf{r}_i - \mathbf{r}_j|$ and $\mu = g\mu_{\mathrm{B}}$ is the magnetic moment of the spins. The summation is over all pairs of lattice sites (i, j), irrespective of their distance. In contrast to the Heisenberg Hamiltonian, the interaction strength does not only depend on the length of the bond between the spins, but also on the angle of the spins with the connecting bonds. Expanding the dipole-dipole coupling to first order in the lattice displacements $\mathbf{u}_i$ we find a Hamiltonian of the same structure as (B.19). Evaluating the summation over pairs of lattice sites and taking the continuum limit, the coupling strength converges towards $B_1^{\mathrm{d}} = (9\pi/4)\mu^2/a^3$ and $B_2^{\mathrm{d}} = -(3\pi/2)\mu^2/a^3$. Comparing the strength of the dipole-dipole interaction to the magneto-elastic constants $B_{1,2}$ we see that the dipole-dipole interaction makes up for a fraction of roughly 5% of the measured magneto-elastic constants in YIG, in agreement with the estimate of Ref. [139].

B.4 Interface and boundary conditions

Solutions at fixed frequencies.— The frequency ω and the transverse component $\mathbf{q}_\perp = q_y \mathbf{e}_y + q_z \mathbf{e}_z$ of the wavevector are conserved at the interfaces. To prepare for the calculation of the transmission and reflection coefficients of the IF and FN interfaces, we therefore need to construct wave-like solutions of the equations of motion (3.11) at fixed ω and $\mathbf{q}_\perp$. In general such solutions are of the form

$$\mathbf{u}_j(t) = \sum_\nu c_\nu \mathbf{u}_{\omega,\mathbf{q}_\perp,\nu} e^{i\mathbf{q}(\nu)\cdot\mathbf{r}_j - i\omega t},$$

$$\mathbf{n}_j(t) = \sum_\nu c_\nu \mathbf{n}_{\omega,\mathbf{q}_\perp,\nu} e^{i\mathbf{q}(\nu)\cdot\mathbf{r}_j - i\omega t}, \qquad (\mathrm{B.22})$$

where we write $\mathbf{q}(\nu) = q_x(\nu)\mathbf{e}_x + \mathbf{q}_\perp$ for the wavevector of the mode ν. In all cases the momentum amplitude $\mathbf{p}_j$ follows from the equalities $\mathbf{p} = -im\omega\mathbf{u}$, so that the momentum amplitude needs not be considered explicitly.

For each combination $(\omega, \mathbf{q}_\perp)$ there are ten such solutions, five of which are propagating or exponentially decaying in the positive x direction and five are propagating or exponentially decaying in the negative x direction. At least one out of each set of modes that propagate in the positive and negative directions, respectively, is decaying [110]. Exponentially decaying solutions have a complex wavenumber q_x. We label the ten solutions by the composite index $\nu = (n, \mathrm{L/R})$ where $n = 1, 2, 3, 4, 5$. The label L is used for solutions that are propagating or exponentially decaying in the positive x direction; the label R is for solutions that are propagating or exponentially decaying in the negative x direction.

The equations of motion determine the prefactors $\mathbf{u}_{\omega,\mathbf{q}_\perp,\nu}$ and $\mathbf{n}_{\omega,\mathbf{q}_\perp,\nu}$ up to an over-all factor. For the propagating modes, we fix this factor by requiring that the energy current carried by that mode is $|c_\nu|^2$ for right-moving modes and $-|c_\nu|^2$ for left-moving modes. The expression for the energy current is, after averaging over one period and using the Fourier representation (3.12),

$$J = \frac{1}{2N_x a} \sum_{\mathbf{q}} \mathrm{Im} \left[\dot{\mathbf{n}}_{\mathbf{q}}^* \cdot \frac{\partial \mathcal{B}(\mathbf{q})}{\partial q_x} \mathbf{n}_{\mathbf{q}} + \ddot{\mathbf{u}}_{\mathbf{q}}^* \cdot \frac{\partial \mathcal{K}(\mathbf{q})}{\partial q_x} \mathbf{u}_{\mathbf{q}} + 2\ddot{\mathbf{u}}_{\mathbf{q}}^* \cdot \frac{\partial \mathcal{D}(\mathbf{q})^\dagger}{\partial q_x} \mathbf{s}_{\mathbf{q}} \right] \qquad \text{(B.23)}$$

This equation is derived for the lattice model at the end of this appendix. A discussion in the continuum limit can be found in Refs. [140, 110, 160].

IF and FN interfaces.— The magnetic medium F exists for $0 < x < L$ with $L = N_x a$, N_x being the number of lattice sites in the x-direction. At $x = L$ there is a boundary to a non-magnetic metal N; at $x = 0$ there is a boundary to a non-magnetic insulator I.

In both the non-magnetic insulator I and the normal metal N we consider phonon degrees of freedom only. The phonon degrees of freedom have displacement $\mathbf{u}'_j$. The equation of motion for the phonon modes at fixed frequency ω and transverse wavevector $\mathbf{q}'_\perp$ in I and N is given by the eigensystem solution of a reduced version of the Hamiltonian (3.26) with $H = H^{\mathrm{pho}}$ and without the magnon amplitudes,

$$\mathbf{u}_j(t) = \sum_{\nu'} c'_{\nu'} \mathbf{u}'_{\omega,\mathbf{q}'_\perp,\nu'} e^{i\mathbf{q}'(\nu')\cdot\mathbf{r}_j - i\omega t} \qquad \text{(B.24)}$$

for $\mathbf{r}_j$ in I or N with the mode index $\nu' = (n', \mathrm{L/R})$, with $n' = 1, 2, 3$. The factors $\mathbf{u}'_{\omega,\mathbf{q}'_\perp,\nu'}$ of the propagating modes are required that the energy current is $|c_{\nu'}|^2$ for right-moving modes and $-|c_{\nu'}|^2$ for left-moving modes. The expression for the energy current in I and N is given by Eq. (B.23) without the terms containing the magnetization amplitude $\mathbf{n}_{\mathbf{q}}$.

The boundary conditions at the IF interface are Eqs. (3.18) and (3.19) of the main text. The boundary condition (3.19) ensures that the energy current (B.23) is continuous at the interface. The boundary conditions for the FN interface are given in Eqs. (3.21) and (3.22) of the main text. In this case, one has to also take into account that magnons can excite conduction electrons in the normal metal [50, 32], which leads to the condition that the energy current carried by the magnon mode is equal to the energy current by the spin current emitted into the normal metal N by the precessing magnetization at $x = L$, which is Eq. (3.22) of the main text.

Reflection and transmission coefficients.— Following the ideas of the Landauer-Büttiker formalism [143], the amplitudes of the normalized coefficients $|c_\nu|^2$ and $|c'_{\nu'}|^2$ which are solutions of the boundary conditions at the interfaces at $x = 0$ and $x = L$ can be recast in the form of reflection and transmission coefficients for the propagating fixed-frequency solutions (B.22). These coefficients are written $R_{\nu\nu'}(\omega, \mathbf{q}_\perp)$ and $T_{\nu\lambda''}(\omega, \mathbf{q}_\perp)$, where only indices ν, ν', and λ'' that correspond to propagating modes are considered.

Energy conservation at the IF interface at $x = 0$ implies the unitarity conditions (3.74) of the main text. There is no unitarity condition for the FN interface at $x = L$ because of the possibility that magnons excite the conduction electrons in the normal metal, which are not accounted for explicitly in our theory. Instead, we define the probability $P_{\nu N}(\omega, \mathbf{q}_\perp)$ that a magnon polaron in mode ν emerging from the FN interface was excited there by an incident spinful excitation of the conduction electrons in N and the probability $P_{N\nu}(\omega, \mathbf{q}_\perp)$ that a magnon polaron in mode ν incident on the FN interface excites a spinful excitation in N by the amount that the sum of reflection and transmission coefficients differ from one, see Eqs. (3.76) and (3.77) of the main text.

Energy current density.— To find the energy current J flowing through an interface between $x = (j-1)a$ and $x = ja$, we write the lattice Hamiltonian H as

$$H = H_< + H_{j-1,j} + H_>, \tag{B.25}$$

where $H_<$ and $H_>$ consist of all terms in H that contain on-site terms and nearest-neighbor bond terms entirely within the regions $x \leq (j-1)a$ and $x \geq ja$, respectively, whereas the Hamiltonian $H_{j-1,j}$ contains the bond terms that connect these two regions. We then have

$$J = \dot{H}_> = \{H_>, H_{j-1,j}\}, \tag{B.26}$$

where $\{\cdot, \cdot\}$ is the Poisson bracket. Using the equations of motion for the amplitudes $\mathbf{u}_j$, $\mathbf{p}_j$, and $\mathbf{n}_j$, this can be recast as

$$J = -\sum_{x_i = ja} \left(\dot{\mathbf{p}}_i \cdot \frac{\partial}{\partial \mathbf{p}_i} + \dot{\mathbf{u}}_i \cdot \frac{\partial}{\partial \mathbf{u}_i} + \dot{\mathbf{n}}_i \cdot \frac{\partial}{\partial \mathbf{n}_i} \right) H_{j-1,j}, \tag{B.27}$$

where the sum is over all lattice sites i with $x = ja$. If we substitute the Fourier representation (3.12) and omit contributions that average to zero after one period,

we find Eq. (B.23). Alternatively, expressing the energy current in terms of the phasor amplitudes $b_{\mathbf{q},\lambda}$ gives

$$J = \frac{\hbar}{L} \sum_{\mathbf{q}} \mathrm{Im} \left[\sum_{\lambda,\lambda'=1}^{3} v_{\mathbf{q},\lambda\lambda'} \dot{b}_{\mathbf{q},\lambda}^{*} b_{\mathbf{q},\lambda'} + v_{\mathbf{q},44} \dot{b}_{\mathbf{q},4}^{*} b_{\mathbf{q},4} - 2 \sum_{\lambda=1}^{3} v_{\mathbf{q},4\lambda} \dot{b}_{\mathbf{q},4}^{*} (b_{\mathbf{q},\lambda} + b_{-\mathbf{q},\lambda}^{*}) \right],$$

(B.28)

with the velocities

$$v_{\mathbf{q},\lambda\lambda'} = \mathbf{e}_{\mathbf{q},\lambda}^{*} \cdot \frac{\partial \mathcal{K}(\mathbf{q})}{\partial q_x} \mathbf{e}_{\mathbf{q},\lambda'} \sqrt{\frac{a^6}{2m^2 \omega_{\mathbf{q},\lambda}^0 \omega_{\mathbf{q},\lambda'}^0}},$$

$$v_{\mathbf{q},4\lambda} = \mathbf{e}_{+} \cdot \frac{\partial \mathcal{D}(\mathbf{q})}{\partial q_x} \mathbf{e}_{\mathbf{q},\lambda} \sqrt{\frac{a^3}{2m \omega_{\mathbf{q},\lambda}^0}}.$$

(B.29)

The diagonal velocities $v_{\mathbf{q},\lambda} \equiv v_{\mathbf{q},\lambda\lambda}$ are equal to the phonon group velocities $v_{\mathbf{q},\lambda} = \partial \omega_{\mathbf{q},\lambda}^0 / \partial q_x$ whereas $v_{\mathbf{q},44} = \partial \omega_{\mathbf{q},4}^0 / \partial q_x$ is the magnon group velocity.

B.5 Inelastic scattering

The main contributions to inelastic magnon and phonon scattering are dominated by three-magnon, four-magnon, three-phonon, and two-magnon-phonon collisions. Here we show how these interactions can be obtained as sub-leading corrections to the isotropic and anisotropic exchange coupling, anisotropic corrections to the periodic lattice potential, and long-range dipole-dipole coupling.

Three-phonon interaction.— Instead of deriving a microscopic three-phonon interaction from an expansion of the lattice potential, we here use an effective description based on a continuum model [43],

$$H^{3\mathrm{p}} = \frac{1}{\sqrt{V}} \sum_{\mathbf{q},\lambda} \sum_{\mathbf{q}_2,\lambda_2} \sum_{\mathbf{q}',\lambda'} U_{\mathbf{q}\lambda,\mathbf{q}_2\lambda_2;\mathbf{q}'\lambda'}^{3\mathrm{p},0} (b_{\mathbf{q},\lambda}^{*} + b_{-\mathbf{q},\lambda})$$

$$\times (b_{\mathbf{q}_2,\lambda_2}^{*} + b_{-\mathbf{q}_2,\lambda_2})(b_{\mathbf{q}',\lambda'} + b_{-\mathbf{q}',\lambda'}^{*})$$

(B.30)

with the phonon-phonon scattering potential

$$U_{\mathbf{q}\lambda,\mathbf{q}_2\lambda_2;\mathbf{q}'\lambda'}^{3\mathrm{p},0} = \frac{1}{6} \left(\frac{\hbar a^3}{2m} \right)^{3/2} K' \delta_{\mathbf{q}+\mathbf{q}_2,\mathbf{q}'}$$

$$\times \frac{q q_2 q'}{\sqrt{\omega_{\mathbf{q},\lambda}^0 \omega_{\mathbf{q}_2,\lambda_2}^0 \omega_{\mathbf{q}',\lambda'}^0}}.$$

(B.31)

In general the anharmonicity constant $K' = K'_{\mathbf{q}\lambda,\mathbf{q}_2\lambda_2;\mathbf{q}'\lambda'}$ can itself be a complex function that depends on the crystal geometry. However it is argued in Ref. [43] that approximating the anharmonicity by a single momentum- and polarization-independent number

$$K' \simeq \frac{1}{3a}(K_1 + 2K_2) \tag{B.32}$$

is well suited for a simplified study. For our model parameters this gives $K' \simeq 2\times 10^{10}$ J/m^3.

Three-magnon interaction.— The magnon number non-conserving three-magnon collisions can be obtained from the sub-leading contributions of the Holstein-Primakoff expansion (3.4) of the pseudodipolar anisotropic exchange (3.6) and the dipole-dipole interaction (B.21). Omitting terms that create or annihilate three magnons, this gives

$$H^{3\mathrm{m}} = -\frac{1}{\sqrt{V}} \sum_{\mathbf{q}} U^{3\mathrm{m},0}_{\mathbf{q},\mathbf{q}_2;\mathbf{q}'} \sum_{\mathbf{q}_2} \sum_{\mathbf{q}'} a^*_{\mathbf{q}} a^*_{\mathbf{q}_2} a_{\mathbf{q}'} \tag{B.33}$$

with

$$U^{3\mathrm{m},0}_{\mathbf{q},\mathbf{q}_2;\mathbf{q}'} = U^{\mathrm{pd},0}_{\mathbf{q},\mathbf{q}_2;\mathbf{q}'} + U^{\mathrm{di},0}_{\mathbf{q},\mathbf{q}_2;\mathbf{q}'}. \tag{B.34}$$

The matrix element from anisotropic exchange reads, with the magnetization direction $\mathbf{e}$ along the (111) direction,

$$U^{\mathrm{pd},0}_{\mathbf{q},\mathbf{q}_2;\mathbf{q}'} = \frac{iDS^{1/2}a^{3/2}}{3}\delta_{\mathbf{q}+\mathbf{q}_2,\mathbf{q}'}$$
$$\times \sum_{\alpha}[\cos(aq_\alpha) + \cos(aq_{2\alpha})]w^2_\alpha, \tag{B.35}$$

where we defined

$$w_x = e^{-2i\pi/3}, \quad w_y = e^{2i\pi/3}, \quad w_z = 1. \tag{B.36}$$

The contribution from dipole-dipole interaction is [82, 80]

$$U^{\mathrm{di},0}_{\mathbf{q},\mathbf{q}_2;\mathbf{q}'} = \sqrt{2\pi^2 M_{\mathrm{s}}\mu^3}\left(\frac{q_z q_+}{q^2} + \frac{q_{2z}q_{2+}}{q_2^2}\right)\delta_{\mathbf{q}+\mathbf{q}_2,\mathbf{q}'}, \tag{B.37}$$

with $M_{\mathrm{s}} = \mu S/a^3$. Although the magnitude of the anisotropic exchange coupling is larger than the dipole-dipole interaction, due to the equality $\sum_\alpha w^2_\alpha = 0$ the leading-order contribution of anisotropic exchange vanishes in the long-wavelength limit, so that the dipole-dipole contribution is dominant.

Four-magnon interaction.— The magnon number conserving four-magnon collisions derive from the sub-leading contribution of the Holstein-Primakoff expansion of the Heisenberg exchange coupling (3.3). This gives the well-known expression [80],

$$H^{4\mathrm{m}} = \frac{1}{V}\sum_{\mathbf{q}}\sum_{\mathbf{q}_2}\sum_{\mathbf{q}'}\sum_{\mathbf{q}'_2} U^{4\mathrm{m},0}_{\mathbf{q},\mathbf{q}_2;\mathbf{q}',\mathbf{q}'_2} a^*_{\mathbf{q}} a^*_{\mathbf{q}_2} a_{\mathbf{q}'} a_{\mathbf{q}'_2} \tag{B.38}$$

with the symmetrized matrix element in the long-wavelength limit

$$U^{\text{4m,0}}_{\mathbf{q},\mathbf{q}_2;\mathbf{q}',\mathbf{q}'_2} = \sqrt{2}Ja^4(\mathbf{q}\cdot\mathbf{q}_2)\delta_{\mathbf{q}+\mathbf{q}_2,\mathbf{q}'+\mathbf{q}'_2}. \tag{B.39}$$

Two-magnon-phonon interaction.— Upon inclusion of exchange-based magnon-phonon coupling, the magneto-elastic coupling (B.19) is extended by spatial derivatives of the spin density [80],

$$H^{\text{me}} = \int \frac{dV}{a^3} \sum_{\alpha,\beta} (A_{\alpha\beta}e_{\alpha\beta}\partial_\alpha\mathbf{s}\cdot\partial_\beta\mathbf{s} + A'_{\alpha\beta}e_{\alpha\alpha}|\partial_\beta\mathbf{s}|^2), \tag{B.40}$$

where again all processes allowed by symmetry in a cubic crystal are taken into account. The coupling tensors are $A_{\alpha\beta} = A_1\delta_{\alpha\beta} + A_2(1-\delta_{\alpha\beta})$ and $A'_{\alpha\beta} = A'(1-\delta_{\alpha\beta})$.

In a simple model these processes can be reproduced by nearest and next-nearest-neighbor Heisenberg exchange coupling (3.3) as well as a next-nearest-neighbor neighbor transverse exchange coupling due to super-exchange via nearest-neighbors. As explained in detail in Sec. 3.2.1, magnon-phonon coupling appears when one takes into account that the magnitudes of the exchange couplings J_{ij}, D_{ij} depend on the precise positions of the lattice atoms. In a simple cubic lattice, symmetry requires that for nearest-neighbor sites i and j the isotropic exchange coupling J_{ij} depends on the distance $r_{ij} = |\mathbf{r}_i - \mathbf{r}_j|$ only. For small displacements $\mathbf{u}_j$ of the lattice atoms, the nearest-neighbor exchange coupling can then be approximated as

$$J \to J + J'\mathbf{u}_{ij}\cdot\mathbf{e}_{ij}, \tag{B.41}$$

where $\mathbf{e}_{ij} = (\mathbf{r}_i - \mathbf{r}_j)/|\mathbf{r}_i - \mathbf{r}_j|$ is the unit vector connecting lattice sites i and j and $J' = dJ/dr_{ij}$. We note that in general the strength of the exchange coupling J_2 between next-nearest-neighbor spins 1 and 2 not only depends on the displacements $\mathbf{u}_1$ and $\mathbf{u}_2$ of the positions of the spins 1 and 2, but (via super-exchange) also on the displacements $\mathbf{u}_3$ and $\mathbf{u}_4$ of the two lattice site positions intermediate between 1 and 2. Denoting the corresponding spatial derivatives by $J'_{2\|}$ and $J'_{2\perp}$, respectively, we find that upon inclusion of next-nearest-neighbor Heisenberg exchange the simple cubic model reproduces the full magneto-elastic magnon-phonon Hamiltonian (B.40), with

$$A_1 = \frac{a^3}{2}J' + \frac{a^3}{\sqrt{2}}(2J'_{2\|} + J'_{2\perp}),$$

$$A_2 = \frac{a^3}{\sqrt{2}}(2J'_{2\|} - J'_{2\perp}),$$

$$A_3 = \frac{a^3}{2\sqrt{2}}(2J'_{2\|} + J'_{2\perp}). \tag{B.42}$$

We specialize to an isotropic medium [87] with the choice $A_1 = A_2$ and $A_3 = 0$. This can be achieved by choosing the Heisenberg exchange constants as $J'_{2\perp} = -2J'_{2\parallel}$ and $J'_{2\parallel} = J'/4\sqrt{2}$. We find a magnon-phonon Hamiltonian of the form

$$H^{\mathrm{mp}} = \frac{1}{\sqrt{V}} \sum_{\mathbf{q},\lambda} \sum_{\mathbf{q}_2} \sum_{\mathbf{q}'} U^{\mathrm{mp},0}_{\mathbf{q},\mathbf{q}_2\lambda;\mathbf{q}'} b^*_{\mathbf{q}_2,4}(b^*_{\mathbf{q},\lambda} + b_{-\mathbf{q},\lambda})b_{\mathbf{q}',4} \tag{B.43}$$

with

$$U^{\mathrm{mp},0}_{\mathbf{q}\lambda,\mathbf{q}_2;\mathbf{q}'} = U^{\mathrm{ex},0}_{\mathbf{q}\lambda,\mathbf{q}_2;\mathbf{q}'} + U^{\mathrm{pd},0}_{\mathbf{q}\lambda,\mathbf{q}_2;\mathbf{q}'}. \tag{B.44}$$

In the continuum limit the matrix element from Heisenberg exchange reads

$$U^{\mathrm{ex},0}_{\mathbf{q}\lambda,\mathbf{q}_2;\mathbf{q}'} = J'Sa^3\sqrt{\frac{\hbar a^3}{8m\omega^0_{\mathbf{q},\lambda}}}i[(\mathbf{e}_{\mathbf{q},\lambda}\cdot\mathbf{q}')(\mathbf{q}\cdot\mathbf{q}_2)$$
$$+ (\mathbf{e}_{\mathbf{q},\lambda}\cdot\mathbf{q}_2)(\mathbf{q}\cdot\mathbf{q}')]\delta_{\mathbf{q}+\mathbf{q}_2,\mathbf{q}'}, \tag{B.45}$$

whereas the contribution from anisotropic exchange is

$$U^{\mathrm{pd},0}_{\mathbf{q}\lambda,\mathbf{q}_2;\mathbf{q}'} = -iD\sqrt{\frac{2\hbar S^2 a^3}{m\omega^0_{\mathbf{q},\lambda}}}\sum_{\alpha\neq\beta} q_\alpha e_{\mathbf{q}\lambda,\beta}. \tag{B.46}$$

To find a numerical value for the coupling constant J', we approximate $J' \approx J/a$.

Relativistic two-magnon-phonon interaction. — As the anisotropic exchange Hamiltonian does not conserve spin, besides the spin-conserving two-magnon-phonon contribution it also yields processes where a phonon is converted into two magnons via

$$H^{\mathrm{rel}} = \frac{1}{\sqrt{V}} \sum_{\mathbf{q},\lambda} \sum_{\mathbf{q}'} \sum_{\mathbf{q}'_2} U^{\mathrm{rel},0}_{\mathbf{q}\lambda;\mathbf{q}',\mathbf{q}'_2} b^*_{\mathbf{q},\lambda} b_{\mathbf{q}',4} b_{\mathbf{q}'_2,4}. \tag{B.47}$$

The matrix element in the long-wavelength limit is

$$U^{\mathrm{rel},0}_{\mathbf{q}\lambda;\mathbf{q}',\mathbf{q}'_2} = -i\sqrt{\frac{\hbar S^2 a^3}{18m\omega^0_{\mathbf{q},\lambda}}}\sum_{\alpha,\beta} q_\alpha w_\alpha w_\beta e_{\mathbf{q}\lambda,\beta}[2D(1-\delta_{\alpha,\beta}) - aD'\delta_{\alpha,\beta}], \tag{B.48}$$

where we again chose the magnetization direction $\mathbf{e}$ along the (111) direction.

Angle-independent models. — For a numerical computation of the inelastic relaxation rates, we replace the matrix elements of these four inelastic interaction channels by a phenomenological model, for which the matrix elements become statistical quantities with zero mean and with a variance chosen in such a way that the angle-averaged transition rates are the same as for the microscopic model. Specifically, for the three-phonon interactions, we set

$$\langle|U^{\mathrm{3p},0}_{\mathbf{q}\lambda,\mathbf{q}_2\lambda_2;\mathbf{q}'\lambda'}|^2\rangle = |u^{\mathrm{3p}}(\omega^0_{\mathbf{q}},\omega^0_{\mathbf{q}_2};\omega^0_{\mathbf{q}'})|^2, \tag{B.49}$$

where the variance $|u^{3\mathrm{p}}(\omega_{\mathbf{q}}^0, \omega_{\mathbf{q}2}^0; \omega_{\mathbf{q}'}^0)|^2$ is given by

$$
\begin{aligned}
|u^{3\mathrm{p}}(\omega, \omega_2; \omega')|^2 &= \frac{1}{V^3 \mathcal{E}_0^{\mathrm{p},0}(\omega) \mathcal{E}_0^{\mathrm{p},0}(\omega') \mathcal{E}_0^{\mathrm{p},0}(\omega_2)} \sum_{\mathbf{q},\lambda} \sum_{\mathbf{q}_2,\lambda_2} \sum_{\mathbf{q}',\lambda'} |U_{\mathbf{q}\lambda,\mathbf{q}_2\lambda_2;\mathbf{q}'\lambda'}^{3\mathrm{p},0}|^2 \\
&\quad \times \delta(\omega - \omega_{\mathbf{q},\lambda}^0)\delta(\omega_2 - \omega_{\mathbf{q}2,\lambda_2}^0)\delta(\omega' - \omega_{\mathbf{q}',\lambda'}^0),
\end{aligned}
\tag{B.50}
$$

where, on the right-hand side of this equation, the matrix element $U_{\mathbf{q}\lambda,\mathbf{q}_2\lambda_2;\mathbf{q}'\lambda'}^{3\mathrm{p},0}$ is taken from the microscopic model, see Eq. (B.31). The density of states $\mathcal{E}_0^{\mathrm{p},0}$ is defined as

$$
\mathcal{E}_0^{\mathrm{p},0}(\omega) = \frac{1}{V} \sum_{\mathbf{q},\lambda} \delta(\omega - \omega_{\mathbf{q},\lambda}^0).
\tag{B.51}
$$

By construction, in the absence of magnon-phonon coupling this change of the model results in the same relaxation matrix $\mathcal{G}^0$ as the microscopic model (B.31).

Similarly, for the three-magnon interaction, the four-magnon interaction, and the two-magnon-phonon interaction we set

$$
\begin{aligned}
\langle |U_{\mathbf{q},\mathbf{q}2;\mathbf{q}'}^{3\mathrm{m},0}|^2 \rangle &= |u^{3\mathrm{m}}(\omega_{\mathbf{q}}^0, \omega_{\mathbf{q}2}^0; \omega_{\mathbf{q}'}^0)|^2, \\
\langle |U_{\mathbf{q},\mathbf{q}2;\mathbf{q}',\mathbf{q}_2'}^{4\mathrm{m},0}|^2 \rangle &= |u^{4\mathrm{m}}(\omega_{\mathbf{q}}^0, \omega_{\mathbf{q}2}^0; \omega_{\mathbf{q}'}^0, \omega_{\mathbf{q}_2'}^0)|^2, \\
\langle |U_{\mathbf{q}\lambda,\mathbf{q}2;\mathbf{q}'}^{\mathrm{mp},0}|^2 \rangle &= |u^{\mathrm{mp}}(\omega_{\mathbf{q}}^0, \omega_{\mathbf{q}2}^0; \omega_{\mathbf{q}'}^0)|^2, \\
\langle |U_{\mathbf{q}\lambda;\mathbf{q}',\mathbf{q}_2'}^{\mathrm{rel},0}|^2 \rangle &= |u^{\mathrm{rel}}(\omega_{\mathbf{q}}^0; \omega_{\mathbf{q}'}^0, \omega_{\mathbf{q}_2'}^0)|^2,
\end{aligned}
\tag{B.52}
$$

with

$$
\begin{aligned}
|u^{3\mathrm{m}}(\omega, \omega_2; \omega')|^2 &= \frac{1}{V^3 \mathcal{E}_0^{\mathrm{m},0}(\omega) \mathcal{E}_0^{\mathrm{m},0}(\omega') \mathcal{E}_0^{\mathrm{m},0}(\omega_2)} \sum_{\mathbf{q}} \sum_{\mathbf{q}_2} \sum_{\mathbf{q}'} |U_{\mathbf{q},\mathbf{q}2;\mathbf{q}'}^{3\mathrm{m},0}|^2 \\
&\quad \times \delta(\omega - \omega_{\mathbf{q},4}^0)\delta(\omega_2 - \omega_{\mathbf{q}2,4}^0)\delta(\omega' - \omega_{\mathbf{q}',4}^0),
\end{aligned}
\tag{B.53}
$$

$$
\begin{aligned}
|u^{4\mathrm{m}}(\omega, \omega_2; \omega', \omega_2')|^2 &= \frac{1}{V^3 \mathcal{E}_0^{\mathrm{m},0}(\omega) \mathcal{E}_0^{\mathrm{m},0}(\omega') \mathcal{E}_0^{\mathrm{m},0}(\omega_2) \mathcal{E}_0^{\mathrm{m},0}(\omega_2')} \sum_{\mathbf{q}} \sum_{\mathbf{q}_2} \sum_{\mathbf{q}'} \sum_{\mathbf{q}_2'} |U_{\mathbf{q},\mathbf{q}2;\mathbf{q}',\mathbf{q}_2'}^{4\mathrm{m},0}|^2 \\
&\quad \times \delta(\omega - \omega_{\mathbf{q},4}^0)\delta(\omega_2 - \omega_{\mathbf{q}2,4}^0)\delta(\omega' - \omega_{\mathbf{q}',4}^0)\delta(\omega_2' - \omega_{\mathbf{q}_2',4}^0),
\end{aligned}
$$

$$
\begin{aligned}
|u^{\mathrm{mp}}(\omega, \omega_2; \omega')|^2 &= \frac{1}{V^3 \mathcal{E}_0^{\mathrm{p},0}(\omega) \mathcal{E}_0^{\mathrm{m},0}(\omega') \mathcal{E}_0^{\mathrm{m},0}(\omega_2)} \sum_{\mathbf{q},\lambda} \sum_{\mathbf{q}_2} \sum_{\mathbf{q}'} |U_{\mathbf{q}\lambda,\mathbf{q}2;\mathbf{q}'}^{\mathrm{mp},0}|^2 \\
&\quad \times \delta(\omega - \omega_{\mathbf{q},\lambda}^0)\delta(\omega_2 - \omega_{\mathbf{q}2,4}^0)\delta(\omega' - \omega_{\mathbf{q}',4}^0),
\end{aligned}
\tag{B.54}
$$

$$
\begin{aligned}
|u^{\mathrm{rel}}(\omega; \omega', \omega_2')|^2 &= \frac{1}{V^3 \mathcal{E}_0^{\mathrm{p},0}(\omega) \mathcal{E}_0^{\mathrm{m},0}(\omega') \mathcal{E}_0^{\mathrm{m},0}(\omega_2')} \sum_{\mathbf{q},\lambda} \sum_{\mathbf{q}'} \sum_{\mathbf{q}_2'} |U_{\mathbf{q}\lambda;\mathbf{q}',\mathbf{q}_2'}^{\mathrm{rel},0}|^2 \\
&\quad \times \delta(\omega - \omega_{\mathbf{q},\lambda}^0)\delta(\omega' - \omega_{\mathbf{q}',4}^0)\delta(\omega_2' - \omega_{\mathbf{q}_2',4}^0).
\end{aligned}
\tag{B.55}
$$

As before, the matrix elements $U_{\mathbf{q},\mathbf{q}2;\mathbf{q}'}^{3\mathrm{m},0}$, $U_{\mathbf{q},\mathbf{q}2;\mathbf{q}',\mathbf{q}_2'}^{4\mathrm{m},0}$, $U_{\mathbf{q}\lambda,\mathbf{q}2;\mathbf{q}'}^{\mathrm{mp},0}$, and $U_{\mathbf{q}\lambda;\mathbf{q}',\mathbf{q}_2'}^{\mathrm{rel},0}$ on the right-hand side of this equation are taken from the microscopic models, see Eqs. (B.34), (B.39), (B.44), and (B.48), respectively.

117

This replacement is motivated by practical considerations — since the absence of an angular dependence considerably simplifies the calculation of the inelastic rates — but also by the physical consideration that as long as impurity scattering is the dominant scattering process, the propagation direction of magnon-polaron modes is subject to fast fluctuations, calling for an effective description in terms of frequencies only. For the implementation in the angular summations in Eq. (3.71) we replace the frequency arguments $\omega_{\mathbf{q},\lambda}^0$ of the phonon modes and $\omega_{\mathbf{q},4}^0$ of the magnon mode by the frequency $\omega_{\mathbf{q},\nu}$ of the corresponding magnon-polaron mode.

B.6 No magnon-phonon coupling

Without magnon-phonon coupling and without inelastic processes, phonon and magnon modes obey separate linearized Boltzmann equations.

Magnons.— For the magnon mode, we denote the isotropic and anisotropic moments of the linearized distribution function by $\psi_{0,\mathrm{m}}(\omega)$ and $\psi_{1,\mathrm{m}}(\omega)$, respectively. The linearized Boltzmann equation for these moments reads

$$
\frac{\partial \psi_{1,\mathrm{m}}(\omega)}{\partial x} = 0,
$$
$$
\frac{\partial \psi_{0,\mathrm{m}}(\omega)}{\partial x} = -\mathcal{G}_{\mathrm{m}}^1(\omega)\psi_{1,\mathrm{m}}(\omega),
\tag{B.56}
$$

with

$$
\mathcal{G}_{\mathrm{m}}^1(\omega) = \frac{v_{\mathrm{m}}(\omega)}{3l_{\mathrm{mi}}(\omega)},
\tag{B.57}
$$

where the magnon-impurity length $l_{\mathrm{mi}}(\omega)$ is given in Eq. (3.57) and the magnon group velocity $v_{\mathrm{m}}(\omega) = \partial\omega_{\mathrm{m}}(q)/\partial q$, with $\omega_{\mathrm{m}}(q) = \mu B + JSa^2q^2$ the magnon frequency.

The magnon mode is fully reflected at the interface at $x = 0$,

$$
R_{\mathrm{m,m}}(\omega, \mathbf{q}_\perp) = 1,
\tag{B.58}
$$

whereas at the FN interface at $x = L$,

$$
R_{\mathrm{m,m}}(\omega, \mathbf{q}_\perp) = 1 - P_{4\mathrm{N}}(\omega, \mathbf{q}_\perp)
$$
$$
= \left| \frac{4\pi M_{\mathrm{s}} JSa^2 q_x(\omega, \mathbf{q}_\perp) - \mu\omega\sigma_{\uparrow\downarrow}}{4\pi M_{\mathrm{s}} JSa^2 q_x(\omega, \mathbf{p}_\perp) + \mu\omega\sigma_{\uparrow\downarrow}} \right|^2,
\tag{B.59}
$$

where

$$
q_x(\omega, \mathbf{q}_\perp) = \sqrt{\frac{\omega - \mu B}{JSa^2} - q_\perp^2}
\tag{B.60}
$$

is the x component of the wavevector of a magnon propagating towards the FN interface. The boundary conditions (3.80) and (3.82) at the IF and FN interfaces become

$$\psi_{1,\mathrm{m}}(\omega, 0) = 0,$$
$$\psi_{1,\mathrm{m}}(\omega, L) = \frac{3}{2}\frac{1 - \mathcal{R}_{0,\mathrm{m}}}{1 + \mathcal{R}_{1,\mathrm{m}}}[\psi_{0,\mathrm{m}}(\omega, L) - \psi_{\mathrm{N}}], \tag{B.61}$$

where $\mathcal{R}_{0,\mathrm{m}}$ and $\mathcal{R}_{1,\mathrm{m}}$ are angular averages of the reflection coefficient $R_{\mathrm{m,m}}$, see Eq. (3.81). The unique solution to these equations is

$$\psi_{0,\mathrm{m}}(\omega, x) = \psi_{\mathrm{N}}(\omega), \quad \psi_{1,\mathrm{m}}(\omega, x) = 0. \tag{B.62}$$

Phonons.— For the phonon modes, we use the label $\lambda = 1$ for the longitudinal mode and the labels $\lambda = 2, 3$ for the transverse phonon modes. The linearized Boltzmann equation for the isotropic and anisotropic moments $\psi_{0,\lambda}(\omega)$ and $\psi_{1,\lambda}(\omega)$ of the distribution function then reads

$$\frac{\partial \psi_{1,\lambda}(\omega)}{\partial x} = \sum_{\lambda'} \mathcal{G}_{\mathrm{p},\lambda,\lambda'}^0(\omega)[\psi_{0,\lambda'}(\omega) - \psi_{0,\lambda}(\omega)],$$
$$\frac{\partial \psi_{0,\lambda}(\omega)}{\partial x} = \sum_{\lambda'} \mathcal{G}_{\mathrm{p},\lambda,\lambda'}^1(\omega)[\psi_{1,\lambda'}(\omega) - \psi_{1,\lambda}(\omega)], \tag{B.63}$$

where the matrices $\mathcal{G}_{\mathrm{p}}^0$ and $\mathcal{G}_{\mathrm{p}}^1$ are

$$\mathcal{G}_{\mathrm{p}}^0 = \frac{3\tau_{\mathrm{pi}}(\omega)^{-1}}{c_{\mathrm{t}}^2(2c_{\mathrm{l}}^3 + c_{\mathrm{t}}^3)} \begin{pmatrix} 2c_{\mathrm{l}}c_{\mathrm{t}}^2 & -c_{\mathrm{l}}c_{\mathrm{t}}^2 & -c_{\mathrm{l}}c_{\mathrm{t}}^2 \\ -c_{\mathrm{t}}^3 & c_{\mathrm{l}}^3 + c_{\mathrm{t}}^3 & -c_{\mathrm{l}}^3 \\ -c_{\mathrm{t}}^3 & -c_{\mathrm{l}}^3 & c_{\mathrm{l}}^3 + c_{\mathrm{t}}^3 \end{pmatrix}, \tag{B.64}$$

$$\mathcal{G}_{\mathrm{p}}^1 = \tau_{\mathrm{pi}}(\omega)^{-1} \begin{pmatrix} 1 & 0 & 0 \\ 0 & 1 & 0 \\ 0 & 0 & 1 \end{pmatrix}. \tag{B.65}$$

Here c_{l} and c_{t} are the longitudinal and transverse phonon velocities and τ_{pi} is the mean scattering time for phonon-impurity scattering, see Eq. (3.59). The equilibration lengths λ_1 and λ_2 corresponding to Eq. (B.65) are

$$\lambda_1 = \tau_{\mathrm{pi}}\sqrt{\frac{c_{\mathrm{t}}^3 + 2c_{\mathrm{l}}^3}{3(2c_{\mathrm{l}} + c_{\mathrm{t}})}}, \quad \lambda_2 = \tau_{\mathrm{pi}}c_{\mathrm{t}}\sqrt{\frac{1}{3}}. \tag{B.66}$$

Without magnon-phonon coupling, phonon modes are fully transmitted at the interfaces, *i.e.*,

$$T_{\lambda\lambda'}(\omega, \mathbf{q}_\perp) = \delta_{\lambda\lambda'}, \quad R_{\lambda\lambda'}(\omega, \mathbf{q}_\perp) = 0, \quad \lambda = 1, 2, 3. \tag{B.67}$$

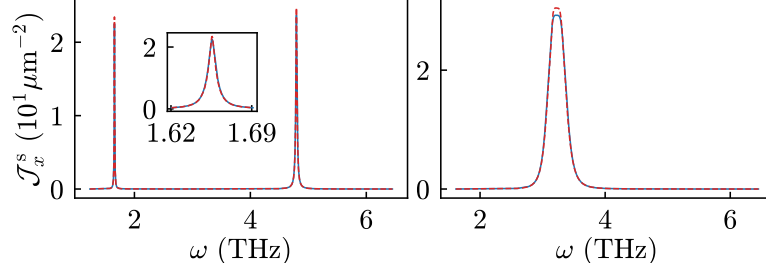Figure B.1: Frequency-resolved spin current $j_x^{\mathrm{s}}(\omega) = \hbar \mathcal{J}_x^{\mathrm{s}}(\omega) \Delta T / T$ for $T = 10\,\mathrm{K}$ at the FN interface for $B = 7\,\mathrm{T}$ (left) and for $B = 9.2\,\mathrm{T}$ (right), calculated from the short-length prediction (3.99) based on the ansatz (3.45) (blue, solid) and the exact result based on Eq. (B.70) (red, dashed). System parameters are taken from Table 3.1. The magnetic field $B = 9.2\,\mathrm{T}$ is the highest magnetic field for which the dispersions of magnons and phonons touch.

The boundary conditions at the IF and FN interfaces at $x = 0$ and $x = L$ are then found to be

$$\psi_{1,\lambda}(\omega, 0) = \frac{3}{2}[\psi_{\mathrm{I}} - \psi_{0,\lambda}(\omega, 0)],$$

$$\psi_{1,\lambda}(\omega, L) = \frac{3}{2}[\psi_{0,\lambda}(\omega, L) - \psi_{\mathrm{N}}]. \tag{B.68}$$

For short systems with length $L \ll \lambda_1$, the solution for the phonon distribution function is $\psi_{0,\lambda} = (\psi_{\mathrm{I}} + \psi_{\mathrm{N}})/2$. For a long system with length $L \gg \lambda_2$, the solution is $\psi_{0,\lambda} = \psi_{\mathrm{I}} + (\psi_{\mathrm{N}} - \psi_{\mathrm{I}})x/L$. A small correction near the FN interface can be obtained from Eq. (3.97) upon taking Eq. (B.65) for the matrices $\mathcal{G}_1$ and $\mathcal{G} = \sqrt{\mathcal{G}_1 \mathcal{G}_0}$ and replacing $\mathbf{u}_{0,0}$ by the three-component vector $(1, 1, 1)^{\mathrm{T}}$.

B.7 Ballistic systems

Strictly speaking the linearization of the polaron distribution with one isotropic and one anisotropic moment as in Eq. (3.45) is only applicable in the diffusive regime. For very short systems the transport is ballistic and the polarons only scatter off the interfaces. In this limit the distributions for left and right moving polarons can be solved directly using the boundary conditions (3.75) and (3.78), without making the ansatz (3.45). Parameterizing wavevectors $\mathbf{q}$ via the frequency ω, the transverse momentum $\mathbf{q}_\perp$, and the propagation direction, the linear-response ansatz for the distribution function reads

$$n_\nu(\omega, \mathbf{q}_\perp, \pm) = n^0(\omega) + \omega \left(-\frac{\partial n^0}{\partial \omega}\right) \psi_\nu(\omega, \mathbf{q}_\perp, \pm). \tag{B.69}$$

To solve for the distribution function, we use a four-component vector notation,

$$\boldsymbol{\psi}(\omega, \mathbf{q}_\perp, +) = (\mathbb{1}_4 - R_\mathrm{I} R_\mathrm{N})^{-1} \tag{B.70}$$
$$\times \, [(\mathbb{1}_4 - R_\mathrm{I}) \boldsymbol{\psi}_\mathrm{I}(\omega) + R_\mathrm{I}(\mathbb{1}_4 - R_\mathrm{N}) \boldsymbol{\psi}_\mathrm{N}(\omega)],$$
$$\boldsymbol{\psi}(\omega, \mathbf{q}_\perp, -) = (\mathbb{1}_4 - R_\mathrm{I} R_\mathrm{N})^{-1} \tag{B.71}$$
$$\times \, [(\mathbb{1}_4 - R_\mathrm{N}) \boldsymbol{\psi}_\mathrm{N}(\omega) + R_\mathrm{N}(\mathbb{1}_4 - R_\mathrm{I}) \boldsymbol{\psi}_\mathrm{I}(\omega)].$$

Here we suppressed the arguments $(\omega, \mathbf{q}_\perp)$ of the matrices R_I and R_N. The corresponding frequency-resolved spin current density $j_x^\mathrm{s}(\omega)$ is, compare with Eq. (3.85),

$$j_x^\mathrm{s}(\omega) = \hbar \omega \left(-\frac{\partial n^0}{\partial \omega} \right) \sum_\nu \int \frac{d\mathbf{q}_\perp}{(2\pi)^3} P_{\nu\mathrm{N}}(\omega, \mathbf{q}_\perp)$$
$$\times \, \psi_\nu(\omega, \mathbf{q}_\perp, +). \tag{B.72}$$

In Fig. B.1 we compare the frequency-resolved spin current density calculated using the exact solution (B.70) and the spin current density based on the ansatz (3.45). While the approximate calculation differs quantitatively up to a factor ~ 1.05, all qualitative features are correctly reproduced.

Bibliography

[1] N. Ashcroft and N. Mermin, *Solid State Physics*. Harcourt College Publishers, New York, 1976, vol. 21.

[2] K. Uchida, S. Takahashi, K. Harii, J. Ieda, W. Koshibae, K. Ando, S. Maekawa, and E. Saitoh, "Observation of the spin seebeck effect," *Nature*, vol. 455, pp. 778–781, 2008.

[3] C. M. Jaworski, J. Yang, S. Mack, D. D. Awschalom, J. P. Heremans, and R. C. Myers, "Observation of the spin-seebeck effect in a ferromagnetic semiconductor," *Nature Materials*, vol. 9, pp. 898–903, September 2010.

[4] K. Uchida, J. Xiao, H. Adachi, J. Ohe, S. Takahashi, J. Ieda, T. Ota, Y. Kajiwara, H. Umezawa, H. Kawai, G. Bauer, S. Maekawa, and E. Saitoh, "Spin seebeck insulator," *Nature Materials*, vol. 9, pp. 894–897, 2010.

[5] K. Uchida, H. Adachi, T. Ota, H. Nakayama, S. Maekawa, and E. Saitoh, "Observation of longitudinal spin-seebeck effect in magnetic insulators," *Applied Physics Letters*, vol. 97, no. 17, p. 172505, 2010. [Online]. Available: http://dx.doi.org/10.1063/1.3507386

[6] K. Uchida, T. Nonaka, T. Kikkawa, Y. Kajiwara, and E. Saitoh, "Longitudinal spin seebeck effect in various garnet ferrites," *Phys. Rev. B*, vol. 87, p. 104412, Mar 2013. [Online]. Available: https://link.aps.org/doi/10.1103/PhysRevB.87.104412

[7] K. Uchida, M. Ishida, T. Kikkawa, A. Kirihara, T. Murakami, and E. Saitoh, "Longitudinal spin seebeck effect: from fundamentals to applications," *Journal of Physics: Condensed Matter*, vol. 26, no. 34, p. 343202, aug 2014. [Online]. Available: https://doi.org/10.1088%2F0953-8984%2F26%2F34%2F343202

[8] B. L. Giles, Z. Yang, J. S. Jamison, and R. C. Myers, "Long-range pure magnon spin diffusion observed in a nonlocal spin-seebeck geometry," *Phys. Rev. B*, vol. 92, p. 224415, Dec 2015. [Online]. Available: https://link.aps.org/doi/10.1103/PhysRevB.92.224415

[9] J. Shan, L. J. Cornelissen, N. Vlietstra, J. Ben Youssef, T. Kuschel, R. A. Duine, and B. J. van Wees, "Influence of yttrium iron garnet thickness and heater opacity on the nonlocal transport of electrically and thermally excited magnons," *Phys. Rev. B*, vol. 94, p. 174437, Nov 2016. [Online]. Available: https://link.aps.org/doi/10.1103/PhysRevB.94.174437

[10] L. J. Cornelissen, K. Oyanagi, T. Kikkawa, Z. Qiu, T. Kuschel, G. E. W. Bauer, B. J. van Wees, and E. Saitoh, "Nonlocal magnon-polaron transport in yttrium iron garnet," *Phys. Rev. B*, vol. 96, p. 104441, Sep 2017. [Online]. Available: https://link.aps.org/doi/10.1103/PhysRevB.96.104441

[11] K. Ganzhorn, T. Wimmer, J. Cramer, R. Schlitz, S. Geprägs, G. Jakob, R. Gross, H. Huebl, M. Kläui, and S. T. B. Goennenwein, "Temperature dependence of the non-local spin seebeck effect in yig/pt nanostructures," *AIP Advances*, vol. 7, no. 8, p. 085102, 2017. [Online]. Available: https://doi.org/10.1063/1.4986848

[12] J. Liu, L. J. Cornelissen, J. Shan, B. J. van Wees, and T. Kuschel, "Nonlocal magnon spin transport in yttrium iron garnet with tantalum and platinum spin injection/detection electrodes," *Journal of Physics D: Applied Physics*, vol. 51, no. 22, p. 224005, may 2018. [Online]. Available: https://doi.org/10.1088%2F1361-6463%2Faabf80

[13] K. Oyanagi, T. Kikkawa, and E. Saitoh, "Magnetic field dependence of the nonlocal spin seebeck effect in pt/yig/pt systems at low temperatures," *AIP Advances*, vol. 10, no. 1, p. 015031, 2020. [Online]. Available: https://doi.org/10.1063/1.5135944

[14] T. Kikkawa, K. Uchida, S. Daimon, Z. Qiu, Y. Shiomi, and E. Saitoh, "Critical suppression of spin seebeck effect by magnetic fields," *Phys. Rev. B*, vol. 92, p. 064413, Aug 2015. [Online]. Available: http://link.aps.org/doi/10.1103/PhysRevB.92.064413

[15] T. Kikkawa, K. Shen, B. Flebus, R. A. Duine, K. Uchida, Z. Qiu, G. E. W. Bauer, and E. Saitoh, "Magnon polarons in the spin seebeck effect," *Phys. Rev. Lett.*, vol. 117, p. 207203, Nov 2016. [Online]. Available: https://link.aps.org/doi/10.1103/PhysRevLett.117.207203

[16] J. Kimling, G.-M. Choi, J. T. Brangham, T. Matalla-Wagner, T. Huebner, T. Kuschel, F. Yang, and D. G. Cahill, "Picosecond spin seebeck effect," *Phys. Rev. Lett.*, vol. 118, p. 057201, Feb 2017. [Online]. Available: https://link.aps.org/doi/10.1103/PhysRevLett.118.057201

[17] T. S. Seifert, S. Jaiswal, J. Barker, S. T. Weber, I. Razdolski, J. Cramer, O. Gueckstock, S. F. Maehrlein, L. Nadvornik, S. Watanabe,

C. Ciccarelli, A. Melnikov, G. Jakob, M. Münzenberg, S. T. B. Goennenwein, G. Woltersdorf, B. Rethfeld, P. W. Brouwer, M. Wolf, M. Kläui, and T. Kampfrath, "Femtosecond formation dynamics of the spin seebeck effect revealed by terahertz spectroscopy," *Nature Communications*, vol. 9, no. 1, p. 2899, 2018. [Online]. Available: https://doi.org/10.1038/s41467-018-05135-2

[18] J. S. Jamison, Z. Yang, B. L. Giles, J. T. Brangham, G. Wu, P. C. Hammel, F. Yang, and R. C. Myers, "Long lifetime of thermally excited magnons in bulk yttrium iron garnet," *Phys. Rev. B*, vol. 100, p. 134402, Oct 2019. [Online]. Available: https://link.aps.org/doi/10.1103/PhysRevB.100.134402

[19] J. Xiao, G. E. W. Bauer, K. Uchida, E. Saitoh, and S. Maekawa, "Theory of magnon-driven spin seebeck effect," *Phys. Rev. B*, vol. 81, p. 214418, Jun 2010. [Online]. Available: http://link.aps.org/doi/10.1103/PhysRevB.81.214418

[20] B. Flebus, K. Shen, T. Kikkawa, K.-i. Uchida, Z. Qiu, E. Saitoh, R. A. Duine, and G. E. W. Bauer, "Magnon-polaron transport in magnetic insulators," *Phys. Rev. B*, vol. 95, p. 144420, Apr 2017. [Online]. Available: https://link.aps.org/doi/10.1103/PhysRevB.95.144420

[21] H. Adachi, K. Uchida, E. Saitoh, J. Ohe, S. Takahashi, and S. Maekawa, "Gigantic enhancement of spin seebeck effect by phonon drag," *Applied Physics Letters*, vol. 97, no. 25, p. 252506, 2010. [Online]. Available: http://dx.doi.org/10.1063/1.3529944

[22] J. Flipse, F. K. Dejene, D. Wagenaar, G. E. W. Bauer, J. B. Youssef, and B. J. van Wees, "Observation of the spin peltier effect for magnetic insulators," *Phys. Rev. Lett.*, vol. 113, p. 027601, Jul 2014. [Online]. Available: https://link.aps.org/doi/10.1103/PhysRevLett.113.027601

[23] S. Daimon, R. Iguchi, T. Hioki, E. Saitoh, and K.-i. Uchida, "Thermal imaging of spin peltier effect," *Nature Communications*, vol. 7, no. 1, p. 13754, 2016. [Online]. Available: https://doi.org/10.1038/ncomms13754

[24] Y. Ohnuma, M. Matsuo, and S. Maekawa, "Theory of the spin peltier effect," *Phys. Rev. B*, vol. 96, p. 134412, Oct 2017. [Online]. Available: https://link.aps.org/doi/10.1103/PhysRevB.96.134412

[25] K. Uchida, H. Adachi, T. An, T. Ota, M. Toda, B. Hillebrands, S. Maekawa, and E. Saitoh, "Long-range spin seebeck effect and acoustic spin pumping," *Nat Mater*, vol. 10, no. 10, pp. 737–741, 10 2011. [Online]. Available: http://dx.doi.org/10.1038/nmat3099

[26] M. Weiler, H. Huebl, F. S. Goerg, F. D. Czeschka, R. Gross, and S. T. B. Goennenwein, "Spin pumping with coherent elastic waves,"

Phys. Rev. Lett., vol. 108, p. 176601, Apr 2012. [Online]. Available: https://link.aps.org/doi/10.1103/PhysRevLett.108.176601

[27] N. I. Polzikova, S. G. Alekseev, V. A. Luzanov, and A. O. Raevskiy, "Electroacoustic excitation of spin waves and their detection due to the inverse spin hall effect," *Physics of the Solid State*, vol. 60, p. 2211, 2018.

[28] L. Zhang and Q. Niu, "Angular momentum of phonons and the einstein–de haas effect," *Phys. Rev. Lett.*, vol. 112, p. 085503, Feb 2014. [Online]. Available: https://link.aps.org/doi/10.1103/PhysRevLett.112.085503

[29] A. Rückriegel, S. Streib, G. E. W. Bauer, and R. A. Duine, "Angular momentum conservation and phonon spin in magnetic insulators," *Phys. Rev. B*, vol. 101, p. 104402, Mar 2020. [Online]. Available: https://link.aps.org/doi/10.1103/PhysRevB.101.104402

[30] L. J. Cornelissen, J. Liu, R. A. Duine, J. B. Youssef, and B. J. van Wees, "Long-distance transport of magnon spin information in a magnetic insulator at room temperature," *Nature Physics*, vol. 11, p. 1022, 2015.

[31] A. Rückriegel and R. A. Duine, "Long-range phonon spin transport in ferromagnet–nonmagnetic insulator heterostructures," *Phys. Rev. Lett.*, vol. 124, p. 117201, Mar 2020. [Online]. Available: https://link.aps.org/doi/10.1103/PhysRevLett.124.117201

[32] S. Hoffman, K. Sato, and Y. Tserkovnyak, "Landau-lifshitz theory of the longitudinal spin seebeck effect," *Phys. Rev. B*, vol. 88, p. 064408, Aug 2013. [Online]. Available: https://link.aps.org/doi/10.1103/PhysRevB.88.064408

[33] M. Schreier, A. Kamra, M. Weiler, J. Xiao, G. E. W. Bauer, R. Gross, and S. T. B. Goennenwein, "Magnon, phonon, and electron temperature profiles and the spin seebeck effect in magnetic insulator/normal metal hybrid structures," *Phys. Rev. B*, vol. 88, p. 094410, Sep 2013. [Online]. Available: http://link.aps.org/doi/10.1103/PhysRevB.88.094410

[34] H. Adachi, K. ichi Uchida, E. Saitoh, and S. Maekawa, "Theory of the spin seebeck effect," *Reports on Progress in Physics*, vol. 76, no. 3, p. 036501, Feb. 2013. [Online]. Available: https://doi.org/10.1088%2F0034-4885%2F76%2F3%2F036501

[35] S. M. Rezende, R. L. Rodríguez-Suárez, R. O. Cunha, A. R. Rodrigues, F. L. A. Machado, G. A. Fonseca Guerra, J. C. Lopez Ortiz, and A. Azevedo, "Magnon spin-current theory for the longitudinal spin-seebeck effect," *Phys. Rev. B*, vol. 89, p. 014416, Jan 2014. [Online]. Available: https://link.aps.org/doi/10.1103/PhysRevB.89.014416

[36] S. M. Rezende, R. L. Rodríguez-Suárez, R. O. Cunha, J. López Ortiz, and A. Azevedo, "Bulk magnon spin current theory for the longitudinal spin seebeck effect," *Journal of Magnetism and Magnetic Materials*, vol. 400, pp. 171 – 177, 2016. [Online]. Available: http://www.sciencedirect.com/science/article/pii/S0304885315304108

[37] L. J. Cornelissen, K. J. H. Peters, G. E. W. Bauer, R. A. Duine, and B. J. van Wees, "Magnon spin transport driven by the magnon chemical potential in a magnetic insulator," *Phys. Rev. B*, vol. 94, p. 014412, Jul 2016. [Online]. Available: https://link.aps.org/doi/10.1103/PhysRevB.94.014412

[38] A. Rückriegel, P. Kopietz, D. A. Bozhko, A. A. Serga, and B. Hillebrands, "Magnetoelastic modes and lifetime of magnons in thin yttrium iron garnet films," *Phys. Rev. B*, vol. 89, p. 184413, May 2014. [Online]. Available: http://link.aps.org/doi/10.1103/PhysRevB.89.184413

[39] C. Kittel, *Introduction to Solid State Physics*. John Wiley and Sons, Inc., New York, 2004.

[40] R. Schmidt and P. W. Brouwer, "Theory of the low-temperature longitudinal spin seebeck effect," *To be published*, 2020.

[41] R. Schmidt, F. Wilken, T. S. Nunner, and P. W. Brouwer, "Boltzmann approach to the longitudinal spin seebeck effect," *Phys. Rev. B*, vol. 98, p. 134421, Oct 2018. [Online]. Available: https://doi.org/10.1103/PhysRevB.98.134421

[42] D. Zhao and G. Tan, "A review of thermoelectric cooling: Materials, modeling and applications," *Applied Thermal Engineering*, vol. 66, no. 1, pp. 15–24, 2014. [Online]. Available: http://www.sciencedirect.com/science/article/pii/S1359431114000854

[43] J. M. Ziman, *Electrons and phonons*, ser. International series of monographs on physics. Oxford: Clarendon Press, 1960. [Online]. Available: https://cds.cern.ch/record/100360

[44] M. Beens, J. P. Heremans, Y. Tserkovnyak, and R. A. Duine, "Magnons versus electrons in thermal spin transport through metallic interfaces," *Journal of Physics D: Applied Physics*, vol. 51, no. 39, p. 394002, 2018. [Online]. Available: http://dx.doi.org/10.1088/1361-6463/aad520

[45] G. E. W. Bauer, E. Saitoh, and B. J. van Wees, "Spin caloritronics," *Nature Materials*, vol. 11, pp. 391–399, April 2012.

[46] A. Slachter, F. L. Bakker, J.-P. Adam, and B. J. van Wees, "Thermally driven spin injection from a ferromagnet into a non-magnetic metal,"

Nature Physics, vol. 6, no. 11, pp. 879–882, 2010. [Online]. Available: https://doi.org/10.1038/nphys1767

[47] A. Brataas, Y. V. Nazarov, and G. E. W. Bauer, "Finite-element theory of transport in ferromagnet–normal metal systems," *Phys. Rev. Lett.*, vol. 84, pp. 2481–2484, Mar 2000. [Online]. Available: https://link.aps.org/doi/10.1103/PhysRevLett.84.2481

[48] X. Waintal, E. B. Myers, P. W. Brouwer, and D. C. Ralph, "Role of spin-dependent interface scattering in generating current-induced torques in magnetic multilayers," *Phys. Rev. B*, vol. 62, pp. 12 317–12 327, Nov 2000. [Online]. Available: https://link.aps.org/doi/10.1103/PhysRevB.62.12317

[49] D. C. Ralph and M. D. Stiles, "Spin transfer torques," *Journal of Magnetism and Magnetic Materials*, vol. 320, no. 7, pp. 1190–1216, 2008. [Online]. Available: http://www.sciencedirect.com/science/article/pii/S0304885307010116

[50] Y. Tserkovnyak, A. Brataas, and G. E. W. Bauer, "Enhanced gilbert damping in thin ferromagnetic films," *Phys. Rev. Lett.*, vol. 88, p. 117601, 2002.

[51] ——, "Spin pumping and magnetization dynamics in metallic multilayers," *Phys. Rev. B*, vol. 66, p. 224403, Dec 2002. [Online]. Available: https://link.aps.org/doi/10.1103/PhysRevB.66.224403

[52] Y. Tserkovnyak, A. Brataas, G. E. W. Bauer, and B. I. Halperin, "Nonlocal magnetization dynamics in ferromagnetic heterostructures," *Rev. Mod. Phys.*, vol. 77, pp. 1375–1421, Dec 2005. [Online]. Available: https://link.aps.org/doi/10.1103/RevModPhys.77.1375

[53] A. Messiah, *Quantum Mechanics*. Dover Publications, 1999.

[54] M. I. D'yakonov and V. I. Perel', "Possibility of orienting electron spins with current," *JETP Lett.*, vol. 13, no. 11, pp. 467–469, 1971. [Online]. Available: http://www.jetpletters.ac.ru/ps/1587/article_24366.shtml

[55] J. E. Hirsch, "Spin hall effect," *Phys. Rev. Lett.*, vol. 83, pp. 1834–1837, Aug 1999. [Online]. Available: https://link.aps.org/doi/10.1103/PhysRevLett.83.1834

[56] J. Sinova, S. O. Valenzuela, J. Wunderlich, C. H. Back, and T. Jungwirth, "Spin hall effects," *Rev. Mod. Phys.*, vol. 87, pp. 1213–1260, Oct 2015. [Online]. Available: https://link.aps.org/doi/10.1103/RevModPhys.87.1213

[57] E. Saitoh, M. Ueda, H. Miyajima, and G. Tatara, "Conversion of spin current into charge current at room temperature: Inverse spin-hall effect,"

Applied Physics Letters, vol. 88, no. 18, p. 182509, 2006. [Online]. Available: http://dx.doi.org/10.1063/1.2199473

[58] S. O. Valenzuela and M. Tinkham, "Direct electronic measurement of the spin hall effect," *Nature*, vol. 442, no. 7099, pp. 176–179, 7 2006. [Online]. Available: http://dx.doi.org/10.1038/nature04937

[59] T. Kimura, Y. Otani, T. Sato, S. Takahashi, and S. Maekawa, "Room-temperature reversible spin hall effect," *Phys. Rev. Lett.*, vol. 98, p. 156601, Apr 2007.

[60] Y. K. Kato, R. C. Myers, A. C. Gossard, and D. D. Awschalom, "Observation of the spin hall effect in semiconductors," *Science*, vol. 306, no. 5703, pp. 1910–1913, 2004.

[61] J. Wunderlich, B. Kaestner, J. Sinova, and T. Jungwirth, "Experimental observation of the spin-hall effect in a two-dimensional spin-orbit coupled semiconductor system," *Phys. Rev. Lett.*, vol. 94, p. 047204, Feb 2005. [Online]. Available: https://link.aps.org/doi/10.1103/PhysRevLett.94.047204

[62] S. Zhang, "Spin hall effect in the presence of spin diffusion," *Phys. Rev. Lett.*, vol. 85, pp. 393–396, Jul 2000. [Online]. Available: https://link.aps.org/doi/10.1103/PhysRevLett.85.393

[63] S. Murakami, N. Nagaosa, and S.-C. Zhang, "Dissipationless quantum spin current at room temperature," *Science*, vol. 301, no. 5638, p. 1348, 09 2003. [Online]. Available: http://science.sciencemag.org/content/301/5638/1348.abstract

[64] J. Sinova, D. Culcer, Q. Niu, N. A. Sinitsyn, T. Jungwirth, and A. H. MacDonald, "Universal intrinsic spin hall effect," *Phys. Rev. Lett.*, vol. 92, p. 126603, Mar 2004. [Online]. Available: https://link.aps.org/doi/10.1103/PhysRevLett.92.126603

[65] Y.-T. Chen, S. Takahashi, H. Nakayama, M. Althammer, S. T. B. Goennenwein, E. Saitoh, and G. E. W. Bauer, "Theory of spin hall magnetoresistance," *Phys. Rev. B*, vol. 87, p. 144411, Apr 2013. [Online]. Available: https://link.aps.org/doi/10.1103/PhysRevB.87.144411

[66] M. Schreier, G. E. W. Bauer, V. I. Vasyuchka, J. Flipse, K.-i. Uchida, J. Lotze, V. Lauer, A. V. Chumak, A. A. Serga, S. Daimon, T. Kikkawa, E. Saitoh, B. J. van Wees, B. Hillebrands, R. Gross, and S. T. B. Goennenwein, "Sign of inverse spin hall voltages generated by ferromagnetic resonance and temperature gradients in yttrium iron garnet platinum bilayers," *Journal of Physics D: Applied Physics*, vol. 48, no. 2, p. 025001, 2014. [Online]. Available: http://dx.doi.org/10.1088/0022-3727/48/2/025001

[67] J. Sinova, S. O. Valenzuela, J. Wunderlich, C. H. Back, and T. Jungwirth, "Spin hall effects," *Rev. Mod. Phys.*, vol. 87, pp. 1213–1260, Oct 2015. [Online]. Available: https://link.aps.org/doi/10.1103/RevModPhys.87.1213

[68] K. Uchida, T. Ota, H. Adachi, J. Xiao, T. Nonaka, Y. Kajiwara, G. E. W. Bauer, S. Maekawa, and E. Saitoh, "Thermal spin pumping and magnon-phonon-mediated spin-seebeck effect," *Journal of Applied Physics*, vol. 111, no. 10, p. 103903, 2012. [Online]. Available: http://dx.doi.org/10.1063/1.4716012

[69] C. M. Jaworski, J. Yang, S. Mack, D. D. Awschalom, R. C. Myers, and J. P. Heremans, "Spin-seebeck effect: A phonon driven spin distribution," *Phys. Rev. Lett.*, vol. 106, p. 186601, May 2011. [Online]. Available: https://link.aps.org/doi/10.1103/PhysRevLett.106.186601

[70] M. Schmid, S. Srichandan, D. Meier, T. Kuschel, J.-M. Schmalhorst, M. Vogel, G. Reiss, C. Strunk, and C. H. Back, "Transverse spin seebeck effect versus anomalous and planar nernst effects in permalloy thin films," *Phys. Rev. Lett.*, vol. 111, p. 187201, Oct 2013. [Online]. Available: https://link.aps.org/doi/10.1103/PhysRevLett.111.187201

[71] K. Uchida, T. Nonaka, T. Ota, and E. Saitoh, "Longitudinal spin-seebeck effect in sintered polycrystalline (mn,zn)fe2o4," *Applied Physics Letters*, vol. 97, no. 26, p. 262504, 2010. [Online]. Available: http://dx.doi.org/10.1063/1.3533397

[72] T. Kikkawa, K. Uchida, Y. Shiomi, Z. Qiu, D. Hou, D. Tian, H. Nakayama, X. F. Jin, and E. Saitoh, "Longitudinal spin seebeck effect free from the proximity nernst effect," *Phys. Rev. Lett.*, vol. 110, p. 067207, Feb 2013. [Online]. Available: https://link.aps.org/doi/10.1103/PhysRevLett.110.067207

[73] M. Schreier, N. Roschewsky, E. Dobler, S. Meyer, H. Huebl, R. Gross, and S. T. B. Goennenwein, "Current heating induced spin seebeck effect," *Applied Physics Letters*, vol. 103, no. 24, p. 242404, 2020/10/06 2013. [Online]. Available: https://doi.org/10.1063/1.4839395

[74] N. Vlietstra, J. Shan, B. J. van Wees, M. Isasa, F. Casanova, and J. Ben Youssef, "Simultaneous detection of the spin-hall magnetoresistance and the spin-seebeck effect in platinum and tantalum on yttrium iron garnet," *Phys. Rev. B*, vol. 90, p. 174436, Nov 2014. [Online]. Available: https://link.aps.org/doi/10.1103/PhysRevB.90.174436

[75] S. Seki, T. Ideue, M. Kubota, Y. Kozuka, R. Takagi, M. Nakamura, Y. Kaneko, M. Kawasaki, and Y. Tokura, "Thermal generation of spin current in an

antiferromagnet," *Phys. Rev. Lett.*, vol. 115, p. 266601, Dec 2015. [Online]. Available: https://link.aps.org/doi/10.1103/PhysRevLett.115.266601

[76] S. M. Wu, W. Zhang, A. KC, P. Borisov, J. E. Pearson, J. S. Jiang, D. Lederman, A. Hoffmann, and A. Bhattacharya, "Antiferromagnetic spin seebeck effect," *Phys. Rev. Lett.*, vol. 116, p. 097204, Mar 2016. [Online]. Available: https://link.aps.org/doi/10.1103/PhysRevLett.116.097204

[77] J. Li, Z. Shi, V. H. Ortiz, M. Aldosary, C. Chen, V. Aji, P. Wei, and J. Shi, "Spin seebeck effect from antiferromagnetic magnons and critical spin fluctuations in epitaxial fef_2 films," *Phys. Rev. Lett.*, vol. 122, p. 217204, May 2019. [Online]. Available: https://link.aps.org/doi/10.1103/PhysRevLett.122.217204

[78] C. Kittel, *Quantum Theory of Solids.* John Wiley and Sons, Inc., New York, 1963.

[79] H. Bruus and K. Flensberg, *Many-body quantum theory in condensed matter physics - an introduction.* United States: Oxford University Press, 2004.

[80] A. G. Gurevich and G. A. Melkov, *Magnetization Oscillations and Waves.* CRC Press, Boca Raton, Florida, 1996.

[81] T. Holstein and H. Primakoff, "Field dependence of the intrinsic domain magnetization of a ferromagnet," *Phys. Rev.*, vol. 58, pp. 1098–1113, Dec 1940.

[82] M. Sparks, *Ferromagnetic-relaxation theory*, ser. McGraw-Hill advanced physics monograph series. McGraw-Hill, 1964.

[83] V. Cherepanov, I. Kolokolov, and V. L'vov, "The saga of yig: Spectra, thermodynamics, interaction and relaxation of magnons in a complex magnet," *Physics Reports*, vol. 229, no. 3, pp. 81–144, 1993.

[84] S. Demokritov, V. Demidov, O. Dzyapko, G. Melkov, A. Serga, B. Hillebrands, and A. Slavin, "Bose–einstein condensation of quasi-equilibrium magnons at room temperature under pumping," *Nature*, vol. 443, pp. 430–433, 2006.

[85] A. A. Serga, V. S. Tiberkevich, C. W. Sandweg, V. I. Vasyuchka, D. A. Bozhko, A. V. Chumak, T. Neumann, B. Obry, G. A. Melkov, A. N. Slavin, and B. Hillebrands, "Bose–einstein condensation in an ultra-hot gas of pumped magnons," *Nature Communications*, vol. 5, no. 1, p. 3452, 2014. [Online]. Available: https://doi.org/10.1038/ncomms4452

[86] M. I. Kaganov and V. M. Tsukernik, "Phenomenological Theory of Kinetic Processes in Ferromagnetic Dielectrics. II. Interaction of Spin Waves with Phonons," *Sovied Phys. JETP-USSR*, vol. 9, no. 1, pp. 151–156, 1959.

[87] A. I. Akhiezer, V. G. Bar'yakhtar, and M. I. Kaganov, "Spin Waves in Ferromagnets and Antiferromagnets. II," *Soviet Physics Uspekhi*, vol. 3, no. 5, pp. 661–676, 1961.

[88] S. Streib, N. Vidal-Silva, K. Shen, and G. E. W. Bauer, "Magnon-phonon interactions in magnetic insulators," *Phys. Rev. B*, vol. 99, p. 184442, May 2019. [Online]. Available: https://link.aps.org/doi/10.1103/PhysRevB.99.184442

[89] A. S. Sukhanov, M. S. Pavlovskii, P. Bourges, H. C. Walker, K. Manna, C. Felser, and D. S. Inosov, "Magnon-polaron excitations in the noncollinear antiferromagnet mn$_3$Ge," *Phys. Rev. B*, vol. 99, p. 214445, Jun 2019. [Online]. Available: https://link.aps.org/doi/10.1103/PhysRevB.99.214445

[90] F. Godejohann, A. V. Scherbakov, S. M. Kukhtaruk, A. N. Poddubny, D. D. Yaremkevich, M. Wang, A. Nadzeyka, D. R. Yakovlev, A. W. Rushforth, A. V. Akimov, and M. Bayer, "Magnon polaron formed by selectively coupled coherent magnon and phonon modes of a surface patterned ferromagnet," 2020.

[91] A. A. Serga, C. W. Sandweg, V. I. Vasyuchka, M. B. Jungfleisch, B. Hillebrands, A. Kreisel, P. Kopietz, and M. P. Kostylev, "Brillouin light scattering spectroscopy of parametrically excited dipole-exchange magnons," *Phys. Rev. B*, vol. 86, p. 134403, Oct 2012. [Online]. Available: https://link.aps.org/doi/10.1103/PhysRevB.86.134403

[92] A. A. Abrikosov, *Fundamentals of the Theory of Metals.* North-Holland, 1988.

[93] J. J. Sakurai, *Advanced Quantum Mechanics.* Pearson Education, Incorporated, 1967.

[94] E. Merzbacher, *Quantum Mechanics.* John Wiley and Sons, Inc., New York, 1998.

[95] R. Yahiro, T. Kikkawa, R. Ramos, K. Oyanagi, T. Hioki, S. Daimon, and E. Saitoh, "Magnon polarons in the spin peltier effect," *Phys. Rev. B*, vol. 101, p. 024407, Jan 2020. [Online]. Available: https://link.aps.org/doi/10.1103/PhysRevB.101.024407

[96] S. M. Rezende, R. L. Rodríguez-Suárez, J. C. Lopez Ortiz, and A. Azevedo, "Thermal properties of magnons and the spin seebeck effect in yttrium iron garnet/normal metal hybrid structures," *Phys. Rev. B*, vol. 89, p. 134406, Apr 2014. [Online]. Available: http://link.aps.org/doi/10.1103/PhysRevB.89.134406

[97] D. J. Sanders and D. Walton, "Effect of magnon-phonon thermal relaxation on heat transport by magnons," *Phys. Rev. B*, vol. 15, pp. 1489–1494, Feb 1977. [Online]. Available: http://link.aps.org/doi/10.1103/PhysRevB.15.1489

[98] P. L. Kapitza, "Heat transfer and superfluidity of helium ii," *Phys. Rev.*, vol. 60, pp. 354–355, Aug 1941. [Online]. Available: https://link.aps.org/doi/10.1103/PhysRev.60.354

[99] G. L. Pollack, "Kapitza resistance," *Rev. Mod. Phys.*, vol. 41, pp. 48–81, Jan 1969. [Online]. Available: http://link.aps.org/doi/10.1103/RevModPhys.41.48

[100] S. R. Boona and J. P. Heremans, "Magnon thermal mean free path in yttrium iron garnet," *Phys. Rev. B*, vol. 90, p. 064421, Aug 2014. [Online]. Available: https://link.aps.org/doi/10.1103/PhysRevB.90.064421

[101] D. Walton, J. E. Rives, and Q. Khalid, "Thermal transport by coupled magnons and phonons in yttrium iron garnet at low temperatures," *Phys. Rev. B*, vol. 8, pp. 1210–1216, Aug 1973. [Online]. Available: https://link.aps.org/doi/10.1103/PhysRevB.8.1210

[102] A. Azevedo, L. H. V. Leão, R. L. Rodríguez-Suárez, A. B. Oliveira, and S. M. Rezende, "dc effect in ferromagnetic resonance: Evidence of the spin-pumping effect?" *Journal of Applied Physics*, vol. 97, no. 10, p. 10C715, 2005. [Online]. Available: http://dx.doi.org/10.1063/1.1855251

[103] A. Kehlberger, U. Ritzmann, D. Hinzke, E.-J. Guo, J. Cramer, G. Jakob, M. C. Onbasli, D. H. Kim, C. A. Ross, M. B. Jungfleisch, B. Hillebrands, U. Nowak, and M. Kläui, "Length scale of the spin seebeck effect," *Phys. Rev. Lett.*, vol. 115, p. 096602, Aug 2015. [Online]. Available: http://link.aps.org/doi/10.1103/PhysRevLett.115.096602

[104] U. Ritzmann, D. Hinzke, A. Kehlberger, E.-J. Guo, M. Kläui, and U. Nowak, "Magnetic field control of the spin seebeck effect," *Phys. Rev. B*, vol. 92, p. 174411, Nov 2015. [Online]. Available: https://link.aps.org/doi/10.1103/PhysRevB.92.174411

[105] M. B. Jungfleisch, A. V. Chumak, A. Kehlberger, V. Lauer, D. H. Kim, M. C. Onbasli, C. A. Ross, M. Kläui, and B. Hillebrands, "Thickness and power dependence of the spin-pumping effect in $y_3fe_5o_{12}$/pt heterostructures measured by the inverse spin hall effect," *Phys. Rev. B*, vol. 91, p. 134407, Apr 2015. [Online]. Available: https://link.aps.org/doi/10.1103/PhysRevB.91.134407

[106] E.-J. Guo, J. Cramer, A. Kehlberger, C. A. Ferguson, D. A. MacLaren, G. Jakob, and M. Kläui, "Influence of thickness and interface on the low-temperature enhancement of the spin seebeck effect in yig films," *Phys. Rev. X*, vol. 6, p. 031012, Jul 2016. [Online]. Available: http://link.aps.org/doi/10.1103/PhysRevX.6.031012

[107] F. Keffer and R. Loudon, "Simple physical theory of spin wave interactions," *Journal of Applied Physics*, vol. 32, no. 3, pp. S2–S7, 1961.

[108] A. I. Akhiezer, V. G. Bar'yakhtar, and M. I. Kaganov, "Spin waves in ferro-magnets and antiferromagnets. i," *Soviet Physics Uspekhi*, vol. 3, no. 4, pp. 567–592, 1961.

[109] M. I. Kaganov and V. M. Tsukernik, "Phenomenological Theory of Kinetic Processes in Ferromagnetic Dielectrics," *Sovied Phys. JETP-USSR*, vol. 7, no. 6, pp. 1107–1112, 1958.

[110] A. Kamra, H. Keshtgar, P. Yan, and G. E. W. Bauer, "Coherent elastic excitation of spin waves," *Phys. Rev. B*, vol. 91, p. 104409, Mar 2015. [Online]. Available: https://link.aps.org/doi/10.1103/PhysRevB.91.104409

[111] K. Shen and G. E. W. Bauer, "Laser-induced spatiotemporal dynamics of magnetic films," *Phys. Rev. Lett.*, vol. 115, p. 197201, Nov 2015. [Online]. Available: https://link.aps.org/doi/10.1103/PhysRevLett.115.197201

[112] S. S.-L. Zhang and S. Zhang, "Spin convertance at magnetic interfaces," *Phys. Rev. B*, vol. 86, p. 214424, Dec 2012. [Online]. Available: https://link.aps.org/doi/10.1103/PhysRevB.86.214424

[113] ——, "Spin and charge transport induced by magnetization dynamics in diffusive ferromagnetic metals," *Phys. Rev. B*, vol. 82, p. 184423, Nov 2010. [Online]. Available: https://link.aps.org/doi/10.1103/PhysRevB.82.184423

[114] S. S. Shinozaki, "Specific heat of yttrium iron garnet from 1.5° to 4.2°k," *Phys. Rev.*, vol. 122, pp. 388–389, Apr 1961. [Online]. Available: http://link.aps.org/doi/10.1103/PhysRev.122.388

[115] Y. Kajiwara, K. Harii, S. Takahashi, J. Ohe, K. Uchida, M. Mizuguchi, H. Umezawa, H. Kawai, K. Ando, K. Takanashi, S. Maekawa, and E. Saitoh, "Transmission of electrical signals by spin-wave interconversion in a magnetic insulator," *Nature*, vol. 464, pp. 262–266, 2010.

[116] C. Du, H. Wang, P. C. Hammel, and F. Yang, "Y3fe5o12 spin pumping for quantitative understanding of pure spin transport and spin hall effect in a broad range of materials (invited)," *Journal of*

Applied Physics, vol. 117, no. 17, p. 172603, 2015. [Online]. Available: http://dx.doi.org/10.1063/1.4913813

[117] P. Yan, G. E. W. Bauer, and H. Zhang, "Energy repartition in the nonequilibrium steady state," *Phys. Rev. B*, vol. 95, p. 024417, Jan 2017. [Online]. Available: https://link.aps.org/doi/10.1103/PhysRevB.95.024417

[118] S. Geller and M. A. Gilleo, "The crystal structure and ferrimagnetism of yttrium-iron garnet, y3fe2(feo4)3," *Journal of Physics and Chemistry of Solids*, vol. 3, no. 1, pp. 30–36, 1957. [Online]. Available: http://www.sciencedirect.com/science/article/pii/0022369757900446

[119] M. A. Gilleo and S. Geller, "Magnetic and crystallographic properties of substituted yttrium-iron garnet, $3y_2o_3 \cdot xm_2o_3 \cdot (5-x)fe_2o_3$," *Phys. Rev.*, vol. 110, pp. 73–78, Apr 1958. [Online]. Available: https://link.aps.org/doi/10.1103/PhysRev.110.73

[120] C. Kittel, "Interaction of spin waves and ultrasonic waves in ferromagnetic crystals," *Phys. Rev.*, vol. 110, pp. 836–841, May 1958. [Online]. Available: https://link.aps.org/doi/10.1103/PhysRev.110.836

[121] A. I. Akhiezer, V. G. Bar'yakhtar, and S. V. Peletminskii, "Coupled magnetoelastic waves in ferromagnetic media and ferroacoustic resonance," *Sov. Phys. JETP*, vol. 9, p. 157, 1958.

[122] E. Schlömann, "Generation of phonons in high-power ferromagnetic resonance experiments," *Journal of Applied Physics*, vol. 31, no. 9, p. 1647, 1960.

[123] D. A. Bozhko, P. Clausen, G. A. Melkov, V. S. L'vov, A. Pomyalov, V. I. Vasyuchka, A. V. Chumak, B. Hillebrands, and A. A. Serga, "Bottleneck accumulation of hybrid magnetoelastic bosons," *Phys. Rev. Lett.*, vol. 118, p. 237201, Jun 2017. [Online]. Available: https://link.aps.org/doi/10.1103/PhysRevLett.118.237201

[124] H. Hayashi and K. Ando, "Spin pumping driven by magnon polarons," *Phys. Rev. Lett.*, vol. 121, p. 237202, Dec 2018. [Online]. Available: https://link.aps.org/doi/10.1103/PhysRevLett.121.237202

[125] J. Holanda, D. S. Maior, A. Azevedo, and S. M. Rezende, "Detecting the phonon spin in magnon–phonon conversion experiments," *Nature Physics*, vol. 14, p. 500, 2018.

[126] R. L. Douglass, "Heat transport by spin waves in yttrium iron garnet," *Phys. Rev.*, vol. 129, pp. 1132–1135, Feb 1963. [Online]. Available: https://link.aps.org/doi/10.1103/PhysRev.129.1132

[127] K. An, K. S. Olsson, A. Weathers, S. Sullivan, X. Chen, X. Li, L. G. Marshall, X. Ma, N. Klimovich, J. Zhou, L. Shi, and X. Li, "Magnons and phonons optically driven out of local equilibrium in a magnetic insulator," *Phys. Rev. Lett.*, vol. 117, p. 107202, Aug 2016. [Online]. Available: https://link.aps.org/doi/10.1103/PhysRevLett.117.107202

[128] M. Agrawal, V. I. Vasyuchka, A. A. Serga, A. D. Karenowska, G. A. Melkov, and B. Hillebrands, "Direct measurement of magnon temperature: New insight into magnon-phonon coupling in magnetic insulators," *Phys. Rev. Lett.*, vol. 111, p. 107204, Sep 2013. [Online]. Available: https://link.aps.org/doi/10.1103/PhysRevLett.111.107204

[129] Q. Xi, B. Liu, Z. Shi, T. Nakayama, J. Zhou, and B. Li, "Thermal relaxation of magnons and phonons near resonance points in magnetic insulators," *EPL*, vol. 129, p. 57001, 2020.

[130] A. J. Princep, R. A. Ewings, S. Ward, S. Tóth, C. Dubs, D. Prabhakaran, and A. T. Boothroyd, "The full magnon spectrum of yttrium iron garnet," *npj Quantum Materials*, vol. 2, no. 1, p. 63, 2017. [Online]. Available: https://doi.org/10.1038/s41535-017-0067-y

[131] L.-S. Xie, G.-X. Jin, L. He, G. E. W. Bauer, J. Barker, and K. Xia, "First-principles study of exchange interactions of yttrium iron garnet," *Physical Review B*, vol. 95, no. 1, pp. 014 423–, 2017.

[132] A. Kreisel, F. Sauli, L. Bartosch, and P. Kopietz, "Microscopic spin-wave theory for yttrium-iron garnet films," *The European Physical Journal B*, vol. 71, no. 1, p. 59, 2009. [Online]. Available: https://doi.org/10.1140/epjb/e2009-00279-y

[133] J. S. Plant, "'pseudo-acoustic' magnon dispersion in yttrium iron garnet," *Journal of Physics C: Solid State Physics*, vol. 16, no. 36, p. 7037, 1983. [Online]. Available: http://stacks.iop.org/0022-3719/16/i=36/a=019

[134] I. Dzyaloshinsky, "A thermodynamic theory of "weak" ferromagnetism of antiferromagnetics," *Journal of Physics and Chemistry of Solids*, vol. 4, no. 4, pp. 241–255, 1958. [Online]. Available: http://www.sciencedirect.com/science/article/pii/0022369758900763

[135] T. Moriya, "Anisotropic superexchange interaction and weak ferromagnetism," *Phys. Rev.*, vol. 120, pp. 91–98, Oct 1960. [Online]. Available: https://link.aps.org/doi/10.1103/PhysRev.120.91

[136] C. Kittel, "Physical theory of ferromagnetic domains," *Rev. Mod. Phys.*, vol. 21, pp. 541–583, Oct 1949. [Online]. Available: https://link.aps.org/doi/10.1103/RevModPhys.21.541

[137] O. S. Latcham, Y. I. Gusieva, A. V. Shytov, O. Y. Gorobets, and V. V. Kruglyak, "Controlling acoustic waves using magneto-elastic fano resonances," *App. Phys. Lett.*, vol. 115, p. 082403, 2019.

[138] J. H. van Vleck, "On the anisotropy of cubic ferromagnetic crystals," *Phys. Rev.*, vol. 52, pp. 1178–1198, Dec 1937. [Online]. Available: https://link.aps.org/doi/10.1103/PhysRev.52.1178

[139] F. Keffer, "Moriya interaction and the problem of the spin arrangements in βMnS," *Phys. Rev.*, vol. 126, pp. 896–900, May 1962. [Online]. Available: https://link.aps.org/doi/10.1103/PhysRev.126.896

[140] A. Kamra and G. E. W. Bauer, "Actuation, propagation, and detection of transverse magnetoelastic waves in ferromagnets," *Solid State Commun.*, vol. 198, p. 35, 2014.

[141] W. Strauss, "14 - magnetoelastic properties of yttrium-iron garnet," *Physical Acoustics*, vol. 4, pp. 211–268, 1968. [Online]. Available: http://www.sciencedirect.com/science/article/pii/B9780123956644500171

[142] Z. Qiu, K. Ando, K. Uchida, Y. Kajiwara, R. Takahashi, H. Nakayama, T. An, Y. Fujikawa, and E. Saitoh, "Spin mixing conductance at a well-controlled platinum/yttrium iron garnet interface," *Applied Physics Letters*, vol. 103, no. 9, p. 092404, 2013. [Online]. Available: https://doi.org/10.1063/1.4819460

[143] S. Datta, *Electronic Transport in Mesoscopic Systems*. Cambridge University Press, Cambridge, 2003.

[144] M. J. M. de Jong, "Transition from sharvin to drude resistance in high-mobility wires," *Phys. Rev. B*, vol. 49, pp. 7778–7781, Mar 1994. [Online]. Available: https://link.aps.org/doi/10.1103/PhysRevB.49.7778

[145] R. E. Troncoso, S. A. Bender, A. Brataas, and R. A. Duine, "Spin transport in thick insulating antiferromagnetic films," *Phys. Rev. B*, vol. 101, p. 054404, Feb 2020. [Online]. Available: https://link.aps.org/doi/10.1103/PhysRevB.101.054404

[146] B. Zare Rameshti and R. A. Duine, "Length scale for magnon-polaron formation from nonlocal spin transport," *Phys. Rev. B*, vol. 99, p. 060402, Feb 2019. [Online]. Available: https://link.aps.org/doi/10.1103/PhysRevB.99.060402

[147] E. Akkermans and G. Montambaux, *Mesoscopic Physics of Electrons and Photons*. Cambridge: Cambridge University Press, 2010.

[148] H. P. Breuer and F. Petruccione, *The theory of open quantum systems.* New York: Oxford University Press, 2002.

[149] A. E. Clark and R. E. Strakna, "Elastic constants of single-crystal yig," *Journal of Applied Physics*, vol. 32, no. 6, pp. 1172–1173, 1961. [Online]. Available: http://dx.doi.org/10.1063/1.1736184

[150] K. Shen, "Pure spin current in antiferromagnetic insulators," *Phys. Rev. B*, vol. 100, p. 094423, Sep 2019. [Online]. Available: https://link.aps.org/doi/10.1103/PhysRevB.100.094423

[151] H. T. Simensen, R. E. Troncoso, A. Kamra, and A. Brataas, "Magnon-polarons in cubic collinear antiferromagnets," *Phys. Rev. B*, vol. 99, p. 064421, Feb 2019. [Online]. Available: https://link.aps.org/doi/10.1103/PhysRevB.99.064421

[152] J. Barker and G. E. W. Bauer, "Thermal spin dynamics of yttrium iron garnet," *Phys. Rev. Lett.*, vol. 117, p. 217201, Nov 2016. [Online]. Available: https://link.aps.org/doi/10.1103/PhysRevLett.117.217201

[153] A. J. Princep, R. A. Ewings, S. Ward, S. Tóth, C. Dubs, D. Prabhakaran, and A. T. Boothroyd, "The full magnon spectrum of yttrium iron garnet," *npj Quantum Materials*, vol. 2, no. 1, p. 63, 2017. [Online]. Available: https://doi.org/10.1038/s41535-017-0067-y

[154] W. Yuan, J. Li, and J. Shi, "Spin current generation and detection in uniaxial antiferromagnetic insulators," *Applied Physics Letters*, vol. 117, no. 10, p. 100501, 2020/10/05 2020. [Online]. Available: https://doi.org/10.1063/5.0022391

[155] J. Li, C. B. Wilson, R. Cheng, M. Lohmann, M. Kavand, W. Yuan, M. Aldosary, N. Agladze, P. Wei, M. S. Sherwin, and J. Shi, "Spin current from sub-terahertz-generated antiferromagnetic magnons," *Nature*, vol. 578, no. 7793, pp. 70–74, 2020. [Online]. Available: https://doi.org/10.1038/s41586-020-1950-4

[156] S. M. Rezende, R. L. Rodríguez-Suárez, and A. Azevedo, "Theory of the spin seebeck effect in antiferromagnets," *Phys. Rev. B*, vol. 93, p. 014425, Jan 2016. [Online]. Available: https://link.aps.org/doi/10.1103/PhysRevB.93.014425

[157] S. M. Rezende, A. Azevedo, and R. L. Rodríguez-Suárez, "Magnon diffusion theory for the spin seebeck effect in ferromagnetic and antiferromagnetic insulators," *Journal of Physics D: Applied Physics*, vol. 51, no. 17, p. 174004, 2018. [Online]. Available: http://dx.doi.org/10.1088/1361-6463/aab5f8

[158] P. R. T. Ribeiro, F. L. A. Machado, M. Gamino, A. Azevedo, and S. M. Rezende, "Spin seebeck effect in antiferromagnet nickel oxide in wide ranges of

temperature and magnetic field," *Phys. Rev. B*, vol. 99, p. 094432, Mar 2019. [Online]. Available: https://link.aps.org/doi/10.1103/PhysRevB.99.094432

[159] D. Reitz, J. Li, W. Yuan, J. Shi, and Y. Tserkovnyak, "Spin seebeck effect near the antiferromagnetic spin-flop transition," *Phys. Rev. B*, vol. 102, p. 020408, Jul 2020. [Online]. Available: https://link.aps.org/doi/10.1103/PhysRevB.102.020408

[160] A. Akhiezer, V. Bar'yakthar, and S. Peletminskii, *Spin Waves*. North Holland, Amsterdam, 1968.

Selbstständigkeitserklärung

Name: Schmidt
Vorname: Rico

Ich erkläre gegenüber der Freien Universität Berlin, dass ich die vorliegende Dissertation selbstständig und ohne Benutzung anderer als der angegebenen Quellen und Hilfsmittel angefertigt habe. Die vorliegende Arbeit ist frei von Plagiaten. Alle Ausführungen, die wörtlich oder inhaltlich aus anderen Schriften entnommen sind, habe ich als solche kenntlich gemacht. Diese Dissertation wurde in gleicher oder ähnlicher Form noch in keinem früheren Promotionsverfahren eingereicht. Mit einer Prüfung meiner Arbeit durch ein Plagiatsprüfungsprogramm erkläre ich mich einverstanden.

_____   _____
Berlin, Datum   Rico Schmidt

Curriculum Vitae

Der Lebenslauf ist in der Online-Version aus Gründen des Datenschutzes nicht enthalten.

Acknowledgements

First and foremost I want to express my deep gratitude to Piet Brouwer who stepped in when the need was greatest after Tamara Nunner ended her academic career and I was left without a supervisor. His neverending optimism, patience, his extensive knowledge and intuition for physical phenomena, and the ability to visualize and explain his thoughts shaped the way I tackle problems.

Throughout my Bachelor and Master studies and the first half of my PhD Tamara Nunner mentored my academic career. I want to thank her for being a great supervisor and always taking her time to share her knowledge and ideas. Her enthusiasm and effort enabled me to do my PhD at the Freie Universität Berlin.

I also want to thank Felix von Oppen – not only for co-supervising my thesis but also for laying the foundation for the spin caloritronic projects when he co-led the project in the DFG priority program "Spin-caloric Transport".

Publications

This thesis is based on the following publications

- *Boltzmann approach to the longitudinal spin Seebeck effect*,
  R. Schmidt, F. Wilken, T. S. Nunner, and P. W. Brouwer,
  Phys. Rev. B **98**, 134421 (2018),
  `https://doi.org/10.1103/PhysRevB.98.134421`

- *Theory of the low-temperature longitudinal spin Seebeck effect*
  R. Schmidt and P. W. Brouwer,
  submitted to Phys. Rev. B

The following publication in preparation is not part of this thesis

- *Transient spin Seebeck effect in ferromagentic insulators*,
  R. Schmidt and P. W. Brouwer,
  in preparation